Iron Catalyst Supported on Carbon Nanotubes for Fischer-Tropsch Synthesis: Experimental and Kinetic Study

A thesis submitted to the

College of Graduate Studies and Research

in partial fulfillment of the requirements for the

Degree of Doctor of Philosophy (Ph.D.)

in the

Department of Chemical Engineering

University of Saskatchewan

By:

Mohammad Reza Malek Abbaslou

Permission to Use

In presenting this thesis in partial fulfillment of the requirements for a doctorate of philosophy degree from the University of Saskatchewan, I agree that the Libraries of this University may make it freely available for inspection. I also agree that permission for extensive copying of this thesis for scholarly purposes may be granted by Dr. Ajay K. Dalai who supervised my thesis, or in his absence, by the Head of the Chemical Engineering Department or the Dean of the College of Graduate Studies. It is understood that due recognition will be given to me and to the University of Saskatchewan in any use of the material within this thesis. Any copying, publication, or use of this thesis or parts of this thesis for financial gain is prohibited without my written permission.

Requests for permission to copy or to make other use of material in this thesis in whole or part should be addressed to:

Head of the Department of Chemical Engineering

University of Saskatchewan

Saskatoon, Saskatchewan

Canada, S7N 5A9

Acknowledgements

I would like to express my deep and sincere gratitude to my Ph.D. supervisor, Professor Ajay K. Dalai. His knowledge, encouragement, guidance and support have been of great value for me during my Ph.D. studies. I should acknowledge that without his support, I was not able to pursue my Ph.D. to completion.

I am deeply grateful to my M.Sc. supervisor and current research advisor, Professor Jafar Soltan at the University of Saskatchewan. His continuous supervision and mentoring with breakthrough ideas has extensively helped me since I have known him.

I warmly thank the members of my advisory committee, Drs. Evitts, Pugsley, Sumner and Wang, for their valuable comments which assisted me to improve the quality of my research project.

I appreciate valuable assistance that I received from the colleagues in the Catalysis and Reaction Engineering Laboratories, and the technicians and secretaries of the Chemical Engineering Department, University of Saskatchewan.

My profound appreciation and love goes to my parents. Although they live a few continents afar, their everlasting and close support was my hope and strength to overcome any problems.

Abstract

The main objectives of the present Ph.D. thesis are comprehensive studies on activity, selectivity and stability of iron catalysts supported on carbon nanotubes (CNTs) for Fischer-Tropsch (FT) reactions. In order to prepare iron catalyst supported on CNTs, it was necessary to study CNT synthesis in bulk scale. Therefore, a part of this research was devoted to the production and characterization of CNTs. High purity, aligned films of multi-walled carbon nanotubes were grown on quartz substrates by feeding a solution of ferrocene in toluene, in a carrier gas of Ar/H_2, into a horizontal chemical vapour deposition (CVD) reactor. Results for CNTs synthesized using a wide range of toluene concentrations indicated that, for carbon concentrations higher than ~9.6 mol/m^3, catalyst deactivation occurs due to encapsulation of iron metal particles.

As the first step of catalyst development for FT reactions a fixed bed micro-reactor system was built and the effects of acid treatment on the activity, product selectivity and stability of iron Fischer-Tropsch catalysts supported on carbon nanotubes were studied. The results of Raman analysis showed that the acid treatment increased the number of functional groups as anchoring sites for metal particles. Fe catalysts supported on CNTs which were pre-treated with nitric acid at 110^oC were more stable and active compared to the un-treated catalysts. In order to study the effects of catalytic metal site position on FT reactions, a method was developed to control the position of the deposited metal clusters on either the inner or outer surfaces of the CNTs. According to the results of the FT experiments, the catalyst with catalytic metal sites inside the pores exhibited higher selectivity (C_5^+ = 36 wt%) to heavier hydrocarbons compared to one with sites on the outer surfaces (C_5^+ = 24 wt%) . In addition, deposition of catalytic sites on the interior surfaces of the nanotubes resulted in a more stable catalyst.

The effects of pore diameter and structure of iron catalysts supported on CNTs on Fischer-Tropsch reaction rates and selectivities were also studied. In order to examine the effects of pore diameter, two types of CNTs with similar surface areas and different average pore sizes (12 and 63 nm) were prepared. It was found that the deposition of metal particles on the CNT with narrow pore size (in the range of larger than 10-15 nm) resulted in more active and selective catalyst due to higher degree of reduction and higher metal dispersion.

Promotion of the iron catalyst supported on CNTs with Molybdinium in the range of 0.5-1 wt % resulted in a more stable catalyst. Mo improves the stability of the iron catalyst by preventing the metal site agglomeration. Promotion of the iron catalysts with potassium increased the activity of FT and water-gas-shift reactions and the average molecular weight of the hydrocarbon products. Promotion of the iron catalyst supported on CNTs with 0.5% Cu and 1wt% K resulted in an active (5.6 mg HC/g-Fe.h), stable and selective catalyst (C_5^+ selectivity of 76%) which exhibited higher activity and better selectivity compared to the similar catalysts reported in the literature. Kinetic studies were conducted to evaluate reaction rate parameters using the developed potassium and copper promoted catalyst. It was found that the CO_2 inhibition is not significant for FT reactions. On the other hand, water effects and presence of vacant sites should be considered in the kinetic models. A first-order reaction model verified that the iron catalyst supported on CNTs is more active than precipitated and commercial catalysts.

The results of the present Ph.D. thesis research provide a map for designing catalysts using carbon nanotubes as a support. The key messages of the present thesis are as follows:

1- If the interaction of the metal site and support is strong, which poses negative effects on the catalytic performance, carbon nanotubes can be one solution.

2- Acid pre-treatments are required prior to impregnating nanotubes with metal salt solution. Also, the strong acid treatment should be used for deposition of catalytic sites inside the pores of nanotubes.

3- The structure and pore size of nanotubes have significant influence on the stability, activity and selectivity of the target catalyst.

4- The position of the catalytic sites has to be selected based on the type of reaction. In the case of Fischer-Tropsch reactions, the deposition of catalytic sites inside the pores of nanotubes results in higher activity, longer life span.

The outcome of this Ph.D. thesis has been published/submitted in the form of 13 journal papers, one patent, one technical report and presented at 11 conferences. The list of publications is given in Appendix A.

Table of Contents

List of Tables

List of Figures

Chapter 1

Introduction and Thesis Outline

- *Reza M. Malek Abbaslou, Jafar Soltan, Ajay K. Dalai, Review on Fischer-Tropsch Synthesis in Supercritical Media. Fuel Processing Technology. 90 (2009) 849-856*

In addition, a portion of this chapter was quoted in the following technical report:

- *Ajay K. Dalai and Reza M. Malek Abbaslou, Biomass conversion technologies to Fischer-Tropsch liquid fuel for transportation, report to NRCan Project, 62 pages (2006).*

Contribution of the Ph.D. Candidate

Literature review was performed by Reza Malek Abbaslou. Data interpretations were conducted by Reza Malek Abbaslou, with assistance from Drs. Soltan and Dalai. All written text was prepared by Reza Malek Abbaslou and discussed with Drs. Soltan and Dalai.

Contribution of this Chapter to the Overall Study

In Chapter 1, an overview on the history of Fischer-Tropsch (FT) process and related active catalysts, mechanism, reaction kinetics and reactors is presented. In addition, the objectives and outline of the thesis are discussed.

1.1 History of Fischer-Tropsch Synthesis

Fischer-Tropsch (FT) synthesis had a challenging history. From 1925 to 1945, the main development took place in Germany, mainly in Franz Fischer's laboratories and synthetic fuel plants during World War II. Between 1955 and 1970, the world energy scene was governed by a plentiful and cheap oil supply. As a result, only slight interest in FT synthesis survived with South African FT industry at Sasol based on extremely cheap and abundant domestic coal. In the 1970s and 1980s, there were forecasts about declining world oil reserves and oil sanctions by major oil producing countries. As a result, coal and heavy oil power plants were considered for production of clean syngas for methanol and FT synthesis [1].

During the last decade, there has been a renewed interest in the use of Fischer-Tropsch technology for the conversion of natural gas, coal and biomass to liquid fuels. Some of the factors are [2]:

a) an increase in the known and remote reserves of natural gas, b) environmental pressure to produce CO_2-neutral fuels from biomass, c) improvements in the cost-effectiveness of Fischer-Tropsch technology, d) escalating of crude oil price.

The use of synthesis gas provides the opportunity to supply a broad range of environmentally clean fuels and chemicals. Almost all hydrogen is manufactured from syngas and there has been a remarkable demand for this basic chemical. Methanol is the second largest consumer of syngas used as octane enhancers in automotive fuels.

The Fischer-Tropsch synthesis can be considered as the third largest consumer of syngas, mostly for transportation fuels and a growing feedstock source for chemicals. Direct application of syngas as fuel (and chemicals) and its use in Integrated Gasification Combined Cycle (IGCC) units are being studied in detail for the generation of electricity (and also chemicals) from biomass, coal and petroleum coke [3].

The price of crude is one of the key factors since the FT products must compete with those produced from crude oil. Despite the several commercial applications of FTS in South Africa, USA, China, Qatar and Malaysia, the wide spread application of FT has not been realized. The reason is embedded in the economic viability of FT plants based on crude oil price, which has varied considerably over the past years. In other words, a substantial ecomomic risk is associated with the construction of an FT complex. It has been estimated that the FT process is viable at crude oil prices of about $20 per barrel for natural gas to liquid fuels (GTL) and $50 for coal to liquid fuels (CTL) [4]. Considering the flactualtions in crude oil price and improvement in FT technology, the history of FT tells that FT plants are economically viable when enterprise is judged over extended periods of time, e.g. one or two decades [4].

1.2 Fischer-Tropsch Synthesis

Fischer-Tropsch synthesis is a catalytic reaction whereby CO and H_2 molecules react on the surface of an active metal (Co, Fe, Ru, Ni, etc.) to produce a variety of heavier gaseous, liquid, and solid hydrocarbons such as paraffins, olefins, wax and oxygenated compounds.

In FT reactions, the oxygen from CO dissociation is removed in the form of water. However, over iron catalysts a significant portion of the oxygen is also discarded as carbon dioxide. The removal of oxygen in the form of CO_2 is often described as a separate consecutive reaction, namely the water-gas-shift (WGS) reaction [5]. Possible reactions of synthesis gas are shown in Table 1.1.

The commercial process consists of three main sections, namely synthesis gas production and purification, Fischer-Tropsch synthesis, and product upgrading and refining. The synthesis gas preparation is about 66 % of the total capital costs. The FT

Table 1.1 Major overall reactions in the Fischer-Tropsch synthesis [5]

	Main Reactions
Paraffins Formation	$nCO + (2n+1)H_2 \rightarrow C_nH_{(2n+2)} + nH_2O$
Olefins Formation	$nCO + 2nH_2 \rightarrow C_nH_{2n} + nH_2O$
Water-Gas-Shift Reaction	$CO + H_2O \leftrightarrow CO_2 + H_2O$
	Side Reactions
Alcohols Formation	$nCO + 2nH_2 \rightarrow C_nH_{(2n+2)}O + (n-1)H_2O$
Boudouard Reaction	$2CO \leftrightarrow C + CO_2$

synthesis section, consisting of FT reactors, CO_2 removal, synthesis gas compression and recycle, and recovery of hydrogen and hydrocarbons, accounts for 22 % of the total costs. Finally, the hydrocarbon upgrading and refining is about 12 % [6]. Consequently, cost reduction of synthesis gas production is the most favourable. However, the efficiency and selectivity of the FT process directly affect the size of the syngas generation section resulting in direct and indirect improvements in economy of the FT process [5]. Similar to other classical catalytic reactions, composition of products depends on the catalysts and operating conditions employed.

1.3 Catalyst for FTS

1.3.1 Active Metal for FT Catalysts

The most common Fischer-Tropsch catalysts are group VIII metals (Co, Ru, and Fe). Iron catalysts have been used because of their low costs in comparison to other active metals (i.e. Co is 230 times more expensive than iron) [5]. The first-generation FT catalysts were prepared using precipitation techniques. New Fe catalyst preparation methods include sintering and fusion of metal oxides with desired promoters. Alkali-promoted iron catalysts have been in commercial uses for the Fischer-Tropsch synthesis for many years [7]. These catalysts provide a high water-gas-shift activity and high selectivity to olefins and show high stability when synthesis gas with a high H_2/CO ratio is converted [5].

Cobalt catalysts produce mainly linear alkanes and give the highest activity and longest lifetime. Supported cobalt catalysts are the standard catalyst for commercial applications. Drawbacks are the high costs of cobalt and low water-gas shift activity. Therefore, cobalt catalysts are favoured for natural-gas-based Fischer-Tropsch processes for the production of middle distillates and high-molecular-weight products.

1.3.2 Catalyst Support

The goal of adding a support is to offer a large surface area for the formation and stabilization of small metal crystallites in the catalyst. Due to strong metal-support interactions the support may also have major effects on the catalyst activity and selectivity. In fact the chemical nature of the support, its texture and surface acidity can influence metal dispersion, properties of reduction, as well as the interaction between metal and support. In the case of iron catalyst for FT reaction, supports are added as a binder to increase the physical properties of catalyst against attrition [8]. Figure 1.1 shows typical iron and cobalt catalysts supported on alumina. Due to the high cost of cobalt, this metal should be dispersed over a support. For both cobalt and iron catalysts, the type of support, porosity, surface properties and corresponding metal-support interactions may result in different catalytic performances [9].

Noticeable discrepancies on the effects of the support on activity and selectivity of supported catalysts for FT reactions have been reported in the literature. Reuel and Bartholomew (1984) have shown an increase in specific activity with similar Co loading on the different supports [10]. Vanhove et al. [11] reported that the chain length of hydrocarbons was relative to the mean pore diameter of the supports in Co/Al_2O_3 catalysts. Ernst et al. (1998) found that the activity for $CO + H_2$ reaction increased with

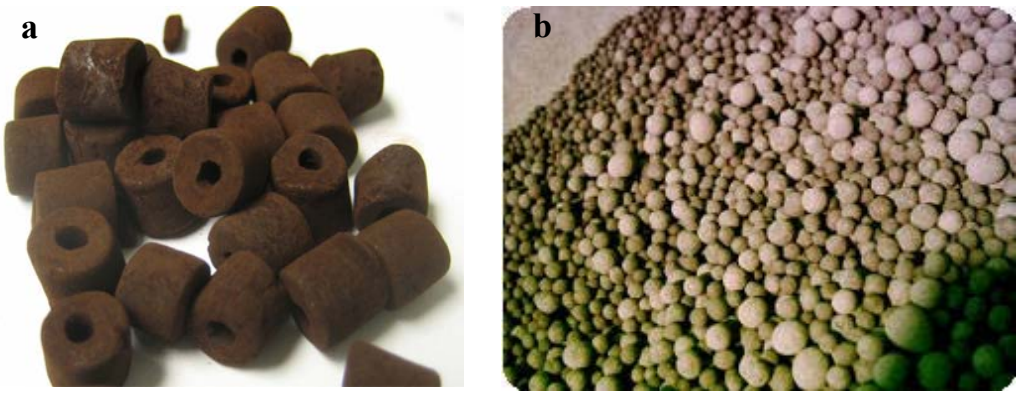

Figure 1.1 Fischer Tropsch catalysts on alumina support a) Fe catalysts b) Co catalysts (www.ceramatec.com/images/Fe-based-ft-catalyst.jpg and www.sarvco.ir/productsCAT.html)

the specific surface area [12]. In addition, the selectivity for high molecular weight hydrocarbons was favoured in the case of catalyst with pore diameter of the support less than 4.0 nm. The studies of Iglesia (1997) showed that the selectivity differences actually arise from an effect of support physical structure on the extent of α-olefin (reactive intermediates) re-adsorption [13]. Khodakov et al. (2002) reported that supports with large pore diameter led to significantly higher C_5^+ selectivities due to different cobalt particle size and reducibility in the wide pore and narrow-pore silica [14]. Jacobs et al. (2002) reported significant support interactions on the reduction of cobalt oxide species in the order $Al_2O_3 > TiO_2 > SiO_2$ [15].

For iron catalysts, it has been shown that the specific FT activity decreased with increasing support content, which may be ascribed to a lower degree of iron reduction and decrease in the effective potassium content of the catalyst. However, the catalyst stability improved with the addition of silica because of the stabilization of iron crystallites during synthesis [16]. O'Brien et al. (2000) have shown that for CO conversions up to about 50%, the iron catalyst is as or more active than supported cobalt catalyst on the same mass basis [17]. Snel (1989) reported that for alumina-silica

supported iron catalysts, the products were always significantly lighter than that produced by unsupported iron catalyst [18]. Differences are attributed to the extent of metal-support interaction and the resulting changes in reducibility. It can be concluded that for traditional supported iron catalysts (alumina and silica) strong metal support interactions result in lower activity along with selectivity toward lighter hydrocarbons.

1.3.3 Catalyst Pre-treatment

The catalysts, synthesized in the form of a metal oxide, are subjected to an activation treatment prior to FT synthesis. Cobalt, nickel, and ruthenium are reduced in H_2 at temperatures between 473 and 723 K. Before reduction, the cobalt is present as the Co_3O_4 spinel phase. A two-step reduction by H_2 of Co_3O_4 to CoO and to Co^0 was observed [5].

Three different methods have been reported and used for pre-treatment and activation of iron catalysts. The common activation treatments for iron catalysts are H_2 reduction, CO reduction, or reduction in synthesis gas (induction). The CO activated catalyst showed the highest conversion while hydrogen activation resulted in the lowest activity [5].

1.4 Classification of FT Processes

Different types of FT processes can be classified based on catalyst, the temperature range, the phases present inside the reactor (i.e. gas-solid or gas-liquid-solid) or the type of reactor. For example, Sasol has commercially developed three distinctly different types of FT processes [19]. The iron-based Low-Temperature Fischer-Tropsch (Fe-LTFT) synthesis is typically performed in the temperature range of 220°C to 270°C and the majority of products are long chain molecules where the reactor is operated with three phases inside the reactor. Another FT system is the cobalt-based Low-Temperature

Fischer- Tropsch (Co-LTFT) synthesis operating towards the lower end of this temperature range which produces a similar product distribution. Either multi-tubular packed bed reactors or slurry phase reactors can be utilized for these two LTFT syntheses. The iron-based High-Temperature Fischer-Tropsch (Fe-HTFT) synthesis is operated at temperatures well above 300°C. A large portion of products is light hydrocarbons that are essentially in the gas phase under the conditions inside the reactor. This two-phase system has been commercially operated in fluidized bed reactors.

1.5 Deactivation

There are many deactivation mechanisms for catalysts, but they can be categorized into six intrinsic mechanisms: (i) poisoning, (ii) fouling, (iii) thermal degradation, (iv) vapor compound formation accompanied by transport, (v) vapor-solid and/or solid-solid reactions, and (vi) attrition/ crushing [20].

Deactivation of iron catalysts during FT reactions has been controversial. Four main mechanisms of deactivation have been described in the literature:

1. It is reported that active iron phases (Fe_xC or metallic α-Fe) are transformed to catalytically less active or inactive phases. It is mostly believed that the active phase is gradually oxidized to magnetite (Fe_3O_4), which is inactive in FT synthesis. It is also proposed that one kind of iron carbide species may be converted to another type of inactive carbide phase [21].
2. The second mechanism proposes that sintering or the loss of catalytic surface area due to ripening or migration and coalescence of the iron phase is a main cause for the deactivation [21].

3. It is also reported that the deposition of inactive carbonaceous compounds (e.g., graphitic carbon, amorphous carbon, coke) on the surface of the catalyst can be one reason for iron catalyst deactivation under FT operating conditions [21].

4. Finally, it has been shown that iron-based catalysts are poisoned and deactivated by sulphur compounds which are present in industrial syngas feeds. [21].

It should be noted that one, or combinations of the aforementioned mechanisms are reported as responsible factors for deactivation of iron catalysts. Supported cobalt catalysts deactivate during extended periods of continuous Fischer-Tropsch synthesis. This deactivation can be due to surface condensation, sulphur poisoning, and oxidation [22].

1.6 Selectivity of FT Reactions

The main feature of FT reactions is the unavoidable production of a wide range of hydrocarbon products. The intrinsic kinetic characteristic of the FTS is stepwise chain growth by which a polymerization of -CH_2- groups on the catalyst surface takes place. [5].

Sixty years ago, Friedel and Anderson [23] showed that plots of $\log(W_n)$ against the carbon number n fit straight lines (W_n is the mass fraction of a particular product). This means that the probability of chain growth α is fundamentally constant. Equation 1.1 is now generally known as the Anderson-Schulz-Flory (ASF) equation:

$$\log\frac{Wn}{n} = n\log\alpha + \log\frac{(1-\alpha)^2}{\alpha} \qquad (1.1)$$

Table 1.2 Selectivity Control in Fischer-Tropsch Synthesis by Process Conditions and Catalyst Modifications [5]

Parameter ↑	Chain Length	Chain Branching	Olefin Selectivity	Alcohol Selectivity	Carbon Deposition	Methane Selectivity
Temperature	↓	↑	×	↓	↑	↑
Pressure	↑	↓	×	↑	×	↓
H_2/CO	↓	↑	↓	↓	↓	↑
Conversion	×	×	↓	↓	↑	↑
Space velocity	×	×	↑	↑	×	↓
Alkali content Iron catalyst	↑	↓	↑	↑	↑	↓

× No effect

Numerous FT studies support that the ASF equation predicts the proportions of methane, to gasoline, to diesel, and waxes. In contrast, according to many practical applications of FT processes, there is an apparent change in the slope of α plots around C_{10} giving two α values, with the second always higher than the first [5].

1.7 Influence of Process Conditions on Selectivity

The process conditions as well as the catalyst can affect the catalyst selectivity. The effect of temperature, partial pressures of H_2 and CO and space velocity will be discussed briefly. Table 1.2 shows the general influences of different parameters on the selectivity [5].

1.7.1 Temperature

An increase in temperature leads to products with a lower carbon number on iron, ruthenium, and cobalt catalysts. Dictor and Bell (1986) reported a decline in the olefin selectivity with increasing temperature for iron oxide powders containing no alkali [24]. However, Donnelly and Satterfield (1989) found an increase in the olefin-to-paraffin ratio on potassium promoted precipitated iron catalysts with increasing temperature [25].

1.7.2 Partial Pressure of H_2 and CO

Most of the studies in the literatur reports that the product selectivity shifts to heavier products and to more oxygenate with increasing total pressure. Lighter hydrocarbons and lower olefin content are favored by increasing H_2/CO ratios [5].

1.7.3 Space Velocity

The selectivity to methane and olefins decreases with a decrease of the space velocity, meanwhile the selectivity towards paraffins remains unaffected [5].

1.7.4 Water Effects on FT Reactions

One of the products of the FT synthesis is water, which is present in varying amounts during synthesis, depending on the conversion, reactor system and catalyst. In the case of iron catalysts it has been shown that water and CO_2 may re-oxidize iron during synthesis [26]. Iron-based catalysts favor extremely the water-gas-shift reaction, and hence the partial pressure of water may have strong unwanted effects on the rate of reaction [27]. There are diffrent views on the effect of water on the activity of cobalt catalysts in FT process. A critical review on the effects of water on cobalt catalyst has been reported by Dalai and Davis (2008) [28].

Water vapor has a significant effect on the reduction behavior of various Co-supported catalysts. Added water vapor has a positive effect on unsupported Co_3O_4 catalyst. In the case of supported Co catalysts, the extent of the effect depends on the amount of water present in the reactor as well as the presence of noble metal promoters such as Pt, Ru, Re, etc. In general, for silica supported catalysts, water effects are positive in the case of higher CO conversion where as for alumina, the effects are negative. For titania supported catalysts, water had little or no impact. In cases of alumina and titania, there are two regimes in which water influences activity, a low

partial pressure regime ($P_{H2O} / P_{H2} < 0.6$) where the effects of water are reversible and at higher pressure regime ($P_{H2O} / P_{H2} > 0.6$) where the effects of water are irreversible [28].

1.8 Reaction Mechanism

The Fischer-Tropsch reaction mechanism has been, and still is, a topic of discussion. There are several detailed reviews on the mechanism and models of hydrocarbon and oxygenate formation during FT reactions [5,9, 29-32]. In general, six elementary reaction steps have been considered for all mechanisms proposed in the literature:

1. Reactant adsorption,
2. Chain initiation,
3. Chain growth,
4. Chain termination,
5. Product adsorption,
6. Re-adsorption and further reaction.

Steps 2 through 4 follow the Anderson-Schulz-Flory (ASF) kinetics model. The final elementary reaction step, re-adsorption, has also been discussed in the literature [21]. Repeatedly, abnormalities have been reported in the ASF product distribution as a result of re-adsorption and reaction of FTS reaction products [5]. In other words, these products can be incorporated into other growing hydrocarbon chains resulting in higher weight hydrocarbon chains. For iron catalysts, three mechanisms have been proposed and used as follows:

1.8.1 Surface Carbide Mechanism

The surface carbide mechanism is the first and perhaps most accepted mechanism for FT reactions on iron [32]. Based on this mechanism, the reactions start with

dissociative adsorption of CO and H_2. This is followed by the formation of CH_2 entities which can combine and insert in growing chains. Abstraction or addition of a hydrogen atom from or to the growing chain terminates the chain growth. In this mechanism, the CH_2 species can be considered either fixed to the catalyst surface, or the CH_2 (and CH and CH_3) species are more mobile and are able to move over the catalyst surface [21].

1.8.2 Surface Enol Mechanism

Based on the enol mechanism, the chain growth starts and takes place through undissociative adsorption of CO. Then, surface hydrogen atoms react with the chemisorbed CO groups to form enolic (HCOH) species. It is followed by a surface polymerization of these enolic groups by loss of water. This mechanism was supported using ^{14}C-tracer [33]. There is an alternative route for this mechanism by which the individual hydrogenation of the enolic groups, forming water and CH_2 groups which can grow chains, as was described in the carbide mechanism [21].

1.8.3 CO Insertion Mechanism

Based on this mechanism, chain growth takes place through insertion of CO molecules in the metal-carbon bonds. As an initiation step, a CO molecule is inserted into the metal-H bond. This is followed by hydrogenation of the formed surface aldehyde species to CH_3 by nearby chemisorbed hydrogen atoms (rate limiting step). Consequently, CO can be inserted into the metal-carbon bond forming enol species. The enol species can be hydrogenated again. Chain growth happens by repeating this step. Hydrogenation of the growing chain which can result in a free olefin chain and an adsorbed hydrogen atom terminates the chain growth [32].

1.9 Kinetics of FT Reactions

Literature review reveals that there is little agreement on the form of the macro kinetic model for the rate of FT reactions [5, 19]. Table 1.3 shows some of the different reaction rate models proposed in the literature. In fact individual research groups have typically proposed a new kinetic equation to describe their own data. However, there are a few common features to the various kinetic models. First of all, a strong inhibiting influence on the reaction rate has been explicitly stated or concluded in numerous publications on the iron-FT synthesis [19]. In the case of Langmuir-Hinshelwood-Hougen-Watson (LHHW) type of kinetic expressions, this phenomenon is expressed as a competitive

Table 1.3 Eley-Rideal and Langmuir-Hinshelwood type FT rate expressions for the iron-based FT synthesis

Ref.	Model	H_2O inhibition	CO_2 inhibition	Vacant site
[40]	kP_{H_2}	×	×	×
[35]	$\frac{kP_{H_2}^{a}P_{CO}}{P_{CO}+aP_{H_2O}}$	√	×	×
[36]	$\frac{kP_{H_2}^{2}P_{CO}}{P_{CO}P_{H_2}+aP_{H_2O}}$	√	×	×
[34]	$\frac{kP_{H_2}P_{CO}}{P_{CO}+aP_{H_2O}+bP_{CO_2}}$	√	√	×
[39]	$\frac{kP_{H_2}^{0.5}P_{CO}}{(1+aP_{CO}+bP_{H_2O})^{2}}$	√	×	√
[38]	$\frac{kP_{H_2}P_{CO}}{(1+aP_{CO}+bP_{H_2O})}$	√	×	√
[41]	$\frac{kP_{H_2}P_{CO}}{P_{CO}+aP_{CO_2}}$	×	√	×
This Thesis	$\frac{k_{FT}.P_{CO}.P_{H2}}{(1+a.P_{H20}+b.P_{CO})^{2}}$	√	×	√
[37]	$\frac{kP_{CO}P_{H_2}}{(1+bP_{CO})^{2}}$	×	×	√

√: it is included in the model
×: it is not included in the model

adsorption between water and carbon monoxide on the catalyst surface [19]. In the case of iron catalyst with high water-gas-shift reaction, an inhibition effect of CO_2 was also included in the rate equations. It has been shown that water has a much more substantial inhibition effect on the FT reaction rate than CO_2 [34]. Indeed, literature review shows that the discrepancies between the popular iron-FT rate expressions have been imbedded in the inhibition terms which are included in the denominator of the kinetic equations. In addition, the presence of vacant sites on iron catalysts has not been completely studied [19]. It can be concluded that the development of FT kinetic equations still requires additional research.

1.10 Reactors for Fischer-Tropsch Synthesis

The reactor type and operation conditions are major factors in the control of product selectivity during FTS. The rapid removal of the large heat of reaction ($-\Delta H$ = 165-204 kJ per mol of CO) is the main problem. This is because high temperature conditions lead to high methane yields, carbon deposition, deactivation and particle destruction. Schematic of the main reactor types are given in Figure 1.2. These reactors can be categorized as follows [1]:

- Multi-tubular fixed bed reactor with internal cooling (Sasol, Shell),
- Circulating fluidized bed reactor with circulating solids, gas recycle and cooling in the gas/solid recirculation loop (Sasol),
- Fluidized bed reactors with internal cooling (Sasol),
- Slurry bubble column reactors with internal cooling tubes (Sasol and Exxon).

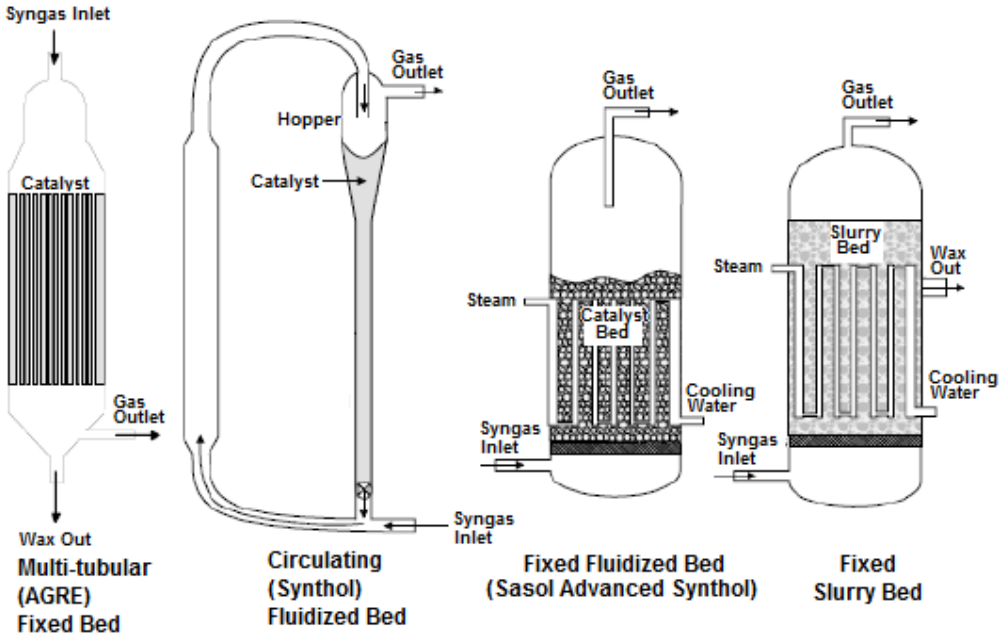

Figure 1.2 Commercial reactors for FT reactions
[http://gekgasifier.pbworks.com/f/1239858419/ft%20reactors.gif]

The earliest FT reactors consist of a hot gas recycle process in the fixed bed reactors. This type of reactor naturally produced high gas flow resistance, catalyst attrition and carbon deposition. In order to keep away from transport limitations, the small particle size used in the fixed FT reactor leads to high pressure drops and as a result high gas compression costs. Generally, the fixed bed reactors produce mainly linear waxes which can be selectively hydro-cracked to diesel.

Due to the obvious disadvantages of the packed bed reactor, circulating fluidized beds (CFBs) were proposed. The main advantage of this type of reactor is efficient heat transfer characteristics and higher gas throughputs than fixed bed reactors. Moreover, because of lower pressure drop gas compression costs are reduced [9].

As opposed to the CFB, the turbulent/fixed fluidized bed (FFB) has a stationary fluidized catalyst bed and an internal heat exchanger submerged in the catalyst bed for

removal of heat. The tubulent fluidized bed reactor is simpler to construct and operate. However, because of the rapid mixing in a fluidized bed system, the catalyst's resistance to attrition is essential. Particle separation units such as cyclones on the exhaust line are also required.

There is extensive interest in the use of a bubble column slurry reactor (BCSR), since it does not exhibit severe catalyst attritions and erosion problems. The main advantages are uniform temperature and easier heat removal. However, separation of catalyst particles is required. The gas bubbles in the liquid phase keep the catalyst particles in a dispersed state. The reactor construction for a bubble column reactor is relatively simple, initial capital costs are low.

To sum up, low temperature operation of the multi-tubular fixed bed reactor or the BCSR will produce wax and consequently high quality diesel while low molecular weight alkenes are well favored in the fluidized bed (turbulent or circulating mode) system.

1.11 Supercritical Media for FT Reactions

Supercritical fluids as their pressure and temperature exceed the corresponding thermodynamic critical point are highly compressible, and their density, solubility and transport properties can be varied by relatively small variations in pressure. More importantly, unique combinations of fluid properties, e.g. liquid-like density and gas-like transport properties can be achieved at certain pressures near the critical region.

Supercritical fluids have been increasingly used as solvents in chemical reactions in the oil, food, pharmaceutical and biochemical industries. Their main advantages are: (1) gases are completely miscible with supercritical fluids resulting in high concentrations compared to liquid solvents; (2) because of liquid like densities, the

ability of supercritical fluids for dissolving non-volatile substances is very similar to conventional liquid solvents; (3) the low viscosity and high diffusivity of supercritical fluids give them superior mass transfer characteristics; (4) high compressibility of supercritical fluids near the critical point induces large changes in density with very small changes in pressure and/or temperature enabling easy separation of the dissolved material from the supercritical fluids; and (5) the surface tension of the supercritical fluids is low enabling easy access into the pores of the catalyst for extraction of non-volatile materials in the pores [42].

Traditional fixed bed FTS reactors operated under heterogeneous catalytic gas phase reaction conditions are susceptible to local overheating of the catalyst surface and condensation of heavy wax into the catalyst pores resulting in short catalyst lifetimes and low conversion. Although reaction rates and product diffusivities are high in the gas phase FTS (GP-FTS), inadequate heat removal during exothermic FTS reaction can increase methane formation. Slurry phase FTS reaction processes work as an alternative reaction media and have been developed to overcome some of the shortcomings of the gas phase process. FTS in liquid phase results in smaller variations in process temperature. Besides, higher solubility in the liquid phase provides enhanced extraction of the heavy hydrocarbons. However, the rate of mass transfer of syngas into the microspores of the catalyst is low in the slurry phase. As a result; the overall reaction rate is considerably lower than that in GP-FTS. Therefore, an ideal medium for FTS would be one with gas-like transport properties and liquid-like heat capacity, thermal conductivity, and solubility characteristics. These considerations have led researchers to look into the application of supercritical fluids and compressed gas solvents as the reaction medium [42].

To conduct the reaction under supercritical conditions, a large amount of solvent with high partial pressure is required during the supercritical Fischer-Tropsch synthesis (SC-FTS). Therefore, recycling system for the solvent is an important addition in the SC-FTS process [42]. As a result, an economic evaluation regarding the viability of the supercritical processes is necessary. This evaluation should cover both the higher capital costs due to the high-pressure apparatus and operating costs related to the compression of the supercritical media for recycling of solvents. Also, the pressure and temperature of the solvent medium and the degree of dilution of the reactants with the solvent should be accurately determined.

In comparison between the GP-FTS and SC-FTS processes, although the bulk mass transport rate in the GP-FTS is higher than in the SC-FTS, the conversion of CO in supercritical media is more than or close to that in the GP-FTS. This is attributed to the rapid desorption and dissolution of heavy hydrocarbons effectively creating more vacant reactive sites available to the reactants. In GP-FTS, it is accepted that local overheating of the catalyst surface causes high degrees of methane selectivity. Thus with better heat transfer in supercritical media, there could be considerable decrease in CH_4 selectivity and CO_2 selectivity. In the SC-FTS the overall product distribution shifts towards heavier products compared to GP-FTS.

The olefin content in supercritical media exceeds those in other reaction phases. The primary products of the FT reaction can be effectively extracted and transported by the supercritical fluid out of the catalyst particles before they are re-adsorbed and hydrogenated to paraffins. Higher thermal conductivity in supercritical phase leads to enhanced heat transfer. The better stability of the catalyst in the supercritical media is related to more uniform temperature distribution inside the supercritical fixed-bed-reactor and to desorption of heavy hydrocarbons.

The benefits of supercritical media for Fischer Tropsch synthesis are clear. For a fair comparison, an economic analysis should also be performed because the capital and operating costs of reaction at higher pressure in supercritical media, and the separation and recycling of large amounts of added liquid in the SC-FTS may outweigh its benefits [42].

1.12 Carbon Nanotubes as Supprot for Fischer-Tropsch Catalysts

For FT reactions, it has been shown that the catalyst activity and selectivity were influenced by nature and structure of support, metal dispersion, metal loading, and preparation method [5]. Most studies on FT catalysts have been carried out with the metals supported on silica, alumina or titania. These supports exhibit strong-metal support interaction (SMSI) for iron and cobalt catalysts resulting in permanent catalyst deactivation [5,16]. It has been suggested that carbon base supports can overcome this problem [28]. In addition, it has been reported that iron catalysts supported on activated carbon show a higher throughput per unit volume than unsupported iron catalysts [43].

A new generation of carbon base supports, i.e., carbon nanotubes (CNTs) with unique properties, have presented remarkable catalytic activities and outperformed other supports. CNTs can be considered as an alternative to conventional supports for a number of reasons [44], such as:

- CNTs are highly pure;
- CNTs possess remarkable mechanical properties, high electrical conductivity and thermal stability;
- CNTs have meso/macro porous structure eliminating diffusion and intraparticle mass transfer in the reactions medium;
- CNTs can be shaped into different forms for using as a support;

- The metal-support interactions on CNTs can be tuned, which can directly influence the catalytic activity and selectivity;
- Their surface area (50-500 m^2/g) and their internal diameter (5-100 nm) can be adjusted;
- The surface of nanotubes can be easily functionalized chemically;
- Their chemical compositions can be changed (nitrogen- or boron-doped CNTs);
- Based on requirement of reaction environment, catalytic sites can be doped either on their external surface or in their inner cavity.

1.13 Objectives, Knowledge Gap and Outline of the Thesis

1.13.1 Main Objective and Knowledge Gaps

As mentioned in the previous section, carbon nanotubes possess unique properties as support for heterogeneous catalysts. Considering the unique properties of CNTs, the main objective of this thesis is to develop a new active, stable and selective iron catalyst supported on CNTs for FT reactions.

In terms of FT synthesis, there are a few studies on the application of CNTs as support for Co and/or Fe catalysts [45-50]. However controversy has encircled the stability of CNT supported FT catalysts. Bahome et al. [46,48] studied Fe-based catalysts supported on carbon nanotubes for use in the FT reaction which were prepared either by incipient wetness or a deposition precipitation method. They have reported that Fe/CNTs catalyst is an active and stable catalyst. However, van Steen and Prinsloo [47] observed a rapid deactivation for Fe/CNT catalyst in FTS. Overall knowledge gaps for CNT supported FT catalysts are as follows,

1. In the open literature, there is quite opposite data [46-48] on the FT activity, stability, and product selectivity of Fe/CNT catalysts. This issue needs more investigation.
2. Since the structure of CNTs including their surface properties and pore diameters can be adjusted, it is not clear whether these factors can influence the catalyst behaviour in a significant manner.
3. No report is available on the effects of active metal loadings and the influence of promoters on the catalytic performance of iron catalysts supported on CNTs.

1.13.2 Outline of the Thesis

In order to study the effects of CNTs as support on the catalytic performance of iron catalysts for FT reactions, it was necessary to produce high quality nanotubes on a large scale using simple, efficient and inexpensive methods. The most common techniques for CNT synthesis are arc discharge, laser ablation and chemical vapor deposition (CVD) techniques. Among those, the chemical vapor deposition technique is the most easily scalable and economically viable method [59]. Therefore, the first part of the present research program was focused on production of high quality nanotubes based on the CVD method. In this study, the focus was on the effects of carbon concentration in the precursor gas on the quality and quantity of carbon nanotubes synthesized by CVD method. Using a CVD reactor, high-purity, aligned multi-wall carbon nanotube films were grown on quartz tubes by injecting a solution of ferrocene and toluene into a horizontal quartz tube at different carbon concentrations and time on stream. The results are discussed in Chapter 2.

It is known that surface properties of CNTs can be modified by acid treatment [51,52]. The interaction of the nanotubes with oxidizing acids can open the caps and

break the tubes which can reduce mass transfer limitations. More importantly, acid treatment can introduce functional groups on the surface of CNTs [51,52]. These functional groups are considered as anchoring sites for metal particles improving catalyst stability. Thus, a part of the Ph.D. research was devoted to the study of the effects of acid treatment on the activity and stability of iron catalysts supported on CNTs. The results are described in Chapter 3.

Carbon nanotubes are different from other supports in that they have graphene layers with a tubular morphology. Theoretical studies revealed that deviation of the graphene layers from planarity causes π-electron density to shift from the concave inner surface to the convex outer surface, leading to different electron density on the exterior and interior surfaces of CNTs [53,54]. This can lead to different catalytic performances for metal particles doped on inner or outer surfaces of the nanotubes. During the Ph.D. program, a method was developed to control the position of catalytic sites, and then the effects of catalytic site position on FT reactions were studied. The results are given in Chapter 4.

In general, the pore size of supported catalysts can influence the particle size distribution, dispersion, extent of reduction, and reactant and product mass transfer rates [5]. To the best of auther's knowledge, the effects of pore size and the diameter of the carbon nanotubes on the catalytic performance of FT catalysts have not been studied. Therefore, a part of the Ph.D. research was allocated to study the effects of nanotubes' pore size on catalytic performance of the iron catalysts supported on CNTs. The outcome of this study is discussed in Chapter 5.

The present deactivation studies on the iron catalysts supported on CNTs showed that one of the main reasons for catalyst deactivation is agglomeration of metal oxide during FT reactions. It has been shown that molybdenum (Mo) can be used as a

structural promoter for iron oxide catalyst over carbon base supports [55]. The results of the addition of Mo as a promoter on FT reactions are discussed in Chapter 6.

Potassium and copper are effective promoters for iron catalysts. It has been shown that the activity and selectivity of iron catalysts for Fischer-Tropsch reactions can be improved by these promoters. Potassium promotion can increase CO chemisorption and decrease H_2 chemisorption. This is due to the fact that potassium donates electrons to iron which enhances CO chemisorption, since CO tends to accept electrons from iron [14]. Copper has been studied as one of the promoters for FT synthesis on iron catalysts, particularly in bubble column slurry reactors. Its function is to decrease the temperature required for reduction of iron oxides.

Although the overall effects of K and Cu promotion have been studied widely, however, the effective quantity range of K and Cu have not been identified [56-58]. In order to develop an efficient catalyst with optimum loading of promoters, several catalysts with different K, Cu and Mo promoters were prepared and their FT activity and stability were studied. The results corresponding to addition of K, Cu and Mo are given in Chapter 7.

A kinetic study was the last step in developing a new catalyst in order to measure the rate parameters for reactor design based on the catalytic performance of the most efficient catalyst. The most efficient catalyst showed remarkable activity and selectivity with potential industrial application. The detailed mass transfer effects on the FT reactions are examined. The results of the kinetic study are given in Chapter 7.

Finally, the overall conclusions of the CNT production and their application as support for iron catalysts for FT reactions and scope for future work are discussed in Chapter 8. During the Ph.D. studies, a fixed bed and a chemical vapor deposition reactor

were designed and built. The specifications of these reactors are given in Appendices B and C.

1.13.3 Structure of the Thesis

The present thesis is provided in the paper-base format. Each chapter has been published or submitted in the form of journal paper. It should be noted that the references, nomenclature and abbreviation are given at the end of each chapter.

1.14 Uncertainty and Error Analysis for Experimental Data

Since a large number of data in the thesis were experimentally obtained, imbedded uncertainties for each analysis have been addressed. Table 1.4 shows the error in experimental data and number of samples corresponding to each analysis. In most cases, uncertainties are calculated using pooled standard deviations.

Consider M series of analyses, and each series with N measurements. This yields to the data set x_{ij} with $M*N$ members, where i = 1, 2,…N and j = 1, 2, … M. The mean of each series is defined by

$$\bar{x}_j = \frac{1}{N}\sum_{i=1}^{N} x_{ij} \tag{1.2}$$

The pooled standard deviation of x is defined by

$$SD_x = \sqrt{\frac{1}{M(N-1)}\sum_{j=1}^{M}\sum_{i=1}^{N}(x_{ij}-\bar{x}_j)^2} \tag{1.3}$$

with degree of freedom, $\nu = M*(N-1)$.

The Student t values are found from the $t_{(95\%,\,\nu)}$ distribution table for 95% of confidence interval and degree of freedom ν [60]. For the present thesis, uncertainties are reported in Table 1.4 in the form of $\pm SD_x.t_{(95\%,\,\nu)}$.

Table 1.4 The error of in the experimental data and the number of samples corresponding to each analysis

Analysis	Chapter	Number of Sample (*M*)	Number of Analysis per Sample (*N*)	Standard Deviation (SD_x)	Student $t_{(95\%,df)}$	Uncertainty
N_2 adsorption (BET analysis< 100 m^2/g))	3-7	20	3	2	2.02	± 6 m^2/g
N_2 adsorption (BET analysis> 100 m^2/g))	3-7	20	3	3	2.02	± 7 m^2/g
N_2 adsorption (Pore volume < 0.1 m^3/g)	3-7	20	3	0.005	2.02	± 0.01 m^3/g
N_2 adsorption (Pore volume > 0.1 m^3/g)	3-7	20	3	0.01	2.02	± 0.03 m^3/g
TPR (reduction peak temperature)	3-7	20	3	3	2.02	± 6°C
TPR (extent of reduction)	3-7	20	3	2	2.02	± 4 %
TEM	2-7	N/A	10 images	N/A	N/A	particle distribution
Activity (%CO of conversion)	3-7	30	3	2	1.96	± 4
Hydrocarbon and CO_2 selectivities	3-7	30	3	1	1.96	± 2
olefin /paraffin ratio (O/P)	3-7	30	3	0.02	1.96	± 0.04
Iron percentage in CNTs	2	40	3	2	1.96	± 4 %
Mass balance for carbon	2	30	5	3	1.96	± 6%
Mass balance for iron	2	40	5	3	1.96	± 6%
Carbon concentration in gas phase (mol Carbon/m^3)	2	1	5	1.9	2.77	± 0.5
Mass balance for carbon (FTS)	3-7	30	5	2	1.96	± 4%

a) Four data comprised of two XRD spectra with 2 full width at half max readings

Nomenclature

M	Number of series of analyses
n	Carbon number
N	Number of measurements in each series of analyses
P	Pressure (MPa)
S	Selectivity (wt%)

SD_x	Pooled standard deviation of x
t	Student t
T	Temperature (^oC)
W_n	Mass fraction of a particular product
x_{ij}	Single experimental data
$\bar{x}_{ij}$	Meanvalue for each each series
α	Chain growth
ν	Degree of freedom for statistical calulations

Abbreviations

ASF	Anderson-Schulz-Flory
BCSR	Bubble column slurry reactor
CFB	Circulating fluidized beds
CNT	Carbon nanotubes
Co-LTFT	cobalt-based Low-Temperature Fischer-Tropsch
CTL	Coal to liquid
Fe-HTFT	Iron-based High-Temperature Fischer-Tropsch
Fe-LTFT	Iron-based Low-Temperature Fischer-Tropsch
FFB	Fixed fluidized bed
FT	Fischer-Tropsch
GP-FTS	Gas phase Fischer-Tropsch synthesis
GTL	Gas to liquid
LHHW	Langmuir-Hinshelwood-Hougen-Watson
SC-FTS	Supercritical Fischer-Tropsch synthesis
WGS	Water-gas shift

References

[1] H. Schulz, Short history and present trends of Fischer-Tropsch synthesis, Applied Catalysis A: General, 186 (1999) 3-12.

[2] A.C. Vosloo, Fischer-Tropsch: a futuristic view, Fuel Processing Technology, 71 (2001) 149-155.

[3] I. Wender, Reactions of synthesis gas, Fuel Processing Technology, 48 (1996) 228-297.

[4] M. J. Economides, The Economics of gas to liquids compared to liquefied natural gas, World Energy. 8 (2005) 136-140.

[5] G. P. Van der Laan, A.A.C.M. Beenackers, Kinetics and Selectivity of the Fischer-Tropsch Synthesis: A Literature Review. Catalysis Reviews: Science and Engineering, 41 (1999) 255.

[6] G.N. Choi, S.J. Kramer, S.T. Tam, J.M. Fox, Design/economics of a natural gas based Fischer-Tropsch plant, in Spring National Meeting, American Institute of Chemical Engineers, Houston, 1996.

[7] V. U. S. Rao, G. J. Stiegel, G. J. Cinquegrane, and R. D. Srivastave, Iron-based catalysts for slurry-phase Fischer-Tropsch process: Technology review, Fuel Processing Technology, 30 (1992) 83-107.

[8] D. B. Bukur, X Lang, D. Mukesh, W. H. Zimmerman, M. P.Rosynek, and C. Li Binder/Support Effects on the Activity and Selectivity of Iron Catalysts in the Fischer-Tropsch Synthesis. Industrial Engineering Chemistry Research, 29 (1990) 1588-1599.

[9] A.A. Adesina, Hydrocarbon synthesis via Fischer-Tropsch reaction: travails and triumphs, Applied Catalysis A: General, 138 (1996) 345-367.

[10] R. C. Reuel, H. C. Barrtholomew, Effects of support and dispersion on the CO hydrogenation activity/selectivity properties of cobalt, Journal of Catalysis, 85 (1984) 78-88.

[11] D. Vanhove, Z. Zhang, L. Makambo, M. Blanchard, Hydrocarbon selectivity in fischer-tropsch synthesis in relation to textural properties of supported cobalt catalysts, Applied Catalysis A: General, 9 (1984) 327-342.

[12] B. Ernst, A. Bensaddik, L. Jilaire, P. Chaumette, A. Kienemann, Study on a cobalt silica catalyst during reduction and Fischer-Tropsch reaction: In situ EXAFS compared to XPS and XRD, Catalysis Today, 39 (1998) 329-341.

[13] E. Iglesia, Design, synthesis, and use of cobalt-based Fischer-Tropsch synthesis catalysts, Applied Catalysis A: General, 161 (1997) 59-65.

[14] A.Y. Khodakov, A. Griboval-Constant, R. Bechara, and V. L. Zholobenko, Pore Size Effects in Fischer Tropsch Synthesis over Cobalt-Supported Mesoporous Silicas, Journal of Catalysis, 206 (2002) 230-241.

[15] G. Jacobs, T. K. Das, Y. Zhang, J. Li, G. Racoillet, B. H. Davis, Fischer-Tropsch synthesis: support, loading, and promoter effects on the reducibility of cobalt catalysts, Applied Catalysis A: General, 233 (2002) 263-281.

[16] D. B. Bukur, C. Sivaraj, Supported iron catalysts for slurry phase Fischer-Tropsch synthesis, Applied Catalysis A: General, 231 (2002) 201-214.

[17] R.J. O'Brien, L. Xu, S. Bao, A. Raje, B. H. Davis, Activity, selectivity and attrition characteristics of supported iron Fischer-Tropsch catalysts, Applied Catalysis A: General, 196 (2000) 173-178.

[18] R. Snel, Supported Iron Catalysts in Fischer-Tropsch Synthesis: Influence of the Preparation Method, Industrial Engineering Chemistry Research, 28 (1989) 654-659.

[19] F. G. Botes, Kinetic and Selectivity Modeling of the Iron-Based Low-Temperature Fischer-Tropsch Synthesis, Ph.D. Thesis, Eindhoven University of Technology, ISBN: 978-90-386-1440-3.

[20] C.H. Bartholomew, Mechanisms of catalyst deactivation, Applied Catalysis A: General, 212 (2001) 17-60.

[21] E. de Smit and B. M. Weckhuysen, The renaissance of iron-based Fischer-Tropsch synthesis: on the multifaceted catalyst deactivation behavior, Chemical Society Review, 37 (2008) 2758-2781.

[22] P.J. van Berge, J. van de Loosdrecht, S. Barradas, A.M. van der Kraan, Oxidation of cobalt based Fischer-Tropsch catalysts as a deactivation mechanism, Catalysis Today, 58 (2000) 321-334.

[23] R.A. Friedel, R.B. Anderson, Composition of synthetic liquid fuels. I. Product distribution and analysis, Journal of American Chemical Society, 72 (1950) 1212-1215.

[24] R. A. Dictor, A. T. Bell, Fischer-Tropsch synthesis over reduced and unreduced iron oxide catalysts, Journal of Catalysis, 97 (1986) 121-136.

[25] T.J. Donnelly, C.N. Satterfield, Product distributions of the Fischer-Tropsch synthesis on precipitated iron catalysts, Applied Catalysis A: General, 52 (1989) 93-114.

[26] S. Storsæter, Ø. Borg, E.A. Blekkan, A. Holmen, Study of the effect of water on Fischer-Tropsch synthesis over supported cobalt catalysts, Journal of Catalysis, 231 (2005) 405-419.

[27] M. Claeys, E. van Steen, Silica supported cobalt Fischer-Tropsch catalysts: effect of pore diameter of support, Catalysis Today, 71 (2002) 419-427.

[28] A.K. Dalai, B.H. Davis, Fischer-Tropsch synthesis: A review of water effects on the performances of unsupported and supported Co catalysts, Applied Catalysis A: General, 348 (2008) 1-15.

[29] J. P. Hindermann, G. J. Hutchings, A. Kiennemann, Mechanistic Aspects of the Formation of Hydrocarbons and Alcohols from CO Hydrogenation, Catalysis Reviews: Science and Engineering, 35 (1993) 1-127.

[30] M. E. Dry, Practical and theoretical aspects of the catalytic Fischer-Tropsch process Applied Catalysis A: General, 138 (1996) 319-344.

[31] R. C. Brady and R. Pettit, Mechanism of the Fischer-Tropsch reaction, the chain propagation step, Journal of American Chemical Society, 103 (1981) 1287-1289.

[32] B. H. Davis, Fischer-Tropsch synthesis: current mechanism and futuristic needs, Fuel Processing Technology, 71 (2001) 157-166.

[33] W. K. Hall, R. J. Kokes, P. H. Emmett, Mechanism studies of the Fischer-Tropsch synthesis: the incorporation of radioactive ethylene, propionaldehyde and propanol, Journal of American Chemical Society, 82 (1960)1027-1037.

[34] W. H. Zimmerman, D. B. Bukur, Binder/support effects on the activity and selectivity of iron catalysts in the Fischer-Tropsch synthesis, Canadian Journal of Chemical Engineering, 68 (1990) 194-199.

[35] M.E. Dry, Advances in Fischer-Tropsch Chemistry. Industrial & Engineering Chemistry Product Research, 15 (1976) 282-291.

[36] W. Shen, J.Zhou, B. Zhang, Kinetics of Fischer-Tropsch Synthesis over Precipitated Iron Catalyst. Journal of Natural Gas Chemistry, 4 (1994) 385-391.

[37] F.G. Botes, B.B. Breman, Development and Testing of a New Macro Kinetic Expression for the Iron-Based Low-Temperature Fischer-Tropsch Reaction. Industrial Engineering Chemistry Research, 45 (2006) 7415-7426.

[38] G.P. Van der Laan, Kinetics, Selectivity and Scale Up of the Fischer-Tropsch Synthesis. Ph.D. Thesis, Rijksuniversiteit Groningen, (1999).

[39] G.P. Van der Laan, A.A.C.M. Beenackers, Intrinsic Kinetics of the Gas-Solid Fischer-Tropsch and Water Gas Shift Reactions over a Precipitated Iron Catalyst. Applied Catalysis A: General, 193 (2000) 39-53.

[40] R. B. Anderson, Catalysts for the Fischer-Tropsch Synthesis, Catalysis, 5 (1956) 257-371.

[41] S. Ledakowicz, H. Nettelhoff, R. Kokuun; W.D. Deckwer, Kinetics of the Fischer-Tropsch Synthesis in the Slurry Phase on a Potassium-Promoted Iron Catalyst. Industerial Engineering Chemistry Process, 24 (1985) 1043-1049.

[42] R. M. Malek Abbaslou, J. Soltan, A. K. Dalai, Review on Fischer-Tropsch Synthesis in Supercritical Media, Fuel Processing Technology, 90 (2009) 849-856.

[43] H.-J. Jung, P.L. Walker Jr., M.A. Vannice, CO hydrogenation over well-dispersed carbon-supported iron catalysts, Journal of Catalysis, 75 (1982) 416-422.

[44] P. Serp, E. Castillejos, Catalysis in Carbon Nanotubes, DOI: 10.1002/cctc.200900283, 2009.

[45] L. Guczi, G. Stefler, O. Geszti, Zs. Koppány, Z. Kónya, É. Molnár, M. Urbánc, I. Kiricsi, CO hydrogenation over cobalt and iron catalysts supported over multiwall carbon nanotubes: Effect of preparation, Journal of Catalysis, 244 (2006) 24-32.

[46] M. C. Bahome, L. L. Jewell, K. Padayachy, D. Hildebrandt, D. Glasser, A. K. Datye, N. J. Coville, Fe-Ru small particle bimetallic catalysts supported on carbon nanotubes for use in Fischer-Tröpsch synthesis, Applied Catalysis A: General, 328 (2007) 243-251.

[47] E. van Steen, F. F. Prinsloo, Comparison of preparation methods for carbon nanotubes supported iron Fischer-Tropsch catalysts, Catalysis Today, 71 (2002) 327-334.

[48] M. C. Bahome, L. L. Jewell, D. Hildebrandt, D. Glasser, N. J. Coville, Fischer-Tropsch synthesis over iron catalysts supported on carbon nanotubes, Applied Catalysis A: General, 287 (2005) 60-67.

[49] A. Tavasoli, R. M. Malek Abbaslou, M. Trepanier, A. K. Dalai, Fischer-Tropsch synthesis over cobalt catalyst supported on carbon nanotubes in a slurry reactor, Applied Catalysis A: General, 345 (2008) 134-142.

[50] A. Tavasoli, M. Trépanier, R. M. Malek Abbaslou, A. K. Dalai, N. Abatzoglou Fischer-Tropsch synthesis on mono- and bimetallic Co and Fe catalysts supported on carbon nanotubes, Fuel Processing Technology, 90 (2009) 1486-1494.

[51] C. Li, K. Yao, J. Liang, Influence of acid treatments on the activity of carbon nanotube-supported catalysts, Carbon, 41 (2003) 858-860.

[52] T. Wang, C. Tseng, Polymeric carbon nanocomposites from multiwalled carbon nanotubes functionalized with segmented polyurethane, Journal of Applied Polymer Science, 105 (2007) 1642-1650.

[53] X. Pan, Z. Fan, W. Chen, Y. Ding, H. Luo AND X. Bao, Enhanced ethanol production inside carbon-nanotube reactors containing catalytic particles, Nature, 6 (2007) 507-511.

[54] M. Menon, A. N. Andriotis and G. E. Froudakis, Curvature dependence of the metal catalyst atom interaction with carbon nanotubes walls, Physics Letters, 320 (2000) 425-434.

[55] W. Ma, E. L. Kugler, J. Wright, and D. B. Dadyburjor, Mo-Fe Catalysts Supported on Activated Carbon for Synthesis of Liquid Fuels by the Fischer−Tropsch Process: Effect of Mo Addition on Reducibility, Activity, and Hydrocarbon Selectivity, Energy Fuels, 20 (2006) 2299-2307.

[56] C. H. Bartholomew, Recent technological developments in Fischer-Tropsch catalysis, Catalysis Letters, 7 (1990) 303-316.

[57] J. Zhang, J. Chen, J. Ren, Y. Li, Y. Sun, Support effect of Co/Al_2O_3 catalysts for Fischer-Tropsch synthesis, Fuel, 82 (2003) 581-586.

[58] R. J. O'Brien, L. Xu, R. L. Spicer, S. Bao, D. R. Milburn, B. H. Davis, Activity and selectivity of precipitated iron Fischer-Tropsch catalysts, Catalysis Today, 36 (1997) 325-334.

[59] R. Andrews, D. Jacques, A.M. Rao, F. Derbyshire, D. Qian, X. Fan, E.C. Dickey, Chen, Continuous production of aligned carbon nanotubes: a step closer to commercial realization, Journal of Chemical Physics Letters, 303 (1999) 467-474.

[60] R.L. Scheaffer, J.T. McClave, Statistics for Engineers, Duxbury Press. Boston, 1982.

Chapter 2

The Effects of Carbon Concentration in the Precursor Gas on the Quality and Quantity of Carbon Nanotubes Synthesized by CVD Method

A similar version of this chapter has been copyrighted and published in the journal of Applied Catalysis A: General.

- *Reza M. Malek Abbaslou, Jafar Soltan, Ajay K. Dalai, Effects of carbon concentration in the precursor gas on the quality and quantity of carbon nanotubes synthesized by CVD method. Applied Catalysis A: General 372 (2010) 147-152.*

In addition a part of this chapter was presented at the following conferences:

- *Reza M. Malek Abbaslou, Ajay K. Dalai, Sectional Analysis of Carbon Nanotubes Synthesis Reactor Using Chemical Vapor Deposition Method, The Canadian Symposium on Catalysis , Kingston, ON (2008).*

- *Reza M. Malek Abbaslou, Ajay K. Dalai, Optimization and generalization of effective parameters for production of high-quality carbon nanotubes 57th Canadian Chemical Engineering Conference, Edmonton, Canada (2007).*

Contribution of the Ph.D. Candidate

The experimental design and experiments were planned and conducted by Reza Malek Abbaslou. The data analyses and interpretations were performed by Reza Malek Abbaslou, with assistance from Drs. Soltan and Dalai. All of the written text was prepared by Reza Malek Abbaslou and discussed with Drs. Dalai and Soltan.

Contribution of this Chapter to the Overall Study

In order to develop an active catalyst supported on carbon nanotubes (CNTs) for Fischer-Tropsch reactions, it was necessary to study and produce CNTs for potential

applications. In this research, the main focus was on characterization methods and the effects of carbon concentration in the precursor gas and time on stream on the quality and quantity of carbon nanotubes.

Abstract

High-purity, aligned multi-wall carbon nanotubes (CNTs) films were grown on quartz substrates in a chemical vapour deposition (CVD) process. In the CVD process, a solution of ferrocene in toluene was injected in a carrier gas of Ar/H_2 into a horizontal quartz tube. The CNTs were analyzed by scanning and transmission electron microscopy, thermo-gravimetric analysis, and Raman spectroscopy. Results for CNTs synthesized using a wide range of toluene concentrations indicated that, for carbon concentrations in the gas phase higher than 9.6 mol/m^3, catalyst deactivation due to encapsulation of metal particles occurs. Sectional analysis of the CVD reactor products showed that more than 40% of the iron particles were deposited in the first 10 cm section of the reactor, wherein diameters of nanotubes (28 ± 20 nm) and iron particles are smaller than that of (48 ± 25 nm) in the exit region of the reactor. The CNT diameter is closely related to the iron particle size on which they grow. In the area close to the reactor inlet, as the nanotube film grows the iron particles become trapped and attached to the dense film of nanotubes and turn into carbon-coated nanospheres on top of the nanotube array.

2.1 Introduction

Carbon nanotubes (CNTs) are rolled graphite layers with different structures, which can be categorized as single-wall or multi-wall nanotubes. CNTs possess unique electronic, thermal and mechanical properties. These properties have resulted in many potential and practical applications for CNTs such as electron field emitters, nanoscale

electronic devices, catalysts, sensors, and reinforcing agents in polymer composites [1-8].

For applications such as composites and catalysts, it is essential to produce high quality nanotubes on a large scale using simple, efficient and inexpensive methods. The most common techniques for CNT synthesis are arc discharge, laser ablation and chemical vapor deposition (CVD) techniques. Among them, the chemical vapour deposition technique is the most easily scalable and economically viable method [9].

The CVD method itself can be categorized into two main groups, namely semi-continuous and continuous methods. In the semi-continuous method, substrates are doped with nano-sized particles of metals such as Fe, Ni, Co and Mo. Afterwards, substrates are heated to a specific temperature in a reactor and a carbon source such as methane, acetylene and CO is passed over the catalyst leading to CNT grow on the metal particles. In the continuous method, catalysts e.g. metalocenes, carbon source and carrier gases (usually including hydrogen and an inert gas), are fed into a horizontal or vertical reactor simultaneously. In this method, metalocenes, such as ferrocene or cobaltocene and carbon source, such as toluene, benzene and xylene, are pyrolized and the CNT film grows on the reactor wall [9]. This method is easier and simpler for commercialization as it consists of one stage and leads to pure products with a minimum amount of catalyst particles, requiring no or minimum processing to yield a usable product for a large number of applications [10].

In general, two different mechanisms of bottom growth and top growth have been proposed for CNT synthesis. Many research groups support the bottom growth mechanism of synthesis of CNTs. In the bottom growth mechanism the carbon source has to diffuse through the CNT array and reach the catalysts on the substrate [11-13].

There are a number of reports on the production of CNTs based on the continuous CVD route discussing either the experimental [14-24] or numerical [25-30] aspects of the process. Andrew et al. [19] reported a method for producing bulk quantities of high-purity aligned multiwall CNTs through the catalytic decomposition of a ferrocene-xylene mixture at temperatures as low as 923 K. Their method has been followed by several groups [10,14,17,21,23-29] that worked to analyze and optimize the operating conditions such as temperature, carrier gas flow rate, reaction time, injection rate, hydrogen percentage and ferrocene concentration in the feed solution. Despite the large number of publications, a literature review on the subject shows that different reported results cannot be easily compared due to different reactor geometries, feed compositions, and flow rates.

This study has focused on the effect of carbon concentration in the gas phase and total carbon deposition, which are independent from reactor geometry. Using a CVD reactor, high-purity, aligned multi-wall carbon nanotube films were grown on quartz tubes by injecting a solution of ferrocene and toluene into a horizontal quartz tube at different carbon concentrations in the gas phase and time on stream. After each run, carbonaceous products were analyzed by SEM, TEM, TGA and Raman spectroscopy methods. Here, toluene was chosen as the carbon source, because the previous research showed that toluene resulted in higher products yields compared to other aromatic hydrocarbons such as benzene, and xylene [10].

2.2 Experimental

The experiments were conducted in a tubular quartz reactor (ID = 22 mm; effective length = 60 cm) placed inside a horizontal electric furnace (ATS, 3 heating zones, 2160 W, 1473 K max. temperature) as shown in Figure 2.1. The details of the experemital

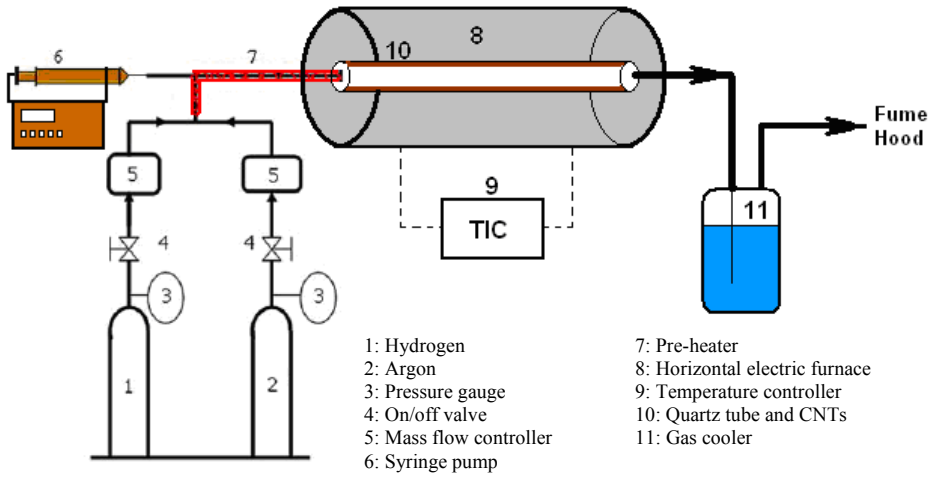

Figure 2.1 Schematic of the experimental setup for CNT synthesis

setup are given in Appendix B. A temperature controller (Eurotherm, USA model 2416) was used to control the furnace temperature. Different amounts of ferrocene (98%, Alfa Aesar Lancaster) were dissolved in toluene (99.8%, Aldrich Chemicals) to obtain the required ratio of Fe/C in the feed solutions. The ferrocene in toluene solution was pumped into the pre-heater by a syringe pump (New era pumps systems, Model NE-1000 multi-phase, Kent Scientific Corporation, USA) to vaporize the liquid feed at 443 K. A carrier gas (argon) mixed with 10 vol % hydrogen carried the vaporized stream of the feed mixture into the reactor. Flow rates of Ar and H_2 were controlled by mass flow controllers (smart mass flow, model 0152, Brooks Instruments Division, Emerson Electric Co. USA).

In a typical run, the reactor system was pre-heated in inert gas to the desired reaction temperature, then the inert gas flow was switched to the carrier gas mixture and the injection of liquid feed mixture was started. The steady injection of the liquid mixture was stopped at the end of the reaction period. After completion of the carbon deposition process, the reactor was cooled down to ambient temperature in inert gas

medium. The quantity of the carbonaceous product was measured by the difference of the reactor weight before and after the reaction. For the sectional analysis of the reaction products at different locations along the reactor, the products were separately removed from each 10 cm segment of the reactor.

To clean up the reactor and remove possible traces of residual carbonaceous materials and iron particles from the reactor walls, after each experiment, the quartz reactor was heated to 950 K in the presence of air stream for 8 hours. As a result, all the attached CNTs and carbonaceous products were burned and residual iron particles were converted to iron oxide. Afterward, the reactor was placed in a vertical furnace and filled with 10 vol% hydrochloric acid for 6 hours to remove the fused iron oxide.

The CNT samples were characterized by thermo-gravimetric analyses (TGA), scanning electron microscopy (SEM), transmission electron microscopy (TEM) and Raman spectroscopy. A 5-7 mg of sample was used for TGA analysis with a Perkin Elmer Pyris Diamond TG/ DTA (Seiko Instruments USA Inc.) system. The sample was heated in air (40-60 ml/min) from 30 to 850^{o}C with a heating rate of 5^{o}C/min. The TGA profiles were used to measure total iron content and amorphous carbon in the CNT samples. For SEM, a Phillips SEM-505 scanning electron microscope operating at 300 kV in SE display mode was used. Prior to analysis, all the samples were gold coated in a sputter coating unit (Edwards Vacuum Components Ltd., Sussex, England).

TEM images were taken using a Philips CM-10 (Netherlands) transmission electron microscope operating at 60 kV. For TEM analysis, the samples were sonicated in distilled water, transferred onto the TEM grid and dried. Raman analyses were carried out with a Raman imaging (Renishaw System 2000) microscope (wire version, 1.3) with laser excitation wavelength of 514 nm, exposure time of 30 s, microscope objective of

50 and continuous grating within the wave number range of 150-3500 cm^{-1}. The uncertainties for the experimental data are given in Section 1-13.

2.3 Results and Discussion

2.3.1 Effects of Carbon Concentration in Gas Phase

Carbon concentration in the gas phase in a CVD reactor can be controlled by the injection rate of the feed solution and the flow rate of the carrier gas. The carbon concentration in the gas phase can be calculated according to Equation 2.1,

$$Cc_i = \frac{Q_c . \rho_c . n_c}{Q_{IH} . M_{cs}} , \qquad (2.1)$$

where Q_c denotes injection rate of feed solution (mL/min), Q_{IH} is flow rate of carrier gas (mL/min), ρ_c is density of the liquid solution (g/mL), n_c is the number of carbon atoms in one molecule of the carbon source in feedstock (for toluene n_c = 7), and M_{cs} is molecular weight of feedstock (g/gmol). Since the flow rate of carrier gas (Q_{IH}) can affect the both iron particle distribution along the reactor and feed residence time in the reactor, the carbon concentrations in the gas phase were only adjusted by changing the injection rate of the feed solution.

In Figure 2.2, the effect of the carbon concentration in the gas phase on the product yield is shown for two different concentrations of ferrocene in toluene. The product yield is defined as the molar ratio of the total products to the total carbon in the feed (Equation 2.2),

$$y_c = \frac{W_c . M_{cs}}{12 . Q_c . \rho_c . n_c} , \qquad (2.2)$$

where y_c denotes product yield and W_c is the total weight of the products (g). It should be noted that by injection of similar quantities of ferrocene, the total amount of

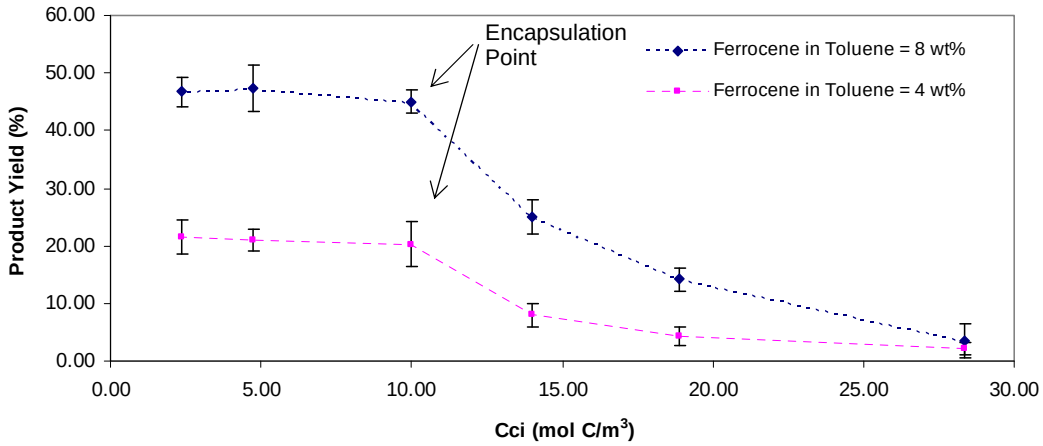

Figure 2.2 Effects of carbon concentration in gas phase on product yield (T = 1053 K, carrier gas = 475 ml/min, total ferrocene = 2.88 g)

deposited Fe was kept constant for all experiments. In other words, to change the carbon concentration in the gas phase in each experiment, the rate of injection of the feed solution and the reaction period were adjusted. However, the total quantity of Fe deposited in each experiment was kept constant and independent.

As can be seen in Figure 2.2, the product yields are almost constant at carbon concentrations in the gas phase lower than 9.6 mol/m^3. As carbon concentration in the gas phase increases, the product yield decreases significantly. Under high carbon concentration conditions, a fraction of un-reacted carbon species left the reactor and a brown sticky liquid was observed at the exit of the reactor. This was observed for two different set of experiments with different ferrocene percentages in the feed, indicating that regardless of the catalyst concentrations, when the carbon concentration in the gas phase is higher than a specific value (9.6 mol/m^3), the product yield decreases considerably. This point is defined as "encapsulation concentration".

Liu et al. [23] studied the influence of injection rate of solution (0.1 to 2.7 mL/min, carrier gas flow rate of 150 mL/min, T = 1173 K, quartz reactor L = 800 mm and ID =

28 mm) using ferrocene as the catalyst and toluene as the carbon source. They reported that a higher injection rate leads to lower product yields. Based on Equation 2.1, the carbon concentration in the gas phase in their experimental conditions was above 50 mol/ m^3 (STP), which was much higher than encapsulation point in this experiment. As a result, they have observed a decreasing trend in product yield with increasing carbon concentration in the gas phase. Similarly, Andrews et al. [10] reported that changes in the carbon partial pressure in the feed affected the formation of co-generated amorphous carbon. They found that optimum nanotube production rates were obtained at the low range carbon partial pressure.

The mechanism for CNT growth on a single metal catalyst has been studied experimentally [33-34] and numerically [35-37]. It is generally accepted that the nanotube growth involves four consecutive steps of 1) the formation of adsorbed surface carbon, 2) dissolution/segregation of carbon species, 3) diffusion of carbon through metal particles and 4) precipitation of carbon in the form of carbon nanotubes. It has been shown that diffusion of carbon through metal particle is the rate limiting step [38] of the process.

Considering this mechanism with the experimental results, it can be concluded that at higher carbon concentration than encapsulation concentration in the gas phase, the rate of step one (formation of adsorbed surface carbon) can exceed the diffusion rate leading to formation of monolayer or multiple layers of carbon on the metal particle. Figure 2.3 shows a TEM micrograph of iron particles, which are confined by layers of carbon at carbon concentration in the gas phase higher than encapsulation point. This phenomenon stops further surface reactions resulting in the confinement of metal particles and formation of carbon-coated nanospheres. Obviously, in the case of lower carbon concentration in the gas phase, the rate of step 1 (formation of adsorbed surface

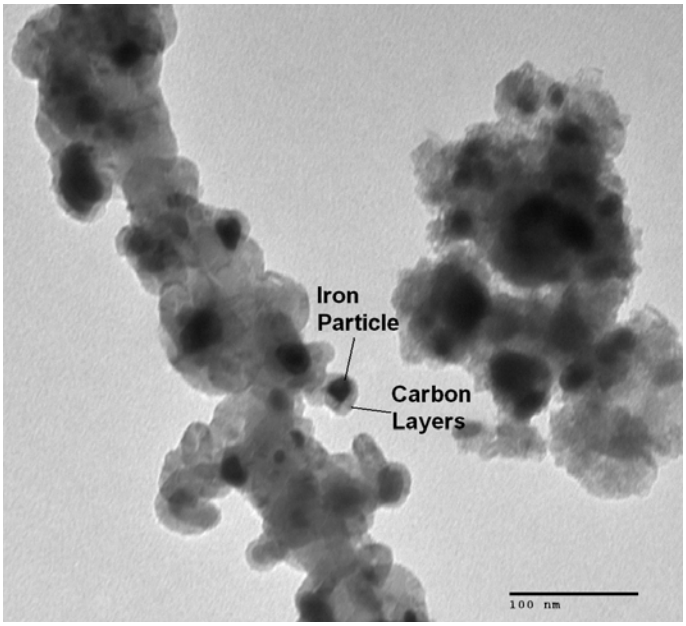

Figure 2.3 TEM image of encapsulated iron particles at Cc_i = 25 mol C/m^3

carbon) is lower than or equal to the rate of diffusion and precipitation of carbon in the form of CNTs resulting in continuous production process.

The effects of carbon concentration in the gas phase on the quality and structure of CNTs were also analyzed using SEM, TEM and Raman spectroscopy. SEM analyses of the samples synthesized at different carbon concentrations in the gas phases are shown in Figure 2.4a and 2.4b. Figures 2.4a and 2.4b indicate that the length of CNTs at carbon concentration in the gas phase of 25 mol/m^3 is 20-30 μm that is 10 times shorter than that of the CNT produced with carbon concentration in the gas phase of 9.6 mol/m^3. In addition, the structure of CNTs has been influenced by change in carbon concentration in the gas phase. As can be seen in Figure 2.4a, the carbon nanotubes which were synthesized at higher carbon concentration in the gas phase are entangled. In the case of lower carbon concentration in the gas phase (Fig 2.4b), a straight and aligned film of nanotubes are obtained.

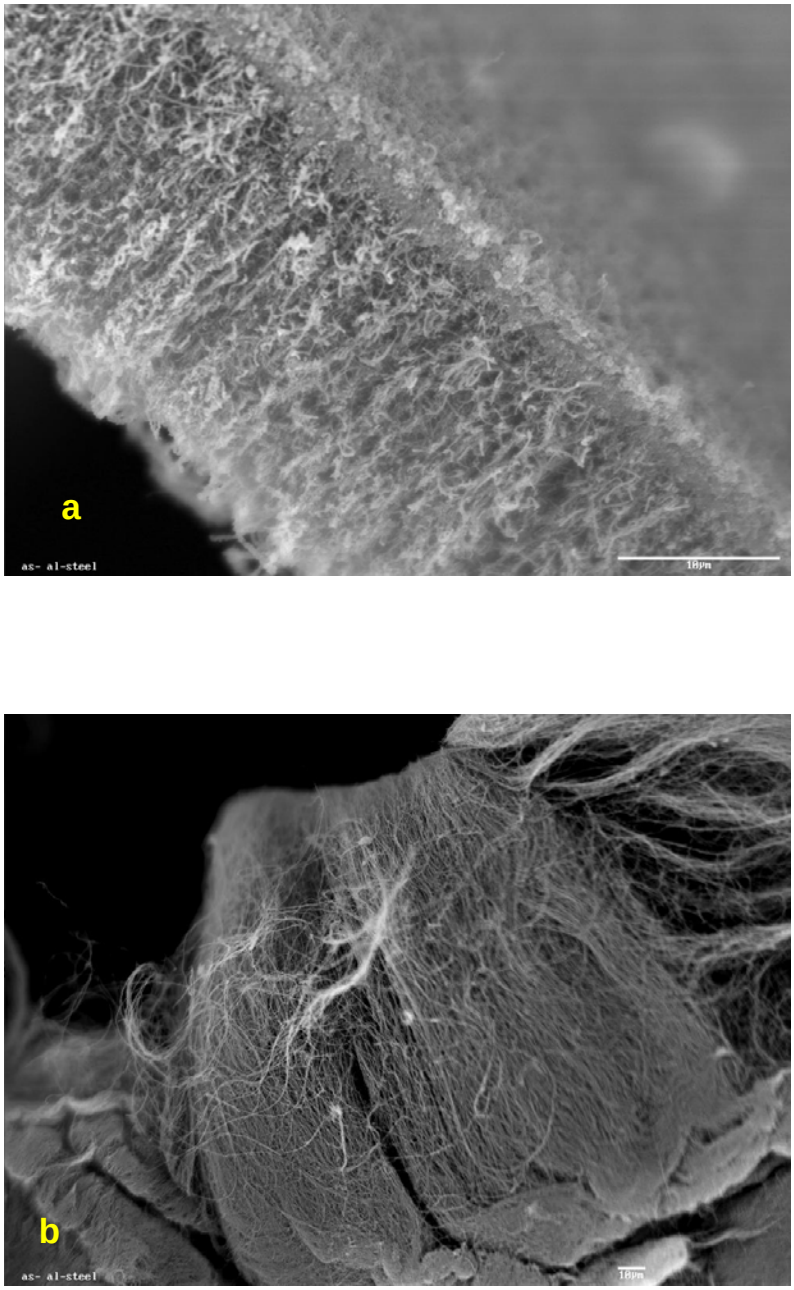

Figure 2.4 SEM images of MWCNT bundles synthesized at different carbon concentrations in the gas phase, a) C_{ci} = 25 mol C/m^3, b) C_{ci} = 9.6 mol C/m^3 (for both cases T = 1050 K, ferrocene in feed solution = 8 wt %)

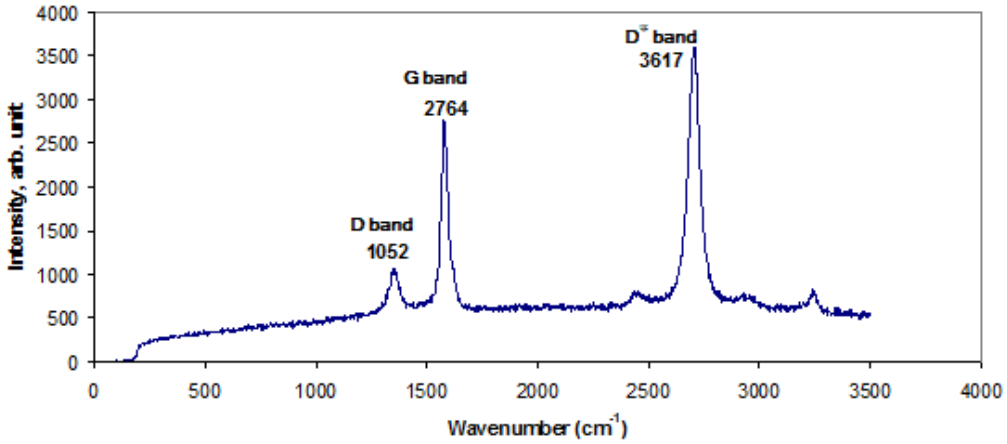

Figure 2.5 Typical Raman spectra for multiwall CNTs at Cc_i = 9.6 mol C/m^3 (T = 1050 K, ferrocene in feed solution = 8 wt %)

Raman spectroscopy is an important characterization tool for study of carbon-based materials including CNTs [31]. Figure 2.5 shows a typical Raman spectra for the synthesized CNTs (C_{ci} = 9.6 mol C/m^3, T = 1050 K, Ferrocene in toluene = 8 wt%). The D band at 1350 cm^{-1} is disorder-induced. The G mode at 1585 cm^{-1} is usually regarded as a G-point vibration of graphite and often is called tangential mode for carbon nanotubes. The D band is not observed in perfect crystal graphite and it is produced by defects or finite size effects. As a result, the relative intensity of the D band with respect to the G band can be used as a measure of the degree of disorder or the concentration of defects [32] in a CNT sample.

Figure 2.6 shows the result of Raman spectroscopy for collected products which were produced with different carbon concentrations in the gas phase. As can be seen in Figure 2.6 at the concentration lower than the encapsulation point, the values of (I_D/I_G) in Raman spectra are almost constant. After encapsulation point, the I_D/I_G value increases with increase in carbon concentration in the gas phase. This indicates that the

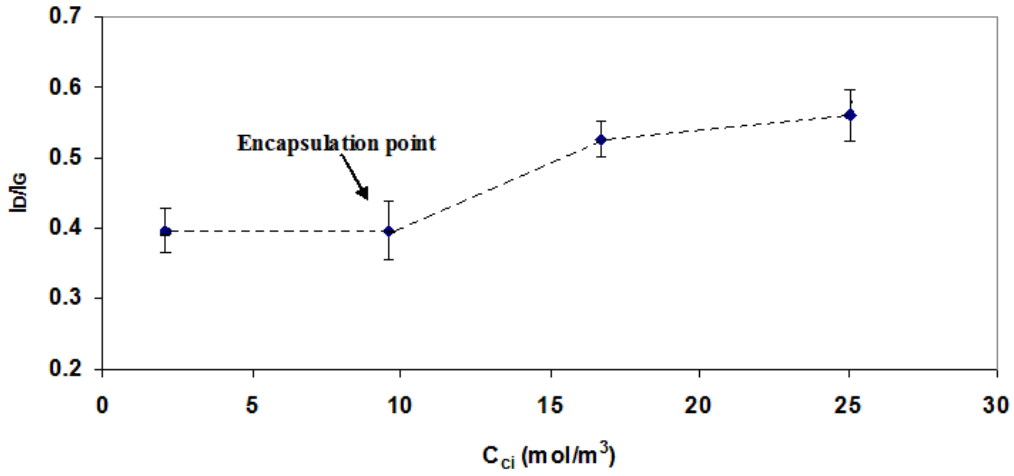

Figure 2.6 The I_D/I_G value for CNTs at different carbon concentration in the gas phase (T = 1050 K, ferrocene in feed solution = 8 wt %)

extent of defects on CNTs structure increases at the higher range of the carbon concentration in the gas phase.

2.3.2 Effect of Time on Stream

In order to analyze the catalyst performance and change in the quality of products during the reaction period, a series of experiments with constant temperature, initial carbon and ferrocene concentrations were conducted within a reaction period of 180 min. In each experiment, once the reaction was completed and the reactor was cooled down, fine powders were removed from the reactor by tapping the reactor tube. After removal of the loose powder product, the fused products, which were attached to the reactor wall, were collected by scratching with a hard brush.

Figures 2.7a and 2.7b show the SEM micrographs of collected powder and fused materials from the reactor. As can be seen in Figure 2.7a, the collected fine powder consists of carbonaceous nanospheres. Figure 2.7b shows that the fused particles collected from the reactor wall are comprised of well-aligned carbon nanotubes. The amount of amorphous carbon on the CNTs which were attached to the wall was also

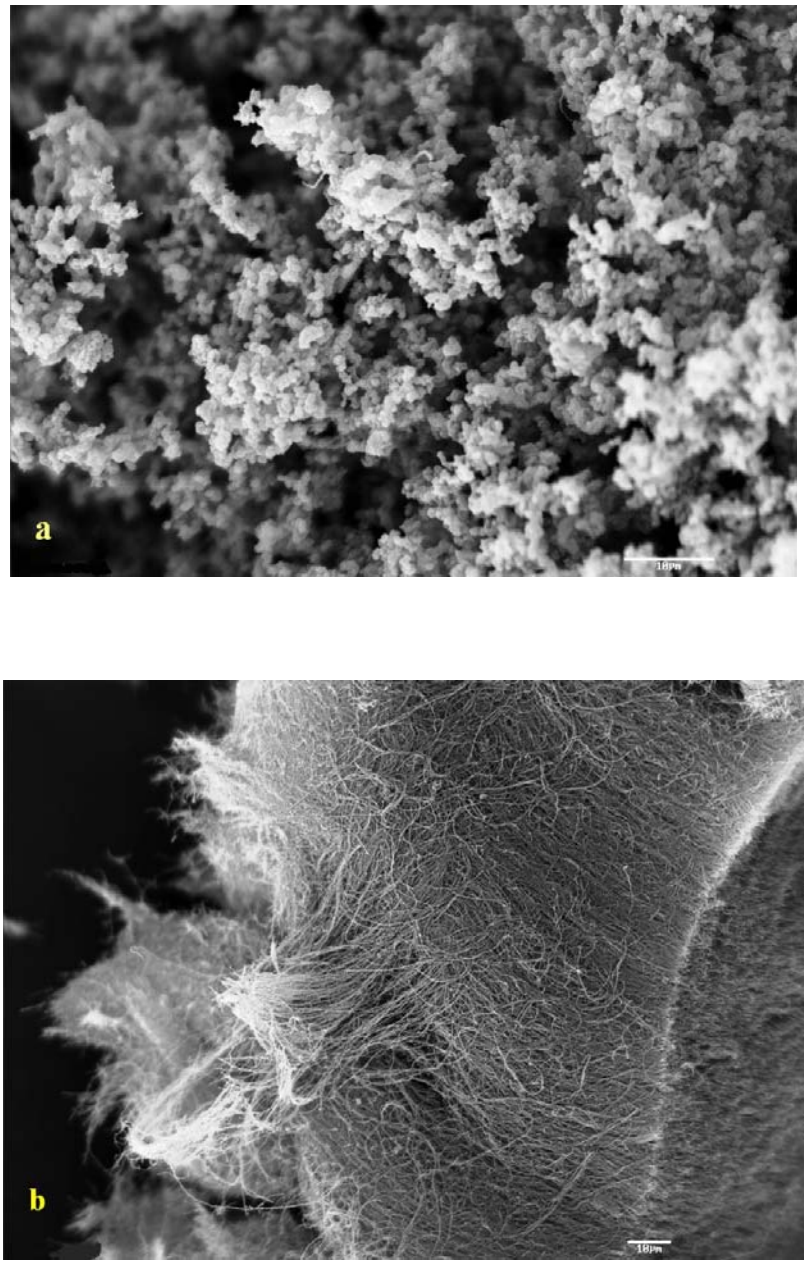

Figure 2.7 SEM images of collected products a) the loose fine powder b) the products which were attached to the wall of the reactor

analyzed by TGA. The details of the analysis method have been reported elsewhere [10].

Figure 2.8 shows the variation of total product deposition and CNT deposition (mg/cm^2) within the various reaction periods. It should be noted that the average total

deposition (mg/cm^2) is the amount of collected sample from a unit area of the reactor wall.

As can be seen from Figure 2.8a, total carbon and CNT depositions increase with time on stream; however, the rates of formation of the two products are different. Since the collected products consist of CNTs and other carbonaceous particles, the difference between total product and CNT depositions indicates the amount of nanospheres in the samples. In other words, as the total deposition increases, the amount of nanospheres in the samples increases significantly (See Figure 2.8b). At the average total deposition of 4 mg /cm^2, the percentage of nanospheres is less than 7%. When, the total deposition is 12 mg/cm^2, average nano-sphere content reaches as high as 40%.

In order to study the quality and quantity of CNTs along the reactor, a sectional analysis of deposited carbon along the CVD reactor was performed. For the sectional analysis, the attached products on the reactor wall were collected from each 10 cm section along the reactor and the carbonaceous products from each section were characterized separately.

Figure 2.9 shows the iron catalyst distribution along the reactor. The data show that more than 40% of catalyst particles have been deposited in the first 10 cm section of the reactor. In comparison, in the last 20 cm section of the reactor, iron percentage is less than 5%. This indicates that a majority of the iron particles are deposited in an area very close to the reactor entrance. TEM analysis on nanotubes (Figure 2.10) from different sections of the CVD reactor shows that the diameter of carbon nanotubes at the entrance region of the reactor (average diameter of 28 ± 20 nm) is smaller than that at the end part of the reactor (average diameter of 48 ± 25 nm). It has been shown that the diameter of the nanotubes is equal to the diameter of the metal particles [9]. Therefore, combination of the higher quantity of iron deposition with smaller diameter in the

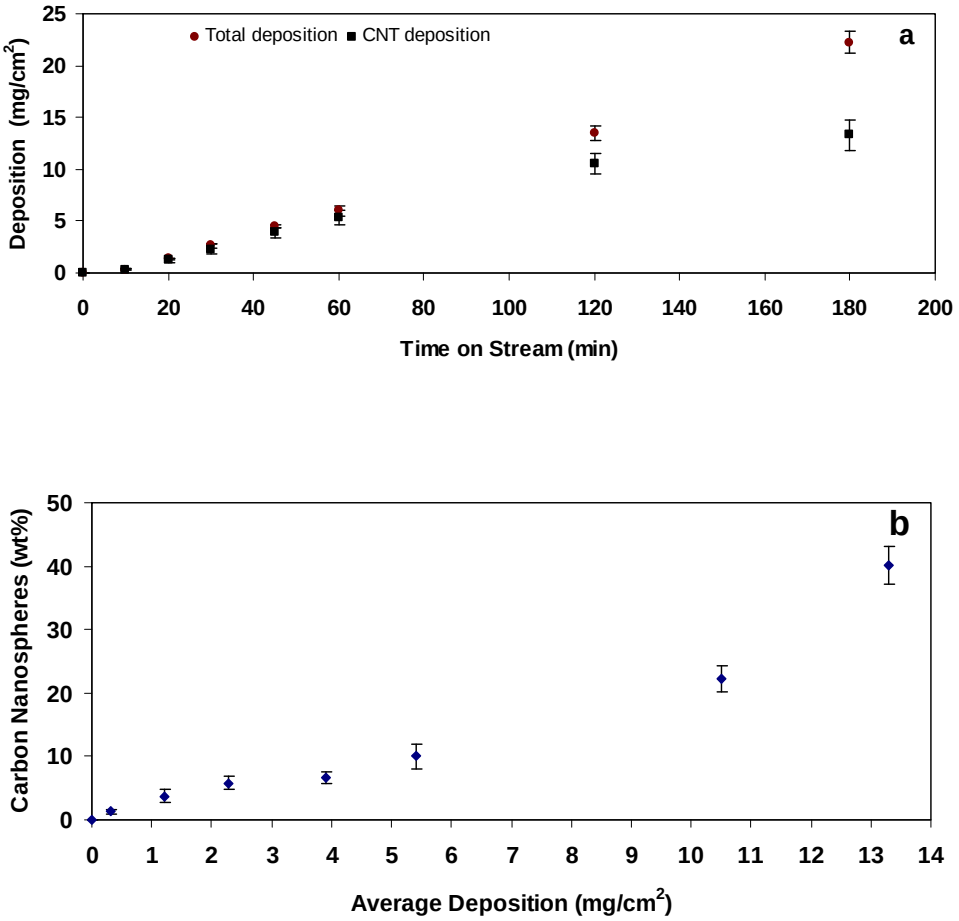

Figure 2.8 The effect of reaction time and total deposition on the quality of products, a) total deposition and CNT deposition vs. reaction time, b) total deposition vs. nanospheres content (T = 1053 K, carrier gas = 475 ml/min, ferrocene in toluene = 8 wt%, C_{ci} = 9.6 mol/m^3)

entrance region of the reactor results in a denser array of nanotubes in the entrance region compared to other areas along the CVD reactor.

Kuwana and Saito [28] have reported a model that can predict the formation process of iron nano-particles from ferrocene decomposition along a CVD reactor. Their model included an axisymmetric two-dimensional computational fluid dynamics (CFD) simulation, the mechanism of nucleation and surface growth of an iron particle, and bi-particle collision.Their numerical results showed that in the region close to the entrance,

the number density is higher and particle diameters are smaller than other areas along the CVD reactor. As a result, one can expect that the CNT forest would be very dense and the channels among

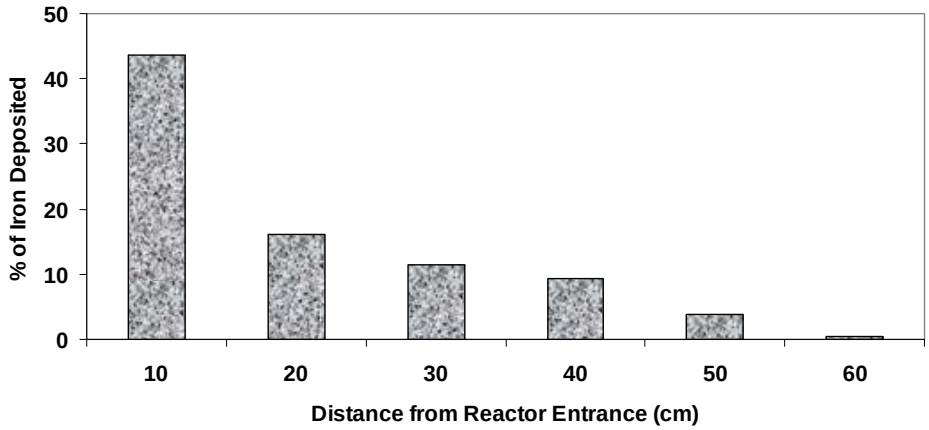

Figure 2.9 Percentage of iron deposited along the reactor (T = 1053 K, ferrocene in toluene = 8 wt%, carrier gas = 475 ml/min, total ferrocene = 2.88 g, C_{ci} = 9.6 mol/m^3)

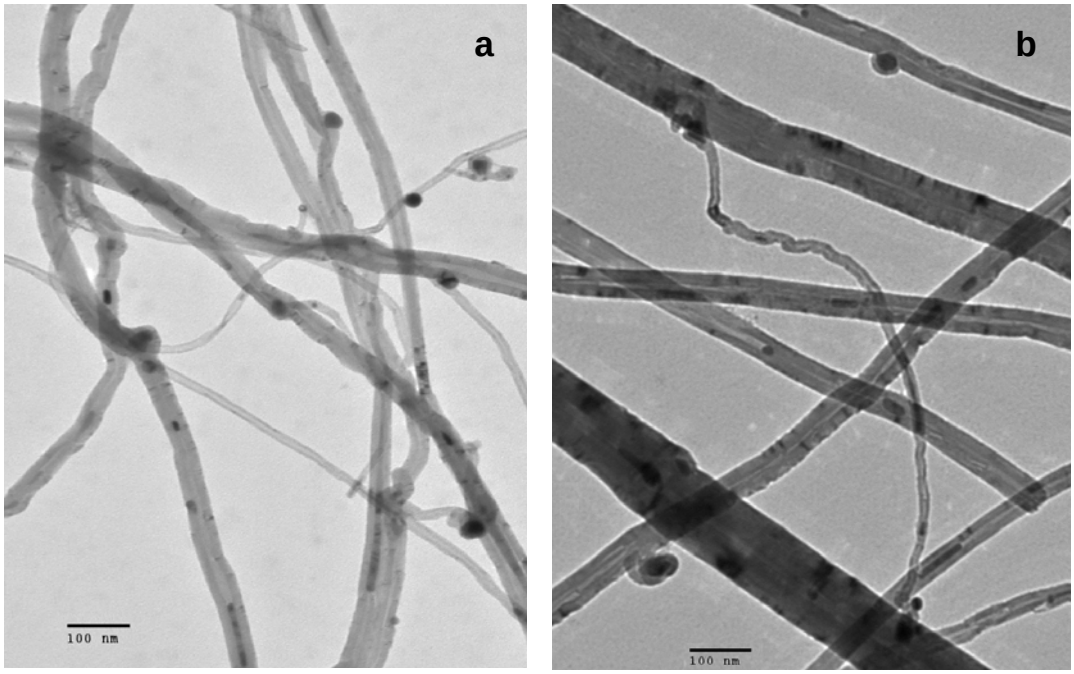

Figure 2.10 TEM micrograph of CNTs a) from entrance region of the reactor and, b) from exit region of the reactor (T= 1053 K, ferrocene in toluene = 8 wt%, carrier gas = 475 ml/min, total ferrocene = 2.88 g, C_{ci} = 9.6 mol/m3)

the nanotubes would be very narrow at the region in the reactor close to the reactor entrance compared to the other areas in the reactor.

During the CNT synthesis, the length of nanotubes increases with time on stream. Thus, it can be postulated that long nanotubes with a dense array can work as a barrier for the iron particle to reach the quartz substrate. As a result, the iron particles attach on CNT forest and turn into carbon nanospheres on top of a CNT array. Figure 2.11 shows the carbon nanospheres on top of CNT array which were collected from entrance region of the reactor within a reaction period of 60 min. At a longer reaction period, the entire surface of the CNT array is covered by carbon nano-spheres.

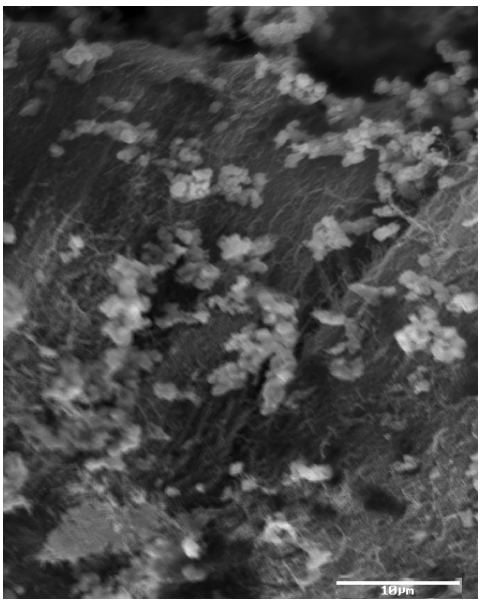

Figure 2.11 SEM micrograph of nanospheres (white spots) on top of the CNT array at a reaction period of 60 min collected from entrance region of the CVD reactor (T = 1053 K, ferrocene in toluene = 8 wt%, carrier gas = 475 ml/min)

2.4 Conclusions

In order to compare the results of different experimental data using different reactor sizes and flow rates, the effect of parameters, namely carbon concentration in the gas phase and total deposition were investigated. At the concentrations higher than the

encapsulation concentration, the product yield decreases significantly due to catalyst deactivation as a result of encapsulation of metal particles with a layer of carbon. Thus, low carbon concentrations in the gas phase are favored for production of CNT using CVD method. A sectional analysis along the CVD reactor indicates that the nanotubes array is denser in the area close to the reactor entrance compared to other regions along the reactor. Therefore, as reaction time prolongs and the nanotubes length increase, the iron particles are deposited on top of the CNT film resulting in formation of carbon nanospheres.

Nomenclature

C_{ci}	Carbon concentration in the gas phase in feed (mol. m^{-3})
M_{cs}	Molecular weight of carbon source ($g.gmol^{-1}$)
n_c	Carbon number in hydrocarbon
Q_c	Injection rate of liquid solution ($mL.min^{-1}$)
Q_{IH}	Flow rate of carrier gas ($mL.min^{-1}$)
t_T	Total reaction time (min)
W_c	Total mass of collected products (g)
y_c	Weight ratio of carbonaceous products to the total
ρ_c	Density of carbon source ($g.mL^{-1}$)

Abbreviations

CNT	Carbon nanotube
CVD	Chemical vapor deposition
SEM	Scanning electron microscopy

TEM	Transmission electron
TGA	Thermo-gravimetric analysis

References

[1] R.H. Baughman, A.A. Zakhidov, W.A. de Heer, Carbon Nanotubes - the Route Toward Applications, Science 297 (2002) 787-792.

[2] W.A. de Heer, A. Chatelain, A. Ugarte, Carbon Nanotube Field-Emission Electron Source, Science. 270 (1995) 1179-1180.

[3] H. Dai, J.H. Hafner, A.G. Rinzler, D.T. Colbert, R.E. Smalley, Nanotubes as nanoprobes in scanning probe microscopy, Nature 384 (1996) 147-150.

[4] P. Serp, M. Corrias, P. Kalck, Carbon nanotubes and nanofibers in catalysis, Applied Catalysis A: General, 253 (2003) 337-358.

[5] R.M. Malek Abbaslou, A. Tavasoli, A.K. Dalai, Effect of pre-treatment on physico-chemical properties and stability of carbon nanotubes supported iron Fischer-Tropsch Applied Catalysis A: General, 355 (2009) 33-41.

[6] M. Trojanowicz, Analytical applications of carbon nanotubes: a review, Trends Analytical Chemistry. 25 (2006) 480-489.

[7] R. Andrews, D. Jacques, D. Qian, T. Rantell, Multiwall Carbon Nanotubes: Synthesis and Application Acc. Chem. Res. 35 (2002) 1008-1017.

[8] X. Gong, J. Liu, R.D. Baskaran, R.D. Voise, J.S. Young, Surfactant-assisted processing of carbon nanotube/polymer composites, Chem. Mater. 12 (2000) 1049-1052.

[9] R. Andrews, D. Jacques, A.M. Rao, F. Derbyshire, D. Qian, X. Fan, E.C. Dickey, J. Chen, Continuous production of aligned carbon nanotubes: a step closer to commercial realization, Journal of Chemical Physics Letters, 303 (1999) 467-474.

[10] N. Das, A. Dalai, J.S. Soltan Mohammadzadeh, J. Adjaye, The effect of feedstock and process conditions on the synthesis of high purity CNTs from aromatic hydrocarbons, Carbon 44 (2006) 2236-2245.

[11] M. Pinault, V. Pichot, H. Khodja, P. Launois, C. Reynaud, M. Mayne-LHermite, Evidence of Sequential Lift in Growth of Aligned multiwalled Carbon Nanotube Multilayers, Nano Letters, 5(2005) 2394-2398.

[12] X. Li, A. Cao, Y. Joon Jung, R. Vajtai, P.M. Ajayan, Bottom-Up Growth of Carbon Nanotube Multilayers: Unprecedented Growth, Nano Letters. 5 (2005) 1997-2000.

[13] L. Zhu, Y. Xiu, D.W. Hess, C. Wong, Aligned Carbon Nanotube Stacks by Water-Assisted Selective Etching, Nano Letters, 5 (2005) 2641-2645.

[14] L. Tapaszto, K. Kertesz, Z. Vertesy, Z.E. Horvath, A.A. Koos, Z. Osvath, et al. Diameter and morphology dependence on experimental conditions of carbon nanotube arrays grown by spray pyrolysis, Carbon 43 (2005) 970-977.

[15] W. Wasel, K. Kuwana, P.T.A. Reilly, K. Saito, Experimental characterization of the role of hydrogen in CVD synthesis of MWCNTs, Carbon 45 (2007) 833-838.

[16] H. Neumayer, R. Haubner, Formation of carbon-nano-fibres and carbon-nanotubes with a vertical flow-reactor, Diamond Related Materials, 13 (2004) 1191-1197.

[17] S. Bai, F. Li, Q. Yang, H. Cheng, J. Bai, Influence of ferrocene/benzene mole ratio on the synthesis of carbon nanostructures, Journal of Chemical Physics Letters, 376 (2003) 83-89.

[18] K.E. Kim, K. Kim, W.S. Jung, S.Y. Bae, J. Park, J. Choi, J. Choo, Investigation on the temperature-dependent growth rate of carbon nanotubes using chemical vapor deposition of ferrocene and acetylene, Journal of Chemical Physics Letters, 401(2005) 459-464.

[19] S.B. Sinnott, R. Andrews, D. Qian, A.M. Rao, Z. Mao, E.C. Dickey, F. Derbyshire,Model of carbon nanotube growth through chemical vapor Deposition, Journal of Chemical Physics Letters, 315 (1999) 25-30.

[20] C. Singh, M.S.P. Shaffer, A.H. Windle, Production of controlled architectures of aligned carbon nanotubes by an injection chemical vapor deposition method, Carbon 41 (2003) 359-368.

[21] A. Aguilar-Elguezabal, W. Antunez, G. Alonso, F.P. Delgado, F. Espinosa, M. Miki-Yoshida, Study of carbon nanotubes synthesis by spray pyrolysis and model of growth, Diamond Related Materials, 15 (2006) 1329-1335.

[22] Y.A. Kim, T. Hayashi, M. Endo, Y. Kaburagi, T. Tsukada, J. Shan, et al. Synthesis and structural characterization of thin multi-walled carbon nanotubes with a partially facetted cross section by a floating reactant method, Carbon 43 (2005) 2243-2250.

[23] X.Y. Liu, B. Huang, N.J. Coville, The Influence of Synthesis Parameters on the production Multiwalled Carbon Nanotube by the Ferrocene Catalyzed Pyrolysis of Toluene, Fullerenes, Nanotubes and Carbon Nanostructures, 10 (2002) 339-352.

[24] K. Kuwana, H. Endo, K. Saito, D. Qian, R. Andrews, E.A. Grulke, Catalyst deactivation in CVD synthesis of carbon nanotubes, Carbon 43 (2005) 253-260.

[25] H. Endo, K. Kuwana, K. Saito, D. Qian, R. Andrews, E.A. Grulke, CFD prediction of carbon nanotube production rate in a CVD reactor, Journal of Chemical Physics Letters, 387 (2004) 307-311.

[26] W. Wasel, K. Kuwana, K. Saito, Chemical and thermal structures of a xylene-based CVD reactor to synthesize carbon nanotubes, Journal of Chemical Physics Letters, 422 (2006) 470-474.

[27] K. Kuwana, T. Li, K. Saito, Gas-phase reactions duringCVDsynthesis of carbon nanotubes: Insights via numerical experiments, Chemical Engineering Science, 61 (2006) 6718-6726.

[28] K. Kuwana, K. Saito, Modeling CVD synthesis of carbon nanotubes: Nanoparticle formation from ferrocene, Carbon 43 (2005) 2088-2095.

[29] K. Kuwana, K. Saito, Modeling ferrocene reactions and iron nanoparticle formation: Application to CVD synthesis of carbon nanotubes, Proceedings of the Combustion Institute, 31 (2007) 1857-1864.

[30] M. Grujicic, G. Cao, B.J. Gersten, Reactor length-scale modeling of chemical vapor deposition of carbon nanotubes, Material Science, 38 (2004) 1819-1830.

[31] A.J. Dresselhaus, A.G. Souza Filho, G. Dresselhaus, R. Saito, M.A. Pimenta, Raman spectroscopy of nanoscale carbons and of an isolated carbon nanotube, Molecular Crystals Liquid Crystals. 387 (2002) 21-29.

[32] E.J. Liang, P. Ding, H.R. Zhang, X.Y. Guo, Z.L. Du, Synthesis and correlation study on the morphology and Raman spectra of CNx nanotubes by thermal decomposition of ferrocene eyethylene diamine, Diamond Related Materials, 13(2004) 69-73.

[33] H. Khodja, M. Pinault, M. Mayne-LHermite, C. Reynaud, Carbon nanotube growth mechanism investigated by ion beam analysis, Nuclear Instruments and Methods in Physics Research Section B: Beam Interactions with Materials and Atoms B, 249 (2006) 523-526.

[34] K. Liu, K. Jiang, C. Feng, Z. Chen, S.A. Fan, A growth mark method for studying growth mechanism of carbon nanotube arrays, Carbon 43 (2005) 2850-2856.

[35] S. Naha, I.K. Puri, A model for catalytic growth of carbon nanotubes, Journal of Appllied Physics. 41 (2008) 1-6.

[36] Y. Zhang, K.J. Smith, A kinetic model of CH_4 decomposition and filamentous carbon formation on supported Co catalysts, Journal of Catalysis, 231 (2005) 354-364.

[37] D. Chen, R. Lodeng, A. Anundskas, O. Olsvik, A. Holmen, Deactivation during carbon dioxide reforming of methane over Ni catalyst, Chemical Engineering Science, 56 (2001) 1371-1379.

[38] S.K. Pal, S. Talapatra, S. Kar, L. Ci, R. Vajtai, T. Borca-Tasciuc, L.S. Schadler, P.M. Ajayan, Time and temperature dependence of multi-walled carbon nanotube growth on Inconel 600, Nanotechnology 19 (2008) 1-5.

Chapter 3

Effect of Pre-treatment on Physico-chemical Properties and Stability of Iron Catalysts Supported on Carbon Nanotubes for Fischer-Tropsch Synthesis

A similar version of this chapter has been copyrighted and published in the journal of Applied Catalysis A: General.

- *Reza M. Malek Abbaslou, Ahmad Tavassoli, Ajay K. Dalai, Effect of pre-treatment on physico-chemical properties and stability of carbon nanotubes supported iron Fischer-Tropsch. Applied Catalysis A: General. 355(2009)33-41.*

In addition part of this chapter was presented at the following conference:

- *Reza M. Malek Abbaslou, Ahmad Tavasoli, Ajay K. Dalai "Activity, Selectivity and Life-time of Iron Catalyst Supported on Carbon Nanotube for Fischer-Tropsch Synthesis", Proceeding of The 25th Annual International Pittsburgh Coal Conference, Pittsburgh, PA, USA (2008)*

Contribution of the Ph.D. Candidate

The experimental design and experiments were planned and conducted by Reza Malek Abbaslou. The data analysis and interpretations were performed by Reza Malek Abbaslou, with assistance from Drs. Tavasoli and Dalai. Dr. Tavasoli was a visiting researcher for a period of one year. All written text was prepared by Reza Malek Abbaslou and discussed with Dr. Dalai.

Contribution of this Chapter to the Overall Study

As the first step in developing a new catalyst supported on carbon nanotubes, the effects of oxidizing acids, such as nitric acid, on the structure and surface properties of nanotubes were investigated. The acid treatment was conducted prior to doping metal particles using the impregnation method.

Abstract

This chapter presents the effects of acid treatment on the activity, product selectivity and life span of iron Fischer-Tropsch (FT) catalysts supported on carbon nanotubes (CNTs). Two different types of CNTs, with low surface area (~21 m^2/g) and high surface area (~170 m^2/g), were prepared and treated with 35 wt% HNO_3 at 25^oC and 110^oC for 16 hours. Fe/CNTs were prepared using incipient wetness impregnation method with iron loading of 10 wt%. The CNT supports and catalysts were characterized by nitrogen adsorption, ICP, TPR, XRD, SEM, TEM and Raman spectroscopy. The acid treatments at 25^oC and 110^oC increased the BET surface area by 18% and 31%. The results of Raman analysis revealed that the acid treatment increased the number of defects which are considered as anchoring site for metal particles. TEM analysis showed that the major parts of the iron particles were distributed inside the acid treated nanotubes. According to the XRD analysis, the acid treatment on both families of CNTs resulted in a decrease in metal particle sizes. The FT synthesis was carried out in a fixed-bed micro reactor (270^oC, 2 MPa, H_2/CO = 1.5) for 120 h. Among the catalysts studied, Fe catalyst supported on pre-treated CNTs at 110^oC was stable and active while the other catalysts experienced rapid deactivations.

3.1 Introduction

Global warming, climate change and high crude oil price have made Fischer-Tropsch (FT) synthesis a viable, clean-energy technology [1,2]. The Fischer-Tropsch process is reliable to convert syngas (a mixture of H_2 and CO with different ratios) obtained from biomass, coal and natural gas to a wide range of hydrocarbons such as gasoline and diesel fuels. The FT process is a surface polymerization reaction which can be catalyzed by iron and/or cobalt at pressures from 1-6 MPa and temperatures from 200 to 350°C [3]. Supported and unsupported iron catalysts have been studied for the conversion of syngas, obtained from gasification of biomass and coal [4,5].

The support for a catalyst provides a large surface area for the formation and stabilization of small metal crystallites in the catalyst. The support may also have significant effects on the catalyst activity and selectivity due to metal-support interactions, porosity and mass transfer limitations. In the FT process, it was found that the catalyst activity and selectivity were influenced by nature and structure of support, metal dispersion, metal loading, and/or preparation method [6]. Most studies on FT catalysts have been carried out with the metals supported on silica, alumina or titania. Also, other supports such as carbon in the form of activated carbon and carbon nanotubes (CNTs) have been investigated in the FT reactions [7-21].

It has been reported that iron catalyst supported on activated carbon shows a higher throughput per unit volume as a result of higher dispersions and/or metal-support interactions and higher olefin selectivity compared to unsupported iron catalysts [19-20]. Considering these catalytic benefits with unique properties of CNTs such as meso-porous and macro-porous structures, straight pores, high thermal conductivity and stability, CNTs can be considered as an ideal and potential support for FT catalysts.

Since their discovery, carbon nanotubes have been studied as a support for different catalytic reactions and have presented remarkable catalytic activities and outperformed other supports [21]. In terms of FT synthesis, there are a few studies on the application of CNTs as support for Co and/or Fe catalysts [11-12,15-18]. However controversy encircled the stability of CNT supported FT catalysts. Bahome et al. [16,18] studied Fe based catalysts supported on carbon nanotubes for use in the FT reaction which were prepared either by incipient wetness or a deposition precipitation method. They have reported that Fe/CNTs catalyst is an active and stable catalyst. However, van Steen and Prinsloo [17] observed a rapid deactivation for Fe/CNT catalyst in FTS.

In this chapter, the influences of pre-treatment on the physicochemical properties and stability of Fe catalyst supported on two different types of CNTs are discussed. It is known that the surface properties of CNTs can be modified by acid treatment [22,23]. The interaction of the nanotubes with oxidative acids can open the caps and break the tubes at imperfections, giving rise to shorter nanotubes which can reduce mass transfer limitations and control the position of metal site, i.e. inside the pore or outer layers of CNTs [24-25]. More importantly, acid treatment can introduce functional groups on the surface of CNTs [23]. These functional groups may work as anchoring sites for metal particles on the inner and outer graphite layers of CNTs. Also, they may affect metal dispersion and stability of active metallic sites. Therefore, the influence of acid treatment on the activity and selectivity of Fe/CNT catalysts for FT synthesis is investigated in this chapter.

3.2 Experimental

3.2.1 CNT Support Preparation

Two types of multiwall carbon nanotubes (MWCNTs) with low surface area (lsa-C) and high surface area (hsa-C) were studied as catalyst supports. The first type of CNTs, i.e. lsa-C, was synthesized using the chemical vapor deposition method in our laboratories. The details were discussed in Chapter 2. Briefly, high-purity, aligned multi-wall carbon nanotube films were grown on quartz tubes by injecting a solution of ferrocene and toluene into a horizontal quartz tube (ID = 22 mm; effective length = 600 mm) placed inside a horizontal electric furnace. The solution of ferrocene and toluene was pumped to the pre-heater by a syringe pump to vaporize the liquid feed at 170^{o}C. A carrier gas (argon) mixed with 10 vol % hydrogen carried the gaseous stream of the feed mixture into the reactor which was maintained at 750^{o}C. After reaction followed by cooling the reactor, the carbonaceous products inside the quartz tube were collected. The carbon products obtained from twenty CNT synthesis runs were combined and thoroughly mixed to supply a homogeneous support material.

The other family of carbon nanotubes (hsa-C) was purchased from mknano Co. (M.K. IMPEX Canada). TEM and SEM analysis revealed that the hsa-C sample contained solely CNTs and no amorphous carbon.

3.2.2 Support Pre-treatment

Both types of CNTs, i.e. lsa-C and hsa-C, were treated in nitric acid at 25^{o}C and 110^{o}C as follows. First, 20 g of lsa-C and hsa-C samples were separately treated with 500 ml of 35 vol% of nitric acid and refluxed at 110^{o}C for 16 hours. These supports are denoted as “ha-lsa-C” and “ha-hsa-C” since they were treated in the “hot acid”. Other series of CNT samples were treated with the same procedure but at room temperature. Similarly these CNTs were called “ca-lsa-C” and “ca-hsa-C” referring to “cold acid”

treatment (please see the abbreviations for samples' denotations). After acid treatments, the CNTs were filtered and thoroughly washed with distilled water until neutral pH was reached. Afterward, the CTNs were dried at 120^{o}C over night.

3.2.3 Catalyst Preparation

The catalysts were prepared according to the incipient wetness impregnation method. For the preparation of the catalyst with 10 wt% Fe, 3.2 g $Fe(NO_3)_3 \cdot 9H_2O$ was dissolved into deionised water. The amount of solution was equal to total pore volume of CNT samples (0.5-0.6 ml/g). To have uniform distribution of the salt solution, small pellets of CNT samples were prepared by pressing under 5 metric tonnes without any binders. Then, the solution was added drop-wise to 4 g of acid treated CNT samples as well as pristine hsa-C sample which is denoted "p-hsa-C". Finally, the catalysts were dried at 120^{o}C for 3 hours followed by calcinations at 350^{o}C for 3 hours.

3.2.4 CNT Supports and Catalysts Characterizations

A Perkin Elmer TG/DTA Thermo-gravimetric differential thermal analyzer (heating rate, 5^{o}C/min; argon flow rate, 40 ml min) was used to analyze the thermal stability of the impregnated supports.

The surface area, pore volume, and average pore diameter of the CNTs and catalysts were measured by an ASAP-2000 Micromeritics system. The samples were degassed at 200^{o}C for 2 h under 50 mTorr vacuum and their BET area, pore volume, and average pore radius were determined.

The morphology of samples was studied by transmission electron microscopy (TEM). Sample specimens for TEM studies were prepared by ultrasonic dispersion of the catalysts in ethanol, and the suspensions were dropped onto a copper grid. TEM investigations were carried out using a Hitachi H-7500 (120 kV). Several TEM

micrographs were recorded for each sample and analyzed to determine the particle size distribution. Also, a Phillips SEM-505 scanning electron microscope operating at 300 kV in SE display mode was used. Prior to analysis, all the samples were gold coated in a sputter coating unit (Edwards Vacuum Components Ltd., Sussex, England).

The reduction behavior of the catalyst precursors was studied by temperature programmed reduction (TPR) using a CHEMBET-3000 equipped with a thermal conductivity detector. Here, 0.1 g of catalyst was placed in U-shaped quartz tube. A 5% hydrogen/nitrogen mixture was introduced (flow rate = 36 ml(STP)/min) and the furnace was ramped from room temperature to 1173 K at 10 K/min. The details for calibration of TPR machine and corresponding calculations are given in Appendix D.

XRD analysis was performed using a Philips PW1840 X-ray diffractometer with monochromatized Cu/Kα radiation. The crystallite diameter was determined by substituting the half-width of a chosen peak into the Debye-Scherrer equation. The details for particle size estimation using Debye-Scherrer method are presented in Appendix E.

Raman analyses of the CNTs were carried out with a Raman imaging (Renishaw System 2000) microscope (wire version, 1.3) with laser excitation wavelength of 514 nm, an exposure time of 30 s, microscope objective of 50, continuous grating within the wave number range of 3500-150 cm^{-1} and laser power of 25%.

3.2.5 Catalytic Measurements

The Fischer-Tropsch synthesis was performed in a fixed-bed micro reactor. The schematic and specifications of the fixed bed reactor are given in Appendix C. Prior to CO hydrogenation, in-situ reduction was conducted according to the following procedure. The catalyst (1 g) was placed in the reactor and diluted with 7 g silicon carbide and pure hydrogen was introduced at a flow rate of 30 ml/min. The reactor

temperature was increased from room temperature to 380°C at a rate of 1°C/min and maintained at this activation conditions for 14 h. After the activation period, the reactor temperature was decreased to 275°C under flowing hydrogen. Brooks 5850 mass flow controllers were used to control the syngas flow rate. Argon was used as the internal standard gas in the reactor feed. The mixed gases (36% CO, 54% H_2, 10% Ar) entered through to the top of the fixed bed reactor. The temperature of the reactor was controlled via a PID temperature controller. Synthesis gas with a space velocity of 1860 ml (STP)/(h.g) was introduced and the reactor pressure was increased to 2 MPa. Products were continuously removed from the vapor and passed through two traps. The uncondensed vapor stream was reduced to atmospheric pressure. The composition of the outlet gas stream quantified using an on-line GC-2014 Shimadzu gas chromatograph. The contents of traps were removed every 24 h, the hydrocarbon and water fractions separated, and then analyzed by Varian 3400 GC. Catalytic activity, product selectivity and stability of catalyst were evaluated during reaction period of 120 hours.

The %CO conversion and FTS rate were calculated as:

$$\%CO = \frac{CO_{in} - CO_{out}}{CO_{in}} \tag{3.1}$$

$$FTS\ rate = \frac{\text{g of hydrocarbons}}{\text{g of Fe . h}} \tag{3.2}$$

The hydrocarbon product (C_i) selectivities $S(C_i)$ were calculated as follows:

$$S(C_i) = \frac{\text{mass of component } C_i}{\sum C_i} \tag{3.3}$$

The Olefin/Paraffin ratio was calculated as follows:

$$O/P(Ci) = \frac{\text{mass of olefins } (C_2 + C_3 + C_4)}{\text{mass of paraffins } (C_2 + C_3 + C_4)} \tag{3.4}$$

The uncertainties for the experimental data are given in Section 1-13.

3.3 Results and Discussion

3.3.1 Support Characterization

SEM images of the p-lsa-C and p-hsa-C reveal that the crude product contains solely CNTs while no other impurities are observed (Figure 3.1a,b). The p-lsa-C sample contains well-aligned nanotubes with high aspect ratios. Their lengths vary between 200 and 500 μm.

TEM pictures of the pristine and acid treated CNT supports are shown in Figure 3.2. As can be seen in Figure 3.2a, in the case of lsa-C sample, residual metal particles were encapsulated in the nanotubes during the synthesis procedure. In fact, these metal particles blocked the pores. This is confirmed with the nitrogen adsorption analysis as lsa-C samples possess low surface area and low pore volume as a result of pore blockage and large outer diameters. Table 3.1 shows the amount of encapsulated metal particles at pristine and acid treated CNTs. ICP analysis revealed that the amount of encapsulated metal content in p-lsa-C was about 4.5wt% which decreased to 3.1 and 1.2wt% for ca-lsa-C and ha-lsa-C supports, respectively. There was no metal detected for the hsa-C samples.

It is expected that doped metals are attached on the exterior layer of lsa-C samples. TEM analysis has shown that diameter of lsa-C varies from 20-80 nm with average diameter of 55 nm.

Figure 3.2b shows that the p-hsa-C sample has uniform structure and their inner and outer diameters vary between 8-12 nm and 10-25 nm, respectively. In the case of p-hsa-C, most of the nanotube caps are closed while the population of open-cap nanotubes increases with the acid treatments, as shown in Figure 3.2c. These phenomena were verified with nitrogen adsorption analysis, as the BET surface area increased by 18 and 31% for

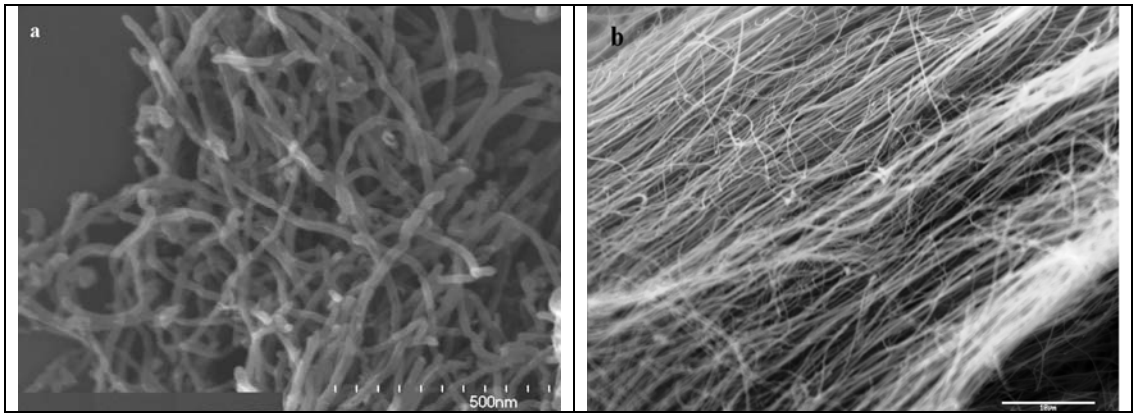

Figure 3.1 SEM images of pristine CNTs a) p-hsa-C, b)p-lsa-C

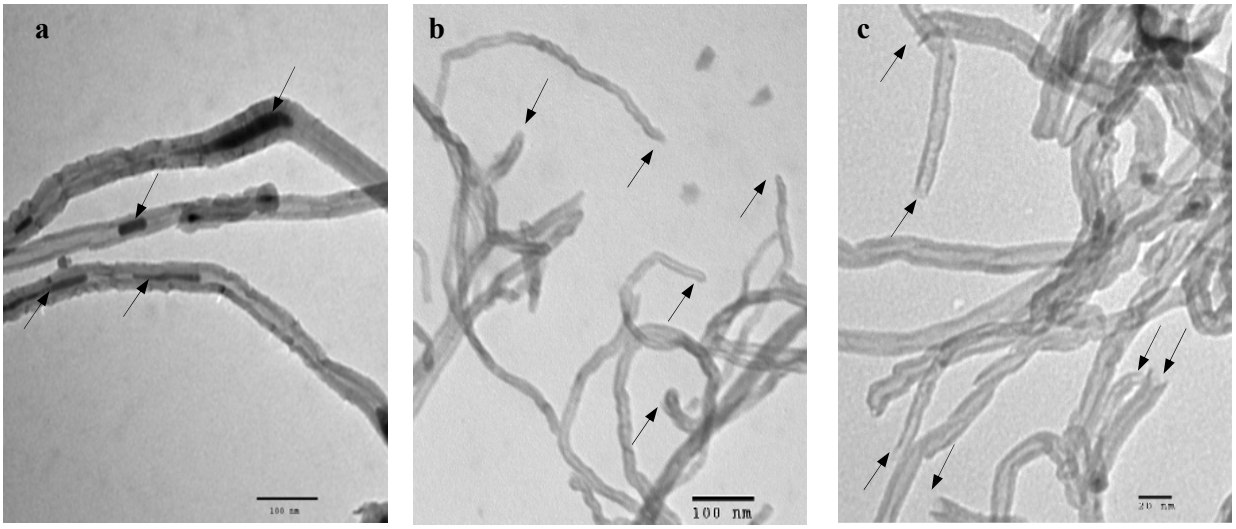

Figure 3.2 TEM images of CNT supports a) ha-lsa-C, arrows show that the inner pores are blocked b) p-hsa-C, arrows show that nanotubes are closed-cap c) ha-hsa-C, arrows point at the open mouths of the nanotubes.

Table 3.1 Characteristic of the CNT supports

Support Name	Treatment	Residual Metal Content %[a]	BET Surface Area (m^2/g)	Total Pore Volume (ml/g)
p-lsa-C	No treatment	4.5	21	0.04
ca-lsa-C	Nitric acid at 25°C	3.1	23	0.04
ha-lsa-C	Nitric acid at 110°C	1.2	27	0.05
p-hsa-C	No treatment	-	170	0.47
ca-hsa-C	Nitric acid at 25°C	-	201	0.54
ha-hsa-C	Nitric acid at 110°C	-	225	0.59

a) measured by ICP-MS method

ca-hsa-C and ha-hsa-C, respectively (Table 3.1). At the same time the pore volume of the CNTs were increased from 0.47 to 0.54 for ca-hsa-C and to 0.59 for ha-hsa-C.

For hsa-C samples, a simple calculation on the enhancement of surface area can give the ratio of open-cap CNTs to the closed caps before and after the acid treatments. Supposing the n_t, n_{cl} and n_{op} are the total number of nanotubes, the number of open-cap nanutubes, and the number of closed-capped nanotubes per unit mass, respectively, and L is the nanotubes average length. The percentage of open-cap CNTs based on measured surface area (A) can be calculated as follows:

$$n_t = n_{cl} + n_{op} \tag{3.5}$$

$$A_{p-hsa-C} = n_t.d_{out}.\pi.L$$

$$A_{ha-hsa-C} = n_{op}.d_{out}.\pi.L + n_{op}.d_{in}.\pi.L + n_{cl}.d_{out}.\pi.L \tag{3.6}$$

$$\frac{A_{p-hsa-C}}{A_{ha-hsa-C}} = \frac{n_t.d_{out}}{n_{op}.d_{out} + n_{op}.d_{in} + n_{cl}.d_{out}} \tag{3.7}$$

For the hsa-C sample with average d_{out} = 20 nm, d_{in} = 10 nm, $A_{p\text{-}hsa\text{-}C}$ = 170.4 m^2/g and $A_{ha\text{-}hsa\text{-}C}$ = 224.9 m^2/g:

$$\frac{n_{op}}{n_t} = 65\% \tag{3.8}$$

The calculation shows that more than 65 percent of closed-cap nanotubes became open-cap due to acid treatment at 110^{o}C. A similar calculation shows that, for acid treatment at 25^{o}C, the percent of open-cap CNTs is 36%.

3.4 Fresh Catalysts Characterization

Thermo gravimetric analysis was used to investigate the presence of any decomposable materials in the uncalcined catalysts. Figure 3.3 shows the results of analysis for Fe/ha-hsa-C catalyst. The data show that the rapid weight loss starts below 200°C and continue up to a temperature of 350°C. Calcining the CNT supported catalysts at 350-400°C for 3 h was expected to remove all the displaceable water and ions present in the catalyst.

Figure 3.4 shows the TEM images of Fe catalyst supported on the pristine and acid treated CNTs. In the case of Fe/ha-hsa-C, the vast majority of iron particles are distributed in the inner pores of the CNTs (Figure 3.4c). This can be attributed to carbon nanotubes' tubular morphology which can induce capillary forces during the impregnation process. It has been shown that liquids with surface tension lower than 190 mN m^{-1} are able to wet and fill the carbon nanotubes inner pores. Water has a surface tension of 72 mN m^{-1}. Therefore, water solution can strongly penetrate and fill the nanotubes' inner pores [27]. Moreover, acid treatment can introduce acidic groups which can decrease the hydrophobicity of the carbon nanotubes and make the surface more accessible to the aqueous solution of the metal precursor [22]. For Fe/p-hsa-C and Fe/ha-lsa-C, most of iron particles were attached to the exterior surface of CNTs. This is because their inner cores are blocked and aqueous solution can only wet the exterior surface (Figure 3.4 a,b).

Table 3.2 shows the metal content for the five different catalysts. ICP analysis of the catalysts revealed that the metal contents obtained are fairly close to those targeted

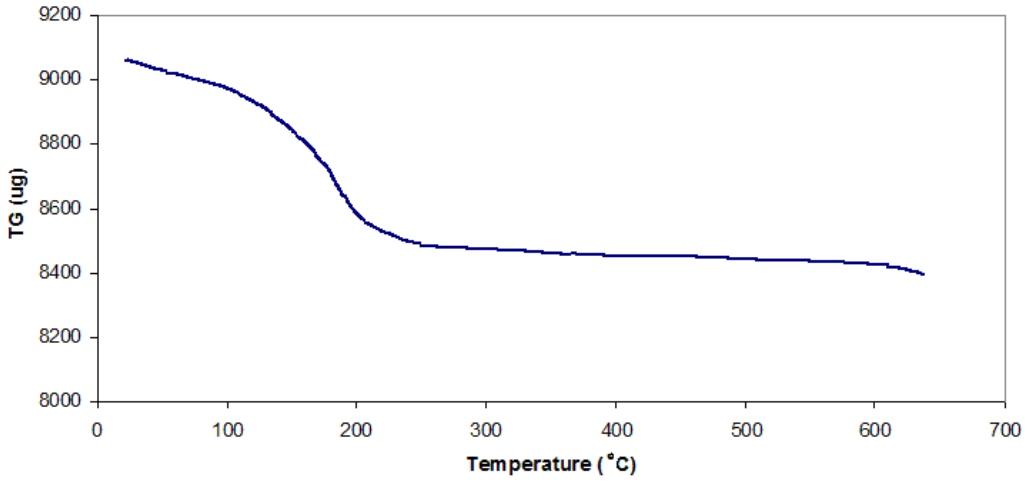

Figure 3.3 Thermo-gravimetric analysis of Fe/ha-hsa-C catalyst in an argon atmosphere

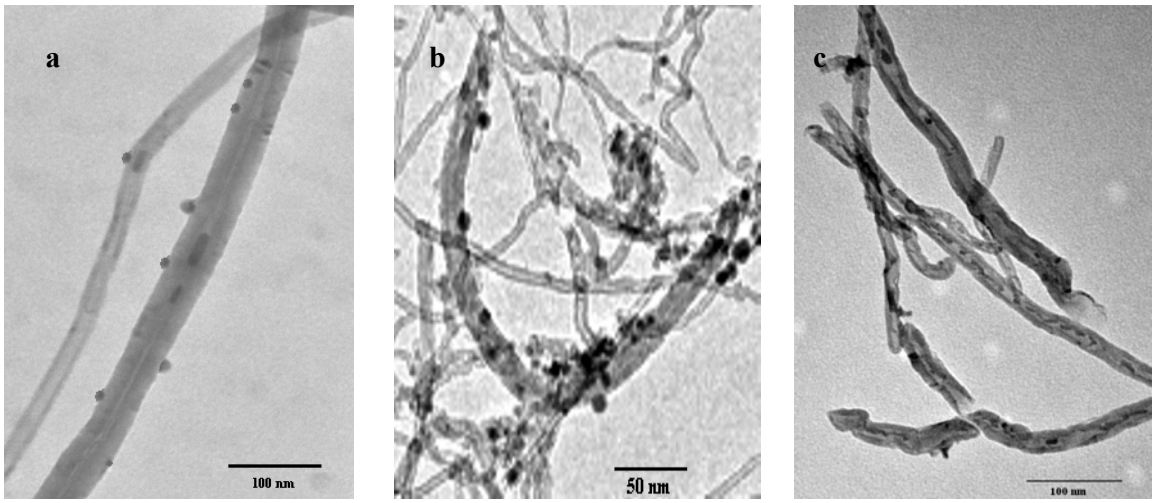

Figure 3.4 TEM images of iron catalyst supported on CNTs, a) Fe/ha-lsa-C, b)Fe/p-hsa-C, c) Fe/ha-hsa-C, dark spots represent iron oxide particles on either the outer or inner surfaces of the nanotubes.

and predicted from the catalyst preparation. In the case of lsa-C supported catalysts, which contain residual iron particles from the CNT production process, the subtraction of total iron content from the residual iron gives the amount of doped and active iron content.

Table 3.2 Characteristic (ICP and N_2 adsorption analysis) of the catalysts studied

Catalyst Name	Targeted Metal Content%	Residual Metal Content %	Total Iron Content %[a]	BET Surface Area (m^2/g)	Total Pore Volume (ml/g)
Fe/ca-lsa-C	10	3.1	12.7	40	0.04
Fe/ha-lsa-C	10	1.2	10.8	46	0.04
Fe/p-hsa-C	10	-	9.7	176	0.47
Fe/ca-hsa-C	10	-	9.5	180	0.51
Fe/ha-hsa-C	10	-	9.6	199	0.56

a) Determined by ICP-MS analysis

Results of nitrogen adsorption analysis for the catalysts are shown in Table 3.2. For the Fe/ca-lsa-C and Fe/ha-lsa-C, the doped metal increased the surface area; however, there is no change in total pore volume. This is because the dispersed iron particles attach to the exterior layer of nanotubes and expand the surface area. The same pattern has been reported by Bahome et al. [16]. Also Table 3.2 shows the results of surface area measurements of 10 wt% Fe loaded hsa-C catalysts. For Fe/ha-hsa-C and Fe/ca-hsa-C catalysts, the loading of 10% Fe decreased the surface area to 199 and 180 m^2/g, respectively. The results show that the BET surface area of the catalysts is lower than that of the supports due to difference in density of iron oxide and CNTs and/or partial blockage of pores. In the case of Fe/p-hsa-C, the surface area is higher than that of the corresponding support. As mentioned, for the CNTs with closed-cap, the loaded metal particles attach to the exterior surface and increase the surface area. For this catalyst, the pore volume did not change. However, pore volumes decreased for Fe/ha-hsa-C and Fe/ca-hsa-C catalysts which can confirm the pore blockage of the treated CNTs.

Figure 3.5 shows XRD patterns of the studied supports as well as calcined iron supported catalysts. All the catalysts for each CNTs families show similar XRD patterns between 2θ values of 10° and 80°. The diffraction peaks match very well with the standard Hematite (Fe_2O_3) phase and iron carbide (Fe_5C_2) phase. For hsa-C support and catalysts the peaks at 2θ of 26 and 43° correspond to graphite layers (multiwall carbon

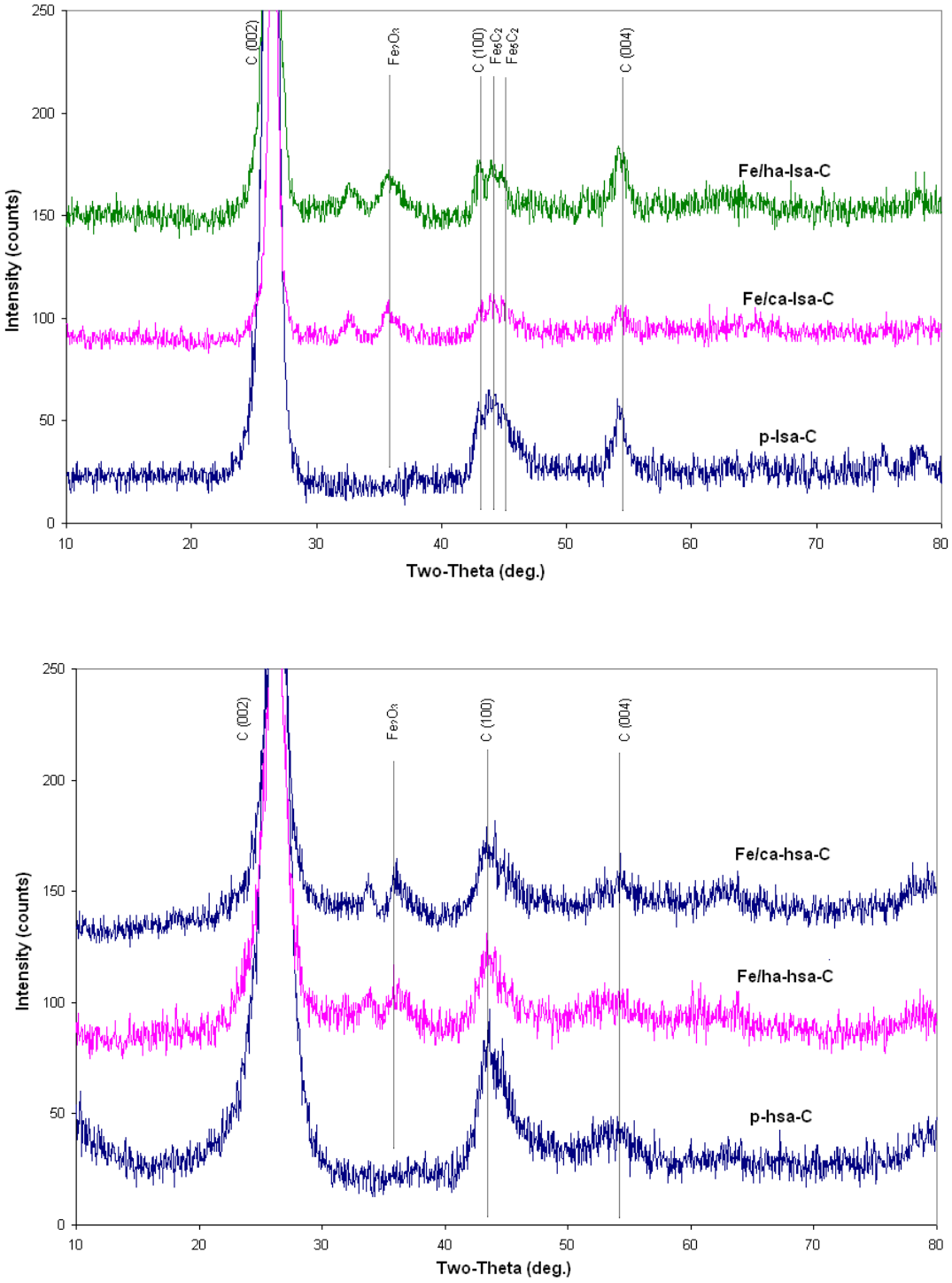

Figure 3.5 XRD spectra for the catalysts studied

nanotubes), while the other peaks in the spectrum of catalysts are related to different crystal planes of Fe_2O_3. The peaks at 33.6 and 35.7^o are the most intense peak of Fe_2O_3 in XRD spectrum of the catalysts. For lsa-C support and catalysts, there are two additional peaks at 43 and 44^o corresponding to iron carbide. These iron particles were encapsulated in the nanotubes in the form of iron carbide during the CNTs synthesis process [28].

Table 3.3 shows the average Fe_2O_3 particle size on the catalysts calculated from XRD spectrum and Debye-Scherrer equation at 35.7^o. The data reveal that for both families of CNT catalysts, the acid treatments resulted in smaller crystalline sizes. This could be ascribed that the acid treatment increases the surface area and also opens the capes on the closed CNTs which in turn leads to better distribution of the metal particles and result in smaller iron cluster sizes. In addition, comparison of Fe/ca-lsa-C and Fe/ha-lsa-C with similar BET surface areas shows that the treatment with nitric acid provides more functional groups resulting in a higher dispersion and smaller particle sizes. To compare the particle size calculated based on XRD and TEM analysis, the size distribution of the particles is shown in Table 3.3. There is a good agreement between the data for average particle size calculated based on XRD and TEM size distribution.

Raman spectroscopy is an important characterization tool for carbon-based material including MWCNTs. The D band at 1350 cm^{-1} is disorder-induced. The G mode at 1585 cm^{-1} is usually regarded as a Raman-allowed G-point vibration of graphite and often called tangential mode for carbon nanotubes. The D band is not observed in perfect crystal graphite and is produced by defects or finite size effect. Thus, the relative intensity of the D band with respect to the G band can be used as a measure of the degree of disorder or the concentration of functionalized groups and defects [29]. The results of Raman spectroscopy in the form of ratio of D band (I_D) and G band (I_G) are

Table 3.3 Particle sizes of the calcined catalysts

Catalyst Name	Particle size[a] (nm)	Particle size[b] (nm)
Fe/ca-lsa-C	14 ± 2	4-20
Fe/ha-lsa-C	11 ± 1	4-15
Fe/p-hsa-C	8 ± 1	3-10
Fe/ca-hsa-C	7 ± 1	3-9
Fe/ha-hsa-C	6 ± 1	3-7

a) measured by XRD
b) measured by TEM

Table 3.4 I_D/I_G ratio of the pristine and acid treated CNTs

Support Name	Treatment	I_D	I_G	I_D/I_G
p-lsa-C	No treatment	1039	2970	0.35 ± 0.06
ca-lsa-C	Nitric acid at 25°C	1405	2554	0.55 ± 0.05
ha-hsa-C	Nitric acid at 110°C	1419	2183	0.65 ± 0.03
p-hsa-C	No treatment	2143	2170	0.98 ± 0.05
ca-hsa-C	Nitric acid at 25°C	1817	1785	1.01 ± 0.06
ha-hsa-C	Nitric acid at 110°C	1926	1513	1.27 ± 0.05

presented in Table 3.4. The data reveal that the acid treatments enhanced the ratio of I_D/I_G indicating an increase in defects along the nanotubes' surface for the both studied CNT families. In the case of hsa-C supports, acid treatment at 25°C and 110°C increased the I_G/I_D from 0.98 to 1.01 and 1.27 respectively, while for lsa-C samples, there was a sharp rise in I_D/I_G ratio from 0.35 to 0.55 and 0.65. This shows that the amount of defects on the CNT surface increases with acid treatment, which in turn leads to smaller metal particles and better metal dispersion on the acid treated CNTs surface which is also confirmed with XRD analysis (Table 3.3).

TPR analyses were performed to evaluate the reducibility of the studied catalysts. Generally, the reduction of iron oxides takes place as below:

$Fe_2O_3 \rightarrow Fe_3O_4 \rightarrow FeO \rightarrow Fe$

It has been postulated that the first peak corresponds to reduction of Fe_2O_3 to Fe_3O_4, and the second peak corresponds to subsequent reduction of Fe_3O_4 to metallic

iron [30]. Also, it has been stated that supported transition metal acts as catalyst for the formation of methane via a reaction of hydrogen with the carbon nanotubes support at high temperatures above 550^{o}C [17]. This was confirmed by measuring the methane concentration as a function of temperature in a separate experiment.

TPR patterns of 10% Fe supported on hsa-C and lsa-C samples are shown in Figure 3.6. For Fe catalyst supported on lsa-C samples, three distinct peaks (A, B and C) can be observed on the TPR spectrum. Peak A and B can be assigned for reduction of Fe_2O_3 to Fe_3O_4 and Fe_3O_4 to Fe, respectively. Peak C may correspond to gasification CNTs at 610^{o}C as can also be seen in the TRP of pristine support (p-lsa-C) in Figure 3.6. For acid treated hsa-C catalysts, TPR analysis revealed an interesting phenomenon for carbon nanotubes supported catalysts. As can be seen in Figure 3.6, there are two close peaks (A1 and A2) for Fe/ca-hsa-C and Fe/ha-hsa-C in contrast to one peak (A) for Fe/p-hsa-C, Fe/ca-lsa-C and Fe/ha-lsa-C at temperature interval of 300-400^{o}C. Peaks A1 and A2 can not correspond to series reduction of iron oxide, since there are two distinct peaks (A and B) for the other studied catalysts. As mentioned above, in the case of Fe/ca-lsa-C, Fe/ha-lsa-C and Fe/p-hsa-C catalysts, the metal particles are mostly distributed on the exterior surface of CNTs but, for Fe/ca-hsa-C and Fe/ha-hsa-C, metal particles are distributed on both inner and outer layers of CNTs. Thus, the presence of peaks A1 and A2 would be related to reduction of iron oxide deposited on the inner and outer sidewalls of CNTs, respectively.

More detailed values for degree of reduction and the total amount of hydrogen consumptions during TPR are given in Table 3.5. The degree of reduction of the metal (DRT) is the ratio of H_2 consumed during reduction from room temperature to 800^{o}C to the calculated amount of H_2 for the complete reduction of metal oxides. For complete reduction of a 10% iron catalyst, 2.67 mmol/g-cat is theoretically required. For all of the

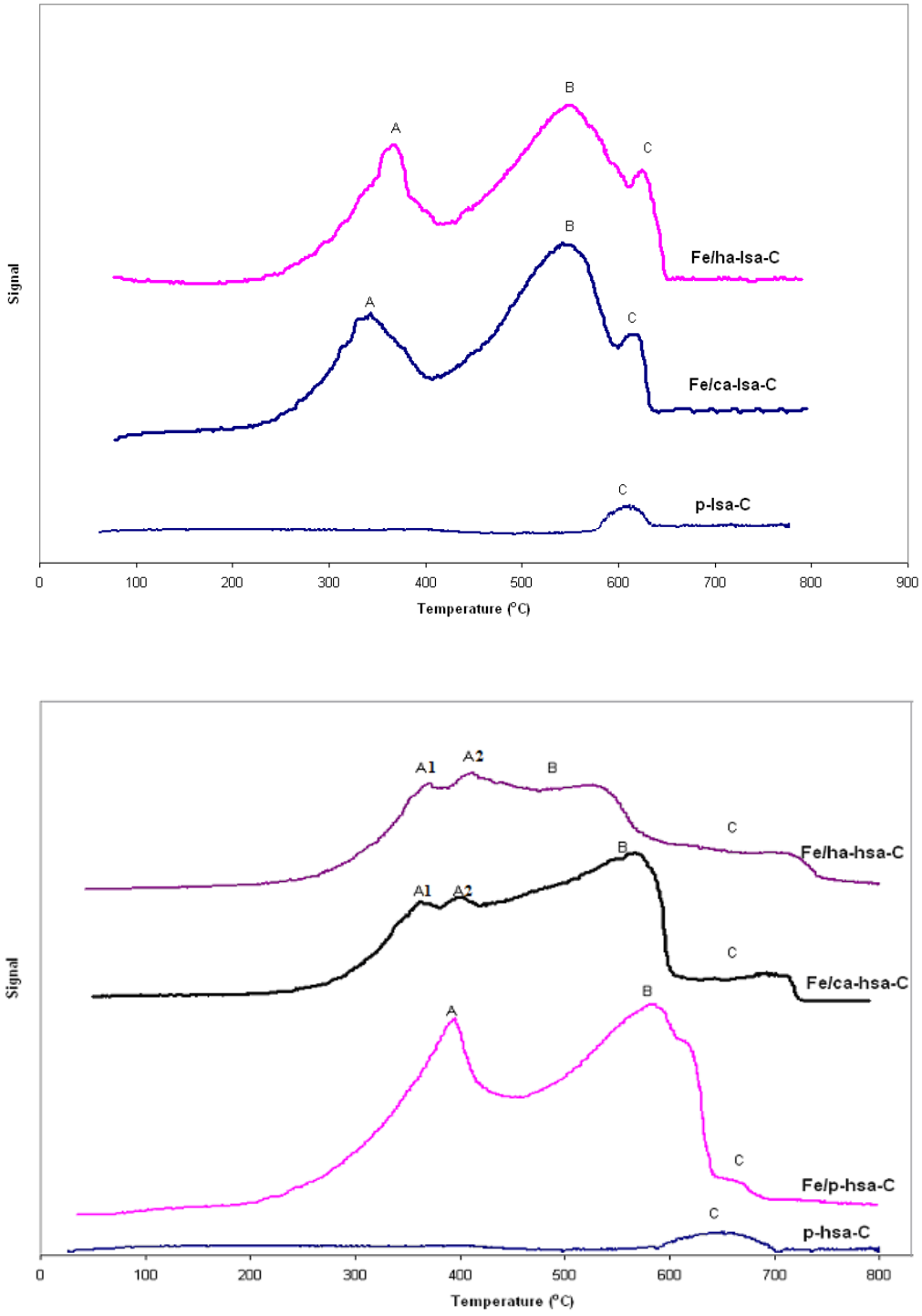

Figure 3.6 TPR profiles of the lsa-C and hsa-C catalysts and supports

Table 3.5 H_2 consumption and degree of reduction determined by TPR over the lsa-C and hsa-C catalysts

Catalyst	Measured H_2 Consumption mmol/g-cat			Degree of Reduction%		DRT%[a]
	Peak A	Peak B	Peak C	Peak A	Peak B	
Fe/p-hsa-C	0.78	0.99	0.04	29	37	66
Fe/ca-hsa-C	0.63	0.77	0.11	24	29	50
Fe/ha-hsa-C	0.72	0.62	0.19	27	23	53
Fe/ca-lsa-C	0.74	0.97	0.09	27	36	63
Fe/ha-lsa-C	0.55	0.92	0.16	21	34	55

Catalysts contain 10 wt % Fe,
a Reduced from RT to 800^{o}C, heating rate: 10 C/min, peak C is not included.

studied catalysts, the degrees of reduction were low despite the high temperature in the TPR-experiment. Fe/p-hsa-C experienced a higher degree of reduction (DRT = 66%) compared to Fe/ca-hsa-C and Fe/ha-hsa-C. In addition, the degree of reduction for Fe/ca-lsa-C is higher than that of for Fe/ha-lsa-C. In general, TPR studies on pristine and acid treated CNT supports (Table 3.5) reveals that acid treatment can result in slightly lower degree of reduction.

3.4.1 Used Catalysts Characterization

Figure 3.7 shows XRD patterns of the used Fe/p-hsa-C, Fe/ha-hsa-C, Fe/ha-lsa-C catalysts after 120 h of FTS reaction at 275 °C. The diffraction peaks match very well with magnetite (Fe_3O_4) phase and the standard carbide (Fe_5C_2) phase. The particle size calculation based on XRD peak broadening reveals significant metal size growth for the used catalysts. As can be seen in the Figure 3.7, in the case of Fe/p-hsa-C, a sharp peak appeared at a two-theta angle of 35.6 indicating considerable metal particle growth whereas, for the catalyst pre-treated with strong acid environment, the metal particle growth is not significant compared to their counterparts. The iron catalysts supported on CNTs without enough acid pre-treatment experienced metal site agglomeration increasing from 8 to 35, 7 to 19 and 14 to 21 nm for Fe/p-hsa-C, Fe/ca-hsa-C and Fe/ca-lsa-C catalysts (see Table 3.7).

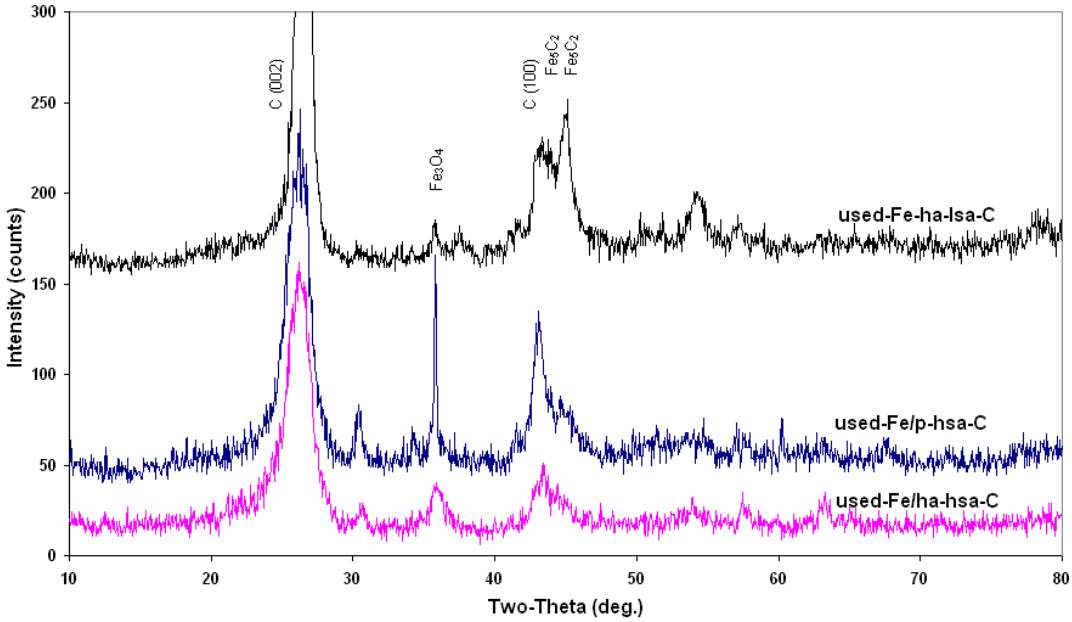

Figure 3.7 XRD spectra for the used catalysts

In terms of carbide phase, XRD analysis revealed that the extent of carbonization varies among the studied catalysts. In the case of used iron catalysts supported on lsa-C support, the presence of intense peaks at two-theta angle of 43 and 44^{o} reveals that the extent of carbide phase is higher compared to that of the lsa-C support and used-Fe/p-hsa-C and used-Fe/ca-hsa-C catalysts.

Part of metallic iron may not be carbonized on the catalyst surface during reaction [14]. But the current XRD patterns cannot disclose this phase, because the catalyst samples were exposed to air after the reaction and any metallic iron would be oxidized.

3.5 Fischer-Tropsch Synthesis

The performance of the iron catalysts supported on two different types of carbon nanotubes in the Fischer-Tropsch synthesis was tested in a fixed bed reactor. All the reactions were performed under a set of standard conditions (275^{o}C, 2 MPa, H_2:CO = 1.5). CO hydrogenation was performed on both p-lsa-C and p-hsa-C supports (blank

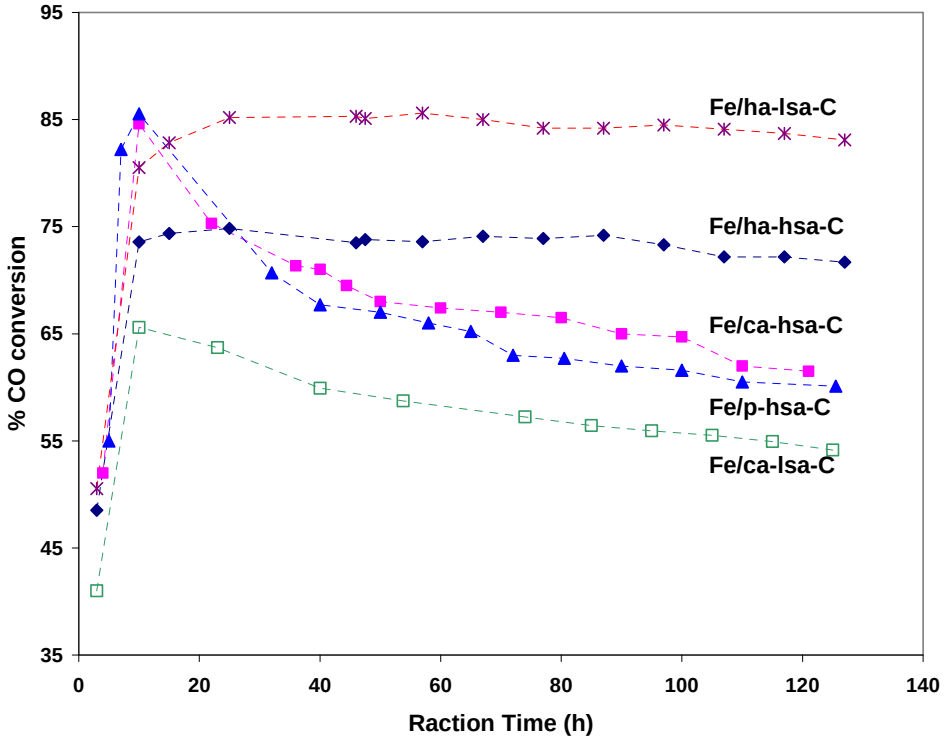

Figure 3.8 Change of syngas conversion with TOS over the catalysts studied

runs with no iron) under the operating conditions as same as used for the metal loaded samples. For p-lsa-C with 4.5% of residual iron form the CNT synthesis process, the main product formed at a very low conversion (1%) was methane with almost no higher hydrocarbons formed. These data show that the residual iron particles left behind CNTs synthesis are not accessible for the reactant CO and hydrogen. In case of p-hsa-C, the CO conversion was almost negligible.

Figure 3.8 shows the variations of CO conversion with the time-on-stream (TOS). All of the catalysts reached their highest activity within 10 hours. Afterward, they showed different stability pattern within a time period of 120 hours. Figure 3.8 shows that Fe catalysts supported on the CNTs treated with nitric acid at 110^{o}C are stable. In the case of Fe/p-hsa-C and Fe/ca-hsa-C syngas conversion drops quickly from a high conversion of 83 and 84% at TOS of 10 h to 60 and 61% at TOS of 120 hours. For

Table 3.6 Activity and selectivity of iron catalyst supported on CNTs in FTS[a,b]

Catalyst	Fe/ha-lsa-C	Fe/ca-lsa-C	Fe/ha-hsa-C	Fe/ca-hsa-C	Fe/p-hsa-C
TOS (h)	10 →140	10 →120	10 →140	10 → 120	10 → 120
%CO	86	66 → 54	74	84 → 61	83 → 60
10^6 * CO rate[c]	5.70	4.43 → 3.63	4.90	5.67 → 4.08	5.61 → 4.1
10^6 * CO_2 rate[c]	1.89	1.24 → 0.87	1.82	2.03 → 1.37	1.98 → 1.37
Selectivity[e]					
CH_4	9	9 → 11	24	29.4 → 38.9	34 → 41
C_2-C_4	21	26 → 27	23	23.1 → 18.9	22 → 19
C_5^+	70	65 → 61	53	47 → 42	44 → 40
CO_2	33	28 → 24	37	35 → 33	36 → 34
O/P ratio[f]	1.65	1.82 → 1.87	0.25	0.04 → 0.08	0.10 → 0.16

a) Process conditions: 1.86 Nl/g-cat/h, 2MPa. All catalysts contain 10wt% Fe, b) Ranges in the data represent catalyst deactivation from low to high TOS; Single values are the average values over the TOS range for stable catalysts. c) mol/s, d) g-HC/ h/ g-Fe, e) HC in wt%; CO_2 in C %, f) $(C_2+C_3+C_4)^{=}$ /$(C_2+C_3+C_4)$

Fe/ca-lsa-C, there is a slow deactivation from 66% CO conversion to 54% within 120 hours. Based on the XRD analysis on the used catalyst, one of the major factors for catalyst deactivation is metal site agglomeration during FT reactions (see Table 3.7). The stability of the catalyst may be attributed to the extent of functional groups and defects and /or the structure of CNT supports. As discussed earlier, the Raman analysis revealed that acid treatment at 110^{o}C could produce defects on the CNT surface. The defects on the surface work as anchoring sites for stable metal particles on the supports surface. Further investigation into the other factors related to catalyst deactivation would be valuable.

The time-on-stream behavior of the catalysts including CO% conversion, CO and CO_2 and FTS rates, methane, CO_2, C_5^+ and olefin to paraffin selectivities are demonstrated in Table 3.6. Corresponding to the highest activity (as shown in Figure 3.8), the Fe/ha-lsa-C catalyst exhibits the highest %CO conversion and CO rate. A comparison of iron catalysts supported on the low surface area CNTs reveals that Fe/ca-lsa-C has lower CO conversion by 20%. This can be ascribed to the smaller particle size and higher dispersion of Fe on ha-lsa-C compared to ca-lsa-C. In other hand, WGS rate

and CO_2 selectivity for Fe/ca-lsa-C is less than that of Fe/ha-lsa-C. This is because the higher FTS rate results in a higher water partial pressure, which causes higher WGS rate.

In the case of iron catalysts supported on high surface area CNTs, Fe/p-hsa-C and Fe/ca-hsa-C have shown similar FTS and WGS activity with a rapid deactivation during a period of 120 hours. The results reveal that mild acid treatment in room temperature does not modify the surface characteristics of CNTs. Raman spectroscopy on p-hsa-C and ca-hsa-C (see Table 3.4) confirms that the extents of surface defects are similar for these two catalysts. Fe/ha-hsa-C exhibited a stable catalytic activity with a CO conversion of 74% which is 10% lower that initial activity of Fe/p-hsa-C and Fe/ca-hsa-C. As discussed in the previous section, most of iron particles are deposited in the inner sidewall of nanotubes (see Figure 3.4c). Thus, there is possibility of pore blockage which is confirmed by declining in catalyst BET surface area and pore volumes. Therefore, it can be speculated that some of the iron particle may be confined inside the CNTs' pore while the iron within the nanotubes is no longer assessable for syngas, resulting in a lower CO rate.

The effects of acid treatment on hydrocarbon selectivities, as defined earlier in equations 3.1 to 3.4 are shown in Table 3.6. Corresponding to the highest activity, the Fe/ha-hsa-C exhibits the lowest CH_4 and higher C_5^+ selectivities, compared to the Fe/ca-hsa-C and Fe/p-hsa-C. As mentioned earlier, for Fe/ha-hsa-C, most of the metal particles are deposited inside the nanotube pores, leading to the peculiar interaction of the interior nanotube surface with the metal particles, which benefits the dissociation of CO and production of higher hydrocarbons [25].

The variation of olefin to paraffin ratio with time on stream for the catalysts are shown in Table 3.6. The data show that the olefin to paraffin ratio increases with time

Table 3.7 Summary table on characteristic and FT performance of the lsa-C and hsa-C catalysts

sample	Fe/ca-lsa	Fe/ha-lsa-C	Fe/p-hsa-C	Fe/ca-hsa-C	Fe/ha-hsa-C
Pre-treatment	Nitric acid at 25°C	Nitric acid at 110°C	-	Nitric acid at 25°C	Nitric acid at 110°C
Fe location	Exterior (pore blocked)	Exterior (pore blocked)	Mostly exterior (closed-cap)	Half exterior (35% open-cap)	Mostly interior (open-cap)
Particle size (nm) (before reaction)	14	11	8	7	6
Particle size (nm) (after reaction)	21	14	35	19	9
Degree of Reducibility	63	55	66	50	53
Catalyst stability	Deactivate	Stable	Deactivate	Deactivate	Stable
%COa	66 → 54	86	83 → 60	84 → 61	74
Catalyst selectivitya (C_{5+} wt%)	65 → 61	70	44 → 40	47 → 42	53

a) Ranges in the data represent catalyst deactivation in terms of %CO conversion and change in C_5^+ wt% from low to high TOS (120 h); Single values are the average values over the TOS range for stable catalysts

on stream in the case of Fe/ca-hsa-C, Fe/p-hsa-C and Fe/ca-lsa-C catalysts. This could be attributed to decrease in olefins hydrogenation reaction rates as a result of decrease in %CO conversion and the residence time.

Since there are many samples, each with numerous characterizations, their characterizations and FT performances are summarized and presented in Table 3.7. Using the same operating conditions and iron loading on two different CNT samples with different structures suggests that the structure of CNTs and the position of metal site i.e. inside or outside of nanotubes' pores have significant influences on the activity and selectivity of FT catalysts (see Table 3.7).

3.6 Conclusions

In this study, the effects of acid treatment on the FTS activity, stability, and product selectivity of iron catalysts supported on two different CNTs with different structures were investigated. Pre-treatment of carbon nanotubes with 35% nitric acid at 25 and 110^{o}C opened the caps, increased the BET surface area and introduced a large number of defects and functional groups on the nanotubes. Also, comparison between pristine and acid pre-treated CNTs shows that acid pre-treatment results in ~20% smaller iron crystalline. For the CNT supports with open cap, capillary force led to confinement of iron particles inside the CNT pores.

FT analysis revealed that iron catalysts supported on pre-treated CNTs at 110^{o}C are very stable and active catalysts during a period of 120 h while iron catalyst supported on pristine and CNTs treated at mild acidic condition were deactivated within the same reaction period. Also, the stability and product selectivity of hsa-C catalyst were improved when the iron particles were attached inside the nanotubes' pores.

Nomenclature

A	Surface area (area/mass unit)
d_{in}	Inner diameter of CNTs (nm)
d_{out}	Outer diameter of CNTs (nm)
L	Average length of CNTs
n_{cl}	Number of nanotubes with close-cap per mass unit
n_{op}	Number of nanotubes with open-cap per mass unit
P	Pressure (MPa)
S	Selectivity (wt%)
T	Temperature (^{o}C)

Abbreviations

BET	Brunauer, Emmett, and Teller
ca	Cold acid
CNT	Carbon nanotubes
FTS	Fischer-Tropsch Synthesis
ha	Hot acid
hsa	High surface area
ICP	Inductively coupled plasma
I_D	Intensity of defect band in Raman spectroscopy
I_G	Intensity of graphite band in Raman spectroscopy
lsa	Low surface area
MWCNT	Multiwall carbon Nanotube
TPR	Temperature programmed reduction
WGS	Water-gas shift
XRD	X-ray diffraction

References

[1] M.E. Dry, Fischer-Tropsch reactions and the environment, Applied Catalysis A: General, 189 (1999) 185-190.

[2] M.J.A. Tijmensen, A.P.C. Faaij, C.N. Hamelinck, M.R.M van Hardeveld, Exploration of the possibilities for production of Fischer Tropsch liquids and power via biomass gasification, Biomass and Bioenergy 23 (2002) 129-152.

[3] G. P. van der Laan, A.A.C.M. Beenackers, Selectivity of the Fischer-Tropsch Synthesis: A Literature Review, Catalysis Reviews, 41 (1999) 255-318.

[4] H. Schulz, Short history and present trends of Fischer-Tropsch synthesis, Applied Catalysis A: General, 186 (1999) 3-12.

[5] T. Riedel, M. Claeys, H. Schulz, G. Schaub, S. Nam, K. Jun, M. Choi, G. Kishan, K. Lee, Comparative study of Fischer-Tropsch synthesis with H_2/CO and H_2/CO_2 syngas using Fe- and Co-based catalysts, Applied Catalysis A: General, 186 (1999) 201-213.

[6] D. B. Bukur, X. Lang, D. Mukesh, W. H. Zimmerman, M. P. Rosynek, and C. Li, Binder/support effects on the activity and selectivity of iron catalysts in the Fischer-Tropsch synthesis, Industrial Engineering Chemistry Research, 29 (1990)1588-1599.

[7] G.L. Bezemer, P.B. Radstakea, U. Falke, H. Oosterbeek, H.P.C.E. Kuipers, A.J. van Dillen, K.P. de Jong, Investigation of promoter effects of manganese oxide on carbon nanofiber-supported cobalt catalysts for Fischer-Tropsch synthesis, Journal of Catalysis, 237 (2006) 152-161.

[8] G.L. Bezemer, P.B. Radstake, V. Koot, A.J. van Dillen, J.W. Geus, K.P. de Jong, Preparation of Fischer-Tropsch cobalt catalysts supported on carbon nanofibers and silica using homogeneous deposition-precipitation, Journal of Catalysis, 237 (2006) 291-302.

[9] G. L. Bezemer, J. H. Bitter, H.P.C.E. Kuipers, H. Oosterbeek, J. E. Holewijn, X. Xu, F. Kapteijn, A. J. van Dillen, and K. P. de Jong, Cobalt Particle Size Effects in the Fischer-Tropsch Reaction Studied with Carbon Nanofiber Supported Catalysts, American Journal of Chemical Society, 128 (2006) 3956.

[10] Z. Yu, Ø. Borg, D. Chen, B.C. Enger, V. Frøseth, E. Rytter, H. Wigum, and A. Holmen, Carbon Nanofiber Supported Cobalt Catalysts for Fischer-Tropsch Synthesis with High Activity and Selectivity, Catalysis Letters, 109 (2006) 43-47.

[11] A. Tavasoli, K. Sadagiani, F. Khorashe, A.A. Seifkordi, A.A. Rohani, A. Nakhaeipour, Cobalt supported on carbon nanotubes-A promising novel Fischer-Tropsch synthesis catalyst, Fuel Processing Technology (2007). doi:10.1016/j.fuproc.2007.09.008

[12] A. Tavasoli, A. M. Rashidi, K. Sadaghiani Zadeh, A. Karimi, A. Kodadadi, Y. A. Mortazavi, (2005) European Patent EP1782885

[13] A. Tavasoli, K. Sadaghiani, A. Nakhaeipour, M. Ghalbi Ahangari, Cobalt Loading Effects on the Structure and Activity for Fischer-Tropsch and Water-Gas Shift Reactions of Co/Al_2O_3, Catalysts, Iranian Journal of Chemistry & Chemical Engineering, 26 (2007) 1-9.

[14] W. Ma, E.L. Kugler, J. Wright, and D.B. Dadyburjor, Mo-Fe Catalysts Supported on Activated Carbon for Synthesis of Liquid Fuels by the Fischer−Tropsch Process: Effect of Mo Addition on Reducibility, Activity, and Hydrocarbon Selectivity, Energy Fuels 20 (2006) 2299-2307.

[15] L. Guczi, G. Stefler, O. Geszti, Zs. Koppány, Z. Kónya, É. Molnár, M. Urbánc, I. Kiricsi, CO hydrogenation over cobalt and iron catalysts supported over multiwall carbon nanotubes: Effect of preparation, Journal of Catalysis, 244 (2006) 24-32.

[16] M.C. Bahome, L.L. Jewell, K. Padayachy, D. Hildebrandt, D. Glasser, A. K. Datye, N. J. Coville, Fe-Ru small particle bimetallic catalysts supported on carbon nanotubes for use in Fischer-Tröpsch synthesis, Applied Catalysis A: General, 328 (2007) 243-251.

[17] E. van Steen, F.F. Prinsloo, Comparison of preparation methods for carbon nanotubes supported iron Fischer-Tropsch catalysts, Catalysis Today, 71 (2002) 327-334.

[18] M.C. Bahome, L.L. Jewell, D. Hildebrandt, D. Glasser, N.J. Coville, Fischer-Tropsch synthesis over iron catalysts supported on carbon nanotubes, Applied Catalysis A: General, 287 (2005) 60-67.

[19] H.J. Jung, P.L. Walker Jr., M.A. Vannice, CO hydrogenation over well-dispersed carbon-supported iron catalysts, Journal of Catalysis, 75 (1982) 416-422.

[20] A.A. Chen, M.A. Vannice, and J. Phillips, Effect of support pre-treatments on carbon-supported iron particles, Journal of Physical Chemistry, 91 (1987) 6257-6269.

[21] P. Serp, M. Corrias, P. Kalck. Carbon nanotubes and nanofibers in catalysis, Review, Applied Catalysis A: General, 253(2003) 337-358.

[22] C. Li, K. Yao, J. Liang, Influence of acid treatments on the activity of carbon nanotube-supported catalysts, Carbon 41, (2003) 858-860.

[23] T. Wang, C. Tseng, Polymeric carbon nanocomposites from multiwalled carbon nanotubes functionalized with segmented polyurethane, Journal of Applied Polymer Science, 105 (2007) 1642-1650.

[24] W. Chen, z. Fan, X. Pan, X. Bao, Effect of Confinement in Carbon Nanotubes on the Activity of Fischer-Tropsch Iron Catalyst, Journal of American Chemical Society, 130 (2008) 9414-9419.

[25] X. Pan, Z. Fan, W. Chen, Y. Ding, H. Luo, X. Bao, Enhanced ethanol production inside carbon-nanotube reactors containing catalytic particles, Nature, 6 (2007) 507-511.

[26] N. Das, A. Dalai, J. S. Soltan Mohammadzadeh, J. Adjaye, The effect of feedstock and process conditions on the synthesis of high purity CNTs from aromatic hydrocarbons, Carbon, 44 (2006) 2236-2245.

[27] J. Tessonnier, L. Pesant, G. Ehret, M. J. Ledoux, C. Pham-Huu, Pd nanoparticles introduced inside multi-walled carbon nanotubes for selective hydrogenation of cinnamaldehyde into hydrocinnamaldehyde, Applied Catalysis A: General, 288 (2005) 203-210.

[28] R. Andrews , D. Jacques, D. Qian, E.C. Dickey, Purification and structural annealing of multiwalled carbon nanotubes at graphitization temperatures, Carbon, 39 (2001) 1681-1687.

[29] A.J. Dresselhaus, A.G. Souza Filho, G. Dresselhaus, R. Saito, M.A. Pimenta, Raman spectroscopyof nanoscale carbons and of an isolated carbon nanotube, Molecular Crystals Liquid Crystals, 387 (2002) 21-29.

[30] H. Hayakawa, H. Tanaka, K. Fujimoto, Studies on precipitated iron catalysts for Fischer-Tropsch synthesis, Applied Catalysis A: General, 310 (2006) 24-30.

Chapter 4

Iron Catalysts Supported on Carbon Nanotubes for Fischer-Tropsch Synthesis: Effect of Catalytic Site Position

A similar version of this chapter has been copyrighted and published in the journal of Applied Catalysis A: General.

- *Reza M. Malek Abbaslou, Ahmad Tavasoli, Jafar Soltan, Ajay K. Dalai, Iron Catalysts Supported on Carbon Nanotubes for Fischer-Tropsch Synthesis: Effect of Catalytic Site Position. Applied Catalysis A: General, 367(2009)47-52.*

In addition, a part of this chapter was presented at the following conference:

- *Reza M. Malek Abbaslou, Ahmad Tavasoli, Jafar Soltan, Ajay K. Dalai (2009) Fe/CNT catalyst for Fischer-Tropsch Synthesis-effect of metal site position. 8th World Congress of Chemical Engineering, Montréal, Canada (2009).*

Contribution of the Ph.D. Candidate

The experimental design and experiments were planned and conducted by Reza Malek Abbaslou. The data analysis and interpretations were performed by Reza Malek Abbaslou, with assistance from Drs. Tavassoli, Soltan and Dalai. All written text was prepared by Reza Malek Abbaslou and discussed with Drs. Soltan and Dalai.

Contribution of this Chapter to the Overall Study

In the Chapter 3, it was shown that the pre-treatment of nanotubes with nitric acid resulted in opening the nanotubes' caps. In addition, this phenomenon leads to the deposition of catalytic sites inside the nanotubes. The main objective of the research presented in this chapter is to present the effects of catalytic site position on FT

reactions. Also, a method to manipulate the catalytic site position on interior or exterior surface of the CNTs through same pre-treatment procedure is introduced.

Abstract

In order to study the effects of catalytic site position on Fischer-Tropsch (FT) reactions, a method was developed to control the position of the catalytic sites on either the inner or outer surfaces of carbon nanotubes (CNTs). TEM analyses revealed that more than 70-80% of iron oxide particles can be controlled to be positioned on the inner or outer surface of the nanotubes. Based on H_2-TPR analysis, deposition of iron oxide inside the nanotube pores resulted in easier reduction of the oxide at a lower temperature (from 418 to 381^{o}C). Catalytic performance of the catalysts in terms of FT experiments were tested in a fixed bed reactor. According to the results of the FT experiments, both catalysts showed similar initial %CO conversion (~90%). However, the catalyst with catalytic sites inside the pores exhibited higher selectivity to heavier hydrocarbons. In addition, deposition of catalytic sites on the interior surfaces of the nanotubes resulted in a more stable catalyst, while its counterpart experienced deactivation within a period of 125 h due to catalytic sites sintering. It is concluded that encapsulation of catalytic sites inside the nanotubes prevents the catalytic site agglomeration.

4.1 Introduction

Fischer-Tropsch Synthesis (FTS) is a potentially promising option for environmentally friendly production of chemicals and fuels from biomass, coal and natural gas [1-2]. In industrial applications, a high-performance catalyst plays an essential role. In the FTS process, the catalyst activity and selectivity are influenced by the nature and structure of support, the nature of the metal, metal dispersion, metal loading, and the catalyst preparation method [3-4]. Most studies on FTS catalysts have

been carried out with the metals supported on silica, alumina or titania. In recent years, other families of supports with a carbonaceous base in the form of activated carbon and carbon nanotubes (CNTs) have been investigated for FT reactions [6-20].

Carbon nanotubes with unique properties such as uniform pore size distribution, meso and macro pore structure, inert surface properties, and resistance to acid and base environment can play an important role in a large number of catalytic reactions [18]. Carbon nanotubes (CNTs) are different compared to other supports in that they have graphene layers with a tubular morphology. Theoretical studies reveal that deviation of the graphene layers from planarity causes π-electron density to shift from the concave inner surface to the convex outer surface, leading to an electron-deficient interior surface and an electron-enriched exterior surface [19-21]. This can influence the structure and electronic properties of substances in contact with either surface. In addition, studies on non-catalytic gas-phase reactions suggest that confinement within small channels could increase the density of reactants, and hence create a locally higher pressure [22] which will favor syngas conversion. However, a probable drawback of deposition of catalytic sites inside the narrow channels is higher mass transfer restriction.

Chen et al. [19] studied the confinement effect of iron particles inside the nanotubes channels for FT reactions. They used closed-cap CNTs for deposition of iron particles on the exterior surfaces of nanotubes using an impregnation method. In order to prepare iron catalyst inside the nanotubes, they used strong acid pre-treatment to open the CNTs' cap. Therefore, their catalysts experienced a different pre-treatment procedure which may affect the catalyst performance [5]. According to their report, the catalytic performance of the iron catalysts supported either inside or outside of the natotubes' channel is similar at pressures less that 2 MPa. However, at higher pressure

(5 MPa), the yield of C_5+ hydrocarbons over the encapsulated iron catalyst is twice that over iron catalyst outside CNTs.

In this research, a method is introduced to manipulate the catalytic site position on the interior or exterior surface of the CNTs through the same pre-treatment procedure. The main objective of the current work is to study the effect of position of the active metal on the FT reaction.

4.2 Experimental

A batch of carbon nanotubes was purchased from mknano Co. (M.K. IMPEX Canada). The CNT sample was treated in nitric acid (60wt%) at 110^{o}C for 16 hours. The catalysts were prepared according to the incipient wetness impregnation method. For the preparation of the catalyst with iron particles inside the nanotube pores (in-Fe/CNT) with 12 wt% Fe, a specified amount of $Fe(NO_3)_3 \cdot 9H_2O$ was dissolved in deionised water. The amount of solution was equal to the total pore volume of the CNT sample (0.62 ml/g). In this case, the metal solution fills the inner pores of the CNTs due to capillary effects. In order to prepare the catalysts with catalytic sites on the exterior surface (out-Fe/CNT), the acid-treated CNT sample was wetted with pure water (the amount of water was equal to the pore volume of the CNT sample). As a result, the inner pores of the CNTs were initially filled with water. Afterward, the metal salt solution was added to the support. In this case, there was no capillary force for the metal solution to move into the nanotubes' pores. However, there might be a slight diffusion of metal salt solution into the water-filled-pores [23]. Subsequently, the impregnated support sample was immediately moved into the drying oven. The schematic of the prepration procedure is given in Figure 4.1. After drying at 120^{o}C and calcination at

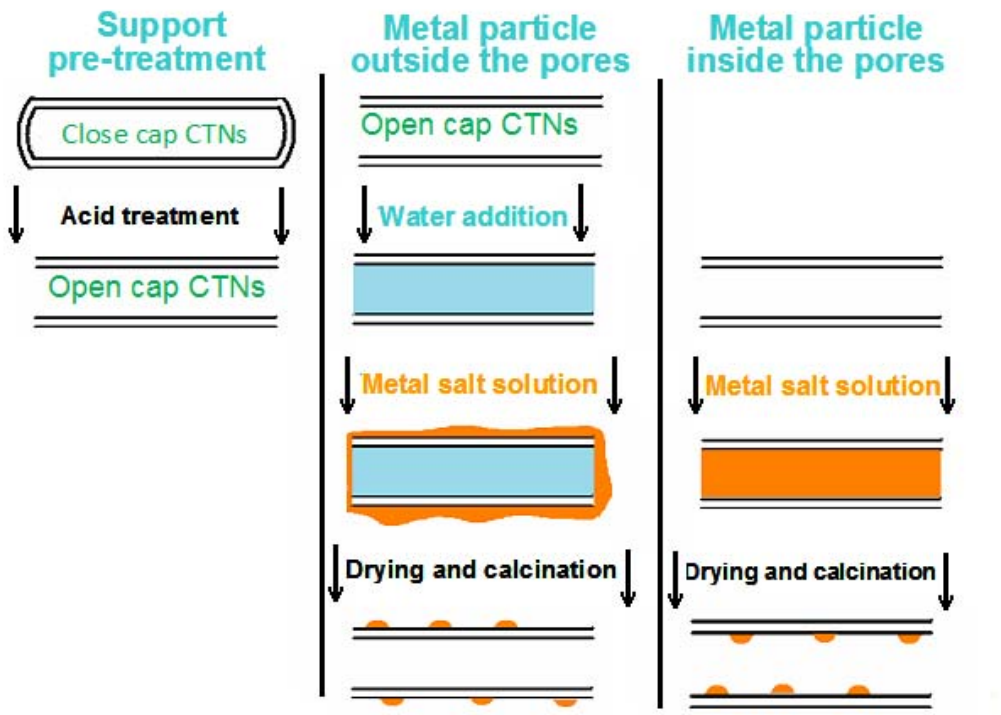

Figure 4.1 The schematic of the preparation procedure for in-Fe/CNT and out-Fe/CNT catalysts

400^{o}C for 3 hours, the catalysts were characterized by nitrogen adsorption, ICP, TPR, XRD, SEM and TEM.

The surface area, pore volume, and average pore diameter of the CNTs and catalysts were measured by an ASAP-2000 Micromeritics system. The samples were degassed at 200^{o}C for 2 h under 50 mTorr vacuum before measurements.

XRD analysis was performed using a Philips PW1840 X-ray diffractometer with monochromatized Cu/Kα radiation. The crystallite diameter was determined by substituting the half-width of a chosen peak into the Debye-Scherrer equation. The details for the particle size estimation using Debye-Sherrer method are presented in Appendix E.

The reduction behavior of the catalyst precursors was studied by temperature programmed reduction (TPR) using a CHEMBET-3000 equipped with a thermal conductivity detector. Here, 0.1 g of catalyst was placed in U-shaped quartz tube. A 5% hydrogen/nitrogen mixture was introduced (flow rate = 36 ml (STP)/min) and the furnace temperature was ramped from room temperature to 1173 K at 10 K/min. The details for calibration of the TPR machine and corresponding calculations are given in Appendix D.

The morphology of the samples was studied by transmission electron microscopy (TEM). Sample specimens for TEM studies were prepared by ultrasonic dispersion of the catalysts in ethanol, and the suspensions were dropped onto a copper grid. TEM micrographs were carried out using a Hitachi H-7500 (120kV). Several TEM micrographs were recorded for each sample and were analyzed to determine the particle size distribution. A Phillips SEM-505 scanning electron microscope operating at 300 kV in SE display mode was also used for the SEM micrographs. For characterization prior to analysis, all the samples were gold-coated in a sputter coating unit (Edwards Vacuum Components Ltd., Sussex, England).

The Fischer-Tropsch synthesis was performed in a fixed-bed micro reactor. The schematic and specifications of the fixed bed reactor are given in Appendix C. Prior to CO hydrogenation, in-situ reduction was conducted according to the following procedure. The catalyst (1 g) was placed in the reactor and diluted with 7 g of silicon carbide. Then, pure hydrogen was introduced at a flow rate of 30 ml/min. The reactor temperature was increased from room temperature to 380^{o}C at a rate of 1^{o}C/min and maintained at this activation condition for 14 h. After the activation period, the reactor temperature was reduced to 270^{o}C under flowing hydrogen. The hydrogen and syngas flow rates were controlled by Brooks 5850 mass flow controllers. Argon was used as the

internal standard gas in the reactor feed. The mixed gases (30% CO, 60% H_2, 10% Ar) entered through the top of the fixed bed reactor. The temperature of the reactor was controlled using a PID temperature controller. Synthesis gas with a space velocity of 2000 ml(STP)/(h g) was introduced and the reactor pressure was increased to 2 MPa. Products were continuously removed from the vapor and passed through two traps. The pressure of the uncondensed gaseous product stream was reduced to atmospheric pressure. The composition of the outlet gas stream was measured using an on-line GC-2014 Shimadzu gas chromatograph. The contents of the traps were removed every 24 h, the hydrocarbon and water fractions were separated, and analyzed by a Varian 3400 GC. Catalytic activity, product selectivity and stability of the catalyst were monitored during the reaction period of 125 hours. The uncertainties for the experimental data are given in Section 1-13.

4.3 Results and discussions

4.3.1 Catalysts Characterizations

SEM images of the crude CNTs revealed that the sample contained solely CNTs and no carbonaceous impurities were observed (Figure 4.2a). The fresh CNT sample contained woven nanotubes with high aspect ratios. TEM micrographs of the fresh and acid treated CNT supports are shown in Figure 4.2b and 4.2c, respectively. Figure 4.2b shows that the fresh CNTs have uniform nanotubes and their inner and outer diameters vary between 5-12 nm and 10-25 nm, respectively. In the case of fresh CNTs, most of the nanotubes' caps are closed while acid treatment resulted in opening the nanotubes' caps, as shown in Figure 4.2c. This is also verified with an increase in the BET surface area from 181 to 234 m^2/g (Table 4.1). The pore volume of the CNTs was also increased from 0.48 to 0.62 ml/g after the acid treatment.

The position of the iron particles inside or outside of the CNTs was verified using several TEM images from each of the catalyst samples. Figure 4.3 shows sample TEM images of in-Fe/CNT and out-Fe/CNT catalysts. Dark spots represent the iron oxides, which are attached inside or outside of the nanotubes. In the case of in-Fe/CNT, the vast majority of the iron particles (80%) are distributed in the inner pores of the CNTs (Figure 4.3a). This can be attributed to carbon nanotubes' tubular morphology which can induce capillary forces during the impregnation process. For out-Fe/CNT catalyst, most of the iron particles (70%) were attached to the exterior surfaces of the CNTs. This is because their inner pores are initially filled with water and the iron salt solution can only contact the outside of the nanotubes and thus the majority of iron oxide particles is attached to the exterior surface of the CNTs (Figure 4.3a, b).

Table 4.1 shows the metal content for the catalysts. ICP-MS analyses of the catalysts revealed that the metal contents of the catalysts were fairly similar and close to

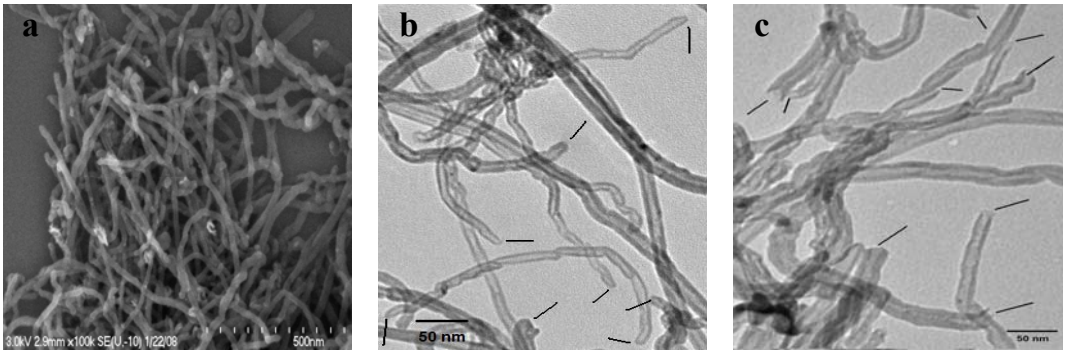

Figure 4.2 a) SEM micrograph of fresh CNT support, b) TEM image of fresh CNT support, c) TEM image of acid treated CNT support (lines show closed- and open-cap nanotubes).

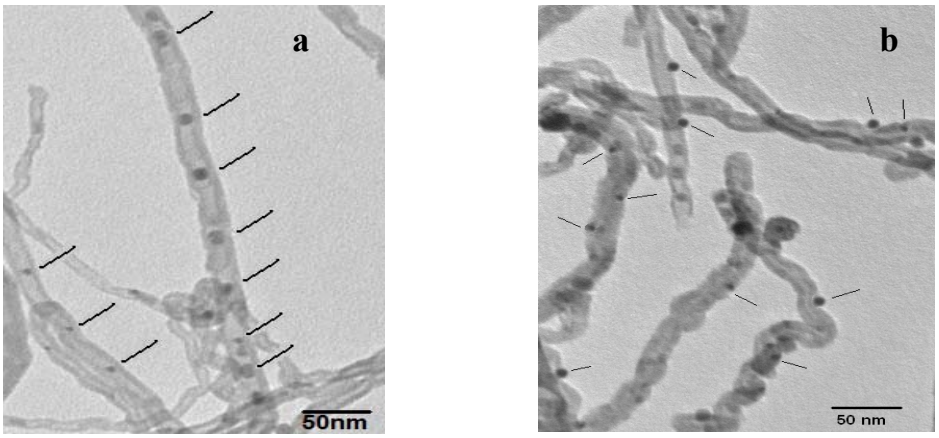

Figure 4.3 TEM image of a) in-Fe/CNT, b) out-Fe/CNT (lines show iron oxide particles).

the target metal content of 12 wt% Fe. Table 4.1 also shows the results of surface area measurements of in-Fe/CNT and out-Fe/CNT. For in-Fe/CNT and out-Fe/CNT catalysts, the loading of 12% Fe decreased the surface area to 199 and 211 m^2/g, respectively. The results show that the BET surface area of the catalysts is lower than that of the supports indicating pore blockage due to iron loading on the supports. However, comparison between BET surface area of in-Fe/CNT and out-Fe/CNT catalysts reveals that the extent of pore blockage in the in-Fe/CNT is higher than that in out-Fe/CNT.

Figure 4.4 shows XRD patterns of the CNT support as well as the calcined catalysts. Both of the catalysts show similar XRD patterns between 2θ values of 10° and 50°. The diffraction peaks match very well with the standard Hematite (Fe_2O_3) phase. For fresh CNT support, in-Fe/CNT and out-Fe/CNT catalysts, the peaks at 2θ of 26^o and 43^o correspond to graphite layers (multiwall carbon nanotubes), while the other peaks in the spectrum of catalysts are related to different crystal planes of Fe_2O_3. The peaks at 33.6^o and 35.7^o are the most intense peak of Fe_2O_3 in the XRD spectrum of the catalysts.

Table 4.1 Metal content and surface properties of the fresh, pre-treated supports and iron catalysts

Catalyst	Metal Content%[a]	BET Surface Area (m^2/g)	Total Pore Volume (ml/g)
Fresh CNT	-	181	0.55
Acid treated CNTs	-	234	0.62
in-Fe/CNT	11.6	199	0.51
out-Fe/CNT	11.9	211	0.59

a) Determined by ICP analysis

Table 4.2 Particle sizes (iron oxide) based on XRD and TEM analysis

Catalyst	d (Fe_2O_3)[a] nm	d (Fe_2O_3)[b] nm
in-Fe/CNT	9±1	6-11
out-Fe/CNT	7±1	5-9
used in-Fe/CNT	11±2	6-12
used out-Fe/CNT	16±2	6-24

a) Based of XRD analysis
b) Based of TEM analysis

Table 4.2 shows the average Fe_2O_3 particle size on the catalysts calculated from XRD spectrum and Debye-Scherrer equation at the most intense peak of 35.7°. The data reveal that both catalysts possess similar sizes of iron oxide particles (7-9 nm). To compare the particle size calculated based on XRD with TEM analysis, the size distribution of the particles is shown in Table 4.3. There is a good agreement between the data for average particle size calculated based on XRD and TEM size distribution.

TPR analyses were performed to evaluate the reducibility of the studied catalysts. TPR patterns of in-Fe/CNT and out-Fe/CNT catalysts are shown in Figure 4.5. Four peaks (A, B, C and D) can be observed on the TPR profile. Generally, the reduction of iron oxides takes place as below [11]:

$Fe_2O_3 \rightarrow Fe_3O_4 \rightarrow FeO \rightarrow Fe$

The first peak (A) can be assigned to the reduction of Fe_2O_3 to Fe_3O_4. The second peak, B, can be assigned to the subsequent reduction of Fe_3O_4 to FeO. Peak C, observed

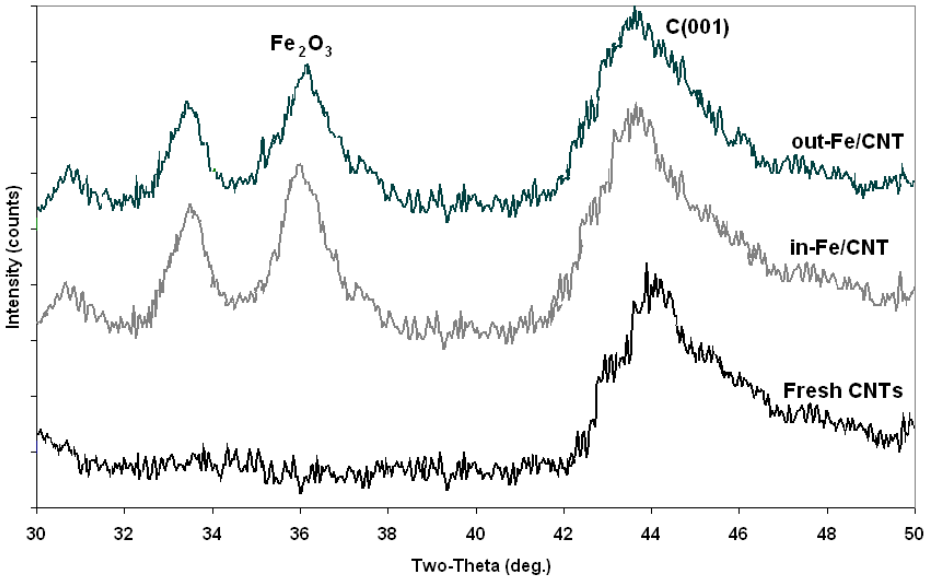

Figure 4.4 XRD patterns of in-Fe/CNT, out-Fe/CNT and fresh CNTs.

Table 4.3 Reduction temperature (°C) based on H_2-TPR analysis

Catalyst	Peak A	Peak B	Peak C
in-Fe/CNT	381	411	567
out-Fe/CNT	418	470	591

at 500-600°C, can be related to the reduction of FeO to metallic Fe. Peak D corresponds to gasification of CNTs at a temperature higher than 600°C. Table 4.3 shows reduction temperature for both catalysts. According to the reduction temperature, deposition of iron oxide particles inside the nanotubes results in a decrease in the temperature of the first TPR peak from 418 to 381°C and that of the second and third from TPR peak from 470 to 411°C and 591 to 567°C, respectively. As reported by other researchers [19], the confinement of iron oxide inside the CNT pore resulted in easier reduction at lower temperature. It can be concluded that iron oxide interacts with the interior CNT wall differently from that with the exterior wall. It has been postulated that the electron deficiency of the interior CNT surface is possibly responsible for this phenomenon.

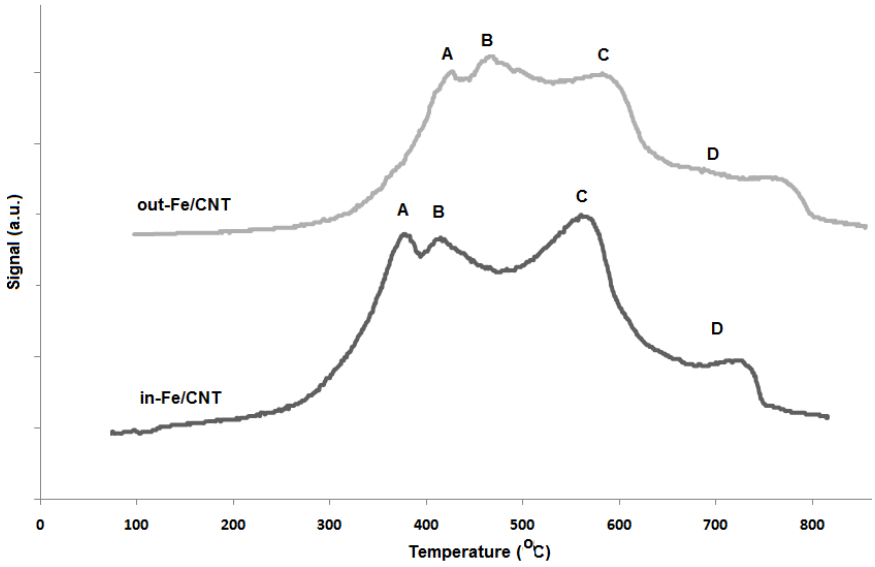

Figure 4.5 H_2-TPR profiles for in-Fe/CNT and out-Fe/CNT catalysts.

4.3.2 Used Catalysts Characterizations

XRD and TEM analyses were conducted to study the particle size of the used catalysts after 125 h of FTS reaction at 270°C The diffraction peaks match very well with magnetite (Fe_3O_4) phase (the XRD spectra are not shown here). The corresponding peaks for iron carbide phase (Fe_5C_2) appeared in the XRD spectra of the

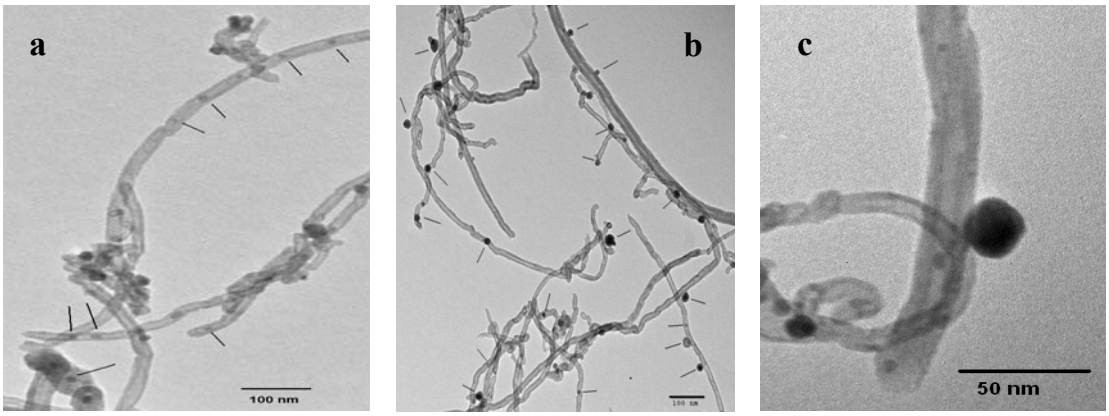

Figure 4.6 TEM image of a) used in-Fe/CNT, b) used out-Fe/CNT (lines point to iron oxide particles) c) used out-Fe-CNT.

used in-Fe/CNT catalyst while there were no noticeable peaks in the used out-Fe/CNT for iron carbide phase. This evidence showed that for the in-Fe/CNT catalyst, the iron carbide content was higher and more stable during the FT reactions.

Based on XRD peak broadening, the particle size calculation revealed particle growth for the used out-Fe/CNT catalysts. In the case of out-Fe/CNT, a sharp peak appeared at a 2θ angle of 35.6° indicating particle growth, whereas, for in-Fe/CNT catalyst, the particle growth is not significant. The out-Fe/CNT catalyst experienced site agglomeration increasing in size from 7 to 16 nm whereas in the case of in-Fe/CNT, the particle sintering changed the particle size from 9±1 to 11±2 nm (see Table 4.2). Figure 4.6 shows TEM images of the used in-Fe/CNT and in-Fe/CNT. As can be seen in Figure 4.6a, the iron oxide particles inside the channels do not experience particle agglomeration. This phenomenon can be related to the interaction of the catalytic sites with the inner surface of the pores and perhaps to the spatial restriction of the CNT channels. However, most of the iron species on the exterior surface agglomerated (Figure 4.6b and 4.6c) resulting in lower catalytic dispersion under FT reactions. From XRD data and particle size distribution, it can be concluded that the deposition of the catalytic sites inside the nanotube pores results in relatively more stable catalyst than that deposited on the exterior surface of the nanotubes.

In order to study the change in particle size distributions and mechanism for the catalytic site agglomeration, several TEM images from fresh and used in-Fe/CNT and out-Fe/CNT catalysts were taken and analyzed. The results are shown in Figure 4.7a and 4.6b. As can be seen in Figure 4.7a, for in-Fe/CNT catalyst, there was a slight shift toward larger particle size with the maximum of 11 nm. However, in the case of used out-Fe/CNT catalyst, the particle size distribution shifted considerably toward larger particles with an average of 18 nm and maximum particle size of 24 nm.

Table 4.4 Product selectivity (wt%) for in-Fe/CNT and out-Fe/CNT

Product Selectivity	in-Fe/CNT	out-Fe/CNT
CH_4	26	40
C_2-C_4	38	36
C_5+	36	24
CO_2	39	40

T = 270°C, P = 2 MPa, space velocity = 2Sl/g-cat/h, CO/H_2 = 2
Hydrocarbon selectivity: wt%, CO2 selectivity (C%), time on stream of 125h

In order to describe the catalytic site agglomeration, two mechanisms, namely atom migration (Ostwald ripening) and crystallite migration (coalescence), are generally considered. According to the Ostwald ripening theory, metal atoms are released from one metal particle and become attached to another metal particle. The difference in surface energy is the driving force for this process. In the case of the coalescence process, the movement of crystallites themselves over the support results in the particle collision and formation of larger particles. In both processes, sintering slows down with time resulting in a stable state [24].

In order to distinguish between these two models, the pattern of particle size distribution after sintering is generally studied. It has been shown that the Ostwald ripening results in a particle size distribution with a tail toward small particle sizes and a steep slope toward larger particle sizes [24-25]. As can be seen in Figure 4.7b, there is a log-normal distribution with a tail toward small particle sizes. Thus, the Ostwald ripening can be considered as the mechanism for metal site agglomeration for iron catalysts supported on the carbon nanotubes. A similar mechanism has been proposed for migration of transition metal over carbon base supports [26].

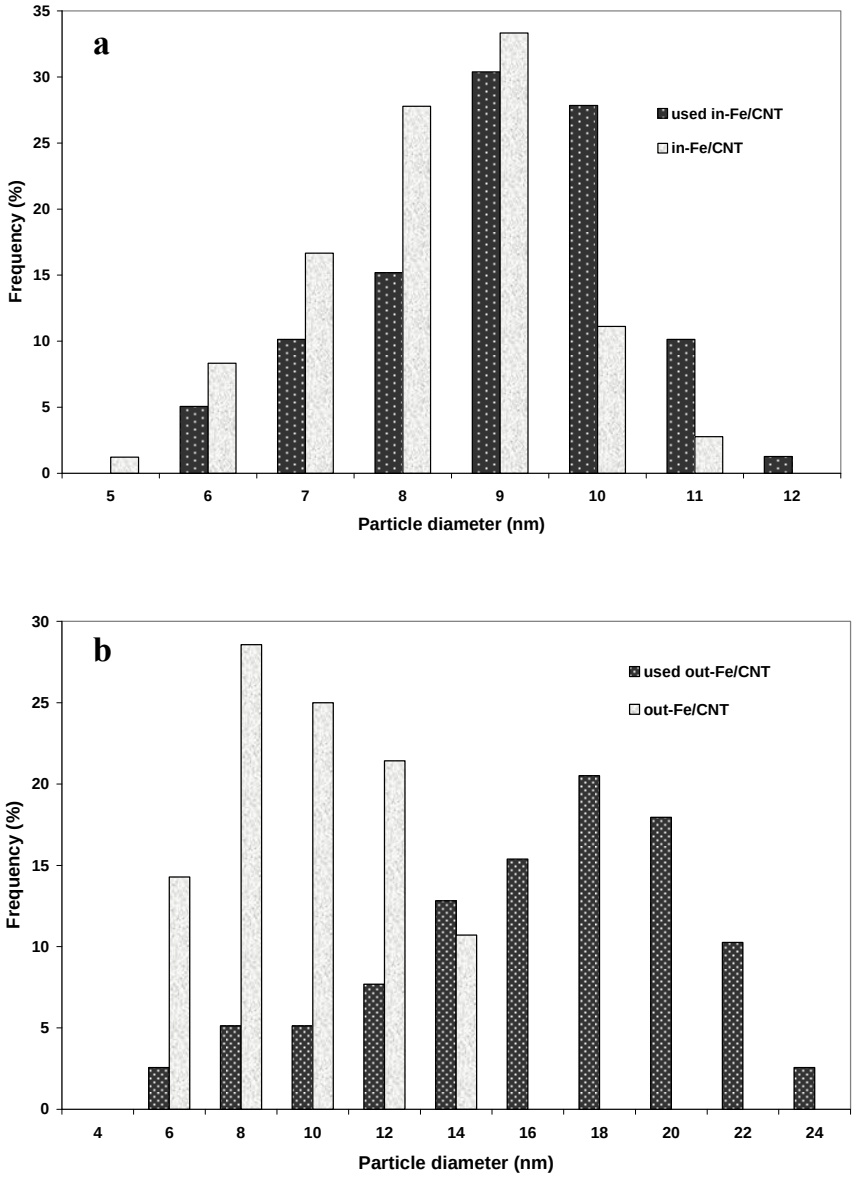

Figure 4.7 Particle size distributions for a) fresh and used in-Fe/CNT, b) fresh and used out-Fe/CNT

4.4 Fischer-Tropsch Synthesis

4.4.1 Catalytic Performance vs. Time on Stream

The performances of the in-Fe/CNT and out-Fe/CNT catalysts for the Fischer-Tropsch synthesis were evaluated in a fixed bed reactor. All the reactions were

performed under a set of standard conditions (270^{o}C, 2 MPa, H_2:CO = 2). CO hydrogenation was performed on the acid treated CNT support (blank runs with no iron) under the same operating conditions as the metal loaded samples. In the blank runs, the main product formed at a very low conversion (1%) was methane with almost no higher hydrocarbons.

Figure 4.8 shows the variations of CO conversion with the time on-stream (TOS). Both catalysts reached their highest activity within 10 hours. Afterward, they showed different stability pattern within a time period of 125 hours. Figure 4.8 shows that in-Fe/CNT is a more stable catalyst compared to out-Fe/CNT. In the case of in-Fe/CNT, syngas conversion decreased slightly from 89 to 85 % in a period of 125 hours, whereas, out-Fe/CNT catalyst showed a quick drop in CO conversion from 91 to 79%. As discussed in the previous section, the catalytic site agglomeration during the FT reaction is believed to be the main reason for deactivation of out-Fe/CNT catalyst.

The product selectivities of the catalysts (CH_4, C_2-C_5, C_5+ and CO_2) after time on stream of 125 h are given in Table 4.4. The data show that CH_4 selectivity of the in-Fe/CNT (25 wt%) catalyst is lower than that of the out-Fe/CNT catalyst (40wt%). Also C_5+ selectivity of the in-Fe/CNT (36 wt%) is higher than that of the out-Fe/CNT (23wt%). CO_2 selectivities of the in-Fe/CNT and out-Fe/CNT catalysts are comparable, indicating similar water gas shift activity for both catalysts. It should be noted that there was a slight shift toward lighter hydrocarbons (3 % decrease in C_5+) during the reaction period for the in-Fe/CNT catalyst. In contrary, the out-Fe/CNT catalyst experienced a decrease of 5 % in CH_4 selectivity in the course of 125 h. This could be related to drop in CO conversion and the increase in particle sizes.

The results of FT reaction product analysis for both in-Fe/CNT and out-Fe/CNT catalysts showed that the deposition of catalytic metals inside the nanotube pores

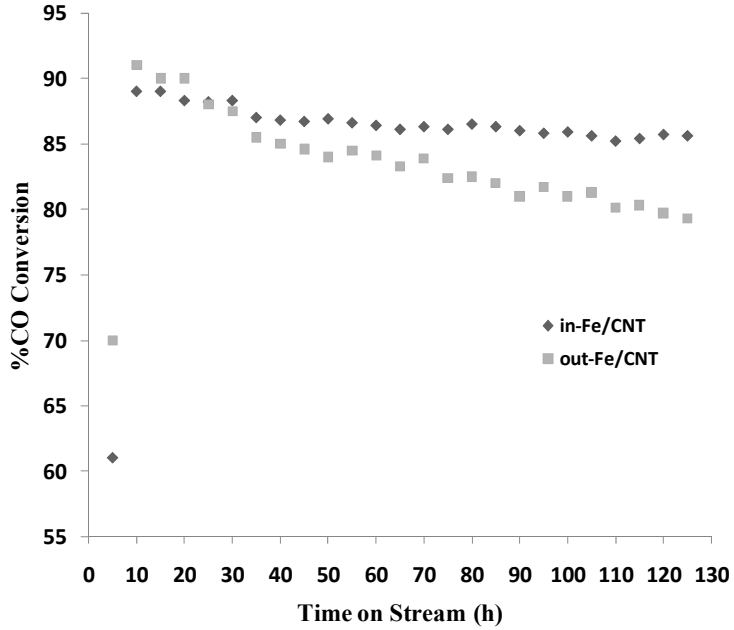

Figure 4.8 Change in %CO conversion with time on stream for in-Fe/CNT and out-Fe/CNT catalysts (Process conditions:, 2 Sl/g-cat/h, P = 2 MPa, H_2/CO = 2, T = 270^{o}C, TOS of 125 h).

enhanced product selectivity of the catalyst. Several reasons can be associated with the improvement in product selectivity. As discussed earlier, H_2-TPR analysis revealed that the reducibility of the in-Fe/CNT catalyst was higher in comparison to the out-Fe/CNT. This phenomenon can result in the formation of more catalytically active carbide species during FTS. In addition, confinement of the reaction intermediates inside the pores can enhance their contact with catalytic sites, favoring the growth of longer chain hydrocarbons. In addition, the inner sides of the CNTs are electron deficient and can enhance the dissociation of CO resulting in production of higher chain hydrocarbons.

4.4.2 Effect of Temperature on Product Selectivity

Catalytic activity and product selectivity of in-Fe/CNT and out-Fe/CNT catalysts were analyzed at different temperatures ranging from 260 to 285^{o}C. Figure 4.9a and 4.8b show %CO conversion and CH_4 selectivity of the in-Fe/CNT and out-Fe/CNT

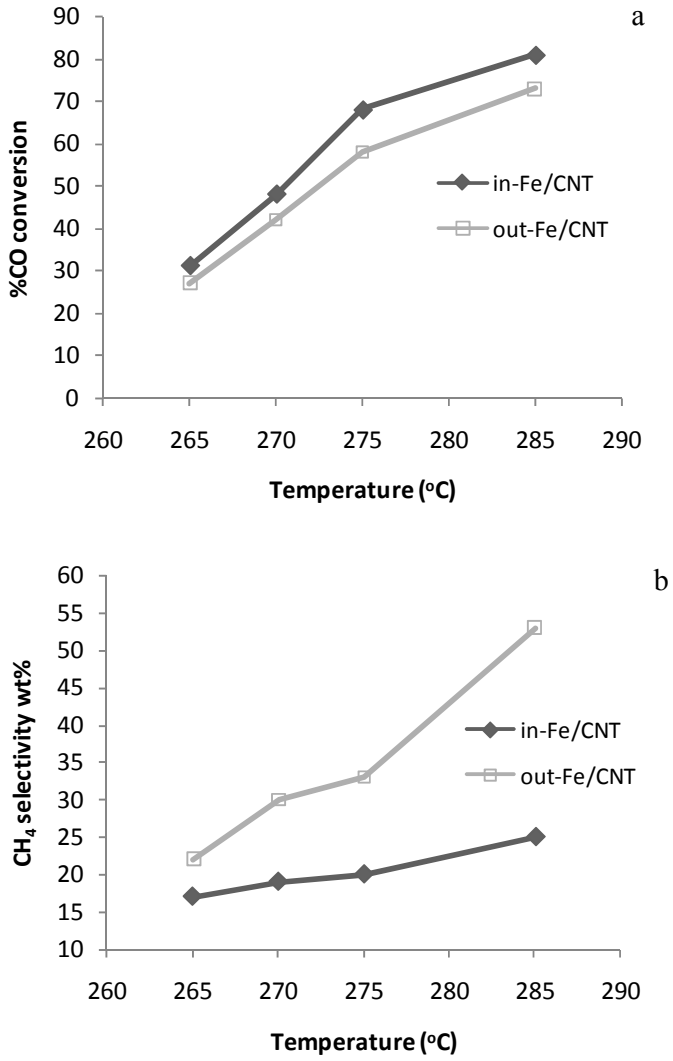

Figure 4.9 Change in catalytic performance with reaction temperature for in-Fe/CNT and out-Fe/CNT catalysts a) %CO conversion, b) CH_4 selectivity (Process conditions: TOS of 25 h, 4 Sl/g-cat/h, P = 2 MPa, H_2/CO = 2)

catalysts at a pressure of 2 MPa and space velocity of 4 SL/g-cat/h and time on stream of 125h. As can be seen in Figure 4.8a, the activity of both catalysts follow similar trends as reaction temperature increases. However, after a reaction period of 125 h, in-Fe/CNT catalyst shows higher CO conversion compared to out-Fe/CNT. The difference between CO conservation for both catalysts is also more pronounced at elevated temperatures. In the case of CH_4 selectivity, which is an undesired by-product of FT

reaction, the in-Fe/CNT catalyst exhibits better performance compared to the out-Fe/CNT catalyst. For the out-Fe/CNT catalyst, with an increase of 25^{o}C in the reaction temperature, the CH_4 selectivity increases from 22 to 53wt%. However, in the case of the in-Fe/CNT catalyst, there is only an increase of 8% in CH_4 selectivity. Generally, in FTS reactions, an increase of temperature results in a shift toward products with a lower carbon number.

The effect of temperature on the FTS reactions is complex. Kinetics of all reactions including primary reactions, secondary reactions (hydrogenations and isomerizations) and chain termination and the chain growth mechanism can be influenced by temperature. In addition, physical properties that control the rate of reaction, such as diffusion, depend on the temperature. In the case of the catalyst with active sites inside the nanopores, the longer contact time for reaction intermediates inside the nanotubes channels (i.d. of 8-10 nm and a length of 0.5-2 μm) can result in a higher selectivity to longer chain hydrocarbons and lower methane selectivity.

4.5 Conclusions

The results of this research show that the deposition of catalytic sites inside the nanotube pores improves the reduction behavior of the CNT catalyst most likely due to difference in electronic properties of the inner and outer surface of the CNTs and confinement effects. In the case of catalysts with catalytic particles inside the pores, confinement of reaction intermediates inside the channels increases the contact time of the reactants with the active sites, resulting in production of heavier hydrocarbons. Another advantage of deposition of catalytic species inside the pores is the physical encapsulation of catalytic particles, which can reduce the site sintering.

Nomenclature

P	Pressure (MPa)
T	Temperature (^{o}C)
%CO	Percent of CO conversion (mol%)

Abbreviations

BET	Brunauer, Emmett, and Teller
CNT	Carbon nanotubes
FTS	Fischer-Tropsch Synthesis
ICP	Inductively coupled plasma
in-Fe/CNT	Iron catalysts deposited on interior surface of carbon nanotubes
out-Fe/CNT	Iron catalysts deposited on exterior surface of carbon nanotubes
SEM	Scanning election microscopy
Sl	Standard liter
TEM	Transition electron microscopy
TOS	Time on stream
TPR	Temperature programmed reduction
WGS	Water-gas shift
XRD	X-ray diffraction

References

[1] M.J.A. Tijmensen, A.P.C. Faaij, C.N. Hamelinck, M.R.M van Hardeveld, Exploration of the possibilities for production of Fischer Tropsch liquids and power via biomass gasification, Biomass and Bioenergy 23 (2002) 129-152.

[2] M. E. Dry, Fischer-Tropsch reactions and the environment, Applied Catalysis A: General, 189 (1999) 185-190.

[3] J. Zhang, J. Chen, J. Ren, Y. Li, Y. Sun, Support effect of Co/Al_2O_3 catalysts for Fischer-Tropsch synthesis, Fuel, 82 (2003) 581-586.

[4] D. B. Bukur, X Lang, D. Mukesh, W. H. Zimmerman, M. P.Rosynek, and C. Li Binder/Support Effects on the Activity and Selectivity of Iron Catalysts in the Fischer-Tropsch Synthesis. Industrial Engineering Chemistry Research, 29 (1990) 1588-1599.

[5] R. M. Malek Abbaslou, A. Tavasoli and A. K. Dalai, Effect of pre-treatment on physico-chemical properties and stability of iron catalysts supported on carbon nanotubes for Fischer-Tropsch synthsis, Applied Catalysis A: General, 355(2009)33-41.

[6] G. L. Bezemer, J. H. Bitter, H. P. C. E. Kuipers, H. Oosterbeek, J. E. Holewijn, X. Xu, F. Kapteijn, A. J. van Dillen, and K. P. de Jong, Cobalt Particle Size Effects in the Fischer-Tropsch Reaction Studied with Carbon Nanofiber Supported Catalysts, American Journal of Chemical Society, 128 (2006) 3956-3964.

[7] Z. Yu, Ø. Borg, D. Chen, B. C. Enger, V. Frøseth, E. Rytter, H. Wigum, and A. Holmen, Carbon Nanofiber Supported Cobalt Catalysts for Fischer-Tropsch Synthesis with High Activity and Selectivity, Catalysis Letters, 109 (2006) 43-47.

[8] A. Tavasoli, K. Sadagiani, F. Khorashe, A.A. Seifkordi, A.A. Rohani, A. Nakhaeipour, Cobalt supported on carbon nanotubes: A promising novel Fischer-Tropsch synthesis catalyst, Fuel Processing Technology, 89 (2008) 491-498.

[9] A. Tavasoli, , A. M. Rashidi, K. Sadaghiani Zadeh, A. Karimi, A. Kodadadi, Y. A. Mortazavi, (2005) European Patent EP1782885.

[10] A. Tavasoli, K. Sadaghiani, A. Nakhaeipour, M. Ghalbi Ahangari, Cobalt Loading Effects on the Structure and Activity for Fischer-Tropsch and Water-Gas Shift Reactions of Co/Al_2O_3, Catalysts, Iranian Journal of Chemistry & Chemical Engineering, 26 (2007) 1-9.

[11] W. Ma, E. L. Kugler, J. Wright, and D. B. Dadyburjor, Mo-Fe Catalysts Supported on Activated Carbon for Synthesis of Liquid Fuels by the Fischer−Tropsch Process: Effect of Mo Addition on Reducibility, Activity, and Hydrocarbon Selectivity, Energy Fuels 20 (2006) 2299-2307.

[12] L. Guczi, G. Stefler, O. Geszti, Zs. Koppány, Z. Kónya, É. Molnár, M. Urbánc, I. Kiricsi, CO hydrogenation over cobalt and iron catalysts supported over multiwall carbon nanotubes: Effect of preparation, Journal of Catalysis, 244 (2006) 24-32.

[13] M. C. Bahome, L. L. Jewell, K. Padayachy, D. Hildebrandt, D. Glasser, A. K. Datye, N. J. Coville, Fe-Ru small particle bimetallic catalysts supported on carbon nanotubes for use in Fischer-Tropsch synthesis, Applied Catalysis A: General, 328 (2007) 243-251.

[14] E. van Steen, F. F. Prinsloo, Comparison of preparation methods for carbon nanotubes supported iron Fischer-Tropsch catalysts, Catalysis Today, 71 (2002) 327-334.

[15] M. C. Bahome, L. L. Jewell, D. Hildebrandt, D. Glasser, N. J. Coville, Fischer-Tropsch synthesis over iron catalysts supported on carbon nanotubes, Applied Catalysis A: General, 287 (2005) 60-67.

[16] H.-J. Jung, P.L. Walker, M.A. Vannice, CO hydrogenation over well-dispersed carbon-supported iron catalysts, Journal of Catalysis, 75 (1982) 416-422.

[17] A. A. Chen, M. A. Vannice, J. Phillips, Effect of support pre-treatments on carbon-supported iron particles, Journal of Physical Chemistry, 91 (1987) 6257-6269.

[18] P. Serp, M. Corrias, P. Kalck. Carbon nanotubes and nanofibers in catalysis, Review, Applied Catalysis A: General, 253(2003) 337-358.

[19] W. Chen, Z. Fan, X. Pan, X. Bao, Effect of Confinement in Carbon Nanotubes on the Activity of Fischer−Tropsch Iron Catalyst, Journal of American Chemical Society, 130 (2008) 9414-9419.

[20] X. Pan, Z. Fan, W. Chen, Y. Ding, H. Luo, X. Bao, Enhanced ethanol production inside carbon-nanotube reactors containing catalytic particles, Nature, 6 (2007) 507-511.

[21] M. Menon, A.N. Andriotis, G. E. Froudakis, Curvature dependence of the metal catalyst atom interaction with carbon nanotubes walls, Physics Letters, 320 (2000) 425-434.

[22] E.E. Santiso, A.M. George, C. H. Turner, M. K. Kostov, K. E. Gubbins, M. Buongiorno-Nardellib, M. Sliwinska-Bartkowiak, Adsorption and catalysis: The effect of confinement on chemical reactions, Applied Surface Science, 252 (2005) 766.

[23] S.J. Lee, A. Gavriilidis, Supported Au Catalysts for Low-Temperature CO Oxidation Prepared by Impregnation, Journal of Catalysis, 206 (2002) 305-313.

[24] C.G. Granqvist, R.A. Buhrman, Size distributions for supported metal catalysts: Coalescence growth versus Ostwald ripening, Journal of Catalysis, 42 (1976) 477.

[25] J. Sehested, A. Carlsson, T.V.W. Janssens, P. L. Hansen, A. K. Datyey, Sintering of Nickel Steam-Reforming Catalysts on $MgAl_2O_4$ Spinel Supports, Journal of Catalysis, 197 (2001) 200-209.

[26] S. H. Joo, S. J. Choi, I. Oh, J. Kwak, Z. Liu, O. Terasaki and R. Ryoo, Ordered nanoporous arrays of carbon supporting high dispersions of platinum nanoparticles, Nature, 412 (2001) 169-172.

Chapter 5

Effects of Nanotubes Pore Size on the Catalytic Performances of Iron Catalysts Supported on Carbon Nanotubes for Fischer-Tropsch Synthesis

A similar version of this chapter has been copyrighted and accepted for publication in the journal of Applied Catalysis A: General.

- *Reza M. Malek Abbaslou, Jafar Soltan, Ajay K. Dalai, Effects of Nanotubes Pore Size on the Catalytic Performances of Iron Catalysts Supported on Carbon Nanotubes for Fischer-Tropsch Synthesis, Applied Catalysis A: General (2010, APCATA-S-09-01614).*

In addition, a part of this chapter was presented and published in proceeding of the following conferences:

- *Reza M. Malek Abbaslou, Jafar Soltan, Ajay K. Dalai, Iron Catalysts Supported on Carbon Nanotubes for Fischer-Tropsch Synthesis: Effect of Pore Size, Energy and Suitability II. 121 (2009) 139-149*

Contribution of the Ph.D. Candidate

The experimental design and experiments were planned and performed by Reza Malek Abbaslou. The data analysis and interpretations were performed by Reza Malek Abbaslou, with assistance from Drs. Soltan and Dalai. All written text was prepared by Reza Malek Abbaslou and discussed with Drs. Soltan and Dalai.

Contribution of this Chapter to the Overall Study

In Chapter 4, it was shown that the deposition of catalytic sites inside the nanotubes' pores improves the catalytic behavior of iron catalysts, most likely due to difference in electronic properties of the inner and outer surface of the CNTs and

confinement effects. Here, the main objective is to evaluate the influence of pore diameter on the extent of those electronic effects as well as on activity and selectivity of the catalysts. Two types of CNTs with different average pore sizes were provided in a way to have comparable surface areas so as to remove the effects of different surface areas.

Abstract

In this chapter, the effects of pore diameter and structure of iron catalysts supported on carbon nanotubes (CNTs), on the reaction rates and product selectivities of Fischer-Tropsch (FT) reactions, are presented. In order to study the effects of pore diameter, two types of CNTs with different average pore sizes (12 and 63 nm), however, with similar surface areas, were prepared. The iron catalysts were prepared using incipient wetness impregnation method and characterized by ICP, BET, XRD, TPR, SEM and TEM analyses. According to the TEM images of iron catalysts supported on narrow-pore CNTs (Fe/np-CNT) and wide pore CNTs (Fe/wp-CNT), a vast majority (~80%) of the iron oxide particles was deposited inside the nanotubes' pores. The TEM and XRD analysis showed that the iron oxide particles on the Fe/wp-CNT (17 nm) were larger than those on Fe/np-CNT sample (11 nm). Temperature programmed reduction analyses of the catalysts showed that the extent of reduction of the Fe/np-CNT catalyst was 17% higher compared to that of the Fe/wp-CNT catalyst. Finally, catalytic performances of both catalysts were evaluated in a fixed bed reactor for FT reactions at 2 MPa and 275^{o}C. At these conditions, the activity of the np-CNT catalyst (%CO conversion of 30) was 2.5 times that of the wp-CNT catalyst (%CO conversion of 12). In addition, the Fe/wp-CNT was more selective toward lighter hydrocarbons with a methane selectivity of 41 % compared to that of the np-CNT catalyst with methane

selectivity of 14.5 %. Deposition of metal particle on the CNT with narrow-pore size resulted in more active and selective catalyst due to higher degree of reduction and higher metal dispersion.

5.1 Introduction

Fischer-Tropsch (FT) synthesis is a potentially attractive technology for production of clean liquid fuels from syngas. The syngas can be supplied through gasification of coal or biomass and reforming of natural gas. FT synthesis proceeds on metal (Fe, Co and Ru) supported catalysts. The efficiency of FT synthesis can be enhanced by design of new catalysts with higher syngas conversion, higher C_5+ yield, and lower methane selectivity [1-2]. In FT processes, the catalyst activity and selectivity are influenced by the nature and structure of support, the nature of the metal, metal dispersion, metal loading, and the catalyst preparation method [3]. A large number of studies on FT catalysts have been carried out using active metals supported on silica, alumina or titania [4]. In recent years, carbon nanotubes (CNTs) have been considered as a potential new support for FT reactions [5-11].

Carbon nanotubes with unique properties such as uniform pore size distribution, meso and macro pore structure, inert surface properties, and resistance to acid and base environment can play an important role in a large number of catalytic reactions [11]. CNTs are essentially composed of graphite layers with a tubular morphology [7-8]. Structural parameters of CNT such as inner and outer diameter and length of nanotubes can be manipulated using different synthesis processes and operating conditions. It has been shown that CNT supports offer improved performance for FT reactions [4-9,12]. In the application of CNT supports, the effects of pore size and diameter of carbon nanotubes on the catalytic performance of FT catalysts have not been elucidated yet. In

general, pore size of supported catalysts can influence particle size distribution, dispersion, extent of reduction, and mass transfer rates [4].

In this chapter, the effects of pore diameter of CNTs on FT reaction rates and selectivities over iron catalysts are presented. Two types of CNTs with different average pore sizes (12 and 63 nm) with comparable surface areas were used.

5.2 Experimental

In order to study the effects of inner pore size of CNTs on the performance of iron catalyst for the FT reactions, two CNT samples with considerably different pore diameters were used. The narrow-pore CNT sample (denoted as np-CNT) was purchased from mknano Co. (M.K. IMPEX Canada). The wide pore CNT sample (denoted as wp-CNT) were synthesized in our laboratories using anodic aluminum oxide (AAO) films along with the chemical vapor deposition method [12]. The procedure for production of wp-CNT is as follows:

The AAO templates were synthesized using the two-step anodization procedure. The electrolysis cell consisted of a graphite cathode and a pure (99.5%) aluminum electrode. DC power was applied to the cell and the electric potential across the electrodes was kept constant for the duration of experimental run. The electrolysis vessel contains 1.3 L of oxalic acid electrolyte solution at a concentration of 0.40 M. The first anodization was then performed with the polished anode at a constant potential of 40.0 V for 1 hour. The anode was then removed and immersed for 40 minutes in a de-oxidation solution at 70°C. The de-oxidation solution consisted of the following mass composition: 92.1% H_2O, 7.0% H_3PO_4, and 0.9% CrO_3.

For the second anodization, the energy potential was kept constant at 40.0 V for a run time of 66 hours. After the second anodization was completed, the electrode

terminals were exchanged and a constant current of 2.00 A was applied through the cell to extract the AAO product from the anode surface. To partially remove alumina from the AAO (for optimum pore diameter), each batch of template was immersed in a 5% H_3PO_4 solution for 30 minutes.

The wp-CNT sample was synthesized from the AAO template in a chemical vapour deposition (CVD) process. The reactor was heated to a constant temperature of 650°C across the length of the template boats under a constant Ar gas flow of 100 mL/min. Once the reaction temperature was reached, acetylene gas was introduced to the system over a span of 2 hours. During this period, Ar gas flow was maintained constant at ratio of 2.5 mL Ar/min: 1.0 mL C_2H_2/min. After two hours, the acetylene flow was stopped while argon flow at 100 mL/min was continued as the reactor was cooled over a 6-hour period. To remove the synthesized CNTs from the pre-existing AAO template, the combined product was magnetically stirred in 250 mL of 23% HF solution for 30 hours. Then, the insoluble carbon was filtered from the solution and dried, leaving a pure CNT product.

Both wp-CNT and np-CNT samples were treated in nitric acid (60wt %) at 110^{o}C for 16 hours. The catalysts were prepared according to the incipient wetness impregnation method. For the preparation of the catalyst with iron particles inside the nanotube pores with 20 wt% Fe, a specified amount of $Fe(NO_3)_3 \cdot 9H_2O$ was dissolved in deionised water. The amount of solution was equal to total pore volume of the CNT samples. In this case, the metal solution filled the inner pores of CNTs due to capillary effects [5]. After drying at 120^{o}C followed by calcination at 400^{o}C for 3 hours, the catalysts were characterized by nitrogen adsorption, inductively coupled plasma (ICP), temperature programmed reduction (TPR), X ray diffraction (XRD), scanning electron microscopy (SEM) and transmission electron microscopy (TEM).

The surface area and pore volume of the CNT supports and catalysts were measured by an ASAP-2000 Micromeritics system. Before analysis, the samples were degassed at 200^{o}C for 2 h under 50 mTorr vacuum. X ray diffraction (XRD) analyses were performed using a Philips PW1840 X-ray diffractometer with monochromatized Cu/Kα radiation. The crystallite diameter was determined by substituting the half-width of a chosen peak into the Debye-Scherrer equation. The details for the particle size estimation using Debye-Sherrer method are presented in Appendix E.

The reduction behavior of the catalyst precursors was studied by temperature programmed reduction (TPR) using a CHEMBET-3000 equipped with a thermal conductivity detector. Here, 0.1 g of catalyst was placed in U-shaped quartz tube. A 5% hydrogen/nitrogen mixture was introduced (flow rate = 36 ml (STP)/min) and the furnace temperature was ramped from room temperature to 1173K at 10 K/min. The details for calibration of TPR machine and corresponding calculations are given in Appendix D.

The morphology of samples was studied by transmission electron microscopy (TEM). Sample specimens for TEM studies were prepared by ultrasonic dispersion of the catalysts in ethanol and the suspensions were dropped onto a copper grid. TEM micrographs were obtained using a Hitachi H-7500 (120kV). Several TEM micrographs were recorded for each sample and analyzed to determine the particle size distribution. A Phillips SEM-505 scanning electron microscope operating at 300 kV in SE display mode was also used. For characterization prior to analysis, all the samples were gold-coated in a sputter coating unit (Edwards Vacuum Components Ltd., Sussex, England).

The Fischer-Tropsch synthesis was performed in a fixed-bed micro reactor. The schematic and specifications of the fixed bed reactor are given in Appendix C. Prior to CO hydrogenation, in-situ reduction was conducted according to the following

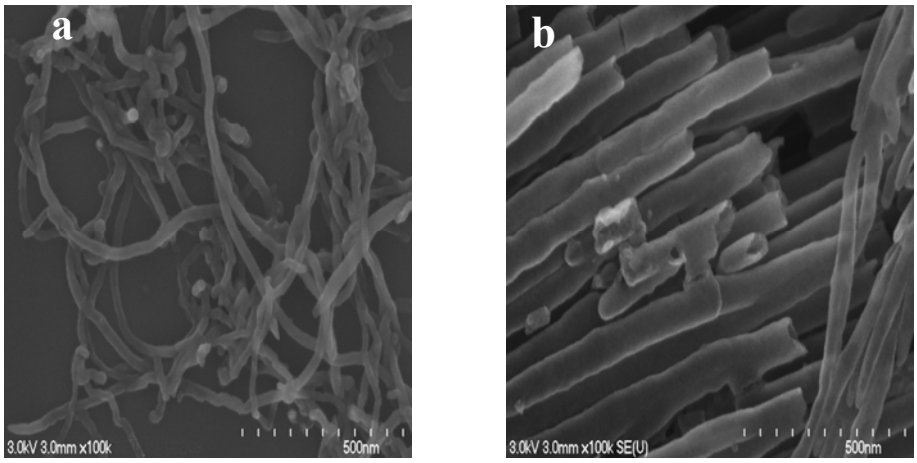

Figure 5.1 SEM micrographs of the CNT supports, a) np-CNT, b) wp-CNT

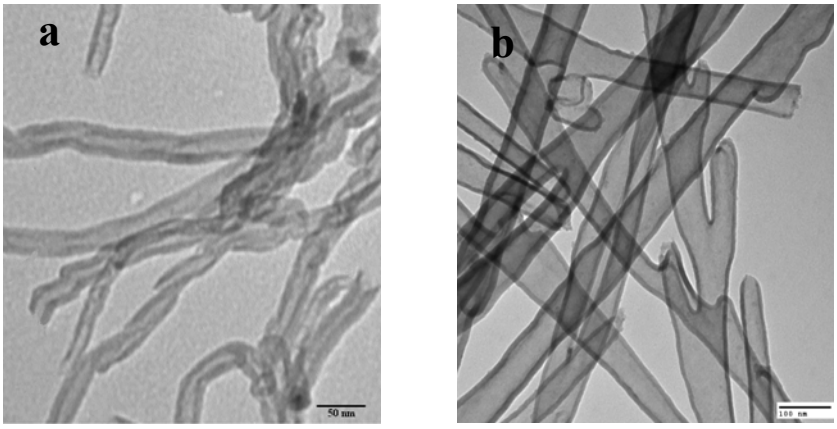

Figure 5.2 TEM images of CNT supports a) np-CNT b)wp-CNT

procedure. The catalyst (0.5 g) was placed in the reactor and diluted with 5 g silicon carbide. Then pure hydrogen was introduced into the reactor at a flow rate of 45 ml/min. The reactor temperature was increased from room temperature to 380^{o}C (at a rate of 1 ^{o}C/min) and maintained at this temperature for 14 h. Then, the reactor temperature was decreased to 275^{o}C under flowing hydrogen. All gas flow rates were controlled by Brooks 5850 mass flow controllers. Argon was used as internal standard gas in the reactor feed. The mixed gases (30% CO, 60% H_2, 10% Ar) entered through

the top of the fixed bed reactor. The temperature of the reactor was controlled via a PID temperature controller. Synthesis gas with a space velocity of 7200 ml(STP)/(h g) was introduced and the reactor pressure was increased to 2 MPa. Products were continuously removed from the vapor and passed through two traps. The pressure of uncondensed vapor stream was reduced to atmospheric pressure. The composition of the outlet gas stream was quantified using an on-line GC-2014 Shimadzu gas chromatograph. The contents of traps were removed every 24 h and the hydrocarbon and water fractions were separated, and analyzed by Varian 3400 GC. Catalytic activity and product selectivity were calculated after a time on stream of 50 hours. The uncertainties for the experimental data are given in Section 1-13.

5.3 Results and Discussion

5.3.1 Characterization of Supports and Catalysts

Scanning electron micro graphs (Figures 5.1a and 5.1b) of the acid-treated and purified CNT samples (np-CNT and wp-CNT) revealed that the samples contained CNTs and no other impurities were observed. Figure 5.1a shows that the np-CNT sample contained woven nanotubes with high aspect ratios (ratio of length to outer diameter of nanotubes is more than 25). For the wp-CNT sample, the SEM image (Figure 5.1b) indicated that the nanotubes were well-aligned and the caps of nanotubes were open.

Transmission electron micro graphs (TEM) of the acid-treated CNT samples are shown in Figures 5.2a and 5.2b. Figure 5.2a shows that the np-CNT nanotubes sample had uniform diameter and their inner and outer diameters varied between 8-12 nm and 20-25 nm, respectively. TEM analysis also revealed that a vast majority (more than 70%) of the np-CNT sample had open caps (Figure 5.2a). As seen in Figure 5.2b, the

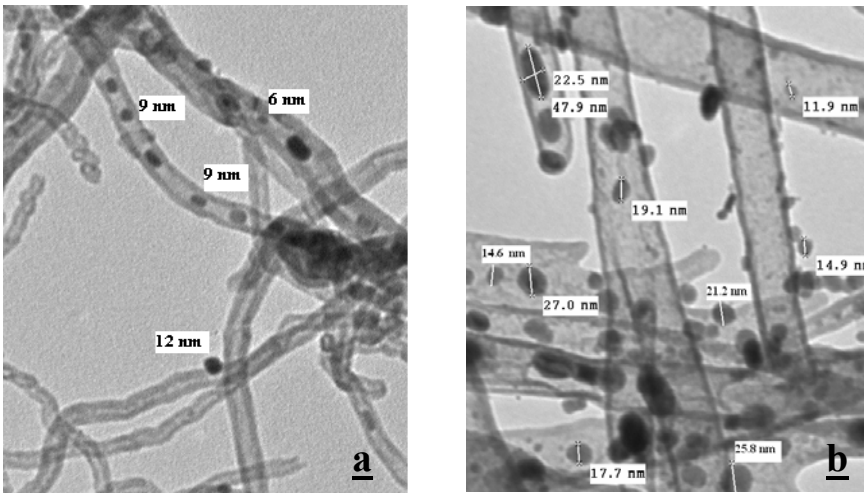

Figure 5.3 TEM images of the iron catalysts a) Fe/np-CNT b) Fe/wp-CNT. Dark spots represent the iron oxide particles inside and out side of the nanotubes

wp-CNT sample was comprised of straight nanotubes with inner diameter of 50-70 nm along with several Y junctions with inner diameter of 20-50 nm. The thickness of the walls varied between 7 and 9 nm.

The particle size distribution and position of iron particles inside or outside of the CNTs were studied using several TEM images from each of the catalyst samples. Figures 5.3a and 5.3b show a representative TEM image of iron catalysts supported on narrow-pore CNT sample (Fe/np-CNT) and iron catalyst supported on wide pore CNT sample (Fe/wp-CNT). Dark spots represent the iron oxide particles which are attached inside or outside of the nanotubes. For both catalysts, a vast majority of iron particles (80%) were distributed in the inner pores of CNTs (Figure 5.3a and 5.3b). This can be attributed to carbon nanotubes' tubular structure, which can induce capillary forces during the impregnation process. In the case of Fe/np-CNT iron oxide particles varied in 4-14 nm range with most abundant particles with a diameter of 8-10 nm. In the case of

Table 5.1 Metal content and surface properties of CNT samples, Fe/np-CNT and Fe/wp-CNT catalysts

Catalyst Name	Metal Content%[1]	BET Surface Area (m^2/g)	Total Pore Volume (ml/g)
np-CNT (support)	0	212	0.58
wp-CNT (support)	0	218	0.55
Fe/np-CNT	19.6	155	0.44
Fe/wp-CNT	20.1	186	0.48

1-Determined by ICP-MS analysis

the Fe/wp-CNT catalyst, particle sizes varied form 5 to 40 nm with most particles in the range of 14 to 25 nm. The data suggest that the inner pore of the nanotubes physically restricted the particle size growth located inside these nanotubes.

Table 5.1 shows the metal content for the Fe/np-CNT and Fe/wp-CNT catalysts. Inductively coupled plasma (ICP) analyses of the catalysts revealed that the metal contents of the catalysts were close (±0.4%) to the target metal content of 20 wt% Fe. Table 5.1 also shows the results of surface area measurements of both CNT supports and corresponding iron catalysts. As discussed earlier, both CNT samples had comparable surface areas (212 m^2/g for np-CNT and 218 m^2/g for wp-CNT). As a result, both Fe/np-CNT and Fe/wp-CNT catalysts held similar metal loading per surface area of the support. According to the N_2 adsorption analysis, the loading of 20% Fe decreased the surface area of Fe/np-CNT and Fe/wp-CNT catalysts to 155 and 186 m^2/g, respectively. These data show that the BET surface area of the catalysts were lower than that of the corresponding supports indicating pore blockage due to iron loading on the supports. However, comparison between BET surface area of the Fe/np-CNT and Fe/wp-CNT catalysts showed that the extent of pore blockage in the Fe/np-CNT was higher than that in Fe/wp-CNT.

Table 5.2 Particle sizes (iron oxide) based on XRD and TEM analysis

Catalyst	Particle size-XRD (nm)	Particle size-TEM (nm)
Fe/np-CNT	11±2[a]	8-10[a]
Fe/wp-CNT	19±1[b]	14-25[b]

a) Fe_2O_3, b) Fe_3O_4

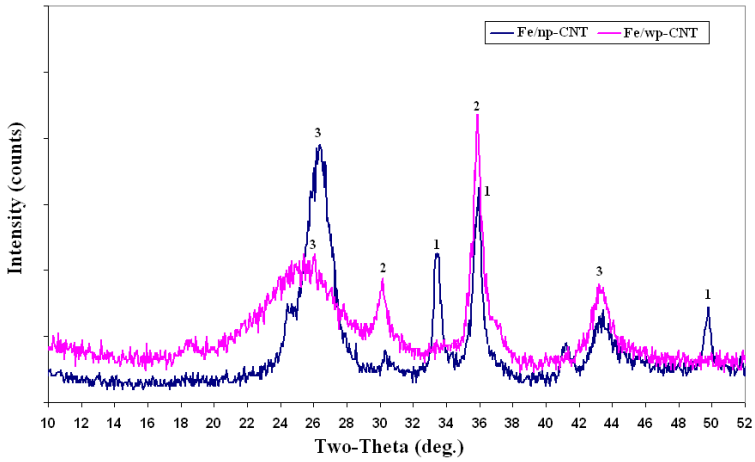

Figure 5.4 XRD spectra of Fe/np-CNT and Fe/wp-CNT (1: Fe_2O_3, 2:Fe_3O_4, 3: CNT)

Figure 5.4 shows XRD patterns of the calcined Fe/np-CNT and Fe/wp-CNT catalysts. For both catalysts, the peaks at 2θ values of 26 and 44° correspond to the graphite layers of multi-walled nanotubes. Surprisingly, the Fe/np-CNT and Fe/wp-CNT catalyst did not show similar XRD patterns. According to the XRD spectra, the diffraction peaks for Fe/np-CNT catalyst matched very well with the standard Hematite (Fe_2O_3) phase, whereas, for Fe/wp-CNT catalysts, the peaks at 2θ of 30 and 35.7° indicated the presence of standard Magnetite (Fe_3O_4) phase. This can be attributed to the different electronic properties of inner surface of CNTs with different pore diameters [15-16].

Table 5.2 shows the average iron oxide particle sizes on the catalysts calculated from XRD spectrum using Debye-Scherrer equation at the most intense peak of 36°. The

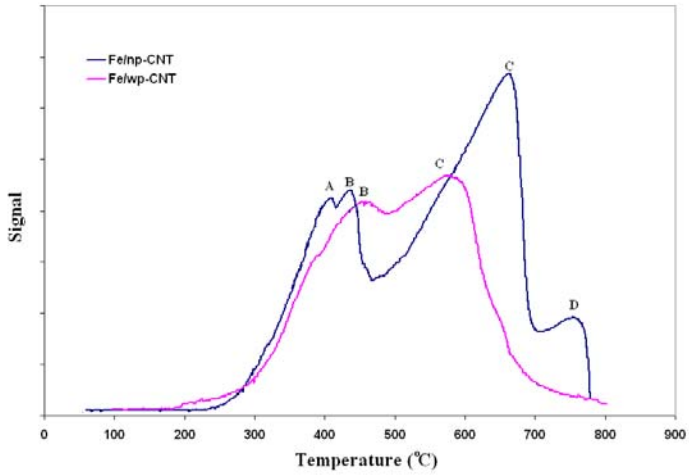

Figure 5.5 H2-TPR profiles for Fe/np-CNT and Fe/wp-CNT catalysts

data verified that the iron oxide particles on Fe/wp-CNT (19 nm) are larger than that on the Fe/np-CNT catalysts (11nm). To compare the particle size calculated based on XRD with TEM analysis, the size distribution of the particles is also shown in Table 5.2. There is a good agreement between the data for average particle size calculated from XRD and the most abundant sizes from TEM analysis.

TPR analyses were performed to evaluate the reducibility of the Fe/np-CNT and Fe/wp-CNT catalysts. TPR patterns of Fe/np-CNT and Fe/wp-CNT catalysts are shown in Figure 5.5. Four peaks (A, B, C and D) can be observed on the TPR profile of the Fe/np-CNT catalyst, whereas, two peaks appear on the TPR profile of the Fe/wp-CNT catalysts. Generally, the reduction of iron oxides takes place according to the following scheme [10]:

$Fe_2O_3 \rightarrow Fe_3O_4 \rightarrow FeO \rightarrow Fe$

In the case of Fe/np-CNT, the first peak (A) can be assigned to the reduction of Fe_2O_3 to Fe_3O_4. The second peak, B, can be assigned to the subsequent reduction of Fe_3O_4 to FeO. Peak C, observed at 500-700 °C, can be related to the reduction of FeO to metallic Fe. Peak D can be attributed to gasification of CNTs at a temperature higher

than 600°C. For Fe/wp-CNT catalyst, since the iron oxide was in the form of Fe_3O_4, the first peak (B) can be related to the reduction of Fe_3O_4 to FeO and the second peak, C,

Table 5.3 Reduction temperature and extent of reduction (from 25-700°C) based on H_2-TPR analysis.

Catalyst	Peak A	Peak B (°C)	Peak C (°C)	Peak D (°C)	Extent of reduction (25-700°C)[a]
Fe/np-CNT	401	438	667	747	79
Fe/wp-CNT	-	459	574	-	62

a) Values for extent of reduction were calculated by considering the fact that the iron oxides on Fe/np-CNT and Fe/wp-CNT were in the form of Fe_2O_3 and Fe_3O_4, respectively.

can be assigned to the subsequent reduction of FeO to Fe. There is a tail (after 650°C) for gasification of wp-CNT as seen in the TPR profile of the Fe/wp-CNT catalyst.

Table 5.3 shows reduction temperatures and extent of reduction for both catalysts. According to the reduction temperature, deposition of iron oxide particles inside the nanotubes with narrow-pores results in a decrease in the temperature of the first TPR peak from 459 to 438°C. However, the onset of second peak (C) was delayed from 574 to 667°C compared to Fe/wp-CNT. Delay in second peak has been reported for different supported iron catalysts [17]. The extent of reduction of the metal is the ratio of the actual H_2 consumed during the temperature programmed reduction (from ambient temperature to 700°C) process to the calculated theoretical amount of H2 needed for the complete reduction of the metal oxides.

According to Table 5.3, the extent of reduction of Fe/np-CNT (79%) was higher than that of Fe/wp-CNT (62%). This can result in relatively more incomplete reduction of the metal sites in the case of the Fe/wp-CNT catalyst and lower FT activity. Theoretical studies [13] and our previous work [14] indicate that deviation of the graphene layers from planarity causes π-electron density to shift from the concave inner surface to the convex outer surface leading to different electronic properties of

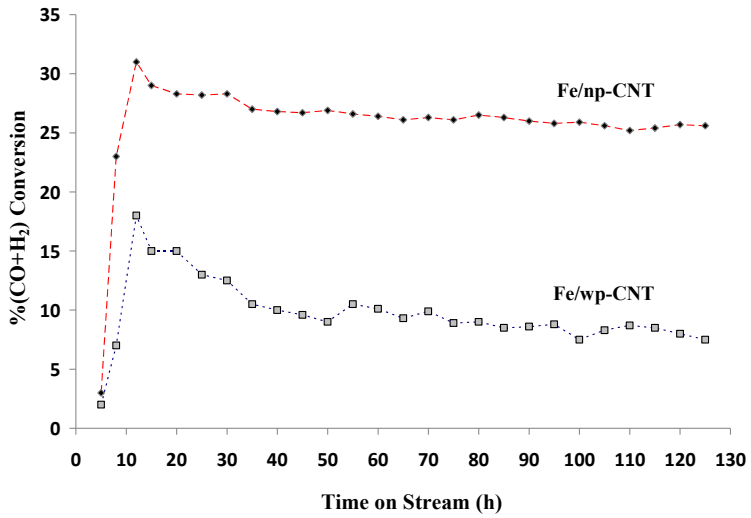

Figure 5.6 Variation of catalytic activity for Fe/np-CNT and Fe/wp-CNT catalysts with time on stream

substances in contact with either inner and outer surfaces of CNTs. Considering the different temperature programmed reduction profiles for iron oxides doped on inner pore of CNTs with different pore diameter, it can be postulated that the extent of shift for electron density could be more for a nanotube with narrow-pore compared to a wide nanotube. Thus, this phenomenon may be attributed to a different interaction of iron oxide with interior surface of the Fe/np-CNT catalyst resulting in higher extent of reduction of this catalyst.

5.4 Fischer-Tropsch Synthesis

The performances of the Fe/np-CNT and Fe/wp-CNT catalysts for the FT synthesis were evaluated in a fixed bed reactor. All the reactions were performed under a set of similar conditions (275^{o}C, 2 MPa, H_2:CO = 2). CO hydrogenation (blank runs with no iron) was performed on the both acid treated CNT supports (np-CNT and wp-CNT samples) under the same operating conditions as the metal loaded samples. The main

Table 5.4 CO conversion and product selectivity of Fe/np-CNT and Fe/wp-CNT

Catalyst activity and product selectivity	Fe/np-CNT	Fe/wp-CNT
$(CO+H_2)$%	25	10
CH_4	15	41
C_2-C_4	37	47
C_5+	48	12
CO_2	19	15

- Process conditions: 7.2 Sl/g-cat/h, 2 MPa, $H_2/CO = 2$, TOS = 120h.
-All catalysts contain 20wt% Fe
-HC in wt%; CO_2 in mol %

product formed at a very low conversion (1%) was methane with almost no higher hydrocarbons.

Figure 5.6 illustrates the change in the activity (% Co conversion) of the Fe/np-CNT and Fe/wp-CNT catalysts over 120 hours. Both catalysts reached their highest activity within 10 hours. Then, they showed different activity patterns. Figure 5.6 shows that Fe/np-CNT is a more active and stable catalyst compared to Fe/wp-CNT. In the case of Fe/np-CNT, syngas conversion decreased slightly from 31 to 26 % in a period of 120 hours, whereas, Fe/wp-CNT catalyst showed a quick drop in CO conversion from 18 to 9%.

The activity, % $(CO+H_2)$ conversion, and product selectivity (CH_4, C_2-C_5, C_5^+ and CO_2) of the catalysts after time on stream of 120 hours is given in Table 5.4. According to the data in Table 5.4, the Fe/np-CNT catalyst showed a CO conversion of 26 %, whereas, activity of the Fe/wp-CNT catalyst was less than 10 %. In addition, C_5+ selectivity of the Fe/np-CNT (48 wt %) was considerably higher than that for Fe/wp-CNT (12 wt %) catalyst.

This study shows that the deposition of iron particles inside the nanotube pores with narrower-pores within the range of studied pore diameters (higher than 10 nm) enhances FT activity and product selectivity. Several possible reasons can be associated with the improvement in the catalyst activity and product selectivity. As discussed

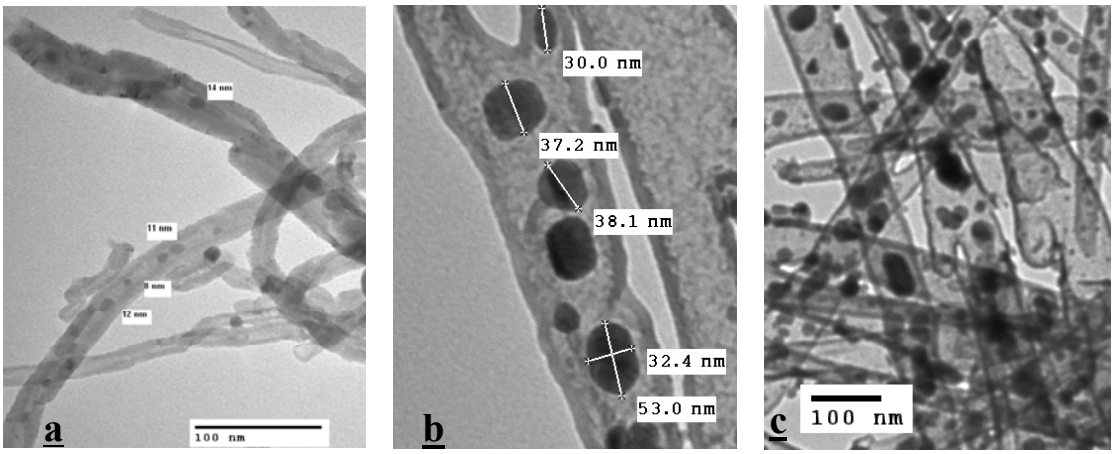

Figure 5.7 TEM images of a)used Fe/np-CNT, b)used Fe/wp-CNT with higher magnification c) used Fe/wp-CNT with low magnification

earlier, H_2-TPR analysis revealed that the reducibility of the Fe/np-CNT catalyst was considerably better in comparison to the Fe/wp-CNT. This phenomenon can result in the formation of more catalytically active carbide species during FTS. Besides, confinement of the reaction intermediates inside the pores can enhance their contact with iron catalysts, favoring the growth of longer chain hydrocarbons.

As given in Table 5.4, CO_2 selectivity for Fe/wp-CNT catalyst was less than that for Fe/np-CNT catalyst. This can be resulted from lower CO conversion for the Fe/wp-CNT catalyst. At a low CO conversion, the amount of the produced water was low which provided a lower water concentration for water-gas-shift reaction during the FT reactions.

Transmission electron microscopy analyses were conducted to study the particle size and structure of the used catalysts after 120 h of FT reactions at 275 °C. Figures 7a and 7b show TEM images of the used Fe/np-CNT and Fe/wp-CNT catalysts. As can be seen in Figure 5.7a, the iron oxide particles inside the channels do not experience considerable particle agglomeration. According to several TEM of used Fe/np-CNT

catalyst, the particle size distribution varied from 7 to 16 nm which is comparable to that of the fresh Fe/np-CNT (6-10 nm) catalyst. This phenomenon can be related to the interaction of the catalytic sites with the inner surface of the pores and perhaps to the spatial restriction of the CNT channels. However, as can be seen in the representative TEM image of Fe/wp-CNT catalyst (Figure 5.7b and 7c), most of the iron species noticeably agglomerated. According to several TEM images, the most abundant particles for fresh Fe/wp-CNT (14-25 nm size range) shifted to 22-38 nm size range after the catalyst used for FT reactions for 120 h. This phenomenon resulted in decrease in FT activity of the catalyst within the reaction period and reaction conditions used in this study.

5.5 Conclusions

The structure and pore diameter of the CNT supports have significant influence on the catalytic performance of the catalysts in FT process. Deposition of the metal sites inside the nanotube with narrow-pore structure resulted in smaller metal particle sizes and better dispersion due to the physical restriction imposed by the CNT pores. In addition, the iron catalyst supported on the narrow-pore support showed higher extent of reduction compared to its counterpart with wide pore structure. This difference is most likely due to difference in electronic properties of the inner surface of the CNTs with different diameters. Higher metal dispersion and better extent of reduction resulted in more active and selective catalysts. In the case of catalysts with metal particles inside the narrow-pores, confinement of reaction intermediates inside the channels may also increase the contact time with active metal sites, resulting in production of heavier hydrocarbons.

Nomenclature

P	Pressure (MPa)
T	Temperature (^{o}C)
%CO	Percent of CO conversion (mol%)

Abbreviations

AAO	Anodic Aluminum Oxide
BET	Brunauer, Emmett, and Teller
CNT	Carbon Nanotubes
CVD	Chemical Vapor Deposition
Fe/wp-CNT	Iron catalysts deposited on wide carbon nanotubes
Fe/np-CNT	Iron catalysts deposited on narrow-pore carbon nanotubes
FTS	Fischer-Tropsch Synthesis
ICP	Inductively Coupled Plasma
SEM	Scanning Election Microscopy
Sl	Standard Litter
TEM	Transition Electron Microscopy
TOS	Time on Stream
TPR	Temperature Programmed Reduction
WGS	Water-Gas Shift
XRD	X-ray Diffraction

References

[1] M.E. Dry, Fischer-Tropsch reactions and the environment, Applied Catalysis A: General, 189 (1999) 185-190.

[2] G. P. van der Laan, A.A.C.M. Beenackers, Selectivity of the Fischer-Tropsch Synthesis: A Literature Review, Catalysis Reviews, 41 (1999) 255-318.

[3] D. B. Bukur, X. Lang, D. Mukesh, W. H. Zimmerman, M. P. Rosynek, C. Li, Binder/support effects on the activity and selectivity of iron catalysts in the Fischer-Tropsch synthesis, Industrial Engineering Chemistry Research, 29 (1990)1588-1599.

[4] A.Y. Khodakov, A. Griboval-Constant, R. Bechara, and V. L. Zholobenko, Pore Size Effects in Fischer Tropsch Synthesis over Cobalt-Supported Mesoporous Silicas, Journal of Catalysis, 206 (2002) 230-241.

[5] R. M. Malek Abbaslou, A. Tavasoli and A. K. Dalai, Effect of pre-treatment on physico-chemical properties and stability of iron catalysts supported on carbon nanotubes for Fischer-Tropsch synthsis, Applied Catalysis A: General, 355(2009)33-41.

[6] A. Tavasoli, R. M. Malek Abbaslou, M. Trepanier, A. K. Dalai, Fischer-Tropsch synthesis over cobalt catalyst supported on carbon nanotubes in a slurry reactor, Applied Catalysis A: General, 345 (2008) 134-142.

[7] W. Chen, z. Fan, X. Pan, X. Bao, Effect of Confinement in Carbon Nanotubes on the Activity of Fischer−Tropsch Iron Catalyst, American Journal of Chemical Society, 130 (2008) 9414-9419.

[8] X. Pan, Z. Fan, W. Chen, Y. Ding, H. Luo, X. Bao, Enhanced ethanol production inside carbon-nanotube reactors containing catalytic particles, Nature, 6 (2007) 507-511.

[9] M. C. Bahome, L. L. Jewell, K. Padayachy, D. Hildebrandt, D. Glasser, A. K. Datye, N. J. Coville, Fe-Ru small particle bimetallic catalysts supported on carbon nanotubes for use in Fischer-Tröpsch synthesis, Applied Catalysis A: General, 328 (2007) 243-251.

[10] W. Ma, E. L. Kugler, J. Wright, and D. B. Dadyburjor, Mo-Fe Catalysts Supported on Activated Carbon for Synthesis of Liquid Fuels by the Fischer−Tropsch Process: Effect of Mo Addition on Reducibility, Activity, and Hydrocarbon Selectivity, Energy Fuels 20 (2006) 2299-2307.

[11] P. Serp, M. Corrias, P. Kalck. Carbon nanotubes and nanofibers in catalysis, Review, Applied Catalysis A: General, 253(2003) 337-358.

[12] I. Eswaramoorthi, V. Sundaramurthy, A.K.Dalai, Partial oxidation of methanol for hydrogen production over carbon nanotubes supported Cu-Zn catalysts, Applied Catalysis A: General, 313 (2006) 22-28

[13] M. Menon, A. N. Andriotis and G. E. Froudakis, Curvature dependence of the metal catalyst atom interaction with carbon nanotubes walls, Physics Letters, 320 (2000) 425-434.

[14] R. M. Malek Abbaslou, A. Tavassoli, J. Soltan , A. K. Dalai, Iron Catalysts Supported on Carbon Nanotubes for Fischer-Tropsch Synthesis: Effect of Catalytic Site Position. Applied Catalysis A: General, 367(2009)47-52

[15] E. E. Santiso, A.M. George, C.H. Turner, M.K. Kostov, K.E. Gubbins, M. Buongiorno-Nardellib and M. Sliwinska-Bartkowiak, Adsorption and catalysis: The

effect of confinement on chemical reactions, Applied Surface Science, 252 (2005) 766-777.
[16] D. B. Bukur, C. Sivaraj, Supported iron catalysts for slurry phase Fischer-Tropsch synthesis, Applied Catalysis A: General, 231 (2002) 201-214.

Chapter 6

Iron Catalyst Supported on Carbon Nanotubes for Fischer-Tropsch Synthesis: Effects of Mo Promotion

A similar version of this chapter has been submitted for publication in the Journal of Fuel:

- *Reza M. Malek Abbaslou, Jafar Soltan, Ajay K. Dalai, Iron Catalyst Supported on Carbon Nanotubes for Fischer-Tropsch Synthesis: Effects of Mo, Journal of Fuel (2010, JFUE-S-10-00355).*

In addition, part of this chapter is accepted for oral presentation in the following conference:

- *Reza M. Malek Abbaslou, Jafar Soltan, Ajay K. Dalai, Structural Promoter for Iron Catalysts Supported on Carbon Nanotubes for Fischer-Tropsch Synthesis, 21st Canadian Symposium on Catalysis, May 9-12, (2010).*

Contribution of the Ph.D. Candidate

The experimental design and experiments were planned and conducted by Reza Malek Abbaslou. The data analysis and interpretations were performed by Reza Malek Abbaslou, with assistance from Drs. Soltan and Dalai. All written text was prepared by Reza Malek Abbaslou and discussed with Drs. Soltan and Dalai.

Contribution of this Chapter to the Overall Study

As discussed in the previous chapters, iron catalyst supported on carbon nanotubes is an active catalyst for Fischer-Tropsch synthesis. However, these catalysts experienced deactivation as a result of active site agglomeration in a reaction period of 120 h. One of the methods to prevent site agglomeration is addition of structural promoters. In this

chapter, the influence of Mo on stability of iron catalysts supported on CNTs is presented.

Abstract

Present studies on the application of carbon nanotubes (CNTs) as support have shown that iron catalysts supported on CNTs are active and selective catalysts for Fischer-Tropsch synthesis (FTS). However, these catalysts experience deactivation as a result of active site agglomerations. In order to study the effects of Mo as a structural promoter, the properties and catalytic performance of unpromoted iron catalysts supported on CNTs were compared with a promoted catalyst with different Mo contents (0.5, 1, 5, and 12 wt%). Promotion of the catalysts with Mo resulted in production of smaller metal particles compared to the unpromoted iron catalyst. According to XRD analysis, Mo species were deposited in their amorphous structure. TPR analyses showed that addition of Mo increased reduction temperature significantly. Based on TEM and XRD analyses, the particle size of the iron oxides in the unpromoted catalyst increased from 16 nm to 25 nm under FT operating conditions, while the particle size of the iron oxide in the Mo promoted catalysts (~12-14 nm) did not change noticeably under the same operating conditions. Activity, selectivity and stability of the unpromoted and Mo promoted catalysts showed that addition of 0.5-1 wt% Mo resulted in a more stable catalyst. Higher contents of Mo (5 and 12 wt%) decreased the activity of the catalysts due to catalytic site coverage and lower extent of reduction. Mo promotion (0.5-12 wt %) increased the selectivity of the catalysts toward lighter hydrocarbons. The promotion of the iron catalyst with 0.5 wt% of Mo stabilized the activity of the catalyst with minimal increase (2%) in methane selectivity.

6.1 Introduction

The Fischer-Tropsch synthesis (FTS) is an established and reliable technology for converting syngas into clean fuels and high value chemicals [1-2]. A high-performance catalyst plays an essential role in industrial applications [3]. In FT reactions, the catalyst activity and selectivity are influenced by the nature and structure of support, the nature of active metal, metal dispersion, metal loading, and the catalyst preparation method [4-5]. So far only iron and cobalt catalysts have proven economically feasibile on an industrial scale [2]. The high water gas shift activity of iron makes it an ideal catalyst for converting hydrogen-lean syngas derived from biomass and coal [1-2].

Carbon nanotubes with unique properties such as uniform and straight pores, meso and macro pore structure, inert surface properties, resistance to acid and base environments, and ease of recovery of metals from spent catalysts can play an important role in a large number of catalytic reactions [6]. CNTs are composed of graphite layers with a tubular morphology. Several research reports including published studies from this research group on the application of CNTs as supports have shown that CNT supports offer enhanced performance for FT reactions [7-17]. However, in terms of catalyst stability, our studies showon that iron catalyst supported on CNTs deactivates mainly due to metal site agglomerations [7, 9].

In order to stabilize active metal sites over the support, structural promoters are used. Ma et al. [18] have studied the effects of Mo addition on the physicochemical and catalytic properties of Fe catalysts supported on activated carbon for the FT reaction. They have reported that Mo was highly dispersed on the support, and the addition of Mo improved Fe dispersion. More importantly, the addition of Mo prevented iron particles from agglomerating under FT reaction conditions. It has also been shown that molybdenum is moderately active for FTS, but selective toward light hydrocarbons [19-

20]. Murchison and Murdick [20] reported that Mo catalyst promoted with alkali was active for conversion of syngas to LPG with high sulfur resistance and low rate of coking. Using the density functional theory, Belosludov et al. [21] have calculated that Mo as a promoter could increase the activation of CO and sulfur-poisoning-tolerance of Fe catalyst.

In the current chapter, the effects of Mo promotion on the activity, stability and selectivity of iron catalysts are presented. It is hypothesized that Mo could work as a structural promoter to prevent particle sintering along with favorable influence on the performance of the iron catalyst supported on carbon nanotubes. In this chapter, performance of the unpromoted iron catalyst is compared with those of promoted iron catalysts with different Mo contents, and the properties of the catalysts before and after FT reactions are reported.

6.2 Experimental

6.2.1 Catalyst Preparation

A batch of carbon nanotubes was purchased from mknano Co. (M.K. IMPEX Canada). Prior to impregnation, the CNT sample was treated in nitric acid (60 wt%) at 110^{o}C for 16 hours. The catalysts were prepared using the incipient wetness impregnation method. For the preparation of the catalysts, first 30 wt% iron was doped in two steps onto the pre-treated CNTs. The doped CNT samples were dried at 120^{o}C overnight. In order to prepare iron catalysts with Mo content of 0.5, 1, 5, 12 wt%, appropriate amounts of $(NH_4)_6Mo_7O_{24}{\cdot}4H_2O$ were dissolved in deionised water and added to the iron catalysts. The catalysts were denoted as xMo-30Fe/CNT (x = 0.5, 1, 5, or 12 wt%). After drying at 120^{o}C and calcination at 400^{o}C for 3 hours, the catalysts were characterized by nitrogen adsorption, inductively coupled plasma (ICP),

temperature programmed reduction (TPR), X-ray diffraction (XRD), scanning electron microscopy (SEM), energy dispersive X-Ray (EDX) analysis, and transmission electron microscopy (TEM).

6.2.2 Characterization of Catalysts

The morphology of the calcined and used (after FT reactions) catalysts was studied by transmission electron microscopy (TEM). Sample specimens for TEM studies were prepared by ultrasonic dispersion of the catalysts in ethanol. The suspensions were then dropped onto a copper grid. TEM analyses were carried out using a Hitachi H-7500 (120 kV) instrument. For each sample, several TEM micrographs were recorded and analyzed to determine the particle size distribution. A Philips SEM-505 scanning electron microscope operating at 300 kV in SE display mode was used for morphological characterizations. Prior to SEM analysis, all the samples were gold-coated in a sputter coating unit (Edwards Vacuum Components Ltd., Sussex, England).

The surface area and pore volume of the catalysts were measured by an ASAP-2000 system from Micromeritics. Prior to analysis, the samples were degassed at 200^{o}C for 2 h under 50 mTorr vacuum. XRD diffractograms of the pure CNTs and the calcined catalysts were conducted using a Philips PW1840 X-ray diffractometer with monochromatized Cu/Kα radiation. Using the Scherrer equation, the average size of the metal oxide crystallites in the calcined catalysts was estimated. The details for the particle size estimation using Scherrer's method are presented in Appendix E.

The temperature programmed reduction profile of the calcined catalysts were recorded using a CHEMBET-3000, equipped with a thermal conductivity detector. The catalyst samples were first purged in a flow of helium at 150^{o}C to remove traces of water, and then cooled to 40^{o}C. The TPR of 100 mg of each sample was performed using 5% hydrogen in nitrogen gas mixture with a flow rate of 40 ml/min. The samples

were heated from 40 to 800^{o}C with a heating rate of 10^{o}C/min. The details for calibration of TPR machine and corresponding calculations are given in Appendix D.

The Fischer-Tropsch synthesis was performed in a fixed-bed micro reactor. The schematic and specifications of the fixed bed reactor are given in Appendix C. Prior to CO hydrogenation, in-situ reduction was conducted according to the following procedure. The diluted catalyst (1 g catalyst and 7 g silicon carbide) was placed in the reactor. Then pure hydrogen was introduced at a flow rate of 30 ml/min. The reactor temperature was increased from room temperature to 380^{o}C at a rate of 1^{o}C/min and maintained at this activation condition for 14 h. After the activation period, the reactor temperature was reduced to 275^{o}C under flowing hydrogen. The hydrogen and syngas flow rates were controlled by two mass flow controllers (Brooks 5850). Argon was used as an internal standard gas in the reactor feed. The mixed gases (45%CO, 45%H_2, and 10% Ar) entered through the top of the fixed bed reactor. The temperature of the reactor was controlled using a PID temperature controller. Synthesis gas with a space velocity of 2000 ml(STP)/(h g) was introduced into the reactor while the reactor pressure was set to 2 MPa. Products were continuously removed after passing through two traps. The pressure of the uncondensed gaseous product stream was reduced to atmospheric pressure. The composition of the outlet gas stream was measured using an on-line GC-2014 Shimadzu gas chromatograph. The contents of the liquid traps were removed every 24 h, the hydrocarbon and water fractions were separated, and analyzed by a Varian 3400 gas chromatograph. Catalytic activity, product selectivity and stability of the catalyst were monitored during the reaction period of 125 hours. The uncertainties for the experimental data are given in Section 1-13.

6.3 Results and Discussions

6.3.1 Characterization of Catalysts

Scanning electron micrographs (Figure 6.1a) of the acid-treated CNTs samples showed that the CNT sample contained CNTs and no other impurities were observed. A transmission electron micrograph (TEM) of the acid-treated CNT sample is shown in Figure 6.1b. As can be seen in the representative micrograph (Figure 6.1b), the nanotubes have uniform diameters and their inner and outer diameters vary between 8-12 nm and 20-25 nm, respectively. TEM analysis also revealed that a vast majority (more than 70%) of the acid-treated nanotubes have open caps. High resolution TEM images of the CNT sample (Figure 6.1c) showed that the carbon nanotubes possess 12-18 graphite layers. There are several sites of defects on the graphite layers (shown in the boxes) on both inner and outer surfaces of the nanotubes. These defects are believed to act as anchoring sites for metal particles to attach to the surface of the nanotubes. Figures 6.2a, 6.2b, and 6.2c show representative TEM images of unpromoted catalyst (30Fe/CNT) and Mo promoted catalysts (1Mo-30Fe/CNT and 12Mo-30Fe/CNT). Dark spots represent the iron oxide particles which are attached inside or outside the nanotubes. For all of the catalysts, a vast majority of the iron particles (80%) are distributed on the inner surface of pores of CNTs. This can be attributed to the carbon nanotubes' tubular structure, which can induce capillary forces during the impregnation process. Figure 6.2c also shows that the Mo species surround and are attached to the iron oxide particles.

Using SEM-EDX point analyses, the presence of Mo species attached to the iron particles was verified. In the case of 12Mo-30Fe/CNT catalyst, the EDX data from three points showed the presence of Mo species with Fe/Mo ratios of 3.6, 3.4 and 4.3.

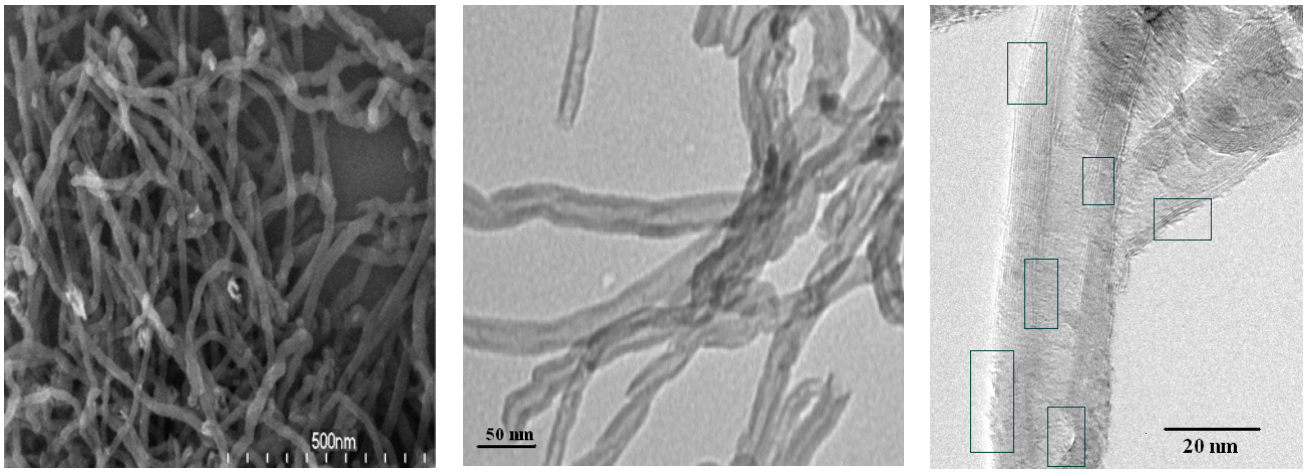

Figure 6.1 a) SEM micrograph of acid treated CNT sample, b) TEM image of acid treated CNT sample with open caps, and c) high resolution TEM image of carbon nanotube showing graphite layers

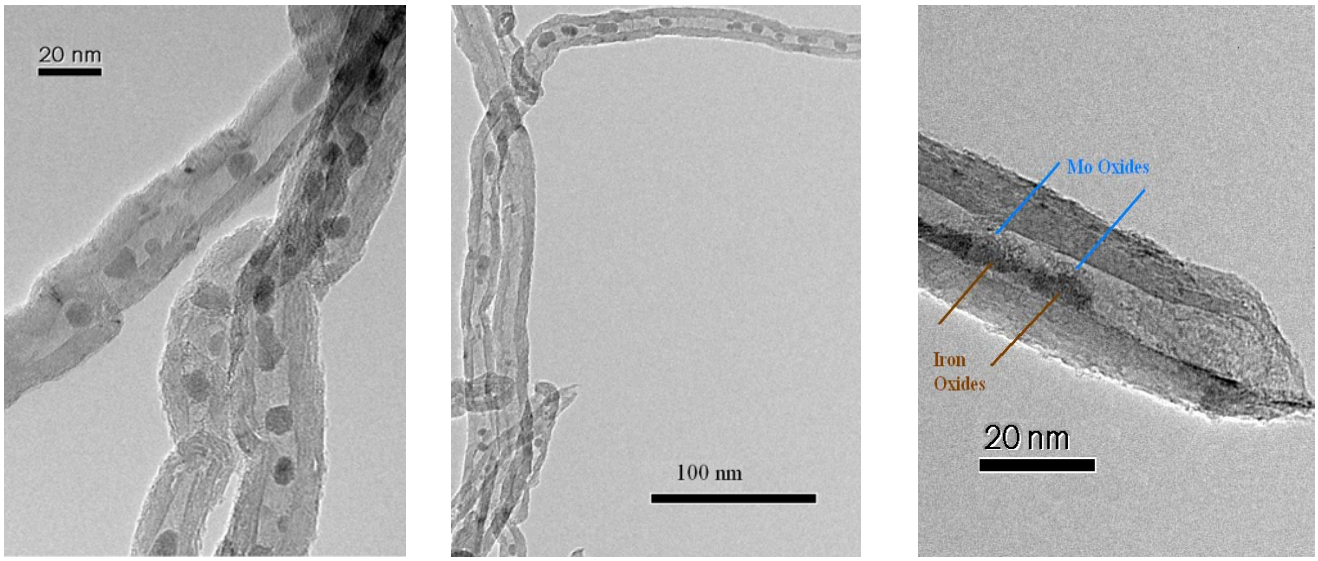

Figure 6.2 TEM micrographs of the unpromoted and Mo-promoted iron catalysts supported on CNTs a) 30Fe/CNT catalyst, dark spots represent iron oxides, b) 1Mo-30Fe/CNT, c)12Mo-30Fe/CNT, Mo species surround iron oxide particles and prevent iron particle from agglomeration during the reduction and FT reactions.

According to Figure 6.2c and the results of EDX, one may expect interactions of Mo and Fe during the catalyst reduction and FT reactions for the Mo promoted catalysts.

Table 6.1 shows the metal content for the unpromoted and promoted catalysts. Inductively coupled plasma (ICP) analysis of the catalysts showed that the metal contents of the catalysts were close (±0.7%) to the target metal contents. Table 6.1 also shows the results of surface area measurements of the CNT sample, unpromoted and Mo promoted catalysts. According to the N_2 adsorption analysis, the loading of 30% Fe decreased the surface area from 220 to 141 m^2/g. Increase in density of CNTs due to iron loading and pore blockage can result in lower surface areas of the loaded catalysts. Promotion of Mo up to 5 wt% did not have a considerable effect on the surface area of the catalysts. This might be attributed to the high Mo dispersion, preventing formation of large particles and any further pore blockage. However, addition of 12 wt% of Mo decreased the catalyst surface by 21 % compared to the unpromoted catalyst resulting in the formation of bigger clusters of Mo species and considerable pore blockage.

Figure 6.3a and 6.3b show XRD patterns of the calcined unpromoted (30Fe/CNT) and Mo promoted (1Mo-30Fe/CNT) catalysts. Both catalysts exhibited similar XRD patterns. The diffraction peaks match very well with the standard Hematite (Fe_2O_3) phase for fresh catalysts and Magnetite for the used catalyst (Fe_3O_4). In addition, the peaks at 2θ values of 26^o and 44^o correspond to the graphite layers of multi-walled nanotubes. Crystallite phase of Mo species did not appear in the XRD spectra of Mo promoted catalysts even with 12 wt % of Mo content. This may be attributed to the amorphous structure of the Mo species in the calcined catalysts [18]. For used 30Fe/CNT, a sharp peak is observed at a two-theta angle of 35.7^o showing the growth in particle size.

Table 6.1 Metal contents and surface properties of CNT sample, unpromoted and promoted catalysts

Catalyst	Fe Content%	Mo Content%	BET Surface Area (m^2/g)
CNT-support	0	0	220
30Fe/CNT	29.4	0	141
0.5Mo-30Fe/CNT	30.3	0.6	140
1Mo-30Fe/CNT	30.7	1.1	143
5Mo-30Fe/CNT	30.1	5.4	134
12Mo-30Fe/CNT	30.7	11.6	111

Table 6.2 Iron oxide particle size for fresh and used catalysts determined by XRD and TEM analyses

Catalyst Name	Fresh Catalysts (nm)-XRD	Fresh Catalysts (nm)-TEM	Used Catalyst (nm) XRD	Used Catalyst (nm) TEM
30Fe/CNT	15 ± 2	8-17	25 ± 2	12-25
0.5Mo-30Fe/CNT	14 ± 1	6-15	15 ± 1	9-17
1Mo-30Fe/CNT	13 ± 2	6-15	14 ± 2	7-17
5Mo-30Fe/CNT	12 ± 1	7-16	13 ± 2	5-16
12Mo-30Fe/CNT	12 ± 1	7-17	14 ± 2	5-16

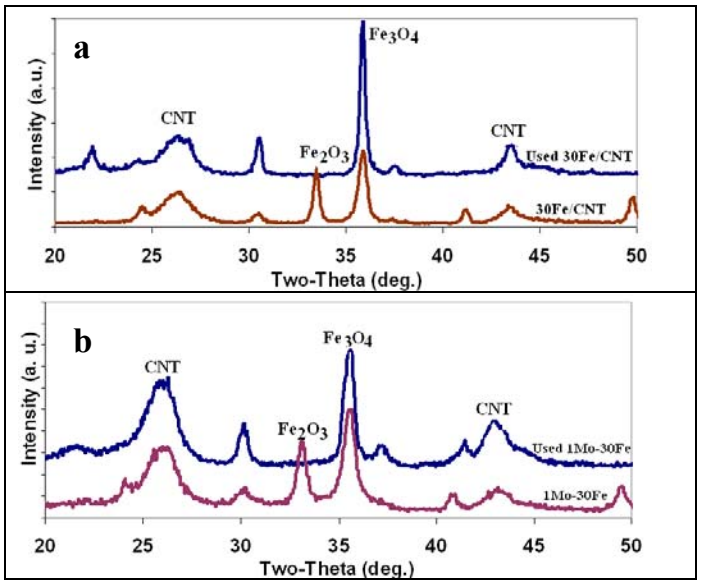

Figure 6.3 XRD pattern of fresh and used catalysts a) 30Fe/CNT, and b)1Mo-30Fe/CNT

Table 6.2 shows the average iron oxide particle sizes on the catalysts calculated from XRD spectra. According to Debye-Scherrer equation at the most intense peak of 36^{o}, the average particle size for fresh 30Fe/CNT catalyst is 15 nm. Addition of Mo to the iron 30Fe /CNT catalyst results in slight decrease in the average particle sizes. For example, the iron oxide particle size for the catalysts with 0.5, 1 and 5% Mo decreased to 14, 13 and 12 nm respectively. To compare the particle sizes calculated based on XRD with TEM analysis, the size distribution of the particles is also shown in Table 6.2. There is a good agreement between the data for average particle size calculated from XRD and TEM analyses.

The reducibility of the unpromoted and Mo-promoted catalysts were studied using TPR analyses. The reduction patterns of the catalysts are shown in Figure 6.4. Three peaks (A, B, and C) can be observed on the TPR profile of the catalysts. According to the TPR pattern of the unpromoted and Mo-promoted catalysts, (Figure 6.4), the first peak (A) can be assigned to the reduction of Fe_2O_3 to Fe_3O_4. Peak B, observed at 600-700 °C, can be related to the reduction of Fe_3O_4 to metallic Fe. Peak C can be attributed to gasification of CNTs at a temperature higher than 600^{o}C. The effects of Mo addition on the reduction temperature can also be seen in Figure 6.4. Promotion of the iron catalyst with Mo results in a significant increase in reduction temperature. In other words, while the reduction temperate for the first peak for unpromoted catalyst is 421^{o}C, addition of 1, 5, and 12 wt% molybdenum increases the reduction temperature to 430, 536, and 590^{o}C, respectively. Higher reduction temperatures can lead to lower extent of reduction. This phenomenon is attributed to the strong interaction of Mo with Fe during the reduction of the catalysts.

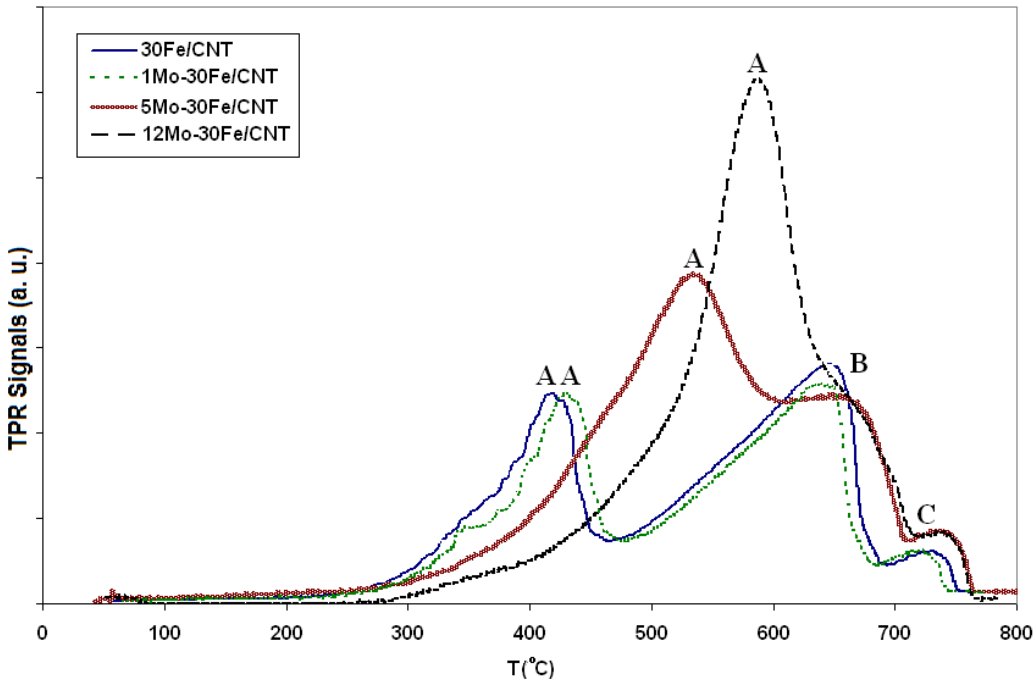

Figure 6.4 Reduction profile from room temperature to 800°C for the unpromoted and Mo-promoted iron catalysts supported on CNTs

6.4 Fischer-Tropsch Synthesis

The performances of the 30Fe/CNT and Mo-promoted catalysts for the Fischer-Tropsch synthesis were evaluated in a fixed bed reactor. All the reactions were performed under a set of similar conditions (275°C, 2 MPa, H_2:CO = 1). CO hydrogenation (blank runs with no iron) was performed on the acid treated CNT supports under the same operating conditions as in the case of metal loaded samples. The main product formed at a very low conversion (1%) was methane with almost no higher hydrocarbons.

Figure 6.5 shows the catalyst activity during a reaction period of 120 h. According to the FT results, the activity (%CO conversion) of the 30Fe/CNT catalyst reached its highest value of 67 % after 10h. Then the catalyst experienced deactivation and the CO conversion decreased to as low as 55% after 120 h operation. Contrary to the un-

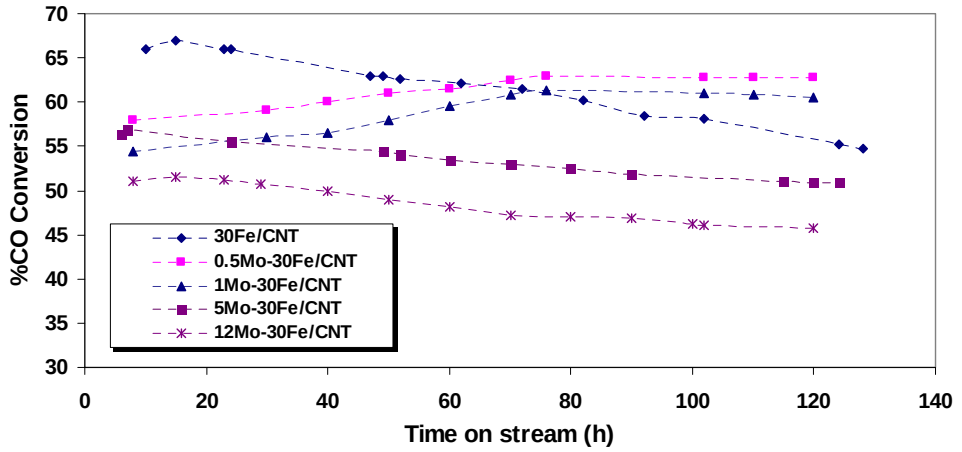

Figure 6.5 Change in % CO conversion with time on stream for the unpromoted and Mo promoted iron catalysts (Process conditions: 2 Sl/g-cat/h, P = 2 MPa, H_2/CO = 1, T = 275°C, TOS of 120 h).

promoted catalyst, 0.5 Mo-30Fe/CNT and 1Mo-30Fe/CNT catalysts reached their highest activity after 70 hours with 64 and 62 % of CO conversion, respectively. Then, their activity remained constant during the next 60 hours.

Further addition of Mo to the iron catalysts (5Mo-30Fe/CNT and 12Mo-30Fe/CNT) resulted in lower activity compared to the unpromoted iron catalysts. As can be seen in Figure 6.5, there was slight decrease in activity of 5Mo-30Fe/CNT and 12Mo-30Fe/CNT catalysts from 56 to 50% and 51 to 46% of CO conversion, respectively, during the reaction period of 120 h, while the activity of the unpromoted iron catalyst varied for 67 to 55%. The lower activity of the promoted catalysts with high content of Mo can be attributed to partial coverage of active metal (iron species) sites by molybdenum species. Besides, as discussed in the previous section, addition of Mo results in higher reduction temperatures (lower extent of reductions) compared to unpromoted catalyst, leading to lower availability of active catalytic sites.

The main reason for addition of Mo to iron catalyst supported on CNTs was to control the metal site agglomeration during FT reactions. In order to study the metallic

Table 6.3 CO conversion and product selectivity of unpromoted and Mo promoted iron catalysts after TOS of 120 hours

Product Selectivity	30Fe/CNT	0.5Mo-30Fe/CNT	1Mo-30Fe/CNT	5Mo-30Fe/CNT	12Mo-30Fe/CNT
% CO Conversion	55	63	60	51	45
Activity (g HC/kg-Fe/h)	533	573	566	450	423
CH_4	16	18	22	25	26
C_2-C_4	30	33	40	44	44
C_5+	53	49	38	31	30
CO_2	40	41	43	43	42
O/P ratio	1.3	1.5	1.5	1.6	1.4

phases and the particle sizes, XRD and TEM analyses were conducted on the used catalysts. Estimated particle sizes are given in Table 6.2. According to the XRD analysis using Debye-Scherrer equation, the average particle size of 30Fe/CNT catalyst increased from 16 nm to 25 nm indicating active site agglomeration during the reaction. A representative TEM micrograph of the used 30Fe/CNT catalyst is also given in Figure 6.6a. As can be seen in Figure 6.6a, the agglomeration of metallic sites has taken place during the reaction period. Thus, the decrease in activity of the 30Fe/CNT catalyst can be attributed to active metal site sintering. According to the data in Table 6.3, in the case of Mo-promoted catalysts the particle size did not change noticeably under the FT operating conditions during 120 h operation. A representative TEM image of the used 1Mo-30Fe/CNT catalyst is given in Figure 6.6b. The stable catalytic activity of 0.5Mo-30Fe/CNT and 1Mo-30Fe/CNT catalyst can be attributed to constant particle sizes of the active metal under the FT operating conditions. Accordingly, it can be concluded that the unstable catalytic performance of 5Mo-30Fe/CNT and 12Mo-30Fe/CNT is not related to the site agglomeration. The decrease in catalytic activity of catalyst with high Mo loadings can be attributed to chemical interaction of the two metals and production of Fe-Mo compounds on the catalytic sites during the FT reactions. According to XRD

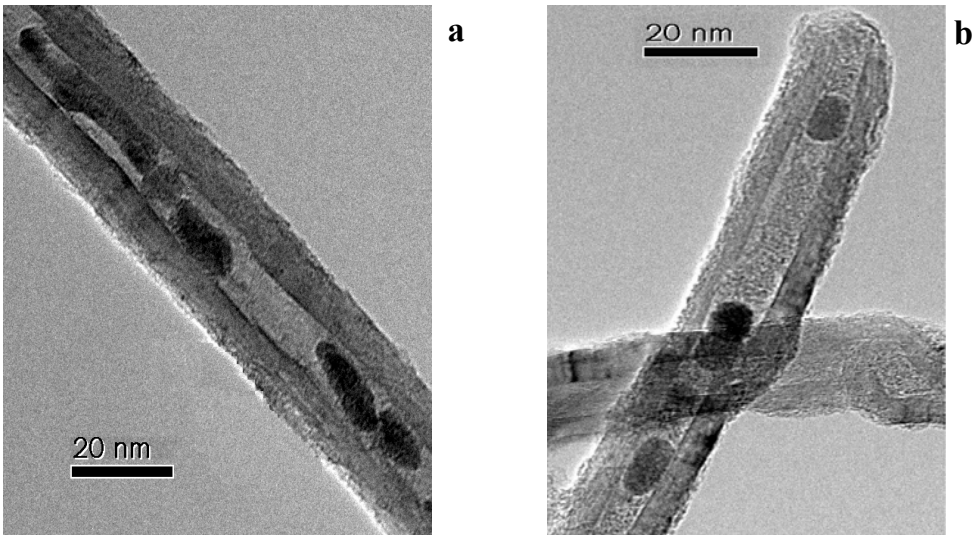

Figure 6.6 TEM images of the used unpromoted and Mo-promoted iron catalysts supported on CNTs a) used 30Fe/CNT catalyst, b) used 1Mo-30Fe/CNT, dark spots present iron oxides.

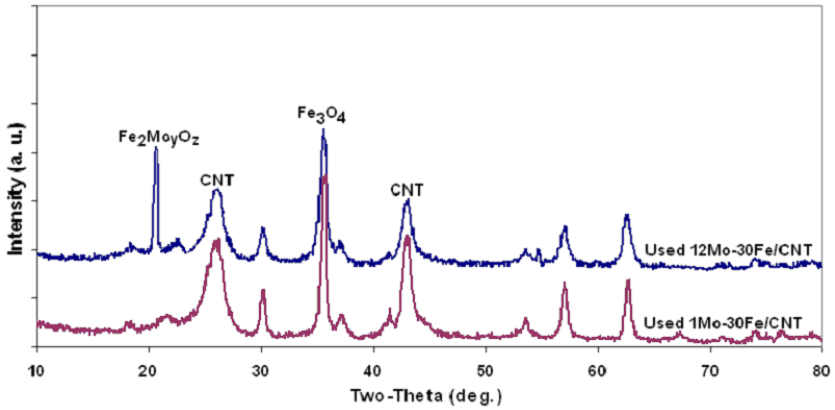

Figure 6.7 XRD spectra of used Mo promoted catalysts

spectra of the used 1Mo-30Fe/CNT and 12Mo-30Fe/CNT (Figure 6.7) catalysts, there is a peak at a two-theta angle of 21.5° which can be assigned to $Fe_2Mo_yO_z$ compounds [18]. The fingerprint peaks of these compounds were not present in the XRD spectrum of Mo-promoted catalyst with minimal amount of Mo (1Mo-30Fe/CNT).

The effects of Mo addition on the catalysts' activity, productivity and selectivity are shown in Table 6.3. Addition of Mo to the iron catalyst results in increase in CH_4

selectivity and decrease in C_{5+} selectivity. As a trend, increase in the Mo content shifts product selectivity toward lighter hydrocarbons. This result is consistent with previous studies with Mo catalysts supported on carbon, SiO_2, and Al_2O_3 [18-20]. As discussed, the addition of Mo increased the reduction temperature leading to lower extent of reduction for iron oxides. Thus, the production of active iron compounds for FT reactions such as iron carbide can be restricted. It has been established that iron carbides are responsible for FT reaction toward higher hydrocarbons [2, 24]. Therefore, one can conclude that minimum amount of Mo along with ability to prevent metal site sintering is beneficial for a CNT supported iron catalyst. Among the catalysts studied in this work, the iron catalysts promoted with 0.5wt% Mo showed slight increase of 2% in CH_4 selectivity with ability to stabilize the particle size distribution and activity of catalyst. It should be noted that promotion of the iron catalyst with less than 0.5% Mo content was not able to stabilize the activity of the catalyst. As can be seen in Table 6.3, addition of Mo did not lead to significant change in CO_2 selectivity and olefin to paraffin ratios in product.

6.5 Conclusions

In this part of the research, the effects of molybdenum addition as a structural promoter to iron catalysts supported on carbon nanotubes (CNTs) were studied. The results of TPR analysis showed that Mo promotion increased the reduction temperature of iron catalysts. However, Mo promotion led to smaller particle sizes compared to unpromoted iron catalysts. The unpromoted iron catalyst showed unstable activity under FT operating conditions due to metal particle agglomerations. At the lower range of Mo contents (0.5 and 1 wt%), the activity (%CO conversion) of the catalysts for FT reactions remained stable (60-63 %) during the FT reactions. The characterization of the

used catalysts showed that promotion of the iron catalysts with Mo prevented agglomeration of the catalytic sites. Further addition of Mo onto the iron catalysts resulted in lower activity along with higher methane production. Therefore, there is a trade off in the addition of Mo. Although, the Mo promotion stabilizes the catalyst activity, it shifts the products' selectivity toward lighter hydrocarbons. Considering the stability and activity of the catalysts studied, promotion of iron catalysts supported on carbon nanotubes with minimum amount of 0.5 wt% of Mo improves catalyst stability and activity by 8% with minor effects on catalyst selectivity (4 % decrease in C_5+ and 2 % increase in methane selectivity).

Nomenclature

P	Pressure (MPa)
T	Temperature (^{o}C)
%CO	Percent of CO conversion (mol%)

Abbreviations

BET	Brunauer, Emmett, and Teller
CNT	Carbon Nanotubes
FTS	Fischer-Tropsch Synthesis
ICP	Inductively Coupled Plasma
SEM	Scanning Election Microscopy
Sl	Standard Litter
TEM	Transition Electron Microscopy
TOS	Time On Stream
TPR	Temperature Programmed Reduction
WGS	Water-Gas Shift

XRD	X-ray Diffraction
30Fe/CNT	Iron catalysts deposited on CNTs with 30% iron loading
xMo-30Fe/CNT	Mo promoted Iron catalysts with x% Molybdenum loading

References

[1] M. E. Dry, Fischer-Tropsch reactions and the environment, Applied Catalysis A: General, 189 (1999) 185-190.

[2] G. P. van der Laan, A.A.C.M. Beenackers, Selectivity of the Fischer-Tropsch Synthesis: A Literature Review, Catalysis Reviews, 41 (1999) 255-318.

[3] M.J.A. Tijmensen, A.P.C. Faaij, C.N. Hamelinck, M.R.M van Hardeveld, Exploration of the possibilities for production of Fischer Tropsch liquids and power via biomass gasification, Biomass and Bioenergy, 23 (2002) 129-152.

[4] J. Zhang, J. Chen, J. Ren, Y. Li, Y. Sun, Support effect of Co/Al_2O_3 catalysts for Fischer-Tropsch synthesis, Fuel, 82 (2003) 581-586.

[5] D. B. Bukur, X. Lang, D. Mukesh, W. H. Zimmerman, M. P. Rosynek, and C. Li, Binder/support effects on the activity and selectivity of iron catalysts in the Fischer-Tropsch synthesis, Industrial Engineering Chemistry Research, 29 (1990) 1588-1599.

[6] P. Serp, M. Corrias, P. Kalck, Carbon nanotubes and nanofibers in catalysis, Review, Applied Catalysis A: General, 253(2003) 337-358.

[7] R. M. Malek Abbaslou, A. Tavasoli and A. K. Dalai, Effect of pre-treatment on physico-chemical properties and stability of iron catalysts supported on carbon nanotubes for Fischer-Tropsch synthsis, Applied Catalysis A: General, 355 (2009) 33-41.

[8] A. Tavasoli, R. M. Malek Abbaslou, M. Trepanier, A. K. Dalai, Fischer-Tropsch synthesis over cobalt catalyst supported on carbon nanotubes in a slurry reactor, Applied Catalysis A: General, 345 (2008) 134-142.

[9] R. M. Malek Abbaslou, A. Tavassoli, J. Soltan , A. K. Dalai, Iron Catalysts Supported on Carbon Nanotubes for Fischer-Tropsch Synthesis: Effect of Catalytic Site Position. Applied Catalysis A: General, 367 (2009) 47-52.

[10] A. Tavasoli, , A. M. Rashidi, K. Sadaghiani Zadeh, A. Karimi, A. Kodadadi, Y. A. Mortazavi, (2005) European Patent EP1782885.

[11] A. A. Chen, M. A. Vannice, and J. Phillips, Effect of support pre-treatments on carbon-supported iron particles Journal of Physical Chemistry, 91 (1987) 6257-6269.

[12] W. Chen, z. Fan, X. Pan, X. Bao, Effect of Confinement in Carbon Nanotubes on the Activity of Fischer−Tropsch Iron Catalyst, Journal of American Chemical Society, 130 (2008) 9414-9419.

[13] X. Pan, Z. Fan, W. Chen, Y. Ding, H. Luo, X. Bao, Enhanced ethanol production inside carbon-nanotube reactors containing catalytic particles, Nature 6 (2007) 507-511.

[14] M. C. Bahome, L.L. Jewell, K. Padayachy, D. Hildebrandt, D. Glasser, A. K. Datye, N. J. Coville, Fe-Ru small particle bimetallic catalysts supported on carbon nanotubes for use in Fischer-Tröpsch synthesis, Applied Catalysis A: General, 328 (2007) 243-251.

[15] E. van Steen, F.F. Prinsloo, Comparison of preparation methods for carbon nanotubes supported iron Fischer-Tropsch catalysts, Catalysis Today, 71 (2002) 327-334.

[16] M. C. Bahome, L.L. Jewell, D. Hildebrandt, D. Glasser, N.J. Coville, Fischer-Tropsch synthesis over iron catalysts supported on carbon nanotubes, Applied Catalysis A: General, 287 (2005) 60-67.

[17] G. L. Bezemer, J. H. Bitter, H. P. C. E. Kuipers, H. Oosterbeek, J. E. Holewijn, X. Xu, F. Kapteijn, A. J. van Dillen, and K. P. de Jong, Cobalt Particle Size Effects in the Fischer-Tropsch Reaction Studied with Carbon Nanofiber Supported Catalysts, Journal of American Chemical Society, 128 (2006) 3956-3964.

[18] W. Ma, E. L. Kugler, J. Wright, and D. B. Dadyburjor, Mo-Fe Catalysts Supported on Activated Carbon for Synthesis of Liquid Fuels by the Fischer−Tropsch Process: Effect of Mo Addition on Reducibility, Activity, and Hydrocarbon Selectivity, Energy Fuels 20 (2006) 2299-2307.

[19] C.B. Murchison, D.A. Murdick, Syngas to LPG over Mo catalysts, Hydrocarbon Processing, 60 (1981) 159-166.

[20] O.W. Dun, E. Gulari, K.Y.S. NG, Fischer-tropsch synthesis on charcoal-supported molybdenum: The effect of preparation conditions and potassium promotion on activity and selectivity, Applied Catalysis A: General, 15 (1985) 247-254.

[21] R.V. Belosudov, S. Sakahara, K. Yajima, S. Takami, M. Kubo, A. Miyamoto, Combinatorial computational chemistry approach as a promising method for design of Fischer-Tropsch catalysts based on Fe and Co, Applied Surface Science, 189 (2002) 245-252.

[22] S. Qin, C. Zhanga, J. Xua, B. Wua, H. Xianga, Y. Li a, Effect of Mo addition on precipitated Fe catalysts for Fischer-Tropsch synthesis, Journal of Molecular Catalysis A: Chemicals, 304 (2009) 128-134.

[23] N. Lohitharn, J.G. Goodwin Jr., E. Lotero, Fe-based Fischer-Tropsch synthesis catalysts containing carbide-forming transition metal promoters, Journal of Catalysis, 255 (2008) 104-113.

[24] B.H. Davis, Fischer-Tropsch Synthesis: Reaction mechanisms for iron catalysts Catalysis Today, 141 (2009) 25-33.

Chapter 7

Promoted Iron Catalysts Supported on Carbon Nanotubes for Fischer-Tropsch Synthesis: Catalytic Performance and Kinetic Study

A similar version of this chapter has been submitted for publication in the Journal of Fuel:

- *Reza M. Malek Abbaslou, Jafar Soltan, Ajay K. Dalai, Promoted Iron Catalysts Supported on Carbon Nanotubes for Fischer-Tropsch Synthesis: Catalytic Performance and Kinetic Study, Journal of Fuel (2010, JFUE-S-10-00367)*

In addition, part of this chapter is accepted for oral presentation in the following conference:

- *Reza M. Malek Abbaslou, Jafar Soltan, Ajay K. Dalai, Kinetic Study of Promoted Iron Catalysts Supported on Carbon Nanotubes for Fischer-Tropsch Synthesis, Nanocatalysis for Fuels and Chemicals Symposium, Pacifichem 2010, Hawaii, USA (Dec. 2010).*

Contribution of the Ph.D. Candidate

The experimental design and experiments were planned and conducted by Reza Malek Abbaslou. The data analysis and interpretations were performed by Reza Malek Abbaslou, with assistance from Drs. Soltan and Dalai. All written text was prepared by Reza Malek Abbaslou and discussed with Drs. Soltan and Dalai.

Contribution of this Chapter to the Overall Study

In the previous chapters, it was shown that deposition of metal catalytic sites inside the narrow-pore nanotubes resulted in active catalysts for FT reactions. In Chapter 6, the effects of Mo promotion on the stability of the iron catalysts under FT operating conditions were discussed. It is known that K and Cu are able to increase activity and shift the product selectivity toward heavier hydrocarbons. In order to develop the most efficient iron catalyst supported on CNTs, several catalysts with different amounts of K and Cu promoters were prepared and their FT activity and selectivity were studied in a fixed bed reactor. The results of catalyst activity and selectivity are elaborated in this chapter. In addition, the results of a kinetic study comparing the activity of the most efficient catalyst with precipitated and commercial catalysts are presented.

Abstract

Effects of potassium and copper promotions on the activity and selectivity of iron catalysts supported on carbon nanotubes (CNTs) for Fischer-Tropsch synthesis (FTS) were studied in a fixed bed reactor (2 MPa, 270^{o}C and $H_2/CO = 1$). It was found that potassium (1-2 wt%) and copper (0.5-1 wt%) promotions did not change the surface area and metal particle sizes compared to the unpromoted iron catalyst. Based on TPR analyses, copper promotion (0.5-1 wt%) decreased the reduction temperature by up to ~120^{o}C. Addition of K (1-2wt%) shifted the products selectivity toward higher molecular weight hydrocarbons. Both K and Cu promoters increased the catalyst activity for FTS and the water-gas-shift (WGS) reaction. However, excess addition of K (2 wt%) and Cu (1 wt%) resulted in catalyst deactivation and lower activity. The most effective catalyst among the studied catalysts showed excellent activity (5.6 mg HC/g-Fe/h) and product selectivity (C_5^+ selectivity of 76 wt%). A kinetic study for the most

effective catalyst was performed using an integral reactor. Mechanistic reaction rate models for the Fischer-Tropsch (FT) reaction and the water-gas-shift (WGS) reaction from the literature were tested. Different combinations of the reaction rate equations (eight FT reaction rate equations and seven WGS reaction rate equations) were evaluated using a nonlinear regression procedure. It was found that a reaction rate equation for the Fischer-Tropsch reaction based on the combined enol/carbide mechanism in which the rate-determining step is the dual site surface reaction between adsorbed formyl and dissociated H_2 describes the experimental data better than other proposed reaction mechanisms. Based on a first order reaction rate model, the kinetic study verified that the K and Cu promoted iron catalyst supported on CNTs is more active than precipitated and commercial iron catalysts under similar operating conditions.

7.1 Introduction

Fischer-Tropsch (FT) processes involve conversion of syngas ($CO+H_2$) into a clean source of energy, mainly diesel and naphtha. Syngas with different hydrogen content can be produced through gasification of coal and biomass and reforming of natural gas [1, 2]. Iron with high water-gas-shift reaction rate is an ideal catalyst for converting hydrogen-lean syngas derived from coal and biomass [2] gasification processes. FT process economy can be improved greatly by developing more selective, active and stable catalysts [3, 4].

The nature of support and promoters can influence the selectivity and activity of FT catalysts [5]. Product selectivity of iron catalysts is generally controlled by promoting it with one or more alkali metals. Potassium is a chemical promoter which can increase wax and alkene yields while decreasing the production of undesirable

methane [6]. Potassium promotion can boost FTS and WGS activities of the catalyst. It is believed that potassium possesses strong basicity and it donates electrons to iron facilitating CO chemisorption. This is because, CO tends to accept electrons from iron during the surface reactions of FTS [7].

In order to facilitate reduction of iron oxide to metallic iron during hydrogen activations, copper has been added to precipitated iron catalysts. Addition of copper minimizes sintering of iron catalysts when activating with hydrogen by lowering the reduction temperature [6]. Although the effects of K and Cu promotions have been studied extensively, there are disagreeing reports on the effects and range of potassium and copper contents of Fe catalysts [2, 4-7].

In the previous chapters, it was shown that iron catalyst supported on carbon nanotubes (CNTs) is selective, active and stable for FT reactions. Carbon nanotubes with unique properties such as meso-macro porous structure, uniform and straight pores and ability to exchange electrons with metal particles have been subject of extensive studies as a support for catalytic reactions [8]. We have reported that surface properties of carbon nanotubes can be modified by acid pre-treatments [9]. In addition, selective deposition of metal particles inside the nanotubes' pores results in improving selectivity and stability of iron catalysts supported on carbon nanotubes [10]. Our studies on iron catalysts supported on carbon nanotubes indicated that molybdenum can prevent catalyst site sintering during the reduction and FT reactions.

In this chapter, the effects of potassium and copper promotions on the selectivity, activity and stability of iron catalysts supported on carbon nanotubes for FTS are presented. Because of the promising performance of K-Cu-Mo promoted catalysts, a kinetic study was conducted in a fixed bed reactor over the most efficient catalyst from this research. The kinetic study was intended to identify an appropriate combination of

rate equations for the Fischer-Tropsch and water-gas-shift reactions and to determine the reaction rate constants which can be used for reactor modeling. The uncertainties for the experimental data are given in Section 1-13.

7.2 Experimental

7.2.1 Catalyst Preparation

A batch of carbon nanotubes was purchased from mknano Co. (M.K. IMPEX Canada). Prior to impregnation, the CNT sample was treated in nitric acid (60 wt%) at 110^{o}C for 16 hours. The catalysts were prepared using incipient wetness impregnation method. For the preparation of the copper-promoted iron catalyst with 0.5 and 1 wt% Cu and 30 wt% Fe, specified amounts of $Fe(NO_3)_3 \cdot 9H_2O$ and $Cu(NO_3)_2 \cdot 3H_2O$ were dissolved in deionised water. This mixture was added dropwise to the CNT sample in two steps. The doped CNT samples were dried at 120^{o}C for 12 hrs. In order to dope potassium (1 and 2 wt% K), specified amounts of KNO_3 were dissolved in deionised water and added to the iron catalysts. The doped CNT samples were dried at 120^{o}C for 12 hrs. All of the catalysts were promoted with 0.5 wt% Mo. To do this, appropriate amounts of $(NH_4)_6Mo_7O_{24} \cdot 4H_2O$ were dissolved in deionised water and added to the iron catalysts. The catalysts were denoted as xCu-yK-30Fe/CNT (x = 0.5 and 1, and y= 1 and 2 wt%). Since all of the catalysts were doped with 0.5 wt% Mo, Mo promotion is not included in the catalyst name. After drying at 120^{o}C and calcination at 400^{o}C for 3 hours, the catalysts were characterized by nitrogen adsorption, inductively coupled plasma (ICP), temperature programmed reduction (TPR), X-ray diffraction (XRD), and transmission electron microscopy (TEM).

7.2.2 Characterization of Catalysts

The morphology of the calcined and used (after FT reactions) catalysts was studied by transmission electron microscopy (TEM). Sample specimens for TEM studies were prepared by ultrasonic dispersion of the catalysts in ethanol. The suspensions were then dropped onto a copper grid. TEM analyses were carried out using a Hitachi H-7500 (120kV) instrument. For each sample, several TEM micrographs were recorded and analyzed to determine particle size distributions.

The surface area and pore volume of the catalysts were measured by an ASAP-2000 system from Micromeritics. Prior to analysis, the samples were degassed at 200^{o}C for 2 hours under 50 mTorr vacuum. XRD diffractograms of the pure CNTs and the calcined catalysts were conducted using a Philips PW1840 X-ray diffractometer with monochromatized Cu/Kα radiation. Using Scherrer's equation, the average sizes of the metal oxide crystallites in the calcined catalysts were estimated. The details for the particle size estimation using Debye-Scherrer method are presented in Appendix E.

Temperature programmed reduction profiles of the calcined catalysts were recorded using a CHEMBET-3000, equipped with a thermal conductivity detector. The catalyst samples were first purged in a flow of helium at 150^{o}C to remove traces of water, and then cooled to 40^{o}C. Temperature programmed reduction (TPR) of 100 mg of each sample was performed using 5% hydrogen in nitrogen gas mixture with a flow rate of 40 ml/min. The samples were heated from 40 to 800^{o}C with a heating rate of 10^{o}C /min. The details for calibration of TPR apparatus and corresponding calculations are given in Appendix D.

Fischer-Tropsch synthesis was performed in a fixed-bed micro reactor. The schematic and specifications of the fixed bed reactor are given in Appendix C. Prior to CO hydrogenation, in-situ reduction was conducted according to the following

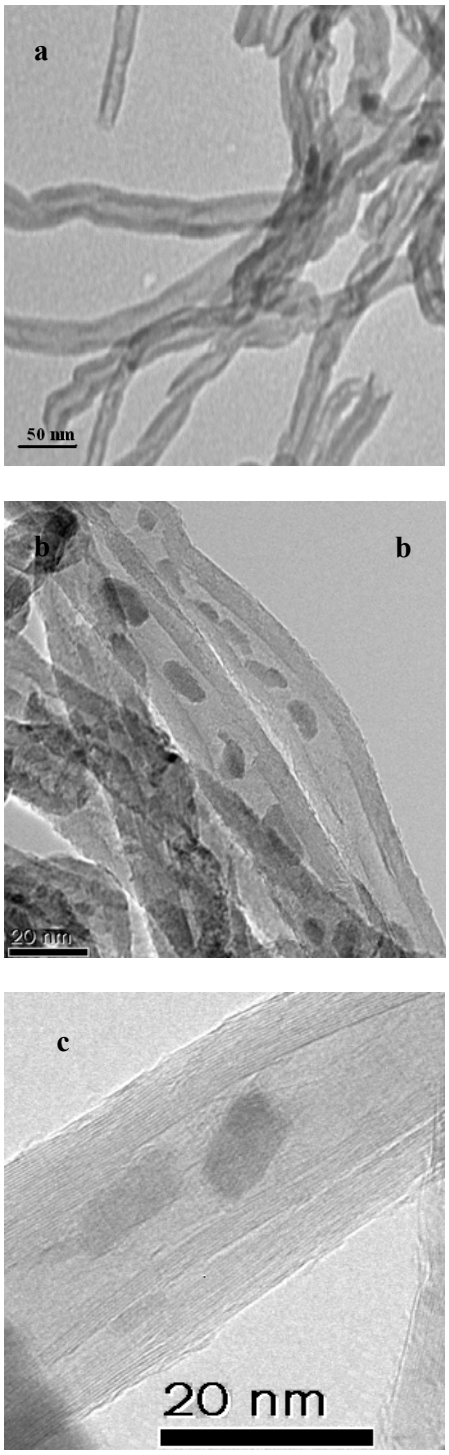

Figure 7.1 TEM micrographs of the acid-treated and K- and Cu- promoted iron catalysts supported on CNTs a) acid treated CNT sample b) 1Cu-1K-30CNT c) high resolution micrograph of 1K-30Fe/CNT showing graphite layers and crystalline structure of iron oxide particle inside the nanotubes' pores.

procedure. The diluted catalyst (1 g catalyst and 7 g silicon carbide) was placed in the reactor. Then, pure hydrogen was introduced at a flow rate of 30 ml/min. The reactor temperature was increased from room temperature to 380^{o}C at a rate of 1^{o}C/min and the reactor was maintained at this activation condition for 14 h. After the activation period, the temperature was reduced to 270^{o}C under flowing hydrogen. The hydrogen and syngas flow rates were controlled by two mass flow controllers (Brooks 5850). Argon was used as an internal standard gas in the reactor feed. The mixed gases (45% CO, 45% H_2, 10% Ar) entered through the top of the fixed bed reactor. The temperature of the reactor was controlled using a PID temperature controller. Synthesis gas with a space velocity of 3600 ml(STP)/(h.g-cat) was introduced into the reactor while the reactor pressure was set to 2 MPa. Reaction products were continuously removed after passing through two traps. The pressure of the uncondensed gaseous product stream was reduced to atmospheric pressure. The composition of the outlet gas stream was measured using an on-line GC-2014 Shimadzu gas chromatograph. The contents of the liquid traps were removed every 24 h. Hydrocarbon and water fractions were separated, and analyzed by a Varian 3400 gas chromatograph. Catalytic activity, product selectivity and stability of the catalyst were monitored during reaction period of 125 hours.

7.3 Results and Discussions

7.3.1 Characterization of Catalysts

Transmission electron micrographs (TEM) of the acid-treated CNT sample and K- and Cu-promoted iron catalysts are shown in Figure 7.1. As can be seen in the representative micrograph of acid treated CNT sample (Figure 7.1a), the nanotubes have uniform diameters and their inner and outer diameters vary between 8-12 nm and 20-25

nm, respectively. TEM analysis also indicates that a vast majority (more than 70%) of the acid treated nanotubes have open caps. Figures 7.1b and 7.1c show representative TEM images of 1Cu-1K-30Fe/CNT and 2K-30Fe/CNT catalysts. Dark spots represent the iron oxide particles which are attached inside or outside of the nanotubes. For all of the catalysts, a vast majority of the iron particles (80%) are distributed on the inner surface of pores of CNTs. This can be attributed to the carbon nanotubes' tubular structure, which can induce capillary forces during the impregnation process. Figure 7.1c also shows the graphite layers (12-18 layers) of nanotubes and crystalline structure of iron oxide particles.

Table 7.1 shows the results of nitrogen adsorption analyses on the CNT sample, unpromoted and Cu- and K-promoted catalysts. According to the N_2 adsorption analysis, loading 30% Fe decreased the surface area from 220 to 140 m^2/g and pore volume from 0.58 to 0.42 ml/g, respectively. Increase in density of CNTs due to iron loading and pore blockage can result in lower surface areas of the loaded catalysts. Promotion of Cu and K did not have noticeable effects on the surface area of the catalysts.

In order to study the structure, oxidation state and metal oxide particle size, XRD analyses were conducted on all of the catalysts studied. The diffraction peaks matched very well with the standard Hematite (Fe_2O_3) phase for fresh catalysts. In addition, the representative peaks (at 2θ angles of 26 and 44^o) for the graphene layers of multi-walled

Table 7.1 Surface properties of unpromoted and K and Cu promoted iron catalysts supported on CNTs.

Catalyst Name	BET Surface Area (m^2/g)	Total Pore Volume (ml/g)	Particle Size (nm)-XRD	Particle Size (nm)-TEM
CNT-support	220	0.58	-	-
30Fe/CNT	140	0.42	15 ± 2	8-17
1K-30Fe/CNT	141	0.39	14 ± 1	6-15
2K-30Fe/CNT	142	0.38	13 ± 2	6-15
0.5Cu-1K-30Fe/CNT	139	0.42	12 ± 1	7-16
1Cu-1K-30Fe/CNT	136	0.40	12 ± 1	7-17

nanotubes were present. Crystallite phase of K and Cu species did not appear in the XRD spectra of the promoted catalysts. This may be attributed to the small amount of these components and their high dispersion.

Table 7.1 shows the average iron oxide particle sizes on the catalysts estimated from XRD peak broadening. According to Scherrer's equation at the most intense peak of 35.7^{o}, the average particle size for fresh 30Fe/CNT catalyst is 15 nm. Addition of K and Cu to the iron 30Fe /CNT catalyst did not result in noticeable change in the average particle sizes. To compare the particle sizes estimated based on XRD with TEM analysis, the size distribution of the particles is also shown in Table 7.1. There is a good agreement between the data for average particle size calculated from XRD and TEM analyses.

The reducibility of the unpromoted and K and Cu promoted catalysts were studied using TPR analyses. The reduction patterns of the catalysts are shown in Figure 7.2. Three peaks (A, B, and C) can be identified on the TPR profile of the catalysts. Generally, the reduction of iron oxides takes place according to the following scheme:

$Fe_2O_3 \rightarrow Fe_3O_4 \rightarrow FeO \rightarrow Fe$

It has been reported that the reduction of Fe_3O_4 to metallic Fe by H2 can be accomplished in one step, and a broad peak has been observed between 377 and 750 °C over precipitated-iron catalysts [11]. According to the TPR pattern of the unpromoted and promoted catalysts, (Figure 7.2), the first peak (A) can be assigned to the reduction of Fe_2O_3 to Fe_3O_4. Peak B, observed at 600-700°C, can be related to the reduction of Fe_3O_4 to metallic Fe. Peak C can be attributed to gasification of CNTs at a temperature higher than 600^{o}C. The effects of K and Cu additions on the reduction temperature can also be seen in Figure 7.2. Promotion of the iron catalysts with Cu resulted in significant decrease in reduction temperature. In other words, while the reduction temperature for

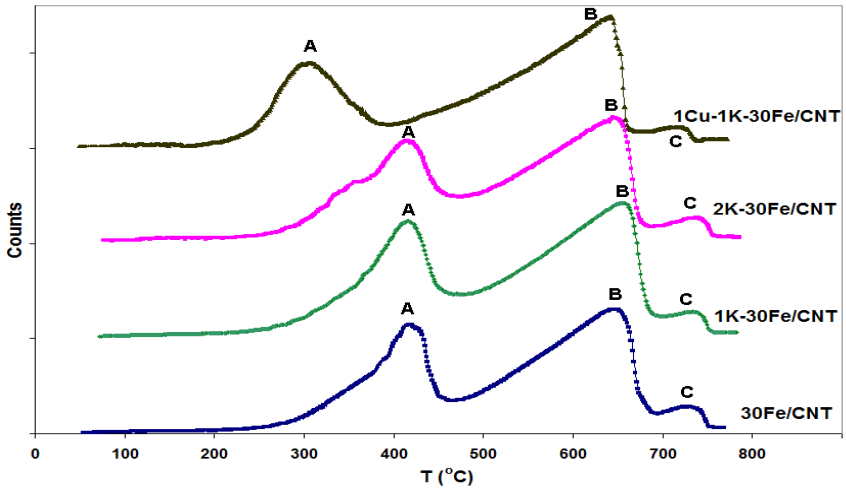

Figure 7.2 Reduction profile from room temperature to 800°C for the unpromoted and K and Cu promoted iron catalysts supported on CNTs.

the first peak for unpromoted catalyst is 421°C, addition of 1 wt% copper decreased the reduction temperature to 304°C. This indicates that copper promotion reduces the temperature at which first reduction step occurs. Lower reduction temperatures can lead to higher extent of reduction. Extent of reduction of the catalyst metal was quantified using amount of H_2 consumed in the TPR process between 25 and 700°C. The thermal conductivity detector (TCD) was calibrated by reducing pure Ag_2O. The corresponding results for the unpromoted and promoted iron catalysts are summarized in Table 7.2. The extent of reduction (from 25 to 800°C) for unpromoted iron catalyst and K-promoted iron catalysts were similar (66-69%).

Table 7.2 Reduction temperature and extent of reduction determined by Temperature Programmed Reduction (TPR) over the unpromoted and K and Cu promoted iron catalysts.

Catalyst Name	Peak A (°C)	Peak B (°C)	Extent of Reduction % (from 25 to 800°C)	Extent of Reduction % (from 25 to 400°C for 5 hr)
30Fe/CNT	421	650	66	50
1K-30Fe/CNT	419	655	72	57
2K-30Fe/CNT	418	652	70	51
0.5Cu-1K-30Fe/CNT	341	643	80	70
1Cu-1K-30Fe/CNT	304	642	84	73

However, addition of 0.5 and 1 wt% Cu resulted in considerable increase in extent of reduction to over 80%. Similar trend was observed for isothermal reduction (400^{o}C for 5 h) for the unpromoted and K and Cu-promoted catalysts. For example, while the extent of reduction for 1K-30Fe/CNT was 57%, addition of 0.5 wt% Cu increased extent of reduction of iron oxide to 70%.

Reduction of metal oxides by hydrogen to the zero valence state in the presence of promoters can be described by a nucleation model [12]. In the nucleation model, metal nuclei accelerate the reduction process as previously formed nuclei grow and new nuclei are formed [12]. Since the reduction temperature of copper(II) oxide is ~150-200 °C, copper oxide will reduce to the metallic state first and it will form sites of nucleation that accelerate the reduction of iron oxide [6]. As can be seen in Figure 7.2 and Table 7.2, addition of K promoter does not influence iron oxides reduction.

7.4 Fischer-Tropsch Synthesis

The activity and selectivity of um-promoted and promoted catalysts were measured in a fixed-bed reactor at a constant GHSV of 3.6 Sl/g-cat/h, 270 K and 2 MPa. CO hydrogenation (blank runs with no iron) was performed on the acid-treated CNT supports under the same operating conditions as the metal-loaded samples. The main product formed at a very low conversion (1%) was methane with almost no higher hydrocarbons.

Figure 7.3 shows the results of CO conversion in the reaction period of 125 h. The unpromoted iron catalyst (30Fe/CNT) showed lowest FT activity along with gradual increase (from 41 to 45%) in CO conversion within the reaction period. The gradual increase in CO conversion may be attributed to slow carbide formation due to presence of Mo [14]. It should be noted that all the catalysts are doped with 0.5 wt% Mo. Among

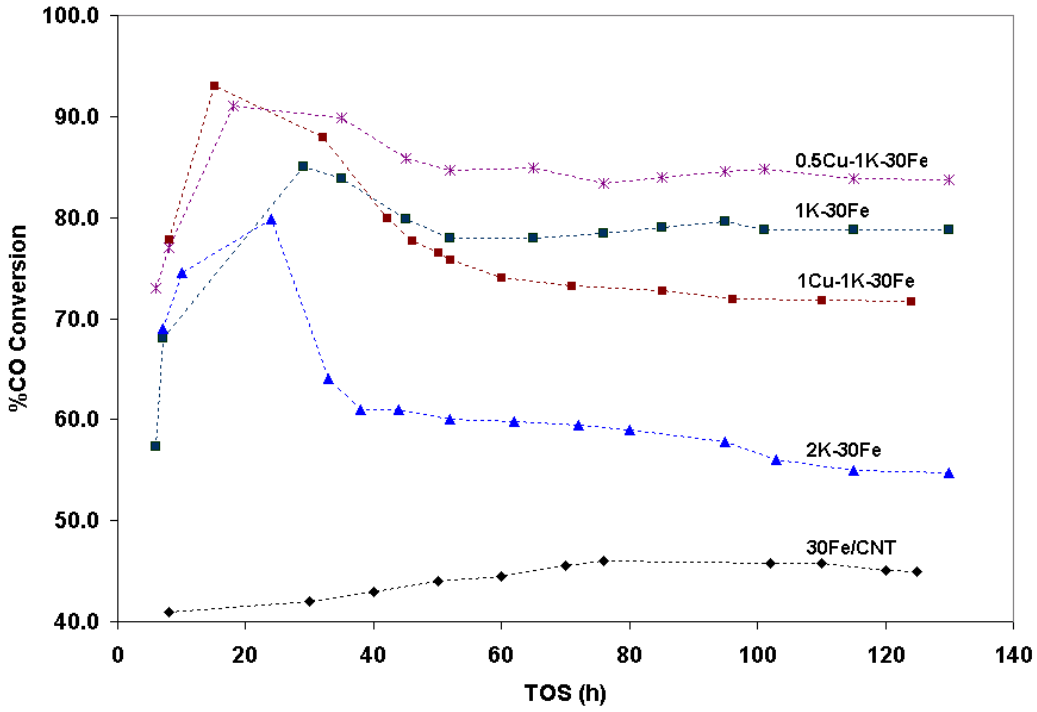

Figure 7.3 Change in %CO conversion with time on stream for unpromoted and K and Cu promoted iron catalysts (operating conditions: 3.6 Sl/g-cat/h, P = 2 Mpa, T = 270^{o}C of 125 h)

the promoted catalysts, 1K-30Fe/CNT catalyst reached to a high CO conversion of 85% after 30 h, experienced 8% decline in FT activity that remained stable until end of reaction period. Increase in catalytic activity in the presence of potassium is related to the ability of K to strengthen the metal-carbon bond and weaken the carbon-oxygen bond. The latter assists in removal of oxygen by hydrogen, which is a fundamental step in FTS. In addition, potassium can facilitate the formation of Fe carbides that are known as active phase species for FT reactions [6].

The catalyst with 2 wt% of potassium (2K-30Fe/CNT) achieved the highest activity of 80%, followed by a sharp decease of 25% in activity in a period of 35 h. Addition of a higher concentration of K (2K-30Fe/CNT) resulted in a decrease in activity compared to the promoted catalyst with a lower amount of K. At higher

promoter concentrations, the active sites may be covered by potassium, resulting in a decline of the catalyst activity. Furthermore, an increase in potassium fosters carbon deposition, which blocks the active surface area, leading to catalyst deactivation [13]. The sudden decrease in CO conversion could be attributed to rapid coke formation on top of active metal sites or formation of heavy wax inside the nanotubes pores.

Addition of 0.5 and 1 wt% Cu on the 1K-30Fe/CNT catalyst increased the initial CO conversion to 90% and 93%, respectively. However, 1Cu-1K-30Fe/CNT catalyst also experienced a gradual deactivation in the course of 125h. The observed increase in activity with addition of copper is in agreement with other reported results [6, 13]. As shown in the previous section (Section 7.3.1), addition of Cu facilitates reduction of iron. Reduced iron oxides can be converted to iron carbides. Iron carbides are believed to be the active site for FT reactions. The copper-promoted catalysts reached their initial and maximum activity (within 15-18 h) faster than the one with only potassium (within 24-28 h). This is due to higher extent of reduction of Cu promoted catalysts.

Table 7.3 shows the catalytic activity and product selectivity of promoted and um-promoted iron catalysts supported on CNTs after time on stream (TOS) of 125 h. The unpromoted catalyst (30Fe/CNT) exhibited highest selectivity toward methane (16%) and light hydrocarbons ($\alpha = 0.7$) compared to the potassium promoted catalysts ($\alpha > 0.8$).

Table 7.3 CO conversion and product selectivity of unpromoted and K and Cu promoted iron catalysts after TOS of 125 hours (3.6 Sl/g-cat/h, $P = 2$ Mpa, $T = 270^{o}$C).

Activity and Product selectivity	30Fe/CNT	1K-30Fe/CNT	2K-30Fe/CNT	0.5Cu-1K-30Fe/CNT	1Cu-1K-30Fe/CNT
CO %	44	77	54	84	70
CH_4	16	5	3	4	6
C_2-C_4	31	19	15	18	22
C_5-C_{11}	45	47	36	45	47
C12+	8	29	46	33	25
CO_2 (C %)	38	42	44	41	43
α	0.70	0.80	0.86	0.82	0.79

Promotion of catalyst with 1 wt% of K resulted in a significant shift in selectivity toward higher hydrocarbons (C_{12}+ selectivity of 29% and $\alpha = 0.8$) and lower methane production (5%). The increase in average molecular weight of hydrocarbon products is due to the increased CO and lower H_2 surface coverage in the presence of potassium. Since, chain terminations result from hydrogenation of the iron-carbon bonds, the presence of potassium enhances the probability of continued chain growth, i.e., formation of higher molecular weight products [6]. According to Table 7.3, K promotion increases water gas shift activity as well.

Addition of higher concentration of K (2K-30Fe/CNT) resulted in slight decrease in CH_4 formation (4%) and increase in C_{12}+ selectivity (46 %). In the presence of potassium, the CO chemisorption is enhanced whereas that of H_2 is suppressed. This results in a lower surface concentration of H_2 and consequently in a lower hydrogenation activity of potassium-promoted catalysts. According to Table 7.3, addition of Cu (0.5 and 1 wt%) to potassium promoted catalyst (0.5Cu-1K-30Fe/CNT and 1Cu-1K-30Fe/CNT) resulted in slight increase in methane selectivity and decrease in heavy hydrocarbon selectivity.

Considering the stability, activity and product selectivity of promoted and unpromoted catalysts, the potassium promoted catalyst with low promoter contents (0.5Cu-1K-30Fe/CNT) can be selected as the most effective catalyst among the catalyst studied for Fischer-Tropsch reactions.

A comparison of activity and selectivity of the most effective catalysts from this work with a number of comparable iron catalysts for FT reactions is given in Table 7.4. Some of data from the literature were calculated based on the information provided in the references for easier comparison. Considering effects of operating conditions on FT reactions, the 0.5Cu-1K-30Fe/CNT catalyst exhibited lowest CH_4 and CO_2 selectivity

Table 7.4 Comparison of performances of unsupported and supported Fe catalysts on various materials.

Ref	Support	*T* (^oC)	*P* (MPa)	H_2/CO	GHSV[1] Sl/g/h (h^{-1})	Activity[1] mg HC/g-Fe/h	%CO mol%	CH_4	C_5+	CO_2	O/P
[a]	CNT	250	2.04	1	3.6 (2600)	0.8	42	3	82	38	4
[a]	CNT	285	2.72	1	10.8 (7800)	5.6	95	6	76	44	3.6
[a]	CNT	270	2.24	2	5.4 (3900)	2	94	11	61	34	2.1
[14]	AC	320	2.04	0.9	3	3.1	84	15	39.4	46	2.2
[15]	CNT	275	0.79	2	(2120)	-	80	14.6	43	-	0.11
[16]	CNT	275	0.79	2	(2142)	-	60	19.3	38.3	-	0.33
[17]	Zr-Ti	270	2.04	1	(1000)	0.97	18.4	15.7	49.8	-	-
[6]	Si	230	1.36	0.6	3.1	0.22	35	3.8	81	42	2.8
[13]	-	250	1.48	1	2	-	83	11.9	54	47.6	2.66

[a]: 0.5 Cu-1K-30Fe/CNT from the present report
1: Numbers in Italic are calculated (for easier comparison) based on the data provided in the corresponding report.

and highest C_5+ selectivity compared to other catalysts given in Table 7.4. In addition, the 0.5Mo-1K-30Fe/CNT catalyst showed very high activity for hydrocarbon production. For example, 0.5Mo-1K-30Fe/CNT catalyst can convert syngas with GHSV of 10.8 Sl/g.cat.h with CO conversion of 95% and catalytic activity of 5.6 g-HC/g-Fe/h. To the best of the auther knowledge, such a high level of activity for a FT catalyst is not reported in the open literature. As far as the commercial viability of iron-based FT catalysts is concerned, a great deal of emphasis has been put on ability of the catalyst to produce 1-alkenes for use in chemical industry. In this thesis, the ratio of olefins to paraffins (O/P ratio) is defined as the ratio of olefinic light gaseous products (C_2-C_4) to paraffinic gaseous products (C_2-C_4). As can be seen in Table 7.4, the product selectivity of 0.5Cu-1K-30Fe/CNT catalyst toward olefins is higher than those reported in literature. In terms of stability, the 0.5Mo-1K-30Fe/CNT catalyst experienced minor deactivation of 4 % in CO conversion from initial stabilaization (40 h) to 450 h.

7.5 Kinetics of FTS Reactions

As discussed in the previous section, the most effective catalyst in this work (0.5Cu-1K-30Fe/CNT) showed excellent catalytic activity and selectivity for FT

reactions. This kinetic study was aimed to (1) identify an appropriate combination of mechanistic-based rate equations for the simultaneous Fischer-Tropsch and water-gas-shift reactions, (2) calculate the reaction rate constants for the most suitable combination of reaction rates which can be used for reactor modeling, and (3) compare the activity of the catalyst with commercial catalysts and other reported iron catalysts in the literature. In order to study the kinetics of FT reactions using K and Cu promoted iron catalyst supported on CNTs, an integral reactor model was used. Isothermal conditions for the fixed-bed reactor were achieved by addition of silicon carbide as filler to the catalyst bed. To eliminate interphase and intraparticle mass transport limitations, a small catalyst size of 60 mesh was used. Using Weisz-Prater and Mears criteria [18], the effects of interphase and intraparticle mass transport resistances were examined and it was found that both transport effects could be neglected. The calculations corresponding to internal and external mass transfer effects are given in Appendix F.

The FT and WGS reactions can be written as follows:

(FT reaction) $nCO + (n + m/2)H_2 \rightarrow C_nH_m + nH_2O$ (7.1)

(Water-gas-shift reaction) $CO + H_2O \leftrightarrow CO_2 + H_2$ (7.2)

where n is the average carbon chain length of the hydrocarbon products and m is the average number of hydrogen atoms per hydrocarbon molecule. The equations describing the reactor model consist of a mass balance for each particular component that may be written as follows,

$$\frac{dF_i}{dz} = r_i \,.\rho_B.A_r \qquad (7.3)$$

with F_i molar flow rate (mol/h) of component *i* (CO, H_2, CO_2, H_2O and C_nH_m), *z* reactor length (cm), *ri* overall reaction rate for each component (mol/g-cat/h), ρ_B catalyst bed density (g-cat/ml), and A_r the cross-sectional surface area of the reactor (cm^2).

Table 7.5 Fischer-Tropsch and water-gas-shift reaction rate models developed in the literature.

FT Model Number	FT Model	WGS Model Number	WGS Model
FT1	$r_{FT} = k_1.P_{H2}$	W1	$r_{WGS} = k_W.P_{CO}$
FT2	$r_{FT} = \frac{k_{FT}.P_{CO}.P_{H2}}{P_{CO} + a.P_{CO2} + b.P_{H20}}$	W2	$r_{WGS} = k_W(P_{CO}.P_{H2O} - P_{CO2}.P_{H2}/K_w)$
FT3	$r_{FT} = \frac{k_{FT}.P_{CO}.P_{H2}^2}{P_{CO}.P_{H2} + a.P_{H2O}}$	W3	$r_{WGS} = \frac{k_W(P_{CO}.P_{H2O} - P_{CO2}.P_{H2}/K_w)}{P_{CO} + c.P_{H2O} + d.P_{CO2}}$
FT4	$r_{FT} = \frac{k_{FT}.P_{CO}.P_{H2}}{P_{CO} + a.P_{CO2}}$	W4	$r_{WGS} = \frac{k_W(P_{CO}.P_{H2O} - P_{CO2}.P_{H2}/K_w)}{(P_{CO} + c.P_{H2O})^2}$
FT5	$r_{FT} = \frac{k_{FT}.P_{CO}.P_{H2}}{(1 + b.P_{CO})^2}$	W5	$r_{WGS} = \frac{k_W(P_{CO}.P_{H2O} - P_{CO2}.P_{H2}/K_w)}{P_{H2}.P_{CO} + c.P_{H2O}}$
FT6	$r_{FT} = \frac{k_{FT}.P_{CO}.P_{H2}^{0.5}}{(1 + a.P_{H_20} + b.P_{CO})^2}$	W6	$r_{WGS} = \frac{k_W(P_{CO}.P_{H2O} - P_{CO2}.P_{H2}^{0.5}/K_w)}{(1 + c.P_{H2O}/P_{H2}^{0.5})^2}$
FT7	$r_{FT} = \frac{k_{FT}.P_{CO}.P_{H2}}{(1 + a.P_{H20} + b.P_{CO})^2}$	W7	$r_{WGS} = \frac{k_W(P_{CO}.P_{H2O} - P_{CO2}.P_{H2}/K_w)}{(1 + c.P_{H2O}/P_{H2}^{0.5} + d.P_{H2O})^2}$
FT8	$r_{FT} = \frac{k_{FT}.P_{CO}.P_{H2}}{(1 + a.P_{H20} + b.P_{CO})}$		

The overall reaction rate for each component (H_2, CO, CO_2, H_2O, and C_nH_m) consisted of the sum of the reaction rates of each chemical reaction (Eqs. 7.1 and 7.2) with the relevant stoichiometric coefficient. For example, $r_{co} = r_{FT} + r_{WGS}$ in which r_{co} is the total rate of consumption of carbon monoxide and r_{FT} and r_{WGS} are the reaction rates of the reactions given by Eqs. 7.1 and 7.2, respectively.

Intrinsic reaction rate equations for the Fischer-Tropsch reaction based on the Langmuir-Hinshelwood-Hougen-Watson (LHHW) and Eley-Rideal (ER) adsorption theories have been developed and used for cobalt- and iron-based catalysts [2,19-26]. The main mechanisms for FT reactions over iron catalysts are the carbide, enolic, and direct insertion theories [2, 21, 25].

Table 7.5 shows a list of ER and LHHW types FT rate expressions that have been proposed for the iron-based FT synthesis [19-24]. Model FT1 is the simple and first order reaction in hydrogen. It has been reported that Equation FT1 is suitable at low CO conversions. Equations FT2, FT3, FT4 and FT 8 are based on Eley-Rideal model with their characteristic of first order denominators. Equation FT2 is a general kinetic model, which considers inhibition by both water and CO_2 with full coverage of catalytic site with CO, H_2O and CO_2. Equation FT3 is consistent with the carbide theory in which CO dissociates on the surface. Adsorbed carbon reacts with hydrogen in the rate-determining step. In the case of Model FT3, hydrogen is incorporated into the inhibition term which implies that the reaction order of hydrogen becomes larger than one, eventually approaching a value of two, as the syngas conversion increases. FT4 only accounts for the CO_2 inhabitation. Equations FT5, FT6 and FT7 are based on the LHHW adsorption model with second order inhibition terms. For these models the effect of vacant sites is also taken into account.

Several mechanisms for the water-gas-shift reaction using single water-gas-shift catalysts and in the presence of FT reactions are proposed in the literature [2]. The two most common mechanisms are formate and direct oxidation mechanisms [23]. In the case of the formate mechanism, the formate species can be formed by the reaction between a carbon monoxide in the gas phase or in the adsorbed state with a hydroxy species or water. Water can provide the hydroxyl intermediate. Finally, the formate intermediate is reduced to adsorbed or gaseous carbon dioxide.

In the case of the direct oxidation mechanism, adsorbed or gas-phase CO is oxidized to CO_2. The oxygen intermediate can be formed from the dissociation of water or CO. A list of rate expressions for water-gas-shift reaction is given in Table 7.5.

It has been reported that for the WGS reaction, a first-order rate in CO (Equation WGS1) is satisfactory. The major drawback of Equation WGS1 is the fact that it does not account for the reversibility of the WGS reaction [19]. This means that it is only applicable when the reaction is far from equilibrium. Equations WGS2-WGS7 are based on the LHHW adsorption model accounting for reversibility of WGS reactions. These rate expressions can be used for catalysts with low WGS activity, where water concentrations are high, as well as for catalysts with high shift activity showing inhibition by CO_2. For the water-gas-shift reaction, a general form of reaction rate was also proposed as follows

$$r_{FT} = \frac{k_W.(P_{CO}.P_{H2O} - P_{CO2}.P_{H2} / K_{we})}{P_{CO} + cP_{H2O} + dP_{CO2}} \qquad (7.4)$$

Here, K_{we} is the equilibrium constant and a known function of temperature as follows[19]:

$$K_{we} = \exp(\frac{4578}{T} - 4.33) \qquad (7.5)$$

The reactor model was solved using the forward Euler method. A multiple nonlinear regression (Gauss-Newton) method (Optimization Toolbox: lsqnonlin Matlab function)

was applied to obtain the values of unknown parameters (k) for the reaction rate equations. The Matlab code is given in Appendix G. Using this nonlinear least squares regression procedure, the difference between calculated molar flow rate of all reactants and products (CO, H_2, CO_2, H_2O and C_nH_m) with experimental flow rates in the exit of reactor were minimized. Confidence limits on the estimated model parameters were calculated at 95%. The unknown parameter estimates were constrained to be greater than or equal to zero in all cases. As a measure of quality of the kinetic predictions of rate equations, the relative variances of the kinetic models were calculated as follows:

Table 7.6 Operating conditions and corresponding CO conversion and CO_2 selectivity

GHSV Sl/g-cat/h	T (^{o}C)	P (MPa)	H_2 / CO	%CO Conversion	CO_2
14.4	275	1.02	2	49	40
10.8	275	2.04	1	74	42
7.2	275	1.02	1	68	44
7.2	275	2.04	1	86	42
12.0	275	3.40	1	81	42
10.8	275	2.04	2	83	35
12.0	255	3.40	1	36	39
21.6	285	2.72	1	60	42
7.2	275	1.02	2	71	39
5.4	275	2.04	1	85	43
3.6	275	1.02	1	84	44
3.6	275	2.04	1	97	43
14.4	275	1.02	1.5	43	40
10.8	275	2.04	1.5	81	37

$$S_{rel} = \left(\sum_{i=1}^{N} \left(\frac{F_i^{\exp} - F_i^{calc}}{F_i^{\exp}} \right)^2 . \frac{1}{N - M} \right)^{1/2} \times 100 \qquad (7.6)$$

where F^{exp} and F^{calc} are experimental and calculated values for molar flow rates at the exit of the reactor. N is the number of experimental data and M is the number of unknown parameters.

The rate measurements were conducted using 0.5Cu-1k-30Fe/CNT catalyst in a fixed-bed reactor. The experimental data were obtained by varying temperature (255, 275 and 285^{o}C), total pressure (1-6 MPa), GHSV (3.6-21.6 Sl/g-cat/h) and CO/H_2 molar ratio (1, 1.5 and 2). Experimental results at different operating conditions consisting of carbon monoxide conversions and the carbon dioxide concentration in product stream are given in Table 7.6. These data were used for the regression analysis.

In order to determine the most suitable reaction expression and mechanism, combinations of the Fischer-Tropsch and water-gas-shift reaction rates given in Tables 7.5 were sequentially evaluated. This included 56 trials of different combination of eight

Table 7.7 Selected results of goodness-of-fit in the form of relative variance using nonlinear regression calculations for different combination of FT and WGS reaction models

FT model	WGS model	S_{rel} molar flow rates
FT1	W2	44.1
FT2	W3	19.8
FT2	W7	14.2
FT3	W5	19.1
FT4	W5	31.8
FT5	W7	30.5
FT6	W6	18.3
FT7	W6	16.0
FT7	W7	6.5
FT8	W6	17.1
FT8	W7	11.3

FT rate and seven WGS rate expressions. For each combination, the S_{rel} values corresponding to molar flow rates of reactants and products were calculated. In order to adjust the parameters, several initial values were tested. With these initial values, similar final results were achieved. Selected combinations of FT and WGS models and corresponding S_{rel} are given in Table 7.6. As can be seen in Table 7.7, the lowest S_{rel} and the best data fit belong to FT7 and W7 combination. FT7 is derived from the combined enol/carbide mechanism in which the rate-determining step is the dual site surface reaction between adsorbed formyl and dissociated H_2. Derivation of this equation is given in Appendix H. FT7 was reported to be the best expression by Yates and Satterfield [27] in a slurry reactor. The results of the nonlinear regression and reaction rate constants for Equations FT7 are given in Table 7.8.

According to the data in Table 7.7, Equation W7 explains the experimental data with the least S_{rel} among the other rate expressions given in this study. For W7, the terms in the denominator account for the effects of vacant sites, site occupation by adsorbed molecular water, and site occupation by hydroxyl groups, respectively. Since there is no

Table 7.8 FT and WGS kinetic parameter estimates at 270°C.

FT model	WGS model	k_{FT} mol/g-cat.h.MPa	a	b	k_{WGS} mol/g-cat.h.MPa	c	d
FT7	W7	0.603	7.439	0.01	26.334	22.110	11.627
FT2	W3	0.111	2.850	0	3.621	17.337	0

Table 7.9 Apparent rate constants (first order reaction) for 0.5Cu-1K-30Fe/CNT, precipitated and commercial iron catalysts at 265°C.

FT model	k_{FT}	100 Fe/0.3 Cu/O.2 K [19]	Commercial Catalyst (Ruhrchemie) [19]	0.5Cu-1K-30Fe/CNT [this thesis]
$r_{FT} = k_{FT}.P_{H2}$	mol/g-cat.h.MPa (catalyst base)	0.065	0.040	0.074
	mol/g-Fe.h.MPa (iron base)	0.066	0.054	0.245

CO term in the denominator, it can be concluded that the effect of adsorption of CO over the active catalytic site for water-gas-shift reaction is not significant.

In order to evaluate CO_2 and H_2O inhabitation over iron catalysts supported on CNTs, the reaction rate constants for FT2 and W3 were calculated by the nonlinear regression method. These rate expressions account for CO_2 adsorption on catalytic sites for FT and WGS reactions. As can be seen in Table 7.8, since the coefficients for CO_2 at the denominator are zero, thus for FT and WGS reaction rates, the CO_2 inhabitation can be neglected. In addition, comparing the results of relative variances for the FT7 and FT5 reactions shows that the water effect on the FT reaction should be included (in the denominator) in the reaction models.

Using first-order models (FT1 and W1) for FT and WGS reactions with Arrhenius-type equations, activation energies were evaluated over a range of temperatures (250-285°C). The activation energy of 78.6 kJ/mol for the Fischer-Tropsch reaction is close but lower than values reported by other researchers [19].

In order to compare the activity of 0.5Cu-1K-30Fe/CNT catalyst with precipitated and commercial catalysts, a first-order kinetic equation form (in hydrogen) was used. Using the first-order kinetics, any inhibition effects are lumped into the first-order rate constant. These inhibition effects will be reflected both in the numerical values of the rate constant and their corresponding activation energies. The results of comparison of performance of our catalyst with a precipitated catalyst and a commercial catalyst (Ruhrchemie) are given in Table 7.9. Based on the apparent rate constants (catalyst weight base), the activity of iron catalyst supported on CNTs is higher than that of precipitated and commercial catalyst at the same temperature [19]. It should be noted that iron loadings on the precipitated and commercial catalysts were 100 wt% and 74 wt%, respectively, while the iron loading on CNT supported catalyst is 30%. Considering the iron loadings, the apparent rate constant for 0.5Cu-1K-30Fe/CNT catalyst is about 4.5 times higher than commercial catalyst under the same operating conditions.

7.6 Conclusions

Promotion of iron catalyst supported on CNTs with potassium increases the activity of FT and water-gas-shift reactions and the average molecular weight of the product hydrocarbons. Addition of copper increases the extent of reduction for hydrogen activation. Excess amount of both K and Cu can result in low FT activity. Among the potassium and copper promoted iron catalysts supported on CNTs, the catalyst with 1 wt% of K and 0.5 wt% of Cu was the most stable and active catalyst in this study. Kinetic studies on the most efficient catalyst (0.5Cu-1K-30Fe/CNT) showed that CO_2 inhibition can be neglected for both FT and water-gas-shift reactions. However, water effects should be considered for FT reactions. In addition, the kinetic model with

presence of vacant catalyst site fitted the experimental results better than full site converge models. First order reaction model verified that the iron catalyst supported on CNTs is more active than precipitated and commercial catalysts.

Abbreviations

BET	Brunauer, Emmett, and Teller
CNT	Carbon Nanotubes
FTS	Fischer-Tropsch Synthesis
Sl	Standard Litter
TEM	Transition Electron Microscopy
TOS	Time on Stream
TPR	Temperature Programmed Reduction
WGS	Water-Gas-Shift
XRD	X-ray Diffraction
30Fe/CNT	Iron catalysts deposited on CNTs with 30% iron loading
xCu-yK-30Fe/CNT	promoted Iron catalysts with x% of copper and y% of potassium loadings

Nomenclature

a, b, c, d	temperature-dependent adsorption coefficients
A_r	cross-sectional surface area of the reactor (cm^2)
F_i	molar flow rate of reactants and products (mol/h)
F^{calc}	predicted data (flow rate)
F^{exp}	experimental data (flow rate)
i	component i (CO, H_2, CO_2, H_2O and C_nH_m),
k_{FT}	Fischer-Tropsch reaction rate constant (Table 7.7and 9),

	mol/gcat/h/MPa
k_W	water-gas shift reaction rate constant (Table 7.5, 7.8and 7.9), mol/g-cat/h/MPa
K_{WE}	water-gas shift reaction equilibrium constant
n	average carbon chain length of hydrocarbon
m	average hydrogen number in hydrocarbons (products)
N	total number of experimental data
M	total number of unknown parameters
P_i	partial pressure of components i (MPa)
r_{CO}	reaction rate for the formation of carbon monoxide (mol/g-cat/h)
r_{FT}	reaction rate of the Fischer-Tropsch reaction (mol/g-cat/h)
r_i	overall reaction rate for each component (mol/g-cat/h),
r_{WGS}	reaction rate of the water-gas-shift reaction (mol/g-cat/h)
S_{rel}	relative variance
T	Temperature (^oC)
z	reactor length (cm),
ρ_B	catalyst bed density (g-cat/ml)
$\%CO$	percent of CO conversion (mol%)

References

[1] M. E. Dry, Fischer-Tropsch reactions and the environment, Applied Catalysis A: General, 189 (1999) 185-190.

[2] G.P. van der Laan, A.A.C.M. Beenackers, Selectivity of the Fischer-Tropsch Synthesis: A Literature Review, Catalysis Reviews, 41 (1999) 255-318.

[3] M.J.A. Tijmensen, A.P.C. Faaij, C.N. Hamelinck, M.R.M van Hardeveld, Exploration of the possibilities for production of Fischer Tropsch liquids and power via biomass gasification, Biomass and Bioenergy, 23 (2002) 129-152.

[4] C.H. Bartholomew, Recent technological developments in Fischer-Tropsch catalysis, Catalysis Letter, 7 (1990) 303-316.

[5] J. Zhang, J. Chen, J. Ren, Y. Li, Y. Sun, Support effect of Co/Al_2O_3 catalysts for Fischer-Tropsch synthesis, Fuel, 82 (2003) 581-586.

[6] R. J. O'Brien, L. Xu, R. L. Spicer, S. Bao, D. R. Milburn, B. H. Davis, Activity and selectivity of precipitated iron Fischer-Tropsch catalysts, Catalysis Today, 36 (1997) 325-334.

[7] Y. Yang, H. Xiang, Y. Xu, L. Bai, Y.Li, Effect of potassium promoter on precipitated iron-manganese catalyst for Fischer-Tropsch synthesis, Applied Catalysis A: General, 266 (2004) 181-194.

[8] P. Serp, M. Corrias, P. Kalck. Carbon nanotubes and nanofibers in catalysis, Review, Applied Catalysis A: General, 253(2003) 337-358.

[9] R.M. Malek Abbaslou, A. Tavasoli and A. K. Dalai, Effect of pre-treatment on physico-chemical properties and stability of iron catalysts supported on carbon nanotubes for Fischer-Tropsch synthesis, Applied Catalysis A: General, 355(2009)33-41.

[10] R.M. Malek Abbaslou, A. Tavassoli, J. Soltan , A.K. Dalai, Iron Catalysts Supported on Carbon Nanotubes for Fischer-Tropsch Synthesis: Effect of Catalytic Site Position. Applied Catalysis A: General, 367(2009)47-52

[11] N. Lohitharn, J.G. Goodwin Jr., E. Lotero, Fe-based Fischer-Tropsch synthesis catalysts containing carbide-forming transition metal promoters, Journal of Catalysis, 255 (2008) 104-113.

[12] N.W. Hurst, S.J. Gentry and A. Jones, Temperature programmed reduction, Catalysis Reviews: Science and Engineering, 24 (1982) 233.

[13] D. B. Bukur, X. Lang, D. Mukesh, W.H. Zimmerman, M.P. Rosynek, and C. Li, Binder/support effects on the activity and selectivity of iron catalysts in the Fischer-Tropsch synthesis, Industrial Engineering Chemistry Research, 29 (1990)1588-1599.

[14] W. Ma, E.L. Kugler, J. Wright, and D.B. Dadyburjor, Mo-Fe Catalysts Supported on Activated Carbon for Synthesis of Liquid Fuels by the Fischer−Tropsch Process: Effect of Mo Addition on Reducibility, Activity, and Hydrocarbon Selectivity, Energy Fuels 20 (2006) 2299-2307.

[15] M.C. Bahome, L.L. Jewell, D. Hildebrandt, D. Glasser, N.J. Coville, Fischer-Tropsch synthesis over iron catalysts supported on carbon nanotubes, Applied Catalysis A: General, 287 (2005) 60-67.

[16] M.C. Bahome, L.L. Jewell, K. Padayachy, D. Hildebrandt, D. Glasser, A.K. Datye, N.J. Coville, Fe-Ru small particle bimetallic catalysts supported on carbon nanotubes for use in Fischer-Tropsch synthesis, Applied Catalysis A: General, 328 (2007) 243-251.

[17] P.N. Dyer, A. F. Nordquist, R. Pierantozzi (1986) Patent US 6602922.

[18] H.S. Fogler, Elements of chemical reaction engineering, second edition, Prentice Hall PTR, (1992)

[19] W.H. Zimmerman, D.B. Bukur, Binder/support effects on the activity and selectivity of iron catalysts in the Fischer-Tropsch synthesis, Canadian Journal of Chemical Engineering, 68 (1990) 194-199.

[20] M.J. Keyser, R.C. Everson, and R.L. Espinoza, Fischer−Tropsch Kinetic Studies with Cobalt-Manganese Oxide Catalysts, Industrial Engineering Chemistry Research, 39 (2000) 48-54.

[21] G.A. Huff, Jr., and C.N. Satterfleld, Kinetic design considerations in the Fischer-Tropsch synthesis on a reduced fused-magnetite catalyst, Industerial Engineering Chemistry Process Des. Dev. 23 (1984) 696-706.

[22] F.G. Botes, Water-gas-shift kinetics in the iron-based low-temperature Fischer-Tropsch synthesis, Applied Catalysis A: General, 328 (2007) 237-242.

[23] G.P. van der Laan, A.A.C.M. Beenackers, Intrinsic kinetics of the gas-solid Fischer-Tropsch and water gas shift reactions over a precipitated iron catalyst, Applied Catalysis A: General, 193 (2000) 39-53.

[24] F.G Botes, B.B. Breman, Development and Testing of a New Macro Kinetic Expression for the Iron-Based Low-Temperature Fischer-Tropsch Reaction, Industrial Engineering Chemistry Research, 45 (2006) 7415-7426.

[25] B.H. Davis, Fischer-Tropsch Synthesis: Reaction mechanisms for iron catalysts Catalysis Today, 141 (2009) 25-33.

[26] B. Sarup, B.W. Wojciechowski, Studies of the Fischer-Tropsch Synthesis on a Colbat Catalyst: Mechanistic Formulation of the Kinetics Selectivity for Higher Hydrocarbon, Canadian Journal of Chemical Engineering, 67 (1989) 620-627.

[27] I.C. Yates, C.N. Satterfield, Intrinsic kinetics of the Fischer-Tropsch synthesis on a cobalt catalyst, Energy Fuels. 5 (1991) 168-176.

Chapter 8

Conclusions and Recommendations

8.1 Summary of Thesis

The main goal of this Ph.D. thesis research was to develop a novel Fe nano-catalyst using new generation of supports, i.e. carbon nanotubes (CNTs) for FT reactions. In order to prepare iron catalysts supported on CNTs, it was necessary to study CNT synthesis in a bulk scale with the ability to control the nanotubes' structure. Among different nanotube production methods, chemical vapor deposition is the easiest method and scalable to commercial level. However, the results of numerous reports cannot efficiently be compared due to discrepancies in results coming from different operating conditions and reactor geometries. In this thesis research, the effects of precursor concentration in gas phase, which is independent from operating conditions and reactor geometry, were studied. It was shown that the CNT production yield significantly decreases beyond a specific condition due to catalyst deactivation. The deactivation resulted from encapsulation of metal particles with layers of carbon deposits. Thus, low carbon concentrations in the gas phase are favoured for production of CNTs using the CVD method.

A sectional analysis along the quartz CVD reactor indicated that the nanotubes' diameter varies along the CVD reactor. In other words, the nanotubes array is denser in the area close to the reactor entrance compared to other regions along the reactor.

Therefore, as reaction time prolongs and the nanotubes' length increases, the iron particles are deposited on top of the CNT film resulting in formation of carbon nanospheres.

In terms of catalyst development for FT reactions, stability, activity and product selectivity were the objective parameters. In order to design a new catalyst supported on CNTs, a procedure was developed. This procedure or road map starts from the improvements of support structure and active site position followed by chemical enhancements of active sites.

To modify the structure and surface of nanotubes, the effect of oxidizing acids were studied. The results showed that acid pre-treatment of nanotubes with concentrated nitric acid before metal doping can result in

1- Opening the nanotubes' caps,
2- Increasing the available surface area by giving access to the inner surface of the nanotubes,
3- Shortening the nanotubes' length,
4- Providing functional groups which can work as anchoring site for metal particles,
5- Decreasing the hydrophobic property of carbon nanotubes, and
6- Deposition of the majority of catalytic sites inside the nanotubes pores.

All of the mentioned effects lead to enhancing the activity and stability of iron catalyst for FT reactions.

One of the advantages of CNTs compared to other conventional supports is that the catalytic sites can be selectively deposited on either the exterior or inner surfaces of the nanotubes. The deposition of catalytic sites on the outer surfaces is possible with filling the inner pores with pure solvent prior to impregnation with metal salt solution.

In the case of FT reactions, confinement and deposition of metal particles inside the nanotubes' pores improved the catalytic performances of the catalysts by,

1- Decreasing the size of catalytic sites by physical restriction of nanotubes' pores,
2- Providing contact with the inner surface which can result in electron transfer from the nanotubes to the catalytic site,
3- Decreasing the reduction temperature and increasing the extent of reduction,
4- Increasing the contact time between reactants and catalytic sites, and
5- Preventing catalytic site agglomeration under FT operation conditions.

The structure of the nanotubes can be adjusted using different operating conditions and different synthesis methods. In this thesis research, it was shown that the pore size theof nanotubes can have a significant influence on the activity and selectivity of iron catalysts for FT reactions. In other words, deposition of iron species on the inner surfaces of the nanotubes with narrow-pores (12 nm) compared to wide pores (63 nm) resulted in

1- Smaller metal particles and higher dispersion,
2- Higher extent of reduction
3- Increasing the stability of catalysts during the FT reactions
4- Improving the activity of the catalysts, and
5- Enhancing the products selectivity while shifting the selectivity toward heavier hydrocarbons.

A deactivation study of iron catalyst supported on CNTs showed that one of the major reasons for the decrease in activity is sintering. Addition of molybdenum as a structural promoter can surround the iron oxide particle and prevent metal site agglomerations. Since molybdenum is active for production of light

hydrocarbons under FT operating conditions, the amount of this promoter was thus optimized.

Potassium and copper are effective promoters for iron catalysts. These promoters are able to improve the activity and selectivity of iron catalysts for Fischer-Tropsch reactions. However, the addition of excess amount of copper and potassium may result in lowering the activity of iron catalysts for FT reactions. Among the potassium- and copper-promoted iron catalysts supported on CNTs, the catalyst with 1 wt% of K and 0.5 wt% of Cu was the most stable and active catalyst in this study.

Results of kinetic studies showed that the new iron catalysts supported on CNTs exhibit higher activity compared to other precipitated and commercial iron catalysts under similar operating conditions. According to analysis of the goodness-of-fit for different models, water effects and the presence of vacant catalyst should be taken into account.

The results of the present Ph.D. thesis research provide a map for designing catalysts using carbon nanotubes as a support. In order to develop a CNT-supported catalysts, one should consider the following:

5- If the interaction of the metal site and support is strong, which poses negative effects on the catalytic performance of the catalysts, carbon nanotubes can be one solution.
6- The structure and pore size of nanotubes have significant influence on the stability, activity and selectivity of the target catalyst.
7- The position of the catalytic sites has to be selected based on the type of reaction.

8- Acid pre-treatments are required prior to impregnating of nanotubes with metal salt solution. In other words, strong acid treatment should be used for deposition of catalytic sites inside the nanotubes' pores.

9- A suitable structural promoter is required if sintering is the deactivation cause under the target operating conditions.

8.2 Recommendations

1- The result of CNT synthesis in our CVD reactor showed that the diameter and quality of nanotubes change along the reactor. Unfortunately, the BET surface area of the CNTs was low (20-50 nm) using our CVD reactor and under allowable operating conditions. It would be very useful to analysze the production CNTs using a long reactor at higher gas flow rates. Higher flow rates of carrier gas may result in uniform distribution of iron nano-particles along the CVD reactor.

2- Modeling of a CVD reactor and the nanotubes' growth over a single metal catalyst would be very useful. The combination of these two models is necessary for reactor design for larger and industrial scales.

3- As discussed in Chapter 5, the effects of the nanotubes' pore diameters (12 and 63 nm) were studied and reported in the present thesis. However, it would be useful to study the effects of pore diameter within a smaller increment (e.g. 10, 20, 30 nm etc.).

4- The effects of higher metal loading than that reported in the present thesis (>30%) on activity and selectivity of iron catalyst supported on CNTs should be taken into account.

5- Carbon nanotubes are in the form of fine powder. In order to use iron catalysts supported on CNTs in a fixed or slurry reactor, it is necessary to palletize these catalysts. Thus, the effect of shape, size and the amount of binders on internal and external mass transfer should be studied.

6- The effects of other chemical and structural promoters such as Mn and Zr should be studied in future research plans on iron catalyst supported on CNTs.

7- It has been shown that the nature and structure of iron catalysts are changed during the activation and FT reactions. In situ analyses such as XRD and EXAFS are useful tools to characterize and interpret the catalytic performances of iron catalysts.

8- Iron catalysts for FT reaction can be activated using H_2, CO and syngas. It has been shown that the activity and selectivity of iron catalyst under these gases are not similar. Thus, it would be valuable to study the effect of each of these gases on the catalytic performance of iron catalyst supported on CNTs.

9- A mechanistic kinetic study of the FT reaction in a slurry reactor is preferable to a fixed-bed reactor. A mechanistic kinetic study using a slurry or spinning basket-reactor is recommended.

Appendix A: Publications from Results of the Thesis

1- R. M. Malek Abbaslou, J. Soltan, A. Dalai, Effects of Nanotubes Pore Size on the Catalytic Performances of Iron Catalysts Supported on Carbon Nanotubes for Fischer-Tropsch Synthesis, Applied Catalysis A: General 379 (2010) 129-134.

2- R. M. Malek Abbaslou and A. K. Dalai, The effect of carbon concentration in the precursor gas on the quality and quantity of carbon nanotubes synthesized by CVD method, Applied Catalysis A. 372 (2010) 147–152.

3- R. M. Malek Abbaslou, A. Tavasoli, A. Dalai, Effect of pre-treatment on physico-chemical properties and stability of carbon nanotubes supported iron Fischer–Tropsch, Applied Catalysis A: General, 355 (2009) 33-41.

4- R. M. Malek Abbaslou, J. S. Soltan, A. K. Dalai, Review on Fischer-Tropsch Synthesis in Supercritical Media, Journal of Fuel Processing Technology, Fuel Processing Technology 90 (2009) 849–856.

5- R. M. Malek Abbaslou, A. Tavasoli, J. Soltan, A. K. Dalai, Iron catalyst supported on carbon nanotubes for Fischer-Tropsch synthesis; effect of metal site position, Applied Catalysis A: General, 367(2009) 47-52.

6- R. M. Malek Abbaslou, J. Soltan, S. Sigurdson, A. K. Dalai, Iron Catalysts Supported on Carbon Nanotubes for Fischer–Tropsch Synthesis: Effect of Pore Size, Energy and Suitability. 121 (2009) 139-149.

7- Tavasoli, R. M. Malek Abbaslou, A. K. Dalai, Deactivation behavior of ruthenium promoted Co/Al2O3 catalysts in Fischer–Tropsch synthesis, Applied Catalysis A: General, 346 (2008) 58–64.

8- Tavasoli, R. M. Malek Abbaslou, M. Trepanier, A. K. Dalai, Fischer-Tropsch synthesis over cobalt catalyst supported on carbon nanotubes in a slurry reactor, Applied Catalysis A: General, 345 (2008) 134–142

9- Tavasoli, M. Irani, R. M. Malek Abbaslou, A. K. Dalai, M. Trépanier, Morphology and deactivation behavior of Co-Ru/Al2O3 Fischer-Tropsch synthesis catalyst, Canadian journal of Chemical Engineering, 86 (2008)1070-80.

10- Tavasoli, M. Trépanier, R. M. Malek Abbaslou, A. K. Dalai, N. Abatzoglou, Fischer-Tropsch synthesis on mono- and bimetallic Co and Fe catalysts supported on carbon nanotubes, Fuel Processing Technology, 90 (2008)1486-1494.

11- R. M. Malek Abbaslou, A. K. Dalai, Iron catalyst supported on carbon nanotubes for Fischer-Tropsch reactions: Effect of Mo promotion, Submitted to the Journal of Fuel (2010).

12- R. M. Malek Abbaslou, J. S. Soltan, A. K. Dalai, Effects K and Cu promotion on catalytic performance of iron catalysts supported on CNTs for Fischer-Tropsch Synthesis, Submitted to the Journal of Fuel (2010).

13- R. M. Malek Abbaslou, A. K. Dalai, Production of Carbon Nanotubes using Iron Catalyst: Sectional Analysis of CVD Reactor, submitted to Nanotechnology (2009).

Refereed Conference Papers/Presentations

1- Reza M. Malek Abbaslou, Jafar Soltan, Ajay K. Dalai, Kinetic Study of Promoted Iron Catalysts Supported on Carbon Nanotubes for Fischer-Tropsch Synthesis, Nanocatalysis for Fuels and Chemicals Symposium, Pacifichem 2010, Hawaii, USA (Dec. 2010).

2- Reza M. Malek Abbaslou, Jafar Soltan, Ajay K. Dalai, Structural Promoter for Iron Catalysts Supported on Carbon Nanotubes for Fischer-Tropsch Synthesis, 21st Canadian Symposium on Catalysis, (May 2010).

3- R. M. Malek Abbaslou, J. Soltan, A. K.Dalai, Fe/CNT Catalyst for Fischer-Tropsch Synthesis-Effect of Metal Site, 8th world conference, 8th World Congress of Chemical Engineering, Montréal, Canada (2009)

4- R. M. Malek Abbaslou, A. Tavasoli, J. Soltan, A. K.Dalai, Iron Catalyst Supported on Carbon Nanotubes for Fischer-Tropsch Catalysts – Deactivation Study, 21st North American Catalysis Meeting , San Francisco, USA (2009)

5- M. Trépanier, A. Tavasoli, Reza M. Malek Abbaslou, A. K. Dalai, Raising the activity and selectivity of cobalt catalysts for Fischer-Tropsch synthesis with a novel carbon nanotubes support in a CSTR, 21st North American Catalysis Meeting , San Francisco, USA (2009).

6- R. M. Malek Abbaslou, A. K. Dalai, Sectional Analysis of Carbon Nanotubes Synthesis Reactor Using Chemical Vapor Deposition Method, The Canadian Symposium on Catalysis , Kingston, ON (2008).

7- A. Tavasoli, R. M. Malek Abbaslou, M. Trepanier, A. K. Dalai, "Fischer-Tropsch synthesis over cobalt catalyst supported on carbon nanotubes in a slurry reactor, The Canadian Symposium on Catalysis, Kingston, ON, (2008).

8- A. Tavasoli, R. M. Malek Abbaslou, A. K. Dalai, "Deactivation behavior of Co-Ru/γ-Al2O3 Fischer-Tropsch synthesis catalyst", 236th ACS National Meeting & Exposition Philadelphia, Pennsylvania, USA (2008).

9- R. M. Malek Abbaslou, A. Tavassoli, A. K. Dalai, Effect of Pre-treatment on the Activity, Selectivity and Life-time of Iron Catalyst Supported on Carbon Nanotube for Fischer-Tropsch Synthesis, The 25th Annual International Pittsburgh Coal Conference, The Westin Convention Center, Pittsburgh, PA, USA (2008).

10- M. Trépanier, A. Tavasoli, R. M. Malek Abbaslou, A. K. Dalai, N. Abatzoglou, Synthesis of hydrocarbons from CO and H2 on carbon nanotubes supported iron-cobalt catalysts, 58th Canadian Chemical Engineering Conference, Ottawa, Canada (2008).

11- R. M. Malek Abbaslou and A. K. Dalai, "Optimization and generalization of effective parameters for production of high-quality carbon nanotubes" 57th Canadian Chemical Engineering Conference, Edmonton, Canada (2007).

Patent (submitted)

1- R. M. Malek Abbaslou and A. K. Dalai, Method for preparing of iron catalysts supported on carbon nanotubes for Fischer-Tropsch Synthesis (submitted to Patent and Industry Liaison Office, University of Saskatchewan, Canada)

Technical Report

1- Ajay K. Dalai and Reza M. Malek Abbaslou, Biomass conversion technologies to Fischer-Tropsch liquid fuel for transportation, report to NRCan Project, 62 pages (2006).

Appendix B: Chemical Vapor Deposition Reactor for Production of Carbon Nanotubes

A chemical vapor deposition reactor was deigned and built in the Pilot Plant area at the Department of Chemical Engineering, University of Saskatchewan. This reactor includes a tubular quartz reactor (ID = 22 mm; effective length = 60 cm) placed inside a horizontal electric furnace (ATS, 3 heating zones, 2160 W, 1473 K max temperature). The schematic of the reactor is shown in Figure B1. In addition a photo of the reactor and controlling units is shown in Figure B2. A temperature controller (Eurotherm, USA model 2416) was equipped to control the furnace temperature. The reactant solution (Ferrocene + Toluene) was pumped to the pre-heater by a syringe pump (New era pumps systems, Model NE-1000 multi-phase, Kent Scientific Corporation, USA). A carrier gas (argon) mixed with 10 vol % hydrogen carried the vaporized stream of the feed mixture into the reactor. Flow rates of Ar and H_2 were controlled by mass flow controllers (smart mass flow, model 0152, Brooks Instruments Division, Emerson Electric Co. USA). The mass flow controllers were calibrated using a bubble flow meter at different flow rates. Figures B4 and B5 shows the calibration curves for Ar and H_2 gases.

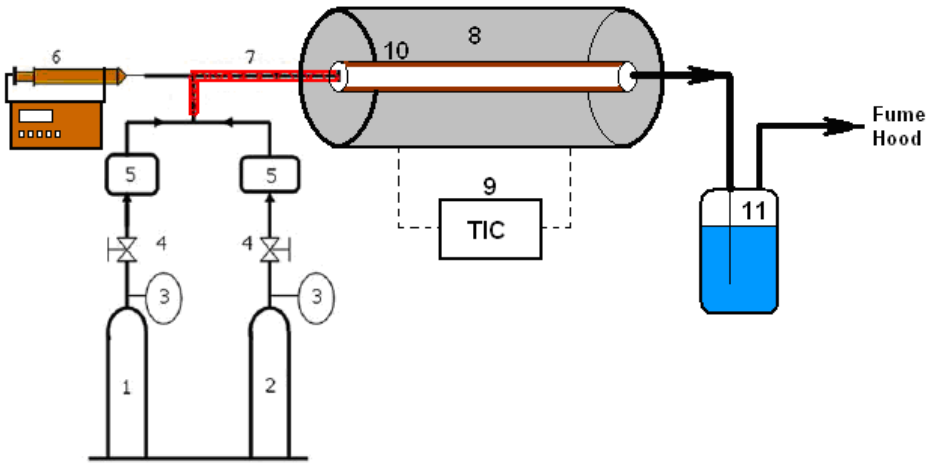

1: Hydrogen
2: Argon
3: Pressure gauge
4: On/off valve
5: Mass flow controller
6: Syringe pump
7: Pre-heater
8: Horizontal electric furnace
9: Temperature controller
10: Quartz tube and CNTs
11: Gas cooler

Figure B1 Schematic of the experimental setup for CNT synthesis

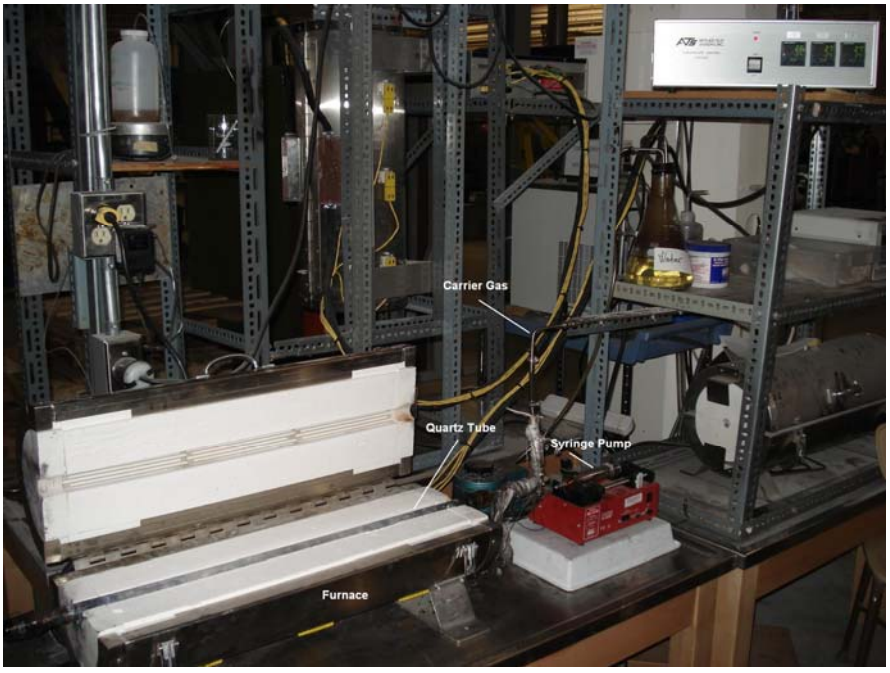

Figure B2 Front view of the CVD reactor for carbon nanotube production

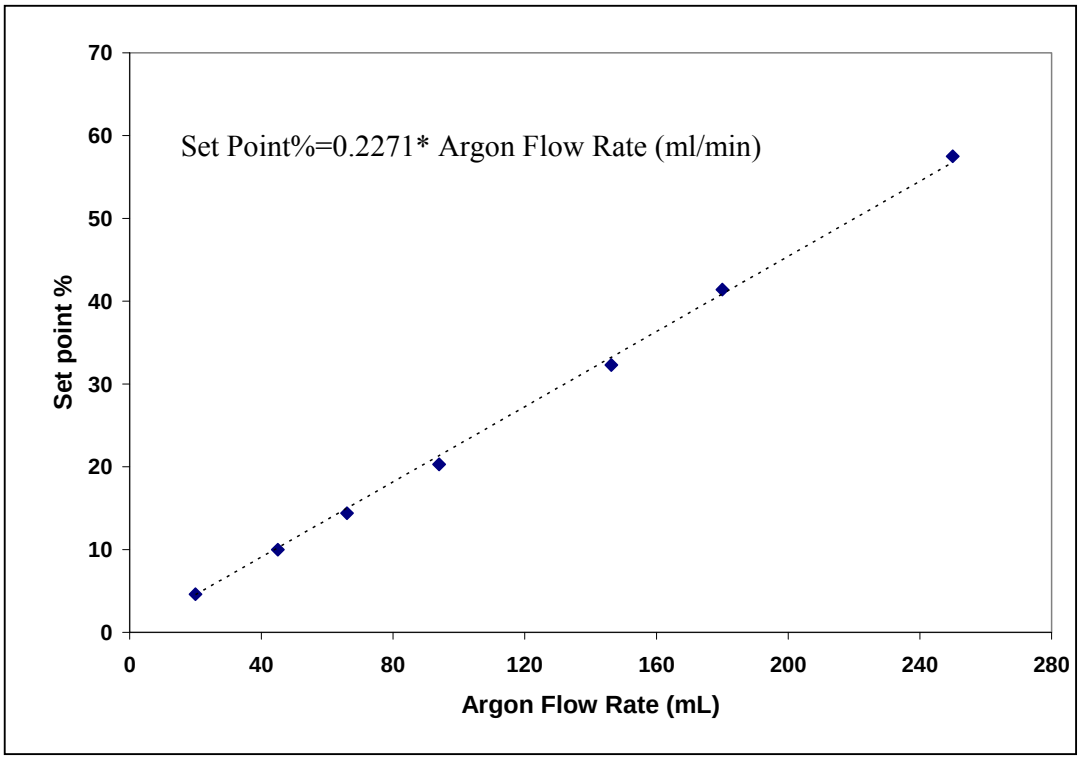

Figure B3 Calibration data for argon mass flow controller used in the CVD reactor

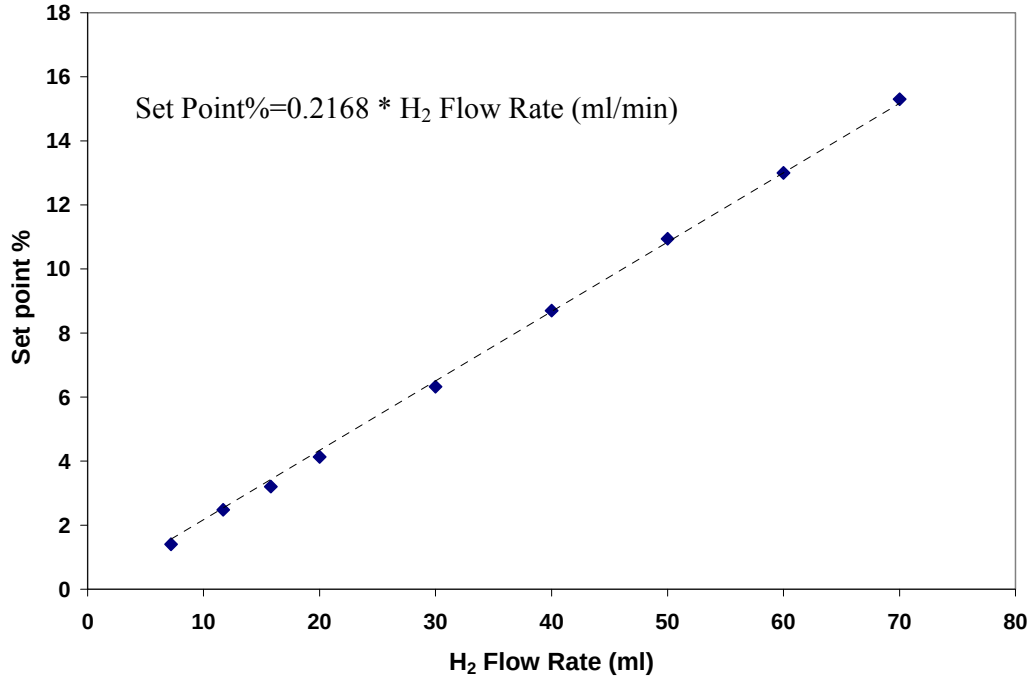

Figure B4 Calibration data for hydrogen mass flow controller used in the CVDreactor

Appendix C: Fixed Reactor Specifications for Fischer-Tropsch Reactions

A fixed bed reactor for Fischer-Tropsch reactions was designed and built in the Pilot Plant area at the Department of Chemical Engineering, University of Saskatchewan. Figures C1 and C2 show the schematic and the front view of the fixed bed reactor, respectively. The setup comprises of three inlet stream lines for Syngas (CO + H_2), H_2 and helium. The flow rate of syngas and H_2 are controlled by two mass flow controller (Brooks 5850, Max pressure 4500 psi, max flow 12 SLPH). Calibration data for syngas and hydrogen are given in Figures C3 and C4. H_2 is used for reduction of catalyst and helium stream is used for pressurizing the reactor. Before entering into the catalytic bed, the feed stream is heated up using a pre-heater (max. temperature of 200 ^oC). The fixed bed reactor (ID 1.43 cm, length 45 cm, catalyst volume 10.5 ml) is heated by a furnace (1360 W, max. temperature 1200^oC) and temperature is controlled by a temperature controller (Eurotherm 2416). The calibration data and temperature profile along the furnace are given in Figures C5 and C6, respectively. As the products of FTS may contain heavy hydrocarbon such as wax (C_{20}+), heating tapes are used to keep the tubing after reactor at 150-200^oC. Afterward, the products enter into a hot condenser (max. volume 75ml, temperature 150-200^oC) to collect wax and heavy hydrocarbons. Then the remaining products are directed to a cold condenser (max. volume 75ml, temperature - 5^oC) to collect water and light hydrocarbons. Finally, the cold condenser is connected to an online gas chromatograph (GC) to analysze gaseous products. Two valves are located under the cold and hot condensers in order to collect liquid products. Liquid products are analyzed using an off line GC.

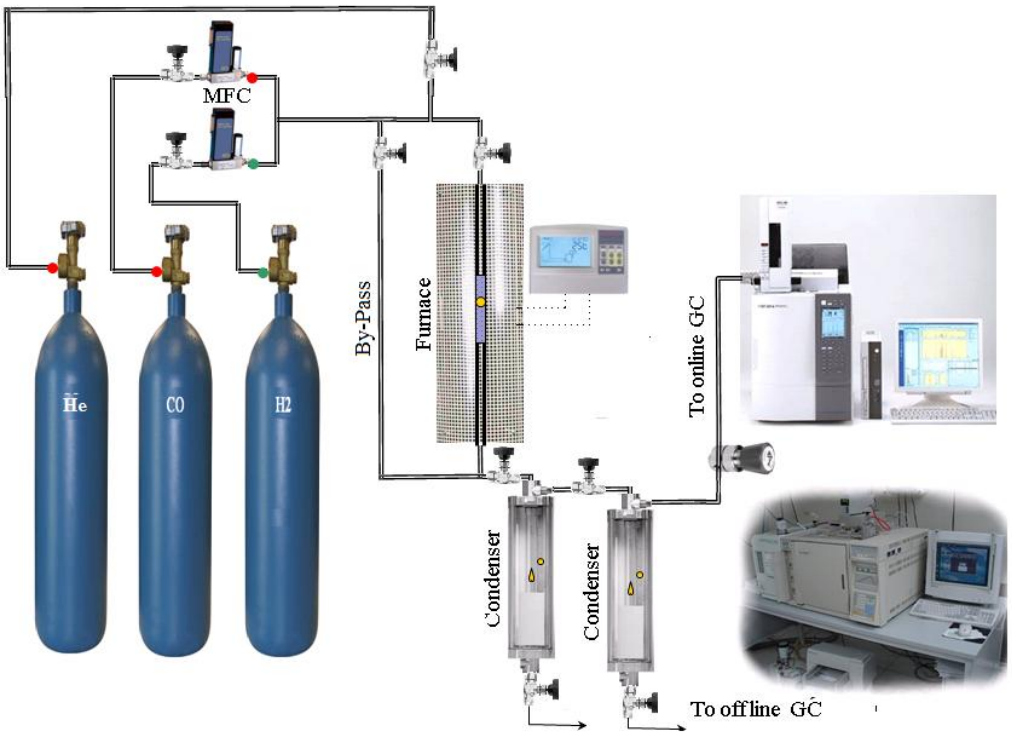

Figure C1 Schematic of the fixed bed reactor for Fischer-Tropsch synthesis

Figure C2 Front view of the fixed bed reactor for Fischer-Tropsch synthesis

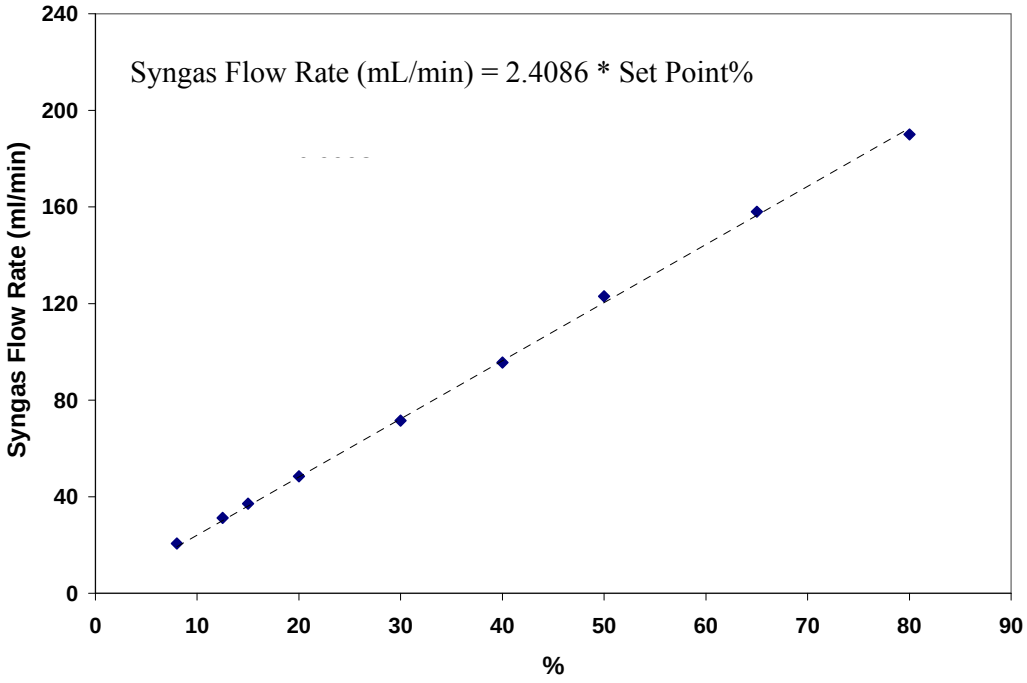

Figure C3 Calibration data for syngas mass flow controller used in the fixed bed reactor

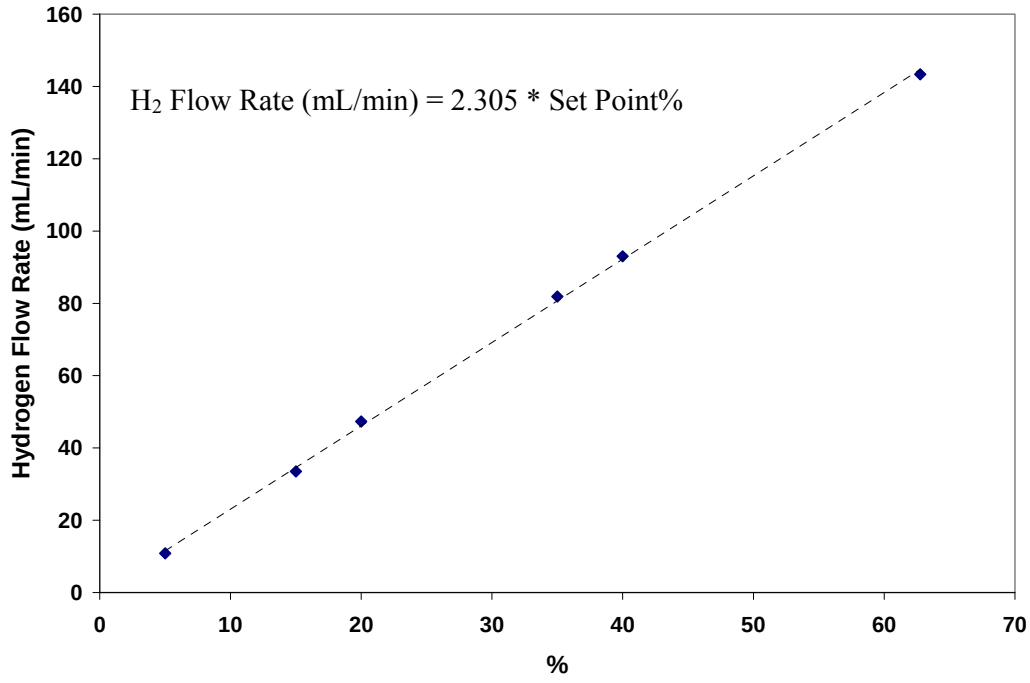

Figure C3 Calibration data for hydrogen mass flow controller used in the fixed bed reactor

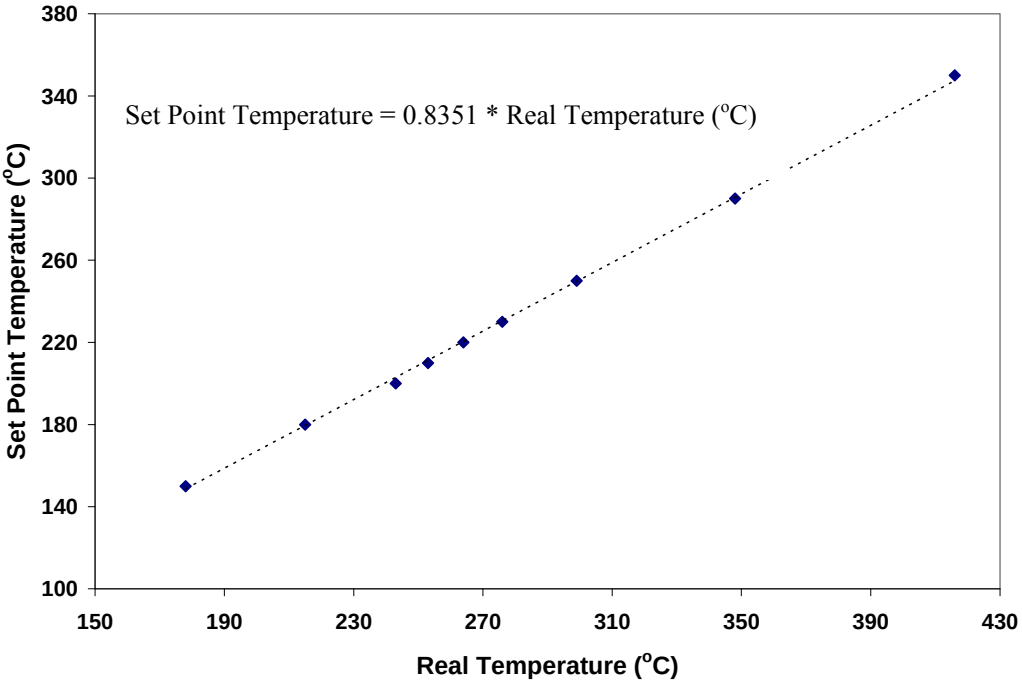

Figure C5 Temperature calibration data for the furnace installed on the FT reactor

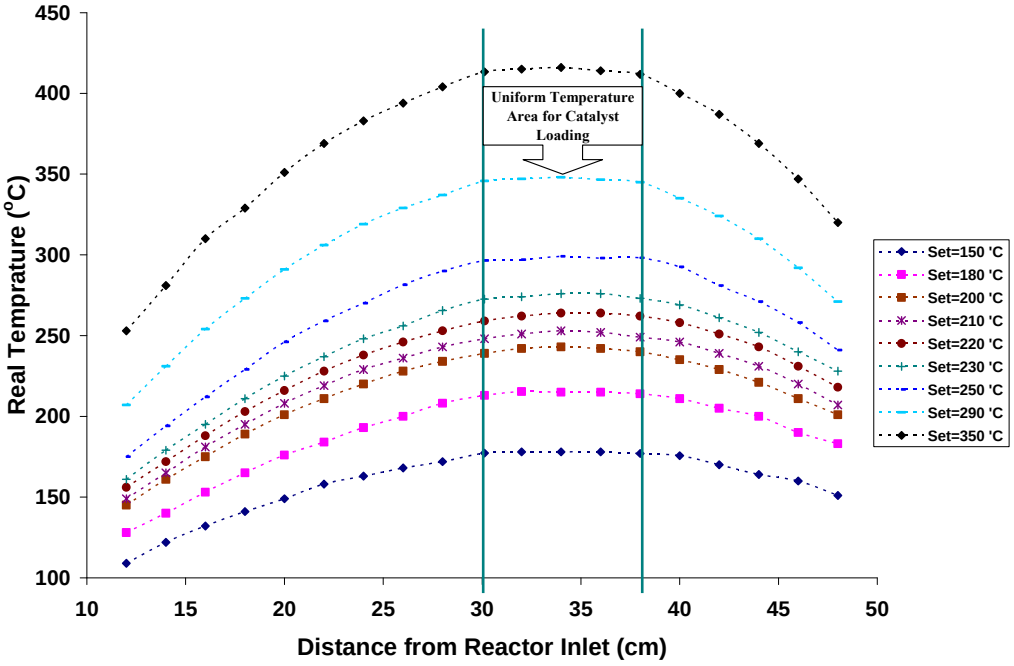

Figure C6 Temperature profile along the furnace installed on the FT reactor

Appendix D: Calibration of Reduction Profile of Catalysts

Temperature programmed reduction profiles of the calcined catalysts were analyzed using a CHEMBET-3000, equipped with a thermal conductivity detector. In order to calibrate hydrogen consumption during the test, a reduction of silver oxide (Ag_2O) was used. Here, 0.027 g of Ag_2O was placed in U-shaped quartz tube. A 5% hydrogen/nitrogen mixture was introduced (flow rate = 36 ml (STP)/min) and the furnace was ramped from room temperature to 400 K at 10 K/min. The reduction profile of Ag_2O is given in Figure D1. Using excel software and Simpson's algorithm (numerical integration), the area under curve were calculated. Based on the area under the curve for a known amount of Ag_2O, the following formula can give the extent of reduction for iron oxides.

If the iron oxide on the calcined catalyst is in the form of Fe_3O_4 then:

Total amount of Fe reduced (g) =(surface under curve)*$(2.85*10^{-9})$*(3/4)*MW_{Fe}

% Extent of reduction = (Total amount of Fe reduced) *100 / (catalyst sample weight * percent of iron loading)

If the iron oxide on the calcined catalyst is in the form of Fe_2O_3 then

Total amount of Fe reduced (g) = (surface under curve)*$(2.85*10^{-9})$*(2/3)*MW_{Fe}

% Extent of reduction = (Total amount of Fe reduced) *100 / (catalyst sample weight * percent of iron loading)

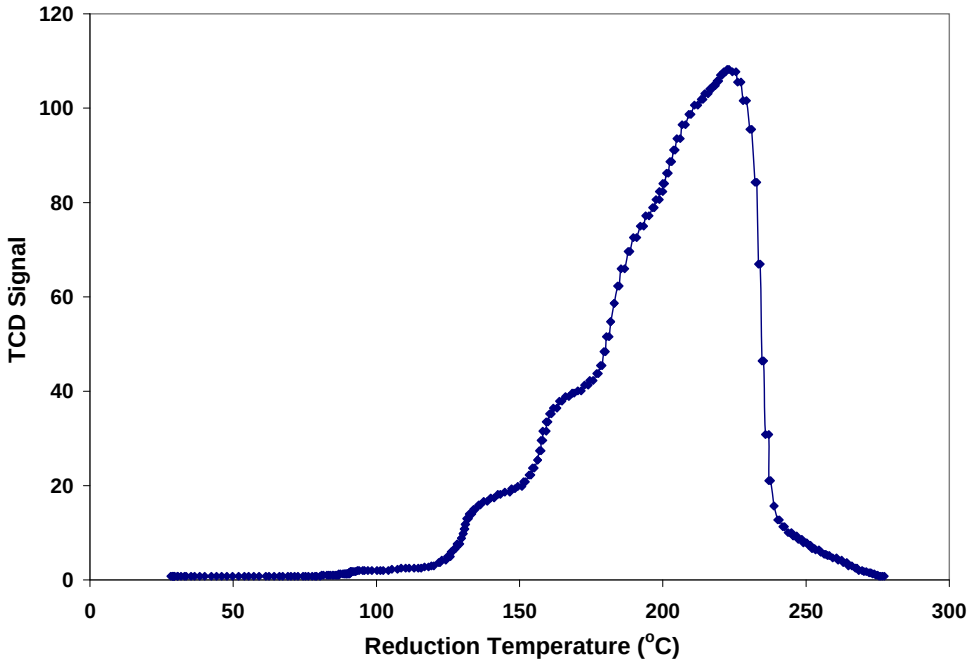

Figure D1 Reduction profile for 0.027 g of Ag_2O under hydrogen stream

Appendix E: Particle Size Estimation using Debye-Sherrer Equation

When X-rays hit and are scattered from a crystal lattice, constructive interference only occurs for certain θ's when the path difference is equal to n wavelengths (Figure E1). This condition can be expressed by the following equation which is known as Bragg's Law:

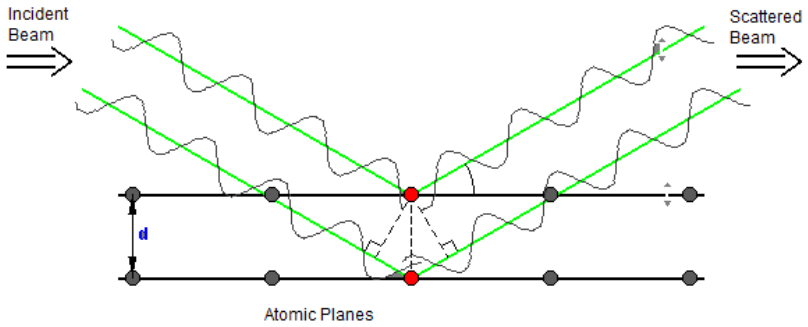

Figure E1 Constructive interference of X-ray scattered from atomic planes

$n\lambda = 2\ d\ sin\ \theta$ (Bragg's law)

where λ is wavelength of X-ray, d is distance between crystalline planes, θ is the beam angle, and n is an integer number. Brarg's Law is applicable to determine crystalline structures of unknown materials. This is done by moving the sample and measuring the intensity with a detector. The results of X-ray diffraction using Bragg's Law are generally shown in the form of intensity vs. beam angle.

When crystallites are larger than 100 nm in size, the intensity peaks are very sharp (Figure E2a). When, crystallites are less than 100 nm in size, appreciable broadening in the X-ray diffraction lines will occur (Figure E2b). These regions and the observed line

broadening can be used to estimate the average size based on Debye-Sherrer equation as follows:

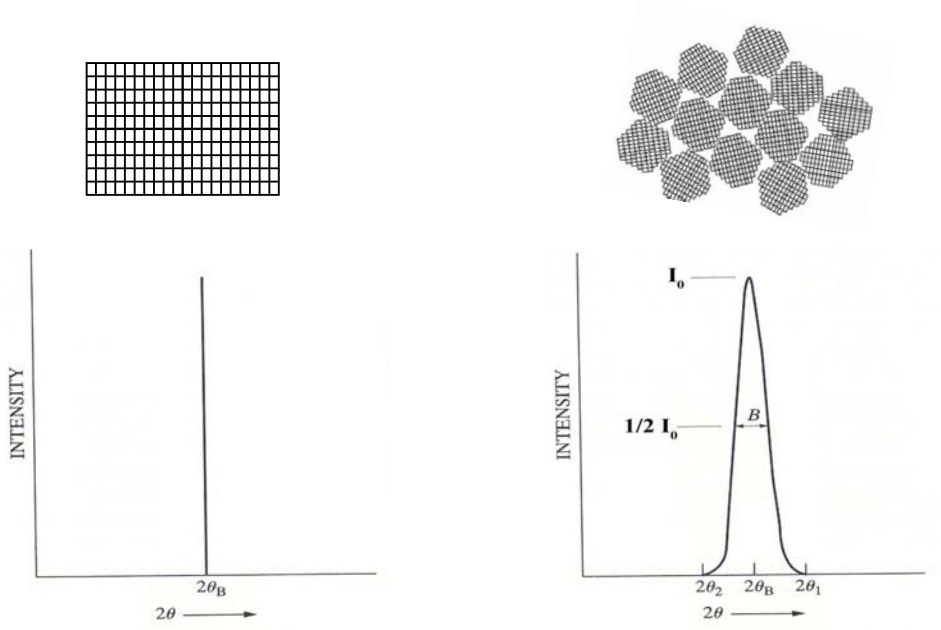

a b

Figure E2 Intensity vs. 2θ for large (a) and small crystalline particles (b)

$$t = \frac{K.\lambda}{B.\cos(\theta_B)} \qquad \text{(Debye-Scherrer Equation)}$$

t = thickness of crystallite

K = constant dependent on crystallite shape (0.89)

λ = x-ray wavelength (0.154 nm)

B = FWHM (full width at half max) or integral breadth

θ_B = Bragg Angle

Appendix F: Internal and External Mass Transfer Calculation for Iron Catalyst Supported on CNTs

Weisz-Prater Criterion for Internal Diffusion

The Weisz-Prater equation shows the ratio of actual reaction rate to a diffusion rate [1]:

$$C_{wp} = \frac{actual \quad reaction \quad rate}{a \quad diffusion \quad rate} \tag{F1}$$

For first-order reactions, the Weisz-Prater criterion can be derived as follows,

$$C_{wp} = \frac{-r'_A.\rho_p.R^2}{D_e.C_{AS}}, \tag{F2}$$

where r'_A is the rate of reaction, ρ_p is the density of pellet (particle), R is the pellet radius, D_e is the effective diffusivity and C_{AS} is the reactant concentration on the surface of catalysts. If C_{wp}<< 1 then one can assume that there is no diffusion limitation.

As discussed in Chapter 7, a first-order reaction rate in hydrogen is able to describe the reaction mechanism. In order to calculate the effective diffusivity, three situations can be considered for the diffusion of reactants inside the catalyst pores including:

1-Knudsen type diffusion of hydrogen inside the nanotubes' pores,

2- Bulk diffusion of hydrogen in gas phase,

3-Bulk diffusion of hydrogen into wax-filled pores.

1-Knudsen Type Diffusion of Hydrogen Inside the Nanotubes' Pores

It has been shown that the diffusion of hydrogen inside the nanotubes may happen through the Knudsen mechanism [2]. Knudsen diffusivity can be calculated as follows,

$$D_k = 0.97 * R_{pore} * \sqrt{\frac{T}{M_A}}, \tag{F3}$$

where T id temtrature, M_A is the gas molecular weight, R_{pore} is the pore diameter, and D_k is the Knudsen diffusion. Using equation F3 and the data provided in Table F1, the value of D_k will be $96.3*10^{-9}$ m^2/s. An equation that relates the effective diffusivity to Knudsen or bulk diffusivity is [1],

$$D_e = \frac{D_k.\varepsilon_p.\sigma}{\tau}, \qquad \text{(F4)}$$

where ε_p is the void fraction of catalyst pellet, σ is the constriction factor, and τ is the tortuosity. Since the nanotubes can be considered straight with a uniform diameter, then σ and τ are assumed to equal unity. Using the data in Table F1, the effective diffusivity will be $D_e = 24.2*10^{-9}$ m^2/s.

Now, Equation F2 gives the value for C_{wp}

$$C_{wp} = \frac{-r'_A.\rho_p.R^2}{D_e.C_{AS}} = \frac{(1.1*10^{-2})*1100*(0.148*10^{-3})^2}{(24.2*10^{-9})*119.7} = 0.09 << 1$$

Since the C_{wp} is less than 1, there is no internal mass transfer limitation for the catalyst under the reaction conditions for the present kinetic study (Chapter 7).

It should be noted that transport rates in nanotubes are reported to be orders of magnitude faster than in the zeolites or in any micro porous materials with the same pore sizes. The exceptionally high transport rates in nanotubes were shown to be a result of the inherent smoothness of the nanotubes [3]. Then higher effective diffusivity can result in smaller C_{wp} values resulting in less probability of internal mass transfer limitations.

2- Bulk Diffusion of Hydrogen in Gas Phase

Suppose that the there is only gas phase inside the pores of the nanotubes. In this case, the value for diffusivity of hydrogen is much higher than the Knudsen diffusion

(D_e = 0.25*10^{-5} m^2/s). Based on the data provided in Table F1 and Equation F2, the value for C_{wp} will be,

$$C_{wp} = \frac{-r'_A.\rho_p.R^2}{D_e.C_{AS}} = \frac{(1.1*10^{-2})*1100*(0.148*10^{-3})^2}{(0.25*10^{-5})*119.7} = 8.8*10^{-4} << 1 .$$

In this situation, diffusion limitations are very unlikely.

3-Bulk Diffusion of Hydrogen into Wax-filled Pores

There is one possibility that the pores of the nanotubes are filled with wax and reactants have to diffuse in the liquid phase. Bulk diffusivity of hydrogen in FT wax can be on the order of 40-50*10^{-9} m^2/s [4] . The hydrogen concentration in liquid phase can be calculated using Henry's law as follows [5],

$$H_{H2} = 2.291*10^7 \exp(\frac{581.8}{T}), \qquad \text{(F5)}$$

in which H is measured in kPa.cm^3/mol and T in Kelvin. At a temperature of 548 K, H_{H2} = 0.792*10^7 kPa.ml/mol. Using Henry's Law,

$$C_{H2} = P_{H2}/H_{H2}. \qquad \text{(F6)}$$

The concentration of hydrogen in wax is 63 mol/m^3. According to data provided in Table F1 and Equation F2, the Weisz-Prater criterion can be calculated as follows;

$$C_{wp} = \frac{-r'_A.\rho_p.R^2}{D_e.C_{AS}} = \frac{(1.1*10^{-2})*1100*(0.148*10^{-3})^2}{(45*10^{-9})*63} = 0.09 << 1$$

It can be concluded that reaction rate is the controlling step.

Mears Criterion for External Mass Transfer

The Mears criterion uses the measured rate of reaction to examine if the external mass transfer can be neglected. Mears proposed that when

$$C_M = \frac{-r'_A.\rho_b.R.n}{k_c.C_A} < 0.15 \qquad \text{(F7)}$$

where n is the reaction order, R is the catalyst particle radius (m), ρ_b is the bulk density of catalyst (kg/m^3), C_A *is the* bulk concentration (kmol/m^3), and k_c is the mass transfer coefficient (m/s)external mass transfer effects are negligible.

The value for k_c can be calculated using Frossling correlation [1]:

$$Sh = 2 + 0.6Re^{1/2}Sc^{1/3} \qquad \text{(F8)}$$

Based on data for physical properties of gas phase under operation conditions, Re and Sc will be

$$Sc = \frac{\mu_g}{\rho_g . D_{H2}} = 0.12$$

$$\mathrm{Re} = \frac{\rho_g . U_g . d_p}{\mu_g} = 1.4$$

According to equation F15

Sh = 2 +0.6*1.4*0.12 = 2.1

and

$$Sh = \frac{k_c . d_p}{D_{H2}} = 2.1$$

then

k_c = 0.075 m/s

Now, Mears criterion canbe calculated as follows,

$$C_M = \frac{-r'_A . \rho_b . R . n}{k_c . C_A} = \frac{(1.1 * 10^{-2}) * 100 * (0.148 * 10^{-3}) * 1}{(0.075) * 109.7} = 2 * 10^{-5} << 0.15 .$$

Therefore, it is certain that external mass transfer effects on the kinetic study can be neglected.

Table F1 Physical and chemical properties of the catalyst and reaction medium for the kinetic study

Parameter	Description	Unit	Value
R	pellet radius	m	$0.148*10^{-3}$
R_{pore}	pore radius	m	$6*10^{-9}$
n	reaction rate	-	1
τ	tortuosity	-	1.1
ε_p	void fraction of pellet (particle)	-	0.252
r'	reaction rate	mol/kg-cat/s	$1.1*10^{-2}$
T	reaction temperature	K	548
P	reaction pressure	kPa	2000
P_{H2}	average partial pressure of hydrogen	kPa	500
C_{H2}	average molar concentration of hydrogen in gas phase	mol/m^3	119.7
ρ_p	density of pellet (particle)	kg/m^3	1100
ρ_b	bulk density of the catalyst bed	kg/m^3	100
ρ_g	bulk density of the gas phase	kg/m^3	14.5
U_g	superficial velocity of gas phase	m/s	$0.62*10^{-2}$
μ_g	viscosity of gas phase	kg/m/s	$1.8*10^{-5}$
D_{H2}	diffusivity of H_2 in gas phase	m^2/s	$1*10^{-5}$

References

[1] H.S. Fogler, Elements of chemical reaction engineering, second edition, Prentice Hall PTR, 1992.

[2] B. J. Hinds, N. Chopra, T. Rantell, R. Andrews, V. Gavalas, L. G. Bachas, Aligned Multiwalled Carbon Nanotube Membranes, Science 303 (2004) 62-65.

[3] A. I. Skoulidas, D. M. Ackerman, J. K. Johnson, and D. S. Sholl1, Rapid Transport of Gases in Carbon Nanotubes, Physical Review Letters 89 (2002) 185901-4.

[4] C. Erkey, J. B. Rodden, and A. Akgerman, Diffusivities of Synthesis Gas and n-Alkanes in Fischer-Tropsch Wax, Energy & Fuels, 4 (1990) 275-276.

[5] X. Zhan, B. H. Davis, Assessment of internal diffusion limitation on Fischer-Tropsch product distribution, Applied Catalysis A: General, 236 (2002) 149-161.

[6] Plots of Transport Data http://www.fuelcellknowledge.org/research_and_analysis/materials/gas_properties_plots/transport_data.pdf, 2010

[7] R.H. Perry, D.W. Green, Perry's Chemical Engineers' Handbook, 7th Edition (1997) McGraw-Hill

Appendix G: Matlab Code for Kinetic Studies

Matlab Function for Differential Equations of Mass Conservations

```
% Reza Malek, Department of Chemical Engineering, University of Saskatchewan
% The following Matlab function solves differential equations for mass conservation for
 %each of components including CO, H2, H2O, CO2, and Hydrocarbons

function exit = DE (x)
global out Pt r1calc r2calc r1exp r2exp

% ********** k1, k2…k7 are unknown parameters in rate equation ********

for m=1:7
k1=x(1);
k2=x(2);
k3=x(3);
k4=x(4);
k5=x(5);
k6=x(6);
k7=x(7);

% ************ inlet flowrates of H2 and CO,  total pressure (Pt)**********

F0=zeros(7,8);

% order       FCO             FH2                  Pt      Nc      Nh
F0(1,:)=[0.096428571  0.192857143 0 0 0  1.02 4.81 10.20];
F0(2,:)=[0.108482143  0.108482143 0 0 0  2.04 5.48 10.48];
F0(3,:)=[0.072321429  0.072321429 0 0 0  1.02 5.55 11.63];
F0(4,:)=[0.072321429  0.072321429 0 0 0  2.04 5.48 11.49];
F0(5,:)=[0.120535714  0.120535714 0 0 0  3.4 5.48 11.50];
F0(6,:)=[0.072321429  0.144642857 0 0 0  2.04 4.71 10.04];
F0(7,:)=[0.216964286  0.216964286 0 0 0  2.72 5.49 11.50];


% ********** bulk density of catalyst and reactor dimensions ************

% density of catalyst (g/ml)
Ro=0.1;
% Reactor length (cm)
l=6.2;
% volume of reactor divided by number of grids (ml)
a=1.61 * l/10000;

%*************** initial conditions ***************************
FCO(1)=F0(m,1);
FH2(1)=F0(m,2);
FCO2(1)=F0(m,3);
FH2O(1)=F0(m,4);
FHC(1)=F0(m,5);
Pt=F0(m,6);
Nc=F0(m,7);
Nh=F0(m,8);
Fargon= 0.1*(FCO(1)+FH2(1)+FCO2(1)+FH2O(1)+FHC(1));
```

```
%************** Partial Pressures along the Reactor **********************

for i=1:10000
Ft(i)=FCO(i)+FH2(i)+FCO2(i)+FH2O(i)+FHC(i)+Fargon;
PCO=Pt*FCO(i)/Ft(i);
PH2=Pt*FH2(i)/Ft(i);
PCO2=Pt*FCO2(i)/Ft(i);
PH2O=Pt*FH2O(i)/Ft(i);
PHC=Pt*FHC(i)/Ft(i);

%************** Reaction Rate Equations ************************

%models for Fischer-Tropsch reactions
%r1(i)=k1*PH2;
%r1(i)=k1*PH2*PCO/(k2*PH2O+PCO);
%r1(i)=k1*PH2*PCO/(k2*PH2O+PCO+k5*PCO2);
%r1(i)=k1*PH2^2*PCO/(k2*PH2O+PH2*PCO);
%r1(i)=k1*PH2*PCO/((k2*PCO+1)^2);
%r1(i)=(k1*(PH2^1.5)*PCO/PH2O)/(1+k2*(PH2^1.5)*PCO/PH2O);
%r1(i)=k1*PH2*PCO/(k2*PCO2+PCO);
%r1(i)=k1*(PH2^0.5)*PCO/((k2*PH2O+k5*PCO+1)^2);
r1(i)=k1*PH2*PCO/((k2*PH2O+k5*PCO+1)^2);
%r1(i)=k1*PH2*PCO/((k2*PH2O+k5*PCO+1));

%Models for Water-Gas-Shift reactions

%r2(i)= k3*(PCO*PH2O-(PH2*PCO2/55));
%r2(i)= k3*(PCO*PH2O-(PH2*PCO2/55))/(k4*PH2O+PCO+k6*PCO2);
%r2(i)= k3*(PCO*PH2O-(PH2*PCO2/55))/(PH2*PCO+k4*PH2O);
%r2(i)= k3*(PCO*PH2O-(((PH2)^0.5)*PCO2/55))/((1+k4*PH2O/(PH2^0.5))^2);
r2(i)= k3*(PCO*PH2O-(((PH2))*PCO2/55))/((1+k4*PH2O/(PH2^0.5)+k6*PH2O)^2);

%************** Differential Equations ************************

FCO(i+1)=-(r1(i)+r2(i))*Ro*a+FCO(i);
 % CO diff. equ.
%
FH2(i+1)=((-(2*Nc+Nh)/(2*Nc))*r1(i) +r2(i))*Ro*a + FH2(i);
% % H2 diff. equ.
%
FCO2(i+1)=r2(i)*Ro*a+FCO2(i);
%  % CO2 diff. equ.
%
FH2O(i+1)=(r1(i)-r2(i))*Ro*a+FH2O(i);
% % H2O diff. equ.
%
FHC(i+1)=(1/Nc)*r1(i)*Ro*a+FHC(i);
% HC diff. equ.
end

%************** Experimental Flow Rates at the Exit of the Reactor **********

Fexp= zeros (7,5);

% order          FCO              FH2             FCO2          FH2O             FHC
Fexp(1,:)=[0.027096429  0.135288458  0.027940854  0.01345043    0.00928263];
Fexp(2,:)=[0.010848214  0.041555834  0.043642366  0.010349196  0.00984888];
Fexp(3,:)=[0.010848214  0.03169476    0.027970313  0.005532589  0.006033298];
Fexp(4,:)=[0.003616071  0.025221239  0.030711295  0.007282768  0.006925009];
```

```
Fexp(5,:)=[0.007340625  0.034334398  0.047881523  0.017432044  0.012405236];
Fexp(6,:)=[0.003182143  0.076512678  0.024475307  0.020188671  0.010346069];
Fexp(7,:)=[0.0091125       0.06105552   0.088752713  0.030346361  0.023481678];

%************** Experimental Partial Pressures at the Exit of the Reactor **********

PCOexp(m)=Pt*(Fexp(m ,1)/(sum(F0(m, 1:2))/0.9));
PH2exp(m)=Pt*(Fexp(m ,2)/(sum(F0(m, 1:2))/0.9));
PCO2exp(m)=Pt*(Fexp(m ,3)/(sum(F0(m, 1:2))/0.9));
PH2Oexp(m)=Pt*(Fexp(m ,4)/(sum(F0(m, 1:2))/0.9));
PHCexp(m)=Pt*(Fexp(m ,5)/(sum(F0(m, 1:2))/0.9));

%************** Experimental Reaction Rate at the Exit of the Reactor **********

% Fischer-Tropsch Reactions

%r1exp(m)=k1*PH2exp(m);
%r1exp(m)=(k1*PH2exp(m)*PCOexp(m))/(k2*PH2Oexp(m)+PCOexp(m));
%r1exp(m)=(k1*PH2exp(m)*PCOexp(m))/(k2*PH2Oexp(m)+PCOexp(m)+k5*PCO2exp(m));
%r1exp(m)=(k1*PH2exp(m)^2*PCOexp(m))/(k2*PH2Oexp(m)+PH2exp(m)*PCOexp(m));
%r1exp(m)=(k1*PH2exp(m)*PCOexp(m))/((k2*PCOexp(m)+1)^2);
%r1exp(m)=(k1*(PH2exp(m)^1.5)*PCOexp(m)/PH2Oexp(m))/(1+k2*(PH2exp(m)^1.5)*PCOexp(m)/PH
2Oexp(m));
%r1exp(m)=(k1*PH2exp(m)*PCOexp(m))/(k2*PCO2exp(m)+PCOexp(m));
%r1exp(m)=(k1*(PH2exp(m)^0.5)*PCOexp(m))/((k2*PH2Oexp(m)+k5*PCOexp(m)+1)^2);
r1exp(m)=(k1*PH2exp(m)*PCOexp(m))/((k2*PH2Oexp(m)+k5*PCOexp(m)+1)^2);
%r1exp(m)=(k1*PH2exp(m)*PCOexp(m))/((k2*PH2Oexp(m)+k5*PCOexp(m)+1));

% Water-Gas-Shift Reactions

%r2exp(m)=k3*(PCOexp(m)*PH2Oexp(m)-((PH2exp(m)*PCO2exp(m))/55));
%r2exp(m)=k3*(PCOexp(m)*PH2Oexp(m)-
((PH2exp(m)*PCO2exp(m))/55))/(k4*PH2Oexp(m)+PCOexp(m)+k6*PCO2exp(m));
%r2exp(m)= k3*(PCOexp(m)*PH2Oexp(m)-
((PH2exp(m)*PCO2exp(m))/55))/(PH2exp(m)*PCOexp(m)+k4*PH2Oexp(m));
%r2exp(m)=k3*(PCOexp(m)*PH2Oexp(m)-
(((PH2exp(m)^0.5)*PCO2exp(m))/55))/((1+k4*PH2Oexp(m)/(PH2exp(m)^0.5))^2);
r2exp(m)=k3*(PCOexp(m)*PH2Oexp(m)-
(((PH2exp(m))*PCO2exp(m))/55))/((1+k4*PH2Oexp(m)/(PH2exp(m)^0.5)+k6*PH2Oexp(m))^2);

%************** Output ****************************************

out(m,:)=[FCO(i) FH2(i) FCO2(i) FH2O(i) FHC(i)];
end
x

for i=1:1:m
   for j=1:1:5
      exit(i,j)=abs(((Fexp(i,j)-out(i,j))));
   end
end
```

Matlab Code for Non-linear Regression

```
clear all
close all
clc
global out r1 r2 Pt x

%************** Main Regression function  *************************

o=optimset('TolFun',1e-12)
x=[0.03  0.01  0.1  0.1 1 0.0009]
[x,resnorm,residual,exitflag]=lsqnonlin(@DE,x,[0 0 0 0 0 0],[10 10 30 7 10 7],o)


%************** Experimental Flow rate at the Exit of the Reactor **********

Fexp= zeros (7,5);

% order     FCO                    FH2              FCO2          FH2O          FHC
Fexp(1,:)=[0.027096429 0.135288458 0.027940854   0.01345043 0.00928263];
Fexp(2,:)=[0.010848214 0.041555834 0.043642366   0.010349196 0.00984888];
Fexp(3,:)=[0.010848214 0.03169476 0.027970313     0.005532589 0.006033298];
Fexp(4,:)=[0.003616071 0.025221239 0.030711295   0.007282768 0.006925009];
Fexp(5,:)=[0.007340625 0.034334398 0.047881523   0.017432044 0.012405236];
Fexp(6,:)=[0.003182143 0.076512678 0.024475307   0.020188671 0.010346069];
Fexp(7,:)=[0.0091125 0.06105552 0.088752713 0.030346361 0.023481678];

% ************* inlet flowrates of H2 and CO,  total pressure (Pt)**********

F0=zeros(6,8);

% order       FCO          FH2          Pt    Nc      Nh
F0(1,:)=[0.096428571 0.192857143 0 0 0 1.02 4.81 10.20];
F0(2,:)=[0.108482143 0.108482143 0 0 0 2.04 5.48 10.48];
F0(3,:)=[0.072321429 0.072321429 0 0 0 1.02 5.55 11.63];
F0(4,:)=[0.072321429 0.072321429 0 0 0 2.04 5.48 11.49];
F0(5,:)=[0.120535714 0.120535714 0 0 0 3.4 5.48 11.50];
F0(6,:)=[0.072321429 0.144642857 0 0 0 2.04 4.71 10.04];
F0(7,:)=[0.216964286 0.216964286 0 0 0 2.72 5.49 11.50];

% ********** k1, k2…k7 are unknown parameters in rate equation ********

for m=1:7
k1=x(1);
k2=x(2);
k3=x(3);
k4=x(4);
k5=x(5);
k6=x(6);
k7=x(7);

%************** Experimental Partial Pressures at the Exit of the Reactor **********

PCOexp(m)=F0(m,6)*(Fexp(m ,1)/(sum(F0(m, 1:2))/0.9));
PH2exp(m)=F0(m,6)*(Fexp(m ,2)/(sum(F0(m, 1:2))/0.9));
PCO2exp(m)=F0(m,6)*(Fexp(m ,3)/(sum(F0(m, 1:2))/0.9));
PH2Oexp(m)=F0(m,6)*(Fexp(m ,4)/(sum(F0(m, 1:2))/0.9));
```

```
PHCexp(m)=F0(m,6)*(Fexp(m ,5)/(sum(F0(m, 1:2))/0.9));

%********** Experimental Reaction Rate at the Exit of the Reactor **********

% Fischer-Tropsch reactions

%r1exp(m)=(k1*PH2exp(m));
%r1exp(m)=(k1*PH2exp(m)*PCOexp(m))/(k2*PH2Oexp(m)+PCOexp(m));
%r1exp(m)=(k1*PH2exp(m)*PCOexp(m))/(k2*PH2Oexp(m)+PCOexp(m)+ k5*PCO2exp(m));
%r1exp(m)=(k1*(PH2exp(m)^2)*PCOexp(m))/(k2*PH2Oexp(m)+PH2exp(m)*PCOexp(m));
%r1exp(m)=(k1*PH2exp(m)*PCOexp(m))/((k2*PCOexp(m)+1)^2);
%r1exp(m)=(k1*(PH2exp(m)^1.5)*PCOexp(m)/PH2Oexp(m))/(1+k2*(PH2exp(m)^1.5)*PCOexp(m)/PH
2Oexp(m));
%r1exp(m)=(k1*PH2exp(m)*PCOexp(m))/(k2*PCO2exp(m)+PCOexp(m));
%r1exp(m)=(k1*(PH2exp(m)^0.5)*PCOexp(m))/((k2*PH2Oexp(m)+k5*PCOexp(m)+1)^2);
r1exp(m)=(k1*(PH2exp(m))*PCOexp(m))/((k2*PH2Oexp(m)+k5*PCOexp(m)+1)^2);
%r1exp(m)=(k1*(PH2exp(m))*PCOexp(m))/((k2*PH2Oexp(m)+k5*PCOexp(m)+1));

%Water-Gas-Shift Reactions

%r2exp(m)= k3*(PCOexp(m)*PH2Oexp(m)-(PH2exp(m)*PCO2exp(m))/55);
%r2exp(m)= k3*(PCOexp(m)*PH2Oexp(m)-
(PH2exp(m)*PCO2exp(m))/55)/(k4*PH2Oexp(m)+PCOexp(m)+ k6*PCO2exp(m));
%r2exp(m)= k3*(PCOexp(m)*PH2Oexp(m)-
(PH2exp(m)*PCO2exp(m)/55))/(PH2exp(m)*PCOexp(m)+k4*PH2Oexp(m));
%r2exp(m)= k3*(PCOexp(m)*PH2Oexp(m)-
((PH2exp(m)^0.5)*PCO2exp(m)/55))/((1+k4*PH2Oexp(m)/(PH2exp(m)^0.5))^2);
r2exp(m)= k3*(PCOexp(m)*PH2Oexp(m)-
((PH2exp(m))*PCO2exp(m)/55))/((1+k4*PH2Oexp(m)/(PH2exp(m)^0.5)+k6*PH2Oexp(m))^2);


PCO(m)=F0(m,6)*(out(m ,1)/(sum(F0(m, 1:2))/0.9));
PH2(m)=F0(m,6)*(out(m ,2)/(sum(F0(m, 1:2))/0.9));
PCO2(m)=F0(m,6)*(out(m ,3)/(sum(F0(m, 1:2))/0.9));
PH2O(m)=F0(m,6)*(out(m ,4)/(sum(F0(m, 1:2))/0.9));

%********** Calculated Reaction Rate at the Exit of the Reactor **********

% Fischer-Tropsch reactions

%r1calc(m)=k1*PH2(m);
%r1calc(m)=k1*PH2(m)*PCO(m)/(k2*PH2O(m)+PCO(m));
%r1calc(m)=k1*PH2(m)*PCO(m)/(k2*PH2O(m)+PCO(m)+k5*PCO2(m));
%r1calc(m)=k1*(PH2(m)^2)*PCO(m)/(k2*PH2O(m)+PCO(m)*PH2(m));
%r1calc(m)=k1*PH2(m)*PCO(m)/((k2*PCO(m)+1)^2);
%r1calc(m)=(k1*(PH2(m)^1.5)*PCO(m)/PH2O(m))/(1+k2*(PH2(m)^1.5)*PCO(m)/PH2O(m));
%r1calc(m)=k1*PH2(m)*PCO(m)/(k2*PCO2(m)+PCO(m));
%r1calc(m)=k1*(PH2(m)^0.5)*PCO(m)/((k2*PH2O(m)+k5*PCO(m)+1)^2);
r1calc(m)=k1*(PH2(m))*PCO(m)/((k2*PH2O(m)+k5*PCO(m)+1)^2);
%r1calc(m)=k1*(PH2(m))*PCO(m)/((k2*PH2O(m)+k5*PCO(m)+1));

%Water-Gas-Shift Reactions


%r2calc(m)=k3*(PCO(m)*PH2O(m)-(PH2(m)*PCO2(m)/55));
%r2calc(m)=k3*(PCO(m)*PH2O(m)-(PH2(m)*PCO2(m)/55))/(k4*PH2O(m)+PCO(m)+k6*PCO2(m));
%r2calc(m)= k3*(PCO(m)*PH2O(m)-(PH2(m)*PCO2(m)/55))/(PH2(m)*PCO(m)+k4*PH2O(m));
%r2calc(m)=k3*(PCO(m)*PH2O(m)-
((PH2(m)^0.5)*PCO2(m)/55))/((1+k4*PH2O(m)/(PH2(m)^0.5))^2);
```

```
r2calc(m)=k3*(PCO(m)*PH2O(m)-
((PH2(m))*PCO2(m)/55))/((1+k4*PH2O(m)/(PH2(m)^0.5)+k6*PH2O(m))^2);
end

%********** Output-Variances **********


VarianceX=0;
SSQ=0;
Variance_r1=0;
Variance_r2=0;
n=[1,2,3,4,5];
for q=1:1:4
Xcalc(q)=(F0(q,1)-out(q,1))*100/F0(q,1);
Xexp (q)=(F0(q,1)-Fexp(q,1))*100/F0(q,1);
VarianceX=(Xcalc(q)-Xexp(q))^2+VarianceX;
SSQ=((Xcalc(q)-Xexp(q))/Xcalc(q))^2+SSQ;
Variance_r1=(r1calc(q)-r1exp(q))^2+Variance_r1;
Variance_r2=(r2calc(q)-r2exp(q))^2+Variance_r2;
end

plot(Xcalc, Xexp, 'o');
VarianceX;
RMSE_FT=(Variance_r1^0.5)/(sum (r1exp));
RMSE_WGS=(Variance_r2^0.5)/(sum (r2exp));
RMSE_X=(VarianceX^0.5)/(sum (Xexp));
result=[x VarianceX  RMSE_X RMSE_FT RMSE_WGS]
SSQ
out
Fexp
r1calc
r1exp
r2calc
r2exp
Xcalc
Xexp
```

Appendix H: Derivation of the Most Suitable Rate Equation

In order to derive the rate equations in Chapter 7, the Langmuir-Hinshelwood-Hougen-Watson approach is used. In other words, one step is assumed to be the rate-determining step and the other steps are at quasi-equilibrium. In addition, the following assumptions are taken into account [1]:

1- One of the pathways including the conversion of CO to the monomer methylene, CH_2, is an irreversible rate-determining step.
2- There is a steady state for concentrations of all intermediates on the catalyst surface.
3- Active catalytic sites (s) are uniform and homogeneously distributed
4- Quasi-equilibrium state is considered for the initial adsorption of hydrogen and carbon monoxide with the gas phase concentrations.
5- Water removal is an irreversible step taking place after CO dissociation.
6- Due to strong adsorption of CO compared to H_2, active sites are more covered by CO or dissociated CO relative to H_2.
7- H_2O may adsorb strongly.

According to the aforementioned assumptions, the most suitable rate model (FT7, Chapter 7) includes the following steps:

$$CO + s \underset{k1'}{\overset{k1}{\leftrightarrow}} COs \qquad \text{(Step 1)}$$

$$COs + Hs \underset{k2'}{\overset{k2}{\leftrightarrow}} HCOs + s \qquad \text{(Step 2)}$$

$$HCOs + Hs \underset{k3'}{\overset{k3}{\leftrightarrow}} Cs + H_2Os \qquad \text{(Step 3)}$$

$$Cs + Hs \underset{k4'}{\overset{k4}{\leftrightarrow}} CHs + s \qquad \text{(Step 4)}$$

$$CHs + Hs \underset{k5'}{\overset{k5}{\leftrightarrow}} CH_2s + s \qquad \text{(Step 5)}$$

$$H_2 + 2s \underset{k6'}{\overset{k6}{\leftrightarrow}} 2Hs \qquad \text{(Step 6)}$$

$$H_2O + s \underset{k7'}{\overset{k7}{\leftrightarrow}} H_2Os \qquad \text{(Step 7)}$$

Assuming the limiting step is Step 3 then

$$r = k_3.\theta_{HCOS}.\theta_{HS} \qquad \text{(H1)}$$

and the other steps are at equilibrium resulting the following equations

$$K_1 = \frac{\theta_{COS}}{P_{CO}.\theta_S} \qquad \text{(H2)}$$

$$K_2 = \frac{\theta_{HCOS}.\theta_S}{\theta_{COS}.\theta_{HS}} \qquad \text{(H3)}$$

$$K_4 = \frac{\theta_{CHS}.\theta_S}{\theta_{CS}.\theta_{HS}} \qquad \text{(H4)}$$

$$K_5 = \frac{\theta_{CH2S}.\theta_S}{\theta_{CHS}.\theta_{HS}} \qquad \text{(H5)}$$

$$K_6 = \frac{\theta_{HS}^2}{P_{H2}.\theta_S^2} \qquad \text{(H6)}$$

$$K_7 = \frac{\theta_{H2OS}}{P_{H2O}.\theta_S} \qquad \text{(H7)}$$

With θ_{HCOS} from Equation H3, Equation H1 will result in

$$r = \frac{k_3.K_2.\theta_{COS}.\theta_{HS}^2}{\theta_S} \qquad \text{(H8)}$$

θ_{HS} can be related to partial pressure of H_2 in gas phase using Equation H6:

$$r = \frac{k_3.K_2.\theta_{COS}.K_6.P_{H2}.\theta_S^2}{\theta_S} \qquad \text{(H9)}$$

θ_{COS} can be calculated from Equation H2:

$$r = k_3.K_2.K_1.P_{CO}.K_6.P_{H2}.\theta_S^2 \qquad \text{(H10)}$$

From assumptions 6 and 7, if it is concluded that only surface carbon and water occupy a significant portion of the total number of sites, then the site balance becomes,

$$\theta_S + \theta_{COS} + \theta_{H2OS} = 1. \qquad \text{(H11)}$$

Substitutions of θ_{COS} and θ_{H2OS} from Equations H2 and H7 result in:

$$\theta_S + K_1.P_{CO}.\theta_S + K_7.P_{H2O}.\theta_S = 1; \qquad \text{(H12)}$$

$$\theta_S = \frac{1}{1 + K_1.P_{CO}. + K_7.P_{H2O}}. \qquad \text{(H13)}$$

Combinations of Equations H10 and H13 give

$$r = \frac{k_3.K_2.K_1.K_6.P_{H2}.P_{CO}}{(1 + K_1.P_{CO} + K_7.P_{H2O})^2}. \qquad \text{(H14)}$$

Equations H14 and H15 are the final formats of the most suitable rate model (FT7) among the different models studied in Chapter 7:

$$r = \frac{k_{FT}.P_{H2}.P_{CO}}{(1 + a.P_{CO} + b.P_{H2O})^2} \qquad \text{(H15)}$$

Reference

[1] G.P. van der Laan, A.A.C.M. Beenackers, Intrinsic kinetics of the gas-solid Fischer-Tropsch and water gas shift reactions over a precipitated iron catalyst, Applied Catalysis A: General, 193 (2000) 39-53.